

Electromagnetic Concepts to Enhance Communication in Harsh RF Environments

by

Seyed Mohammad Amjadi

A dissertation submitted in partial fulfillment
of the requirements for the degree of
Doctor of Philosophy
(Electrical Engineering)
in the University of Michigan
2019

Doctoral Committee:

Professor Kamal Sarabandi, Chair
Professor Anthony Grbic
Professor Nick A. Kotov
Professor Eric Michielssen
Professor Amir Mortazawi

Seyed Mohammad Amjadi

smamjadi@umich.edu

ORCID iD: 0000-0001-7079-940X

© Seyed Mohammad Amjadi
All rights reserved
2019

To my beloved mother and father

Acknowledgements

At the outset, I would like to express my sincere gratitude to my advisor, Professor Kamal Sarabandi, for his guidance, encouragement and extreme support all the way through the course of my PhD. It was an absolute privilege for me to have him not only as my mentor but also as my friend and as my lifelong inspiration. I had more than five amazing years full of passion and excitement working with him to complete this research adventure. I am greatly indebted to my doctoral committee, Professor Eric Michelssen for all the fruitful discussion we had almost every week during the first year of this research work, Professor Anthony Grbic and Professor Amir Mortazawi for all their useful advice and guidance throughout my graduate courses and for their insightful feedback on this research, and Professor Nick Kotov a great professor of chemistry whom I have found the unique opportunity to collaborate with over the past year during which I learned a lot from him. Dr. Adib Nashashibi helped me a lot with laboratory and fabrication works, and it is only appropriate that I express my gratitude to him here.

I would like to take the opportunity to express my thanks to all my teachers who have taught me since my childhood: my high school teachers, my undergraduate teachers, and my graduate teachers. I would like to specifically thank Professor Fawaz Ulaby and Professor Ehsan Afshari, for offering fantastic courses in the area of Electromagnetics and RF circuits out of which I grasped quite a lot.

My thanks are due to my former and current fellow lab-mates in the Radiation Laboratory for their friendship and sharing their views especially, Dr. Leland Pierce, Dr. Mani Kashanianfard, Dr. Jiangfeng Wu, Dr. Meysam Moallem, Dr. Armin Jam, Micheal Benson, Behzad Yektakhah, Menglou Rao, Mohammad Mousavi, Navid Barani, Mostafa Zaki, Tanner Douglas, Dr. Amr Ibrahim, Dr. Jihun Choi, Mohammadreza Sanamzadeh, Milad Zolfagharloo Koochi, Suhyun Nam, and Omar Bakry.

I have been truly blessed to have many wonderful friends in Ann Arbor and elsewhere in the United States who have added spice to my Ph.D life while I have being miles away from my family for the past five years. I would never forget all the wonderful moments we had together. I thank all.

Last but foremost, words have no power to express my appreciation to my beloved parents, Narges and Rasool and my two sisters Saeedeh and Hamideh for their unconditional love, affection, and support. Wherever I am standing today, I certainly owe it to them.

Mohammad Amjadi
January 2019
Ann Arbor

Table of Contents

Dedication	ii
Acknowledgements.....	iii
List of Figures.....	viii
List of Tables	xvii
Abstract.....	xviii
CHAPTER 1 Introduction.....	1
1.1 Background and Motivation.....	1
1.2 Channel Capacity Enhancement in Wireless Communications	5
1.2.1 Internal (self-) Interference Cancellation	6
1.2.2 External Interference Cancellation	10
1.3 Sub-Surface Communication	19
1.4 Contributions.....	21
1.5 Thesis Organization.....	22
CHAPTER 2 Internal (Self-) Interference Cancellation in Wireless Transceivers	25
2.1 Overview	25
2.2 Single-Port Cavity-Backed Slot Antenna (CBSA).....	26
2.2.1 Principle of Operation of the Wideband Cavity-Backed Slot Antenna.....	27
2.2.2 Microstrip to Cavity Transition.....	36
2.2.3 Experimental Results.....	40
2.3 Dual-Port Cavity-Backed Slot Antenna for Full-Duplex Applications.....	44
2.3.1 Dual-Polarized Slotted Cavity.....	45
2.3.2 Cancelation Mechanism	49
2.3.3 Microstrip Feed	51
2.3.4 Waveguide Feed.....	53
2.3.5 Simulation and Experimental Results	61
2.4 Conclusion.....	67

CHAPTER 3	External Interference Cancelation in Wireless Communications ..68
3.1	Overview 68
3.2	Signal Segregation Algorithm using an Iterative Approach (ASSIA) 72
3.2.1	Formulation of ASSIA 72
3.2.2	Mutual Coupling Considerations..... 80
3.2.3	Synthesis Method for Beamforming 81
3.2.4	Convergence Analysis 85
3.2.5	Interference Segregation..... 91
3.2.6	Comparison with Other Techniques 93
3.2.7	Performance Analysis in a Complex Environments 100
3.3	Closely-spaced Nulls Synthesis Method (CNSM) 110
3.3.1	Formulation of CNSM..... 110
3.3.1.1	Two Closely-spaced Signals 111
3.3.1.2	Multiple Closely-spaced Signals 118
3.3.2	Simulation Results and Comparison with Other Methods 122
3.4	Mutual Coupling Mitigation in Multiple Antenna Systems 126
3.4.1	Theory of Feed-Forward Coupling Technique 126
3.4.2	Simulation and Experimental Results of the Feed-Forward Coupling..... 134
3.5	Experimental Results of CNSM..... 143
3.6	Conclusion..... 148
CHAPTER 4	Subsurface Communication150
4.1	Overview 150
4.2	Surface Wave Propagation along the Drilling Pipe..... 151
4.3	Compact Surface-Wave Launcher at HF Band 155
4.4	The Effects of the Bends Along the Drilling Path..... 162
4.5	Experimental Verification 165
4.6	Conclusion..... 168
CHAPTER 5	Where Next170
5.1	Research Summary..... 170
5.2	Future work and Challenges..... 171
5.2.1	Full-Duplex Repeaters for 5G Networks..... 171
5.2.2	Radar Calibration 172
5.2.3	Simplifying the Antenna Structure 173
5.2.4	Applying ASSIA to Fourier Transform, MPM and ML-Based Methods..... 173

5.2.5	Super-Resolution Radars	174
5.2.6	Ultra-Miniatured Surface-Wave Transducer	175
5.2.7	SCTL-Based Radar Systems	175
APPENDIX A		177
REFERENCES.....		185

List of Figures

Figure 1-1: Evolution of communication over time. Image taken from JustiNfo [1].	2
Figure 1-2: Digital and analogue self-interference cancellation in transceivers.	6
Figure 1-3: Different antenna cancellation anatomies.	7
Figure 1-4: A full-duplex BS provides services for multiple half-duplex MSs. Co-channel signals of frequencies f_1 and f_2 arrive at the BS from different directions. Spatial signal segregation algorithms are required to separate these correlated signals at the BS.	11
Figure 1-5: Ray tracing simulation results obtained by EMTerrano simulator for a scenario in Downtown Manhattan. A large number of rays arrive at the receiver array from both the communication transmitter and the jammer.	14
Figure 1-6: (a) Two wideband monoconical antennas illuminated by a plane wave from $\varphi = 0$. Antenna A is shadowed by antenna B. (b) the radiation pattern of antenna A shows significant deviation from omni-direction pattern. This is caused by antenna B shadowing along direction $\varphi = 0$.	16
Figure 1-7: Natural gas production in the U.S. from 1990 to 2040. Shale gas is projected to constitute 49% of the total U.S. gas production in 2040. Data from U.S. Energy Information Administration (EIA) [130].	19
Figure 1-8: The mechanism of hydraulic rotary-drilling. The hydraulic power is provided by the drilling fluid flowing through the drill pipe where it then carries the cuttings back to the surface through the annular space between the drill pipe and the sides of the borehole	20
Figure 1-9: A schematic of the topics covered in the dissertation. Chapter 2 describes methods for self-interference cancellation in wireless transceivers. The focus of chapter 3 is on techniques and algorithms for suppression of external interference. In chapter 4, a telemetry technique for subsurface communication is introduced.	23
Figure 2-1: The thin rectangular cavity fed by a waveguide (a) front view (b) side view. $L_x = L_y = 1.2 \lambda_L$, $H = 0.15 \lambda_L$, $b = 0.07 \lambda_L$.	28

Figure 2-2: The electric field distribution inside the cavity when excited by TE_{10}^Z mode through a waveguide (a) $f = 0.8 f_0$, (b) $f = 1.1 f_0$. Except for the region around the excitation port, $E_y = 0$ everywhere in the cavity..... 28

Figure 2-3: The slotted cavity (a) front view (b) side view. $L_S = 0.45\lambda_L$, $W_S = 0.14\lambda_L$, $S_x = S_y = 0.5\lambda_L$ 29

Figure 2-4: The electric field distribution inside the slotted cavity at $x = 0.15 L_x$ when excited by TE_{10}^Z mode through a waveguide (a) $f = 0.77 f_0$ (b) $f = 1.27 f_0$ 29

Figure 2-5: The magnitude of the reflection coefficient for the slotted cavity shown in Figure 2-3. 31

Figure 2-6: The slotted cavity loaded with metallic septa (a) front view (b) side view. $W_S' = 0.23 \lambda_L$, $L_A = 0.67 \lambda_L$, $L_B = 1.15 \lambda_L$, $W_A = W_B = 0.074 \lambda_L$, $y_A = 0.088 \lambda_L$, $y_B = 0.33 \lambda_L$ 31

Figure 2-7: The reflection coefficient for the slotted cavity loaded with metallic septa shown in Figure 2-6..... 32

Figure 2-8: The electric field distribution inside the slotted cavity loaded with metallic septa excited by TE_{10}^Z mode through a waveguide at $x = 0.2 L_x$. (a) $f = 0.7 f_0$, (b) $f = f_0$, (c) $f = 1.1 f_0$, (d) $f = 1.3 f_0$ 33

Figure 2-9: The distribution of E_z inside the slotted cavity loaded with metallic septa excited by TE_{10z} mode at $z = W_A$ (a) $f = 0.7 f_0$ (b) $f = 0.9 f_0$ (c) $f = 1.1 f_0$ (d) $f = 1.3 f_0$ 34

Figure 2-10: The distribution of E_y across the radiating slots of the CBSA shown in Figure 2-6 at (a) $f = 0.7 f_0$ (b) $f = 0.9 f_0$ (c) $f = 1.1 f_0$ (d) $f = 1.3 f_0$ 35

Figure 2-11: The gain of the CBSA shown in in Figure 2-6 versus frequency. 35

Figure 2-12: The proposed end-launch microstrip to reduced-height waveguide transition. 37

Figure 2-13: The S-parameters of the 7-port network in (a) is used in (b) for circuit simulation and optimization. 37

Figure 2-14: The reflection and transmission coefficient of the transition shown in Figure 2-12. 39

Figure 2-15: The configuration of the cavity-backed slot antenna fed by a microstrip line. 39

Figure 2-16: The cavity-backed slot antenna 3D printed out of silver fed by a microstrip line (a) cavity top view (b) cavity bottom view (c) microstrip top layer (d) microstrip bottom layer (e) assembled antenna..... 41

Figure 2-17. The measured and simulated reflection coefficient of the fabricated CBSA shown in Figure 2-16(e).....	42
Figure 2-18. Measured and simulated co-pol. and cross-pol. radiation pattern in H-plane at (a) $f = 8$ GHz, (b) $f = 9$ GHz, (c) $f = 10$ GHz, (d) $f = 11$ GHz, (e) $f = 12$ GHz.	43
Figure 2-19. Measured and simulated co-pol. and cross-pol. radiation pattern in E-plane at (a) $f = 8$ GHz, (b) $f = 9$ GHz, (c) $f = 10$ GHz, (d) $f = 11$ GHz, (e) $f = 12$ GHz.	43
Figure 2-20. The Measured and simulated antenna gain.	44
Figure 2-21. The slotted cavity loaded by multiple metallic septa (a) radiating slots on the front side (b) feeding slots on the back side, (c) metallic septa inside the cavity.	46
Figure 2-22. The slotted cavity loaded by multiple metallic septa (a) side view, (b) front view.	47
Figure 2-23. The mechanism of shrinking the slots size by appropriately placing the septa. The center-to-center distance between adjacent slots radiating slots is decreased as frequency increases.	48
Figure 2-24. The cross polarized radiation caused by the cross polarized electric field generated across each slot is cancelled by that of the adjacent slot within the main beam due to the structure symmetry.	48
Figure 2-25. The schematic of the feeding topology. The coupling between channels due to depolarization represented by E^C is significantly reduced by this method.	50
Figure 2-26. The microstrip feed laid out on the back side of the cavity.	52
Figure 2-27. A perspective cut view of the air-dielectric microstrip line suspended over ground plane and supported by quarter-wavelength stubs short-circuited to the antenna body to provide mechanical support.	52
Figure 2-28. The coaxial-to-waveguide transition feeding the cavity.	54
Figure 2-29. The electric field distribution along the cross section of the waveguide feed when the waveguide port is excited. (a) $f = 5$ GHz, (b) $f = 6$ GHz, and (c) $f = 7.5$ GHz.	55
Figure 2-30. The electric field distribution across the waveguide feed when the waveguide port is excited. E_y is an even function of y and E_x is an odd function of y (a) E_y at $f = 5$ GHz, (b) E_x at $f = 5$ GHz, (c) E_y at $f = 6$ GHz, (d) E_x at $f = 6$ GHz, (e) E_y at $f = 7.5$ GHz, (f) E_x at $f = 7.5$ GHz.	56

Figure 2-31. Tangential magnetic field on the microstrip line when the waveguide port is excited. (a) $f = 5$ GHz, (a) $f = 6$ GHz, (c) $f = 7.5$ GHz. The current at the microstrip terminal is very small.	57
Figure 2-32. The feeding topology composed of a rectangular waveguide, an air-dielectric parallel plate transmission line, and a broadside-coupled stripline. (a) Perspective view, (b) cut view.	58
Figure 2-33. The electric field distribution along the transition shown in Fig (a) $f = 5$ GHz, (b) $f = 6$ GHz, (c) $f = 7.2$ GHz.	59
Figure 2-34. The electric field distribution along the transition shown in Fig (a) $f = 5$ GHz, (b) $f = 6$ GHz, (c) $f = 7.2$ GHz.	60
Figure 2-35. The fabricated antenna. (a-d) Different parts of the antenna 3D printed out of HP PA12 Nylon. (e and f) The metalized and assembled antenna.	62
Figure 2-36. The simulated and measured S-parameters. (a) Reflection coefficient, and (b) isolation.	63
Figure 2-37. The measured radiation pattern (a) V-pol H-plane (b) H-pole H-plane (c) V-pole E-plane (d) H-pole E-plane.	64
Figure 2-38. The measured antenna gain.	65
Figure 2-39. The S-parameters of the antenna shown in Figure 2-32.	66
Figure 3-1. External interference including jamming signals, multipaths of the signal, or signal coming from the other users can reduce the channel capacity of a wireless link.	68
Figure 3-2. A MIMO system in a multipath environment. The jamming signal results in erroneous channel estimation.	69
Figure 3-3. The proposed modified MIMO system.	70
Figure 3-4. Circular array of omnidirectional antennas illuminated by a number of interfering and desired signals.	73
Figure 3-5. The sketch of a uniform circular array illuminated by a plane wave.	74
Figure 3-6. The normalized effective length of the array given by (3-40). The condition $\Delta\phi_b > \Delta\phi_a$ is necessary for the convergence of the algorithm.	86
Figure 3-7. The maximum side-lobe level versus number of signals required for convergence for an array with the effective length given by (3-46).	89
Figure 3-8. The LDR mode where jammer cancellation is accomplished by turning the transmitter on and off with a pattern known to the receiver. The directions of	

arrival and levels of the jammer is estimated during the off cycle and used to cancel the jammer signal during the on-cycle.	90
Figure 3-9. Estimated directions of arrival versus iteration number. The red lines represent the truth and the symbols denote the estimated values.	93
Figure 3-10. Estimated magnitudes of the signals versus iteration number. The red lines represent the truth and the symbols denote the estimated values.	94
Figure 3-11. The RMSE in estimating φ_4 versus SNR_4 using different techniques for the scenario in which four correlated signals of different SNRs listed in Table 3-2 are impinging on the array.	96
Figure 3-12. The Computation burden of ASSIA compared to other methods for the four-signal scenario.....	97
Figure 3-13. The RMSE in estimating φ_7 versus SNR_7 using different techniques for the scenario in which seven correlated signals of different SNRs listed in Table 3-3 are impinging on the array.	99
Figure 3-14. (a) An example scenario for HDR mode, (b) detected signals (Center frequency component) for this scenario.....	102
Figure 3-15. (a) An example scenario for LDR mode. (b) Detected signals (Center frequency component) for when the transmitter is off, (c) Detected signals (Center frequency component) when the transmitter is on.....	103
Figure 3-16. Number of DoAs of the desired (black pentagrams) and the jamming (red squares) signals and $S/(J+N)$ after mitigation (green circles) in HDR mode for 38 receiver locations.	106
Figure 3-17. Number of DoAs of the desired (black pentagrams) and the jamming (red squares) signal and $S/(J+N)$ after mitigation (green circles) in LDR mode for 11 receiver locations.	106
Figure 3-18. The sketch of the received rays for (a) Receiver location 1, (b) Receiver location 2. The receiver operates in HDR mode in these locations.....	107
Figure 3-19. The sketch of the received rays for (a) Receiver location 3, (b) Receiver location 4. The receiver operates in LDR mode in these locations.	108
Figure 3-20. $S/(J+N)$ after cancellation versus S/J before cancellation for 4 different receiver locations demonstrated in Figure 3-15 and Figure 3-16.....	109
Figure 3-21. The plot of functions $F(\varphi)$, $F_s(\varphi)$, and the array pattern denoted by $L_{\text{eff}}(\varphi)$. .	111
Figure 3-22. $G(\varphi_0)$ versus φ_z for $\Delta\varphi = 0.3\text{BW}$ for different array sizes. $G(\varphi_0)$ is maximized at $\varphi_z = 0.7\pi$ and $\varphi_z = 0.55\pi$ for $M = 6$ and $M = 24$ respectively.....	113

Figure 3-23. G_F/G_{FS} versus the circular array elements number with inter-element spacing of $\lambda/3$ for $\Delta\varphi = \pi/12$	114
Figure 3-24. GF and GFs versus nulls separation for a 12-element circular antenna array with element spacing of $\lambda/3$	114
Figure 3-25. The search region shown in gray over which $F(\varphi)$ is realized for different values of φ_{null}^1 and φ_{null}^2 . Also, shown is the focused pattern of the array in direction $\varphi_d = 0$	116
Figure 3-26. The search region for φ_{null}^1 and φ_{null}^2 . It is assumed that $\varphi_1 < \varphi_2$	116
Figure 3-27. The plot of the error function given by (3-70) calculated within the search region for two different scenarios: (a) only one signal is arriving from $\varphi = 80^\circ$ (b) two closely spaced signals are arriving from $\varphi_1 = 70^\circ$ and $\varphi_2 = 80^\circ$	117
Figure 3-28. The plot of functions $F_N(\varphi)$, $F_{SN}(\varphi)$, and the array pattern for $N = 4$	119
Figure 3-29. G_{FN} versus number of the signals for $M = 12$ and $\Delta\varphi_{min} = \pi/12$	120
Figure 3-30. The nulls locations scheme for arrays with large number of elements assuming $\varphi_0 = 0$	122
Figure 3-31. The percentage of error in the DoA estimation of signal 2 normalized to half power beamwidth as a function of ρ_{12} . In this scenario, $SNR_1 = SNR_2 = 15$ dB and $\varphi_2 - \varphi_1 = 0.125$ BW. MPM and Root MUSIC with spatial smoothing methods failed in this scenario.	123
Figure 3-32. The percentage of error in the DoA estimation of signal 2 normalized to half power beamwidth as a function of $SNR_1 = SNR_2 = SNR$ for the second experiment. In this scenario, $\rho_{12} = 0.5$ and $\varphi_2 - \varphi_1 = 0.125$ BW. MPM and Root MUSIC with spatial smoothing methods failed in this scenario.	124
Figure 3-33. The percentage of DoA estimation error normalized to half power beamwidth as a function of $SNR_1 = SNR_2 = SNR_3 = SNR$ and for different signals angular separation for the three-signal scenario where $\rho_{13} = \rho_{23} = 0.85$ and $\rho_{12} = 0.5$. ML-AP, MPM, and Root MUSIC with spatial smoothing methods failed to resolve the signals in this experiment.....	125
Figure 3-34. Near-field coupling cancellation for two adjacent biconical antennas using feed-forward paths. (Transmit mode demonstration when antenna A is excited) ..	127
Figure 3-35. The schematic of the feed-forward current. (a) Low frequency (b) High frequency. The feed-forward current path on the antennas is frequency dependent. As frequency increases, the feed-forward current path length on the antennas is decreased.	129

Figure 3-36. The phase of the feed-forward current at point M when antenna A is excited which is obtained by a full-wave simulation. The phase variation is less than $\pm 16^\circ$ 131

Figure 3-37. Phase of S_{21} for the two-element array shown in Figure 3-31 (red line) and phase of the feed-forward current (black line)..... 131

Figure 3-38. (a) The geometry of the feed-forward lines applied to a 12-element circular array of mono-conical antennas (b) vector representation of the coupling cancellation scheme by the feed-forward currents. In (b), S_{21} and S_{31} are the scattering parameters of the array before applying the feed-forward lines and S_{21}^{ff} and S_{31}^{ff} are the scattering parameters due to the feed-forward lines. 132

Figure 3-39. Phase of S_{21} for the 12-element circular array shown in Figure 3-35(a) before inserting feed-forward lines. Similar to the two-element array, the phase of S_{21} is approximately a linear function of frequency. 133

Figure 3-40. The scattering parameters of the two-element array before and after applying coupling mitigation technique. (a) Reflection coefficient (b) Coupling coefficient. 135

Figure 3-41. The radiation pattern of antenna (a) without the feed-forward lines, and (b) with the feed-forward lines are applied. The shadowing effect is reduced after applying feed-forward lines. 136

Figure 3-42. The total current intensity on the antennas before and after applying the feed-forward technique (a) low frequency (b) high frequency. 136

Figure 3-43. The feed-forward lines configuration applied to the 12-element circular array of mono-conical antennas. (a) Top view (b) Side view. 137

Figure 3-44. The fabricated 12-element circular mono-conical antenna array out of copper and the tin surface finished feed-forward strips printed on 30 mil RT5880. (a) Disassembled (b) Assembled by means of soldering. 138

Figure 3-45. Current distribution on the 12-element circular array of mono-conical antennas obtained by full-wave simulation (a) without feed-forward paths (b) with feed-forward paths. The induced current on the other antennas due to the near-field coupling is mitigated by the excited feed-forward current. 139

Figure 3-46. Simulated and measured scattering parameters of the 12-element circular array. (a) Reflection coefficient (b-g) Coupling coefficients..... 140

Figure 3-47. Simulated and measured radiation pattern of the deriving antenna in the circular array in the azimuth plane. The shadowing effect is reduced when the feed-forward transmission lines are introduced between the array elements. The radiation nulls are removed at all frequencies. 142

Figure 3-48. The measured average gain deviation of each antenna in the 12-element array from isolated antenna in the azimuth plane before (red line) and after (black line) applying the feed-forward paths. 143

Figure 3-49. The experimental setup consisting a two-port vector network analyzer and a 12-element circular array of diameter $d = 1.65 \lambda$ composed of mono-conical antennas. Directive horn antennas of maximum dimension $D = 3 \lambda$ are placed at a distance of $L = 66 \lambda$ from the receiver to create impinging plane waves on the circular array. 144

Figure 3-50. The simulated and measured radiation patterns, $|I_{\text{eff}}(\varphi)|$, of each mono-conical antenna element of the circular array shown in Figure 3-46 in azimuth plane. The red line represents the radiation pattern of the isolated antenna. 144

Figure 3-51. The percentage of error of the estimated DoAs normalized to the half power beamwidth versus correlation coefficient for different angular separation of signals obtained from the measurement setup shown in Figure 3-46. In this experiment, $\text{SNR}_1 = \text{SNR}_2 = 20\text{dB}$ 147

Figure 3-52. The percentage of error of the estimated DoAs normalized to the half power beamwidth versus correlation coefficient for different angular separation of signals obtained from the simulation of the same scenario as the one shown in Figure 3-46 considering a circular array without any imperfection. In this simulation, $\text{SNR}_1 = \text{SNR}_2 = 20\text{dB}$ 147

Figure 3-53. The percentage of error of the estimated DoAs normalized to the half power beamwidth versus SNR for different angular separation of signals computed from the measured data using the measurement setup shown in Figure 3-46. In this experiment $\rho_{12} = 0.5$ 148

Figure 4-1. The geometry of the cylindrical conductor coated with a lossy dielectric (mud) immersed in another lossy dielectric medium (soil). (a) Cross section view, (b) Side view. 152

Figure 4-2. (a) The imaginary part of βz and (b) the real part of $\alpha \rho_{\text{soil}}$ versus frequency for different humidity conditions of the background soil: $0.05 < \epsilon''_{\text{soil}} < 0.3$ which corresponds to $15\mu\text{S} < \sigma_{\text{soil}} < 100\mu\text{S}$ at 6 MHz. 154

Figure 4-3. The proposed low-profile surface wave launcher. (a) Cross-section side view inside the borehole (b) launcher side view. 156

Figure 4-4. The equivalent circuit model of the launcher shown in Figure 4-3. 157

Figure 4-5. The current distribution on the launcher (a) helical conductor, (b) inner conductor (drill pipe). 159

Figure 4-6. The electric field around the launcher. (a) Radial (E_ρ), (b) axial (E_z), 159

Figure 4-7. Normalized $|E_p|$ on the SCTL for different soil moisture conditions. (a) $\epsilon_{\text{soil}} = 2.6-j0.05$, $f = 6.3$ MHz, (b) $\epsilon_{\text{soil}} = 3.3-j0.1$, $f = 6.08$ MHz, (c) $\epsilon_{\text{soil}} = 4-j0.2$, $f = 5.9$ MHz (d) $\epsilon_{\text{soil}} = 5-j0.3$, $f = 5.7$ MHz. 160

Figure 4-8. The Electric field distribution along SCTL of length $L = 10\lambda$ immersed in a soil/rock medium of permittivity $\epsilon_{\text{soil}} = 2.6-j0.05$ at $f = 6.3$ MHz. (a) Radial electric field (E_p), (b) axial electric field (E_z). 161

Figure 4-9. (a) The reflection and (b) the transmission coefficients for the SCTL of length $L = 300\text{m}$ terminated by the launcher shown in Figure 4-3 at both ends for different dielectric constants of the soil. The transmission loss can be as low as 30 dB/Km and as high as 90 dB/Km for dry and wet soil conditions..... 162

Figure 4-10. A 90°-bend SCTL of total length $L = 150\text{m}$ which is analyzed by a full-wave solver to examine the bend effects for different radii of curvature. 163

Figure 4-11. (a) The reflection and (b) the transmission coefficients for the 90°-bend SCTL of length $L = 150\text{m}$ shown in Figure 4-10 immersed in a soil/rock medium of permittivity $\epsilon_{\text{soil}} = 2.6-j0.05$ and terminated by the launcher at both ends for different radii of curvature..... 164

Figure 4-12. The electric field distribution E along a 90°-bend ($R_{\text{curvature}} = 0.16\lambda = 5\text{m}$) on a 5λ -long SCTL immersed in a soil/rock medium of permittivity $\epsilon_{\text{soil}} = 2.6-j0.05$ at $f = 5.9$ MHz. 165

Figure 4-13. The designed transducer at VHF. 166

Figure 4-14. The fabricated transducer a VHF band. 167

Figure 4-15. The experimental setup for testing the transducer. A 4AWG wire of length $L = 9.3\lambda = 20\text{m}$ is used as the SCTL. The wire is terminated by the transducer at both ends. One transducer is excited by the network analyzer to measure the reflection coefficient. The transmitted power is $P_t = 10$ dBm. The receiving side is connected to the spectrum analyzer to measure the transmission loss..... 167

Figure 4-16. The measured transmission and reflection coefficient for the SCTL shown in Figure 4-15..... 168

Figure 5-1. (a) Half-duplex repeater, (b) full-duplex repeater. Full-duplex antenna systems enable full-duplex repeaters to increase the throughput of the 5G networks. 172

Figure 5-2. ASSIA-CNSM enables super cross-range resolution radars. 175

Figure 5-3. The borehole and drilling tools. The region between the blade boundary and the drilling pipe is the available space to accommodate the launcher. Further miniaturized surface-wave launcher is required to fit within this space..... 176

Figure 5-4. An SCTL-based radar system for monitoring the ground formations. 176

List of Tables

Table 2-1. The dimensions of the transition shown in Figure 2-12	38
Table 2-2. The dimensions of the CBSA shown in Figure 2-6.....	39
Table 2-3. The dimensions of the transition shown in Figure 2-15	40
Table 2-4. The side lobe levels in E and H planes at different frequencies.....	44
Table 2-5. Comparison of the cavity-backed slot antennas with the proposed CBSA	45
Table 2-6. Dimensions of the cavity shown in Figure 2-21	61
Table 2-7. Dimensions of the microstrip feed shown in Figure 2-26	61
Table 2-8. Dimensions of the waveguide feed shown in Figure 2-28	61
Table 2-9. The optimized values of the feed parameters shown in Figure 2-32.....	65
Table 2-9. The optimized values of the feed parameters shown in Figure 2-32.....	66
Table 3-1. The summary of ASSIA	82
Table 3-2. The directions of arrival and SNRs for the four-signal scenario.....	96
Table 3-3. The directions of arrival and SNRs for the seven-signal scenario	99
Table 3-4. The directions and SNRs of the sources for the first experiment.....	123
Table 3-5. The optimized parameters of the 12-element circular array shown in Figure 3-40	138
Table 4-1. The relative dielectric constant of soil/rock for low moisture contents from 1 MHz to 15 MHz.	153
Table 4-2. The optimized values of the launcher dimensions shown in Figure 4-3	157
Table 4-3. The transmission loss of the drill pipe-drilling mud SCTL compared with the existing short dipole antenna method at 6 MHz for a transmission distance of 300 m	162

Abstract

Given the limited spectrum resources, planning of the future wireless networks such as fifth generation and beyond to be deployed in very congested and complex electromagnetic environments requires techniques for efficient co-channel external and internal (self-) interference cancelation. Benefited from electromagnetic concepts, signal processing techniques, or combination of both, the first part of this research reports on workable solutions for 1) the mitigation of self-interference issue in wireless transceivers for enabling full-duplex communication and 2) the cancelation of external interference caused by the other users, multipath effects, or jammers.

To develop the antenna system for enabling self-interference cancelation, in the first step, a compact, single-port slot antenna is designed which provides a minimum gain of 11 dB and an aperture efficiency of 65% over 40% fractional bandwidth. Next, the antenna is evolved to a common-aperture two-port antenna system with a very high level of isolation between channels over a wide bandwidth yet maintaining consistent radiation characteristics. A low-loss air-dielectric microstrip feed is designed which can be integrated with the other parts of the antenna and is amenable to 3D printing technology. The proposed decoupling method can potentially provide nearly 90 dB of channels isolation over 44% fractional bandwidth. For the fabricated antenna, a minimum isolation of 55 dB and a minimum gain of 10 dB is measured over the entire band.

To manage external interference, novel array signal segregation algorithms have been developed to spatially retrieve the desired signals in the presence of strong interfering signals.

Using a uniform circular array, the algorithms are formulated to account for mutual coupling among array elements. A frequency domain Array Signal Segregation using an Iterative Approach (ASSIA) is presented to estimate the directions of arrival, magnitudes and phases of the signals' spectral components. A statistical analysis in a complex environment with Rayleigh fading characteristics shows that ASSIA radio with a 12-element circular array can improve the signal to jammer ratio from -20 dB to at least +2 dB in more than 70% of occasions. In conjunction with ASSIA, a super-resolution signal detection algorithm based on a novel Closely spaced Nulls Synthesis Method (CNSM) is then developed which, for the first time, demonstrates capability of an antenna array in resolving direction of arrival of closely spaced correlated signals in the absence of a priori knowledge of the number of the incident signals. It is demonstrated that the proposed ASSIA-CNSM is superior to the other super-resolution Directions of Arrivals (DoA) estimation techniques such as Maximum Likelihood method. To improve the performance of the proposed algorithms, an efficient feed-forward technique is presented to mitigate the mutual coupling effects in multiple antenna systems.

Subsurface communication is another challenging task mainly due to the very lossy ground formations. In smart directional drilling, for instance, the existing telemetry methods do not meet the required data-rate for real time monitoring and controlling purposes. The second part of this work reports on a robust, cost-effective and high data-rate communication technique for enabling long-distance communication in drilling process. The concept of using the drilling tools as a Single Conductor Transmission Line (SCTL) is introduced and a very compact SCTL transducer that fits inside the borehole is designed at low HF band. The

transducer provides 2% fractional bandwidth and can be used to enable data transmission at a data rate of 60 kbps.

CHAPTER 1 Introduction

1.1 Background and Motivation

With the world drowning in data traffic, the need to enhance the efficiency of the communication systems is, now, more than ever. Over the course of years, communication, as a key to human development, has evolved from its infancy to maturity. The history of this evolution is briefed in Figure 1-1 [1]. In its very beginning stages, smoke, light, or drums were used to convey messages. Communication by flags was another way of signaling in navies which is still being used by sailors in some circumstances. Optical telegraphy invented in 1792 by Claude Chappe was the first system of conveying information over long distances by means of visual signals using towers with pivoting shutters and was popular in the late eighteenth century. Thanks to the invention of electric battery in 1799 by Alessandro Volta, electric telegraph was developed in 1837 by Samuel Morse as the first wired communication line and became operational in 1844 when it was used to make a link from Washington to Baltimore using copper wires. Telephony emerged with the invention of telephone in 1870 by Alexander Graham Bell and could provide communication over several hundred miles. The foundation of wireless communication was laid by the works of Oersted, Ampere, Faraday, Gauss, Maxwell, and Hertz. In 1820, Oersted showed that an electric current generates a magnetic field. In 1831, Michael Faraday demonstrated that a moving magnet in the vicinity of a conductor induces current on the conductor deducing that a changing



Figure 1-1: Evolution of communication over time. Image taken from JustiNfo [1].

magnetic field produces an electric field. In 1864, James C. Maxwell put all these observations together and predicted the existence of electromagnetic radiation and

formulated the basic theory of electromagnetics which was verified experimentally later on in 1887 by Heinrich Hertz. However, it was not until 1894, when Oliver Lodge used the results of these works to make a sensitive device capable of detecting radio signals called coherer to demonstrate wireless communication. In 1897, Guglielmo Marconi published a patent demonstrating a wireless telegraph system and launched the Wireless Telegraph and Signal Company. Long-distance wired and wireless communications became feasible by the invention of vacuum tube by Fleming in 1904 and vacuum triode amplifier by Lee De Forest in 1906. Amplitude Modulation (AM) and Frequency Modulation (FM) introduced by Edwin Armstrong in 1920 and 1933 respectively were other significant developments in radio communication.

Mid-twentieth century witnessed the invention of the transistor by Walter Brattain, John Bardeen, and William Shockley in 1947, the integrated circuit in 1958 by Jack Kilby and Robert Noyce, and the laser by Townes and Schawlow in 1958. With the advent of these technologies, development of small-size, and high-speed electronic circuits for construction of lightweight wireless transceivers could be conceived. In the early 1980s, communication companies started to replace copper wires with fiber optic cables as the infrastructure to provide extremely high-speed data transmission. The first cellular mobile network was developed in 1981 as an effective way of assigning frequency spectrum to different users while minimizing co-channel interference to provide communication services for maximum number nomadic users. To enhance the throughput of the wireless networks in congested environments, different forms of channel access schemes viz. Frequency Division Multiple Access (FDMA), Time Division Multiple Access (TDMA), Code Division Multiple Access (CDMA), and Polarization Diversity Multiple Access (PDMA) have been developed [2]. The

origin of FDMA dates back to 1900 when Marconi invented a “Tuned Circuit” to enable frequency division multiplexing. By the advent of computer technology in 1950’s, TDMA was introduced in which users’ signals are transmitted in separate time slots. The invention of CDMA or spread spectrum also dates back 1950’s. In CDMA, hence the name, the users’ signals are isolated by orthogonal codes. CDMA requires a large bandwidth for each user and is more immune to interference or jamming as the jamming signals is converted to wideband noise-like signal after demodulation by the receiver. Multiple Input Multiple output (MIMO) technique is another groundbreaking technology that is fueled by better understanding of electromagnetic and wave propagation and has adopted into communication systems to provide diversity and multiplexing gain in rich multipath environments through Eigen beam forming, Space-Time coding, and Spatial Multiplexing. MIMO has resulted in lower required transmit power, greater range, more noise immunity and higher throughputs [3].

We are now at the dawn of the modern communication era facing a significant growth in mobile data traffic and number of the wireless devices. Albeit, the advances in both software and hardware have been very phenomenal, there is still room to leverage the available spectrum in wireless communication systems.

Subsurface communication is another area for which more efficient techniques are still needed to be developed. In borehole drilling for exploration and extraction of oil and gas, for instance, bilateral communication between downhole and the surface is required for monitoring the conditions at the tip of the drill bit to ensure cost-effective use of expensive drilling rigs, to prevent tools failure, and to steer the drill bit towards the target region. Measurement While Drilling (MWD) data transmission is currently carried out by different

techniques such as acoustic mud pulse telemetry [4], [5] wired drill pipe technology [6], and electromagnetic wireless links [7], [8]. In acoustic mud pulse telemetry, the data is converted to pressure fluctuation which is then transmitted through the annular drilling mud fluid. Mud-pulse telemetry, however, provides a very low data rate and is not reliable. Wired drill pipe technology utilizes electrical cables built into the drill pipe. This technology offers much faster data transmission but has not turned to common practice as the required equipment is still expensive and is prone to failure. Electromagnetic wireless links provides faster data transmission compared to acoustic mud pulse telemetry but cannot be established over long distances due to huge signal attenuation through the very lossy ground formations [9]. Alternative techniques must be explored for more efficient subsurface communication among which, not least are those in which the available infrastructures are genuinely cashed in.

The impetus behind this research work is to provide solutions for some of the challenges of today's and tomorrow's communication systems by exploiting electromagnetic concepts, signal processing techniques or combination of both.

1.2 Channel Capacity Enhancement in Wireless Communications

In wireless communications, as described above, different multiple access technologies have been developed to increase their spectral efficiency as measured by the number of information bits successfully communicated per seconds per Hertz. After all, the upper limit of the capacity of the existing wireless networks is imposed by co-channel interference. Co-channel interference can be either internal or external both of which have been addressed in this dissertation.

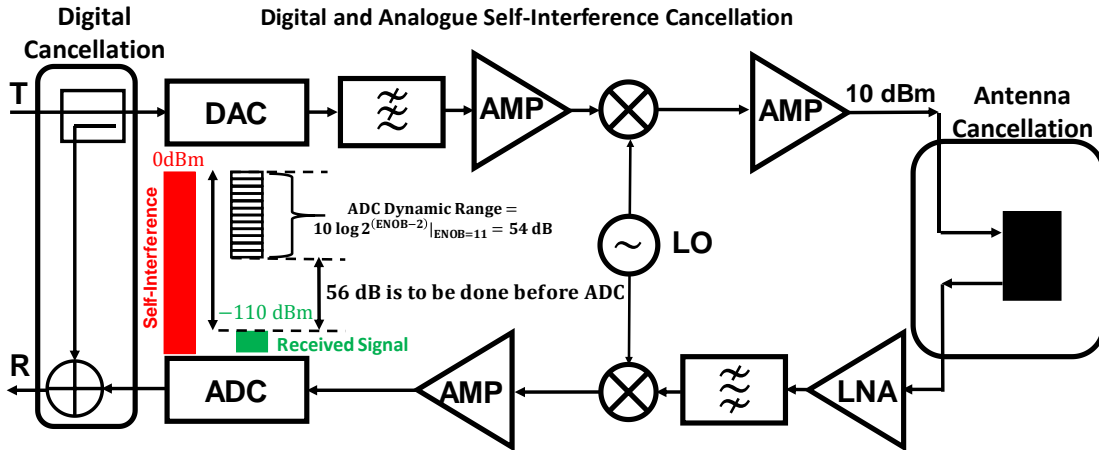


Figure 1-2: Digital and analogue self-interference cancellation in transceivers.

1.2.1 Internal (self-) Interference Cancellation

Current transceivers contain transmitter and receiver pairs put closed together which operate in time-division duplex or frequency-division duplex modes meaning they transmit and receive either at different times or over different frequency bands. Enabling a wireless node to transmit and receive at the same time and over the same frequency bands i.e. operating in full-duplex, offers the potential to double the channel capacity. This, however, requires a daunting amount of co-channel self-interference cancellation. Co-channel self-interference refers to the strong signal leaking from the transmitter to the receiver which kills the desired communication signal being received by the transceiver. The required level of cancellation is around 110 dB for femtocells and even more for larger cells as the transmit power is proportional to the cell size. The recent moves towards development of short-range wireless networks with lower transmit power such as 5G and Wi-Fi have propelled substantial research for realizing full-duplex systems as the self-interference issue is more amenable to treat in such networks. In theory, since the transmit signal is known, it is possible

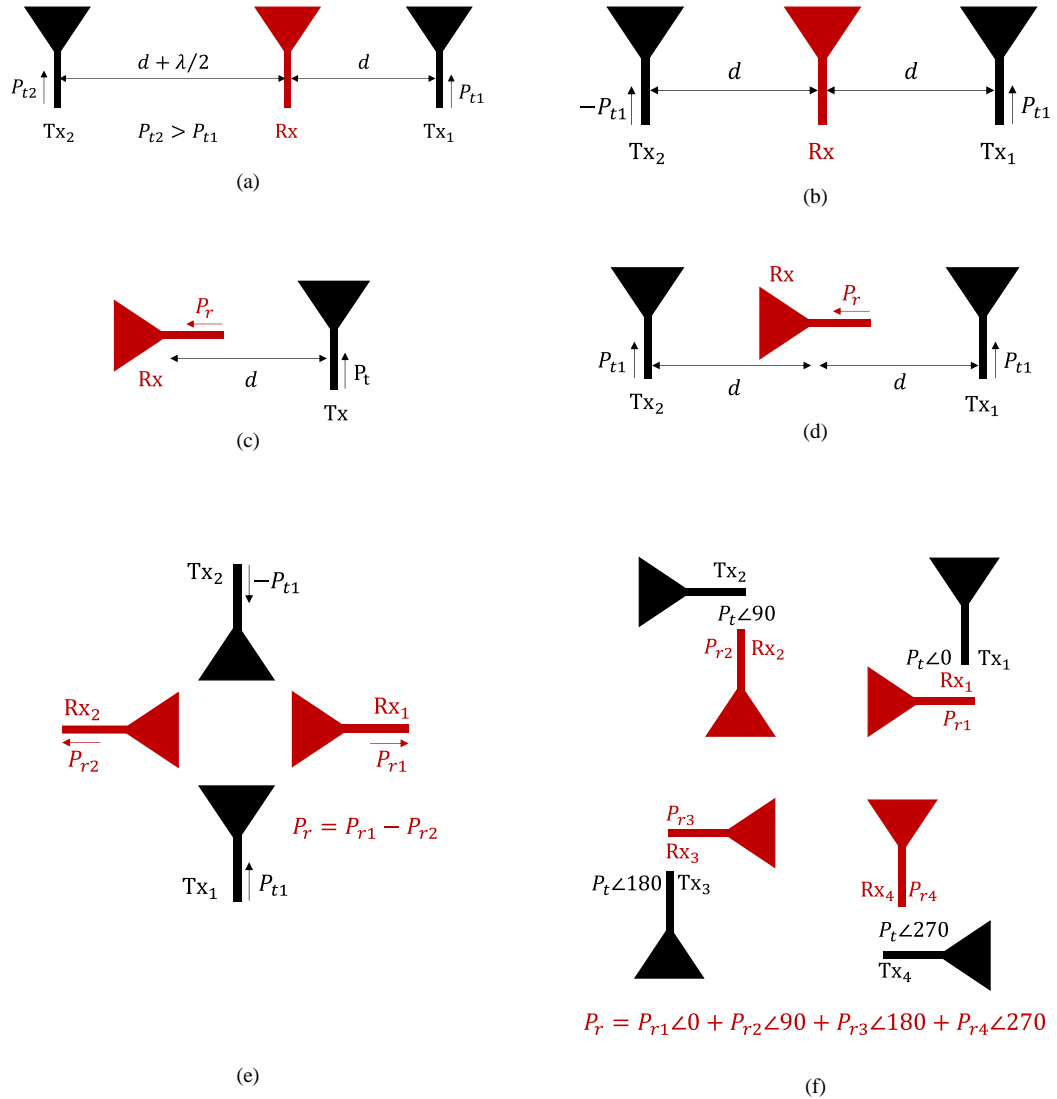


Figure 1-3: Different antenna cancellation anatomies.

to tap a copy of the transmitted signal with appropriate phase and gain and subtract it from the received signal, provided that the transfer function from TX to RX is known. This can be done in both digital and analogue domains as shown in Figure 1-2 . The achievable level of self-interference cancellation in digital domain is, however, limited by the dynamic range of the Analogue-to-Digital-Convertor (ADC). The maximum Effective Number of Bits (ENOB) of the commercial ADCs is 11 which provides a Dynamic Range (DR) of $DR = 6(ENOB - 2) = 54$ dB which is by far less than the required cancellation level [10]. Besides,

other factors such as oscillator phase noise, nonlinearities of amplifiers and mixers, and the error in the estimation of the transfer function from TX to RX further reduce the performance of digital cancellation. This suggests that, the self-interference signal should be suppressed to a great extent (≈ 60 dB) before ADC in analogue domain. Analogue cancellation can be implemented through either analogue circuitry or proper antenna structures. Antenna cancellation refers to different configurations for the transmitting and receiving antennas at a single node that provides more isolation between the transmitter and the receiver. Multiple variations of this method are shown in Figure 1-3. Figure 1-3(a) shows the scheme in which two antennas are used as the transmitter antennas whose distances from the co-polarized receiver antenna differs by half a wavelength [11]. If the magnitudes of the transmit signals from Tx_1 and Tx_2 are adjusted appropriately to compensate for different free-space path losses, then the coupled signal from Tx_1 to the receiver will be equal in magnitude and out-of-phase with that of from Tx_2 to the receiver and ,thereby, perfect decoupling can be obtained. In practice, however, due to the fabrication errors, the isolation will not be perfect. In another method shown in Figure 1-3(b), an architecture similar to Figure 1-3(a) where now the transmit antennas are placed at similar distances from the receiver and the Tx antennas are fed with equal-magnitude and out-of-phase signals [12]. The problem with this method is that the transmit radiation pattern has a null in the boresight direction. Figure 1-3(c) demonstrates the case where orthogonal polarizations are used for simultaneous transmit and receive [13]. In practice, the isolation level achieved by this method does not exceed 40 dB for collocated antennas. Figure 1-3(d) shows another method in which orthogonal polarizations are used for transmission and reception [14]. Appropriately designed, around 35 dB of isolation between the transmitter and the receiver can be achieved

by this technique Using two pairs of antennas with orthogonal polarizations in a four-fold symmetry arrangement as shown in Figure 1-3(e) is another approach reported in the literature [15]. Two antennas of the same polarization are excited out of phase and used as transmitting antennas and the other two are used as receiving antennas whose received signals are combined out-of-phase. Although, infinite isolation can be theoretically obtained by this method using ideal hybrids, the realized isolation level is significantly degraded when the phase and amplitude imbalances of the actual hybrids are introduced. Figure 1-3(f) shows a co-polarized full-duplex antenna system with circular polarizations [16, 17, 18, 19]. In this arrangement, four pairs of antennas with four-fold symmetry are used to generate circular polarizations. A phase progression of 90° is applied to the transmit/receive signals before dividing/combining. The theoretic isolation level is infinite in case of perfect hybrids. However, the isolation obtained by this method is very sensitive to the hybrid imbalances as the distance between adjacent antennas is very small. In practice, the achieved isolation barely reaches 45 dB. Chapter 1 of this dissertation focuses on the design and fabrication of compact broadband antenna systems for enabling full-duplex communication. Cavity-Backed Slot Antenna (CBSA) is chosen as the base structure for its compactness. Microstrip antenna is another low-profile antenna that may be used for this application. However, microstrip antennas, when used as the elements of an array, are susceptible to scan blindness due to surface wave generation. Surface wave propagation in the substrate of the antenna arrays also results in less radiation efficiency and more mutual coupling between elements. Surface wave obstruction is the advantage of the slot antennas over microstrip antennas in array configurations. The bandwidth of the vast majority of CBSAs is very limited. The first CBSA was introduced in 1969 by Lindberg [20] for satellite communications which provided

less than 20% bandwidth. A broadband version of [20] using ridged waveguide was later reported in 1974 [21] with a return loss better than 9 dB over 31% bandwidth. The length of the slots in the structures reported in [20], [21] is about one wavelength which is not suitable for array applications due to the occurrence of the grating lobes. More recently, a novel low-profile cavity design was integrated with a miniaturized slot antenna to create a small form factor CBSA but shows low bandwidth [22]. Different techniques have been employed to enhance the bandwidth and the gain of CBSAs while keeping the antenna compact. By using an off-center microstrip-fed slot configuration [23], a compact substrate-integrated CBSA is designed in [24] which offers 19% bandwidth. The bandwidth of other reported CBSAs [25, 26, 27, 28, 29, 30, 31, 32, 33, 34] do not exceed 21%. In chapter 1, first, a single channel broadband CBSA better performance compared to [35, 36, 37], is designed. The antenna is then evolved to a dual channel fully-populated common-aperture CBSA with very high isolation between channels.

1.2.2 External Interference Cancellation

External interference caused by other communication transmitters or jammers is another issue that severely affect the performance of wireless communication systems. External interference could also be introduced unintentionally due to multipath effects. Based on Shannon-Hartley theorem, the maximum rate at which the information can be transmitted over a specific bandwidth is given by [38]:

$$C = \int_B \log_2 \left(1 + \frac{S(f)}{I(f) + N(f)} \right) df \quad (1-1)$$

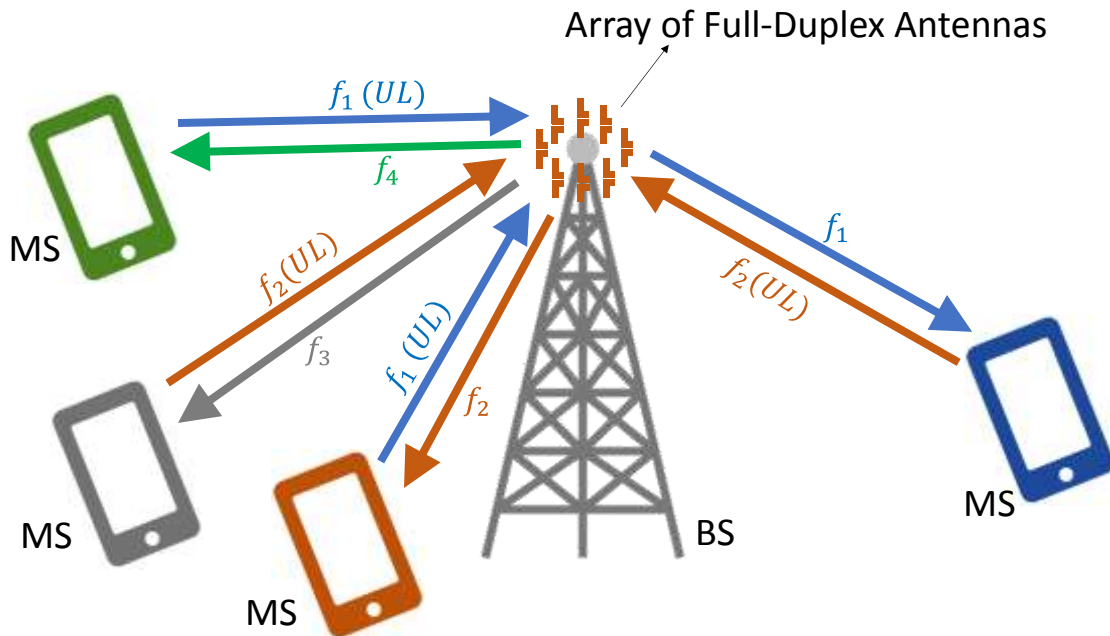


Figure 1-4: A full-duplex BS provides services for multiple half-duplex MSs. Co-channel signals of frequencies f_1 and f_2 arrive at the BS from different directions. Spatial signal segregation algorithms are required to separate these correlated signals at the BS.

where C is the channel capacity, B is the channel bandwidth, $S(f)$ is the signal power spectrum, $I(f)$ is the interference power spectrum, and $N(f)$ is the noise power spectrum. Co-channel interference from other wireless nodes causes the channel capacity to drop. Multipath interference is another issue which degrades the performance of Single-Input-Single-Output (SISO) systems. MIMO has been developed as an efficient technique that enables segregating interfering signals from desired signal through spatial multiplexing. Consider a Base Station (BS) providing services to half-duplex Mobile Stations (MSs) within a cell of mobile network as shown in Figure 1-4. BS assigns a unique channel to each user for the downlink (DL) so that each MS can filter out other signals. If an array of full-duplex antennas is used at the BS, then multiple MSs may share the same frequency band for the

Uplink (UL). Co-channel signals from different users can, then, be segregated, should spatial signal segregation algorithms be used at the BS. In such networks, multiple co-channel signals (signals of frequencies f_1 and f_2 in the uplink shown in Figure 1-4) impinge on the BS from different directions. In real scenarios, due to multipath effects, the directions of arrival (DoA) of the signals at the BS can be even larger than the number of MSs sharing the same frequency band some of which may arrive with close angular proximity. This cellular network requires efficient and computationally cost-effective algorithms to be utilized by the BS processors to spatially detect and separate all signals.

Deliberate co-channel interferences generated by stationary or portable smart jammers are more difficult to tackle as jamming signals are usually much stronger than the desired signals. Different jamming cancellation techniques have been extensively examined for the last few decades. Early attempts focused on the method of antenna null steering in the direction of a jammer based on which a patent was filed in 1959 by Paul W. Howells for radar applications [39]. The idea was further explored by Sidney Applebaum who led the foundation for establishing the concept of adaptive arrays for maximizing the signal to interference ratio in time-varying environments in 1965. However, his work was not published until 1976 [40]. Since then a variety of adaptive beamforming techniques have been conceived [41, 42, 43, 44, 45, 46, 47, 48] . Applebaum assumes there is only one Direction of Arrival (DoA) for the desired signal and this direction is known. It is also assumed that the statistics (covariance matrix) of the interfering signals is known by the receiver. To relax the latter requirement, Frost developed another algorithm [49] in which correcting phase is applied to array elements to focus the beam in the known direction of arrival of the desired signal and optimized the magnitude weighting factors to minimize the

total received power. Again, Frost method assumes a single known direction of arrival and ignores the fact that by minimizing the total received power, the contribution from the desired signal may also be significantly reduced. Duvall introduced another method [50] to improve upon Frost algorithm to ensure the desired signal is not significantly reduced when minimizing the total received power. Duvall forms a fictitious array composed of pairs of the original array in such a way as the new array elements (adjacent pairs) have a null in the direction of the desired signal. Then, he minimizes the total received power of the fictitious array. This way, the desired signal is not entered into the equations. As mentioned, interference mitigation by Applebaum, Frost, or Duvall methods is accomplished based on three key assumptions: 1) the desired signal arrives from a single direction 2) the direction of the desired signal is known, and 3) the jammer signal and the desired signals are uncorrelated. The third limitation has been relaxed in the literatures by using spatial smoothing techniques [51, 52, 53, 54]. In another effort, a new beamformer based on Duvall approach is reported in [55] to cancel out $M - 1$ coherent jamming signals by using $2M$ elements. This method still assumes a single direction of arrival for the desired signal and requires this direction to be known. For realistic scenarios pertaining to complex multipath environments in which a large number of the desired and jamming signals of different levels arriving from different unknown directions as shown in Figure 1-5 [56], neither of these assumptions hold true. Hence, any proposed beamforming method needs be accompanied by a DoA estimator to discern the DoA of the desired signal. The traditional eigenstructure-based direction finding techniques such as MUSIC [57, 58, 59, 60, 61, 62, 63, 64] or ESPRIT [65, 66, 67, 68, 69, 70] cannot estimate direction of arrivals of fully correlated signals. A



Figure 1-5: Ray tracing simulation results obtained by EMTerrano simulator for a scenario in Downtown Manhattan. A large number of rays arrive at the receiver array from both the communication transmitter and the jammer.

spatial smoothing preprocessing scheme as well as its improved version [71] are conceived to distinguish the DoA of coherent signals. In [72], the capability of the spatial smoothing method is further enhanced by using a set of forward and complex conjugate backward sub-arrays simultaneously and, hence, the number of the identifiable DoAs of coherent signals is increased. A preprocessing conjugate gradient method in combination with spatial and temporal smoothing technique for DoA estimation of correlated signals is proposed in [73] which exhibits fast convergence rate. Cumulant-based algorithm [74] and Matrix Pencil method [75], [76] are used effectively to find the DoAs of coherent signals. These methods, however, need to have the exact knowledge of the number of the impinging signals on the receiver array for estimation of DoAs. Hence, model order estimation techniques such as Minimum Descriptive Length (MDL) criterion [77] and Akaike information theoretic

criterion [78, 79, 80] are needed to estimate the number of the impinging signals. These methods are based on finding the larger eigenvalues of the data covariance matrix and can be used if the signals are not coherent. In case of coherent (fully correlated) signals, preprocessing techniques such as spatial smoothing or forward-backward averaging [81] has to be run to decorrelate the signals. Forward-backward averaging technique, however, is not able to decorrelate more than two coherent signals. Although, spatial smoothing techniques can be used to decorrelate multiple signals, their performance in estimating weak sources is severely affected in the presence of strong interfering sources. Another class of direction finding techniques are Spectral Estimation Methods such as MVDR (Minimum Variance Distortionless Response) [82], Linear Prediction [83] and Maximum Likelihood [84, 85, 86, 87, 88, 89, 90]. Basically, in spectral estimation methods, the directions of arrival are found by searching for the local maximums in the spatial spectrum calculated for all directions. These techniques relax the requirement about the a priori knowledge regarding the number of signals. However, when the dynamic range of the signals arriving from different directions is not small, both eigenstructure-based and spectral estimation methods fail to detect DoAs of the low-level signals. This is a major problem needs to be addressed, since the desired signals arriving from different directions are usually much smaller than the jamming signals. Also, a difficulty arises when a large number of low-level components of a strong jammer signal arriving from other directions (due to multipath effect) are comparable to the desired signals. In this case, these small jamming signals which are correlated with the very larger ones must be accurately detected and removed before the desired signals can be retrieved. This discussion suggests that more reliable algorithms are needed that 1) can handle multiple

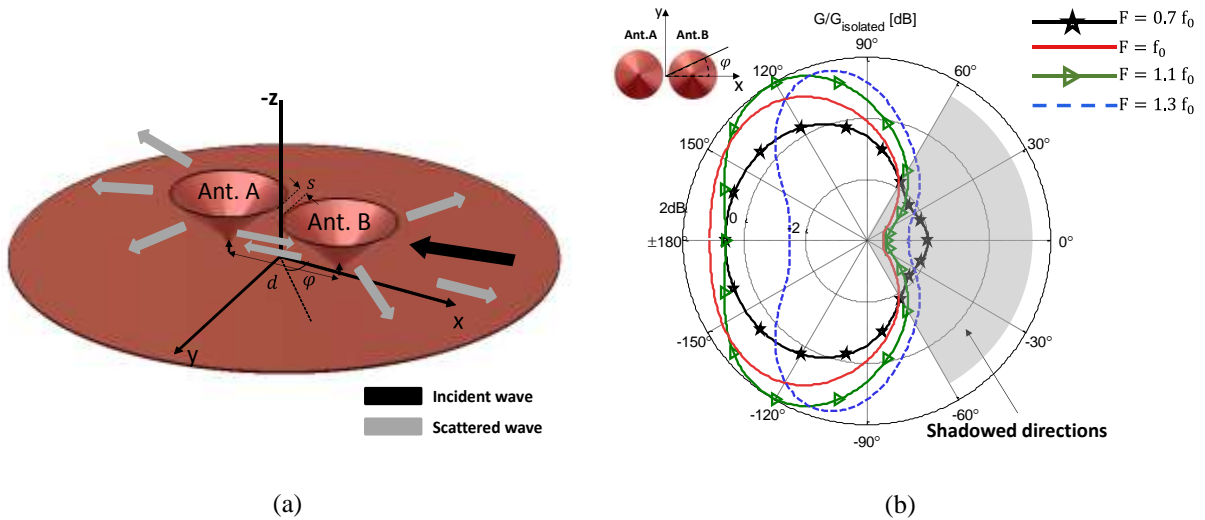


Figure 1-6: (a) Two wideband monoconical antennas illuminated by a plane wave from $\varphi = 0$. Antenna A is shadowed by antenna B. (b) the radiation pattern of antenna A shows significant deviation from omni-direction pattern. This is caused by antenna B shadowing along direction $\varphi = 0$.

DoAs for the desired signal, 2) do not require a priori knowledge of DoAs of the desired or interference signals, and 3) do not require the interference signals and the desired signals to be uncorrelated.

Another issue pertains to mutual coupling and shadowing effect when multiple antennas are used to reduce interference and to mitigate multipath effects. The maximum inter-element spacing in antenna arrays is usually limited by half a wavelength to achieve the required gain and to suppress grating lobes, leads to a dense antenna array configuration. The required high density comes with its own drawbacks, especially for non-planar arrays, due to electromagnetic interactions between the array elements. Such adverse effects include shadowing (forward scattering), near-field coupling between elements which in principle alters the radiation pattern and the input impedance of the individual elements. Deviation from radiation pattern and input impedance characteristics of an isolated antenna element, introduces much difficulty in adaptive array beamforming since the element pattern and the

magnitude and phase of the signal at an element port are affected by the other elements in the array. This difficulty is compounded for very wideband arrays as the coupling mechanisms are very strong functions of frequency. The smaller is the center-to-center or edge-to-edge inter element spacing, the stronger is the mutual coupling and its adverse effects. Typically, broadband omnidirectional antennas have a relatively large 3D geometry. A larger antenna size leads to a smaller edge-to-edge distance between adjacent antennas. Hence, broadband systems are more likely to suffer from the undesired effects of mutual coupling. Figure 1-6 shows a pair of broadband monoconical antennas spaced by half a wavelength at the center frequency of operation as well as the radiation pattern of the excited antenna. Significant deviation from the omnidirectional pattern is observed due to shadowing effect. Scattered field in the forward direction is strongest for all objects and is almost 180° out of phase with the incident wave. This phenomenon is responsible for shadowing effect in the near-field region and has the effect of obscuring signals along directions connecting pairs of non-planar array elements.

To trim these undesirable effects, different modeling and mitigation techniques have been studied and reported in the literature. These methods can be mainly classified into computational and physical approaches both of which have received fairly noticeable attention in recent years. Computational methods are based on calculating the mutual coupling matrix and use it in post processing beam-forming algorithms to compensate for the coupling effects. To compute the coupling matrix, four different approaches have been reported so far: open-circuit voltage method [91], calibration method [92], full-wave method [93] and receiving mutual impedance method [94], [24] among which full-wave method provides the highest accuracy. It should be noted that if the coupling matrixes for both

transmitting and receiving modes are exactly known, it is possible to achieve the maximum array gain. However, this requires exact knowledge of antenna array architecture and its platform. Another issue pertains to the signal-to-noise ratio and non-uniform radiation pattern of array elements due to shadowing and mutual coupling. That is in situations where SNR is low and direction of arrival of the maximum signal happens to be in the low-gain portion of some array elements. The overall array gain and beamwidth as well as the receiver SNR are degraded compared to an equivalent array that has elements with uniform radiation pattern. For this reason, in addition to computationally compensating for the mutual coupling, different physical techniques have been implemented to ensure a high-level of input signal-to-noise-ratio at each antenna for all directions of arrival of the signals in multi-path environments. In [95], a mushroom like electromagnetic bandgap (EBG) structure is utilized to reduce the coupling between two microstrip antennas based on the suppression of the surface wave's propagation. In another effort, the coupling between planar or non-planar antennas is reduced by creating slits in the common ground plane [96]. Metamaterial insulators are used to mitigate the coupling between closely spaced elements [97], [98]. Near-field cancellation method [99], [100], transmission line decouplers [101], and capacitively loaded loop magnetic resonators [102] are among alternative methods for mutual coupling reduction which is usually used to improve pattern diversity [103], [104]. The aforementioned techniques, however, are suitable for narrowband applications and moreover mostly are not applicable for non-planar antennas except for the method reported in [96].

Chapter 3 of the dissertation is devoted to development of novel algorithms for spatial super-resolution signal detection to enhance the capacity of wireless networks [105].

Moreover, a feed-forward technique is proposed to physically reduce the coupling among the array elements of broadband multiple antenna systems.

1.3 Sub-Surface Communication

Tuning into subsurface communication in Chapter 4, a new concept is utilized to develop a low-cost signal transmission technique which is tailored for data communication in directional hydraulic drilling process. Drilling is the critical part in the process of oil and gas extraction. The history and projection of the U.S. natural gas production is illustrated in Figure 1-7. Shale gas will contribute about 50% of the total U.S. gas production by 2040. This covers a significant portion of the total required energy in the U.S. In order to minimize the cost and make the extraction process very efficient, bilateral real-time data communication for controlling and monitoring purposes during extraction process has become a standard for which there is still need for more effective methods to prevent tools

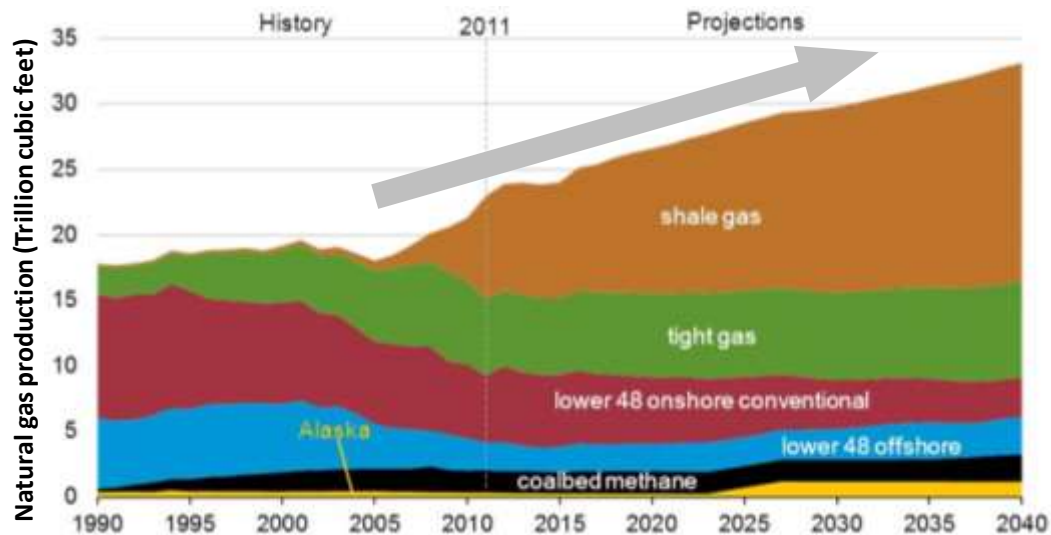


Figure 1-7: Natural gas production in the U.S. from 1990 to 2040. Shale gas is projected to constitute 49% of the total U.S. gas production in 2040. Data from U.S. Energy Information Administration (EIA) [130].

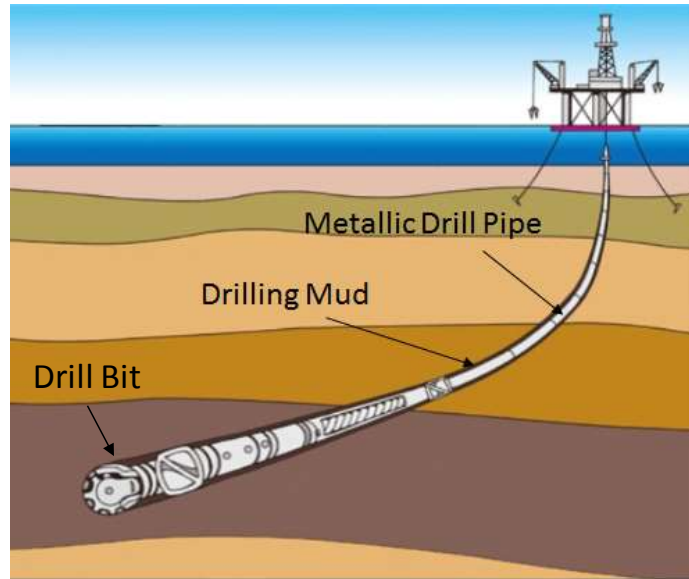


Figure 1-8: The mechanism of hydraulic rotary-drilling. The hydraulic power is provided by the drilling fluid flowing through the drill pipe where it then carries the cuttings back to the surface through the annular space between the drill pipe and the sides of the borehole

failure and to steer the drill bit towards the target region. The mechanism of hydraulic drilling is shown in Figure 1-8. The drilling fluid is pumped down the drilling pipes at extremely high pressure and provides mechanical torque to the drill bit for cutting the rock and is then circulated back up the annulus. The idea is stemmed from the fact that the permittivity of the drilling fluid is higher than the subsurface rock offering a promising possibility of using metallic drilling-pipe coated by the drilling mud as a Single Conductor Transmission Line (SCTL) [106, 107, 108]. Effectively excited, such transmission line supports TM surface wave that propagates along the metallic pipe [109]. By this technique, the attenuation rate of the transmitted signal from downhole to the surface and vice-versa can be considerably reduced compared to electromagnetic wireless method as the surface wave on the SCTL, once excited, is not subject to spherical wave propagation path loss. The major bottleneck towards realization of this method is imposed by the very limited available space inside the

borehole. The borehole diameter is by far smaller than the required space for utilizing traditional surface wave launchers such as coaxial horns [109, 110, 111]. To round this bottleneck, a novel very compact TM surface wave transducer is introduced in this chapter.

1.4 Contributions

Some of the challenges of today's and tomorrow's communication systems ranging from throughput enhancement of wireless systems to improved data communication techniques for subsurface communications are addressed in this dissertation. This has been accomplished by exploiting ideas stems from electromagnetic concepts, signal processing techniques or combinations of both. The outline of this research contributions is listed below:

1. Introducing a technique for mutual coupling and shadowing effect mitigation in broadband multiple antenna systems to make the radiation pattern of each antenna element more like that of the isolated antenna thus achieving more efficient signal processing in MIMO systems.
2. Development of an algorithm to estimate the directions of arrival, magnitudes and phases of the signals' spectral components whose magnitudes spread over a very large dynamic range to spatially and spectrally separate the communication signals of interest from the very strong interfering signals without a priori knowledge regarding their directions of arrival.
3. Development of a spatial super-resolution signal detection algorithm capable of resolving correlated signals impinging on the receiver with angular proximity smaller than the array beamwidth using a uniform circular array. This is accomplished in two steps: 1) the directions of arrival and amplitudes of signals

with angular spacing larger than the array beamwidth are detected using the Array Signal Segregation using an Iterative Approach and 2) signals with angular proximity smaller than the array beamwidth are separated using a novel Closely-spaced Nulls Synthesis Method (CNSM).

4. Design of a novel compact high-gain full-band sub-array of slot antennas with consistent radiation characteristic over the entire bandwidth including high-gain and low cross-polarization, and high front-to-back-ratio.
5. Development of a novel technique to design compact broadband common-aperture slot antenna with two ports having a very high level of isolation for full-duplex wireless communications, full-duplex repeaters, and FMCW radar systems.
6. Introducing the concept of wellbore telemetry using drill pipes as the conductor of Single Conductor Transmission Line (SCTL) to satisfy the need for cost-effective and real-time data communication in drilling process and designing a very compact and conformal SCTL launcher at HF-band which fits inside the borehole.

1.5 Thesis Organization

In chapter 1, first, a pedigree of radio communication and its evolution over the course of years is given. An overview of the status quo in communication systems and challenges to be addressed is then briefed. In wireless communication, nailing the focus down to approaches reported to date for channel capacity enhancement, it is inferred that interference is the major problem that limits the throughput of the wireless networks. Thereafter, turning into subsurface communication, the difficulties pertaining to long-

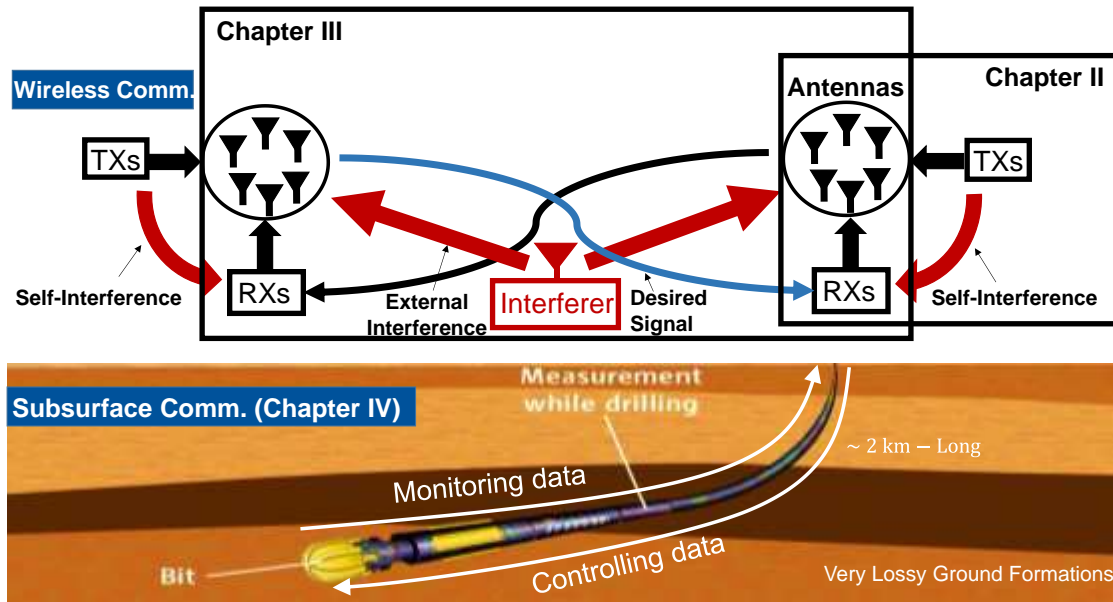


Figure 1-9: A schematic of the topics covered in the dissertation. Chapter 2 describes methods for self-interference cancellation in wireless transceivers. The focus of chapter 3 is on techniques and algorithms for suppression of external interference. In chapter 4, a telemetry technique for subsurface communication is introduced.

distance underground communication and the drawbacks of the existing techniques are pointed out. Also, the necessity as well as the feasibility of developing techniques and compact reliable apparatus capable of circumventing huge signal attenuation due to very lossy ground formations is discussed.

Figure 1-9 demonstrates the focuses of Chapter 2-4. In chapter 2, novel compact antenna systems for self-interference cancellation for enabling full-duplex communications are introduced. Beside compactness, the main features of the proposed antennas are wide bandwidth, high level of isolation between transmit and receive terminals, consistent radiation characteristic such as high gain, low cross-polarization, high front-to-back ratio over a wide bandwidth, and identical transmit and receive radiation pattern. Different fabrication techniques are then described, and their performances are compared.

Chapter 3 deals with development of novel algorithms and techniques for external (intentional or deliberate) interference cancellation in wireless communication systems. An iterative signal segregation algorithm is developed to spatially separate the desired communication signals from co-channel interfering signals even the desired signal is much smaller than the interference, should their angular separation be larger than the array beamwidth. The algorithm also helps to mitigate the multipath effects. The proposed signal segregation algorithm is then evolved to a super-resolution signal detection technique for resolving multiple closely-spaced correlated signals using a novel closely spaced nulls synthesis method [112] which is different from conventional null steering technique [113]. Also, a feed-forward technique is introduced to mitigate mutual coupling in antenna arrays to facilitate beamforming and signal processing in MIMO systems.

In chapter 4, a new concept for real-time data communication in borehole drilling is introduced to address the disadvantages of the current methods in terms of reliability, data rate and range. In this method, the drill-pipe is used as the conductor of the SCTL that supports TM surface wave. A compact TM surface wave transducer that fits inside the borehole is also designed to effectively transform TEM wave in the coaxial cable to TM surface wave on the SCTL.

Winding up this research work, Chapter 5 highlights the potential for adopting the proposed concepts into other applications and researches. This chapter is wrapped up by presenting future directions and possible research opportunities for radio communication in its explosion era.

CHAPTER 2 Internal (Self-) Interference Cancellation in Wireless Transceivers

2.1 Overview

The ever-increasing demand for wireless communications arising from the emerging technologies such as the Internet of Things (IoT) has put stringent conditions on the efficient use of the available frequency spectrum. The traditional approaches for enhancing the spectral efficiency of wireless systems such as advanced modulation methods, advanced coding, and Multiple Input Multiple Output (MIMO) techniques have been fully expended. The predicted increase in spectral efficiency using MIMO concept is based on unrealistic premises that the channel can be accurately estimated and that the channel matrix has full rank [114]. However, the capacity gain of MIMO channels is limited in real operating scenarios due to 1) erroneous channel estimation particularly in time-varying and low SNR channels and 2) high level of channel fading correlation as the size of the MIMO system gets large [114]. As the aforesaid methodologies for enhancing the channel capacity reach their maximum potential, alternatives must be created to push the limits not by discarding the foregoing achievements but by building on them. One of the possible solutions to be integrated with MIMO to meet the challenges of the future ultra-dense networks is to replace the current prevalent time-division and frequency-division duplex transceivers with full-duplex transceivers. In contrast to the formers in which transmitting and receiving are operated either at different times or over different frequencies, full-duplex transceivers are

designed to transmit and receive data at the same time and over the same frequency band resulting in a twofold increase in the channel capacity of the system. Although, in an actual full-duplex system identical polarizations should be exploited for transmitting and receiving, enabling full-duplex operation using orthogonal polarizations has still two advantages: 1) facilitating channel estimation as the size of the channel matrix becomes smaller and 2) reducing system complexity through reducing the number of required transmitters and receivers. Operating in full-duplex, however, requires perfect self-interference suppression which has been extensively studied recently. Self-interference refers to the strong signal coupling from the transmitter to the co-located receiver whose level is much larger than the desired received communication signal to be detected. As mentioned in Section 1.2.1, a combination of different cancelation techniques implemented in both digital and analogue domain must be envisioned. Different antenna cancelation schemes as one of the effective methods in analogue domain were also discussed most of which suffer from bulkiness, high sensitivity to hybrid imbalances, and bandwidth limitation. In this chapter, first a single channel broadband slot antenna is designed. Then, an antenna cancellation technique is introduced based on which a compact antenna system is then developed which can provide an unprecedented level of self-interference cancelation over 45% fractional bandwidth.

2.2 Single-Port Cavity-Backed Slot Antenna (CBSA)

Low profile, wideband, and lightweight antenna elements that can maintain consistent radiation characteristics, e.g. gain, direction of maximum radiation, polarization, etc., are of high demand for various radar and communication applications. Microstrip and

slot antennas are among the most utilized low-profile antennas. Microstrip antennas, when used as the elements of an array, provide limited bandwidth and are susceptible to scan blindness due to surface wave generation. Surface wave propagation in the substrate of the antenna arrays also results in reduction of the radiation efficiency and unwanted mutual coupling between elements. Surface wave obstruction is the advantage of the Cavity-Backed Slot Antennas (CBSA) over microstrip antennas in array configurations. In this section, a compact 2×2 array of CBSAs fed by a microstrip line as building block of large arrays [115] is presented. First the bandwidth of a waveguide-fed thin slotted-cavity is substantially increased by appropriately loading the cavity with metallic septa. The effect of the added septa is twofold. The metallic septa excite certain evanescent modes inside the cavity which results in bandwidth enhancement towards the lower frequencies. Moreover, it allows the resonant frequencies of the cavity be brought closer together to achieve wideband behavior. For a waveguide-fed CBSA, 60% bandwidth is realized by this technique. Then a compact end-launch microstrip to waveguide transition with 40% bandwidth is designed as the antenna feed. The bandwidth of the proposed microstrip-fed four-element CBSA is twice the recent CBSA array with the same gain reported in [34] noting that the dimension of the array in [34] is even larger than the presented four-element array.

2.2.1 Principle of Operation of the Wideband Cavity-Backed Slot Antenna

Consider a thin rectangular cavity excited by a waveguide at the center of the cavity broad wall shown in Figure 2-1 . The excitation mode at the feed waveguide is assumed to be TE_{10}^z mode. Due to the discontinuity at $z = 0$, the field tends to transform to TE^x inside the cavity. The TE^x mode generated by a magnetic Hertz vector potential $\mathbf{\Pi}_m = \Pi_{mx} \hat{x}$ must

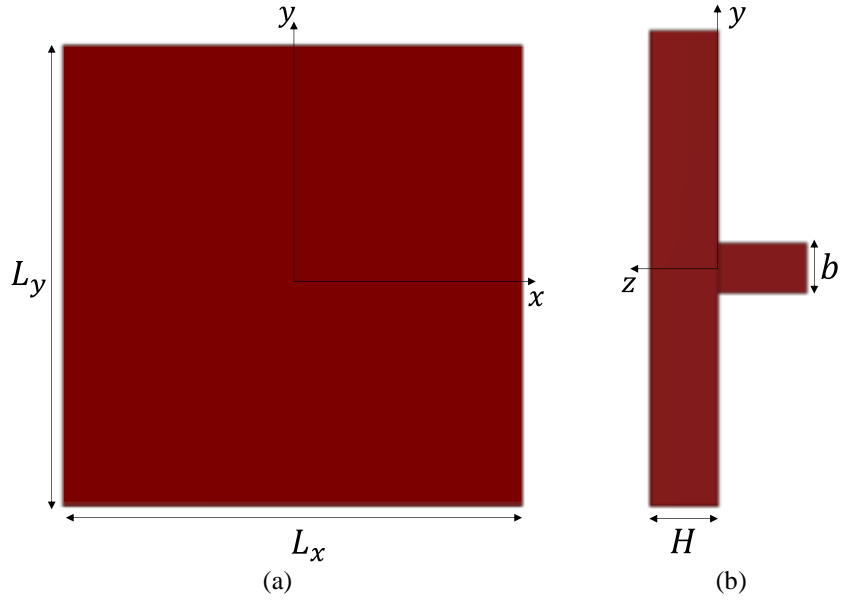


Figure 2-1: The thin rectangular cavity fed by a waveguide (a) front view (b) side view. $L_x = L_y = 1.2 \lambda_L$, $H = 0.15 \lambda_L$, $b = 0.07 \lambda_L$.

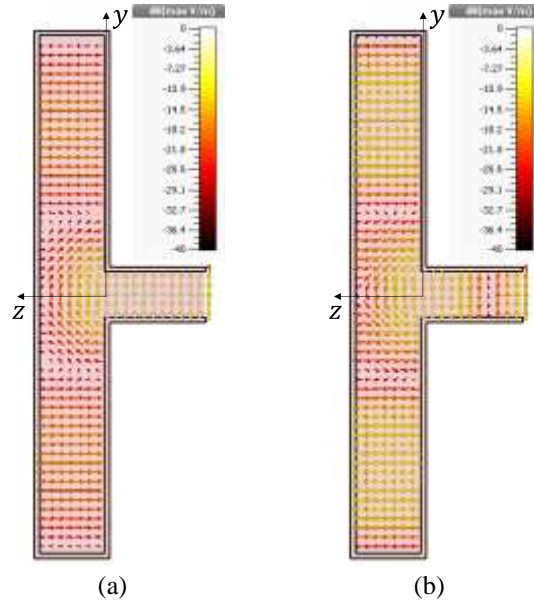


Figure 2-2: The electric field distribution inside the cavity when excited by TE_{10}^Z mode through a waveguide (a) $f = 0.8 f_0$, (b) $f = 1.1 f_0$. Except for the region around the excitation port, $E_y = 0$ everywhere in the cavity.

satisfy the source-free wave equation:

$$\nabla^2 \Pi_m + k^2 \Pi_m = 0 \quad (2-1)$$

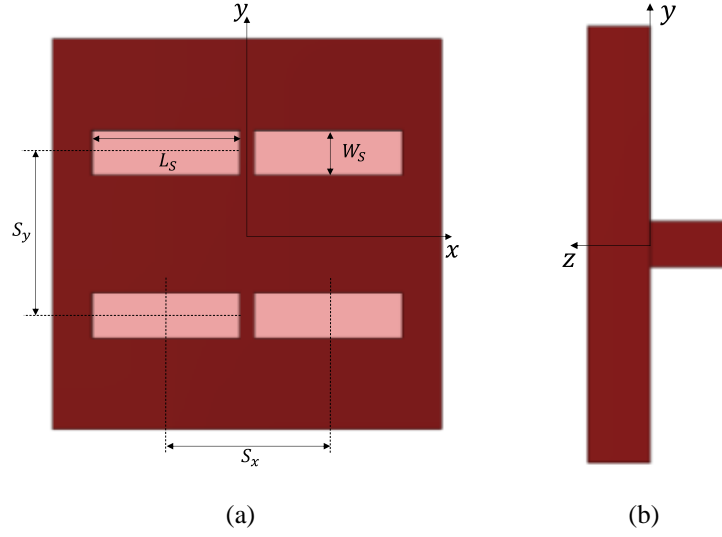


Figure 2-3: The slotted cavity (a) front view (b) side view. $L_S = 0.45\lambda_L$, $W_S = 0.14\lambda_L$, $S_x = S_y = 0.5\lambda_L$.

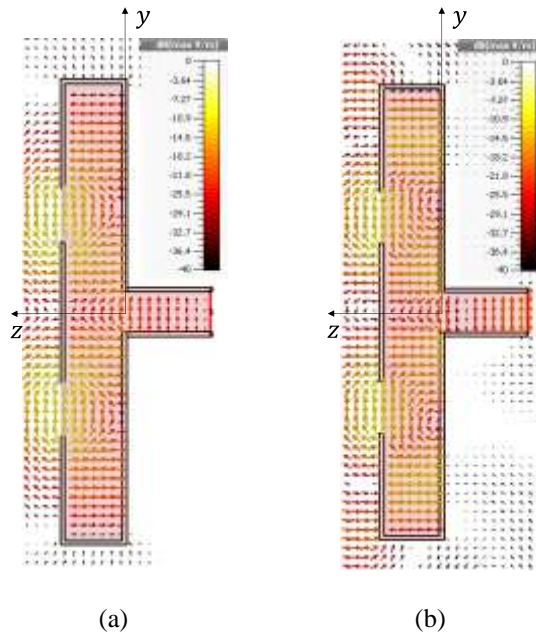


Figure 2-4: The electric field distribution inside the slotted cavity at $x = 0.15 L_x$ when excited by TE_{10}^z mode through a waveguide (a) $f = 0.77 f_0$ (b) $f = 1.27 f_0$.

where \mathbf{E} and \mathbf{H} are given by:

$$\mathbf{E} = i\omega\mu\nabla \times \Pi_m \quad (2-2)$$

$$\mathbf{H} = \nabla \nabla \cdot \Pi_m + k^2 \Pi_m \quad (2-3)$$

The electric field at the feeding aperture is given by:

$$\mathbf{E} = \hat{\mathbf{y}}E_y = \hat{\mathbf{y}} E_0 \cos \frac{\pi x}{a} \quad (2-4)$$

Expanding (2), the electric field for TE^x mode inside the cavity is obtained as:

$$E_x = 0 \quad (2-5)$$

$$E_y = i\omega\mu \frac{\partial \Pi_{mx}}{\partial z} \quad (2-6)$$

$$E_z = -i\omega\mu \frac{\partial \Pi_{mx}}{\partial y} \quad (2-7)$$

In a thin cavity ($H \ll \lambda$), the propagation mode is essentially TE_{mno}^x . The subscripts m , n and 0 indicates the number of field variations in x , y , and z directions respectively. This implies that Π_{mx} has no variation in the direction normal to the cavity broad walls (z -direction). Therefore, referring to (2-6), $E_y = 0$ inside the cavity. Non-zero y -component of the electric field is required so that the field can be transformed from TE_{10}^z at the excitation port to TE^x inside the cavity. Otherwise, this transformation fails, and the incident wave is totally reflected back. Therefore, Π_{mx} needs to have variation in the z -direction so as to generate non-zero electric field in y -direction in the cavity. The electric field distribution across the cavity cross section, when the cavity is excited by TE_{10}^z mode, is illustrated in Figure 2-2. As can be seen, $E_y = 0$ everywhere inside the cavity except for the region around the excitation port. Once the radiation slots are cut out on the cavity as illustrated in Figure 2-3, due to the structure perturbation in z -direction, the Hertz vector potential Π_{mx} develops variations in the z -direction around the radiating slots at some frequencies and in turn, the field is transformed from TE_{10}^z to TE^x . The frequencies at which the radiation occurs is governed by the location and the size of the radiating slots. The electric field distribution across the cavity cross section at resonant frequencies, when four symmetric slots of

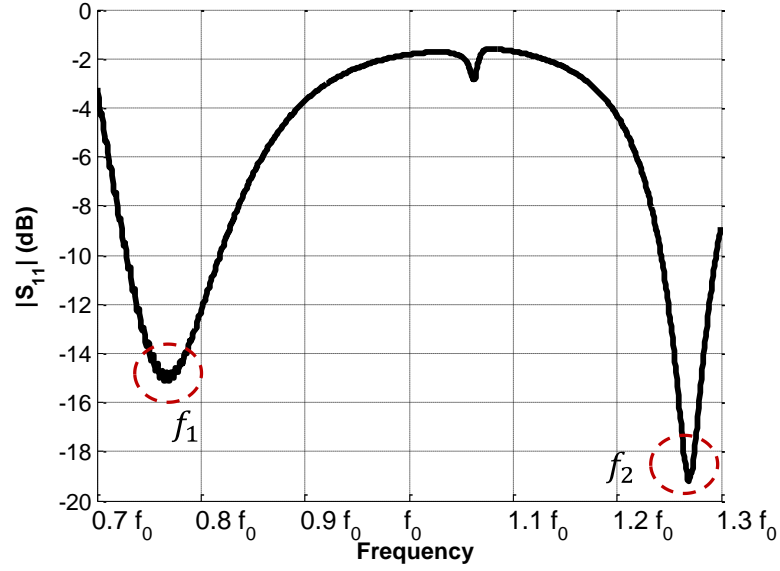


Figure 2-5. The magnitude of the reflection coefficient for the slotted cavity shown in Figure 2-3.

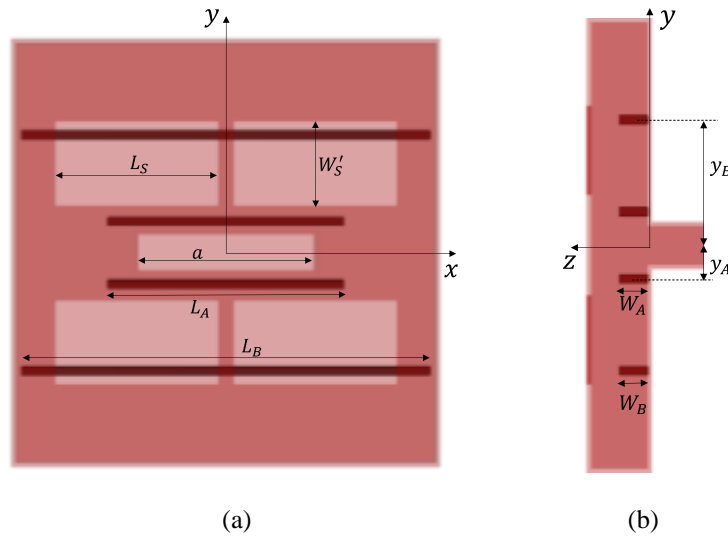


Figure 2-6. The slotted cavity loaded with metallic septa (a) front view (b) side view. $W_s' = 0.23 \lambda_L$, $L_A = 0.67 \lambda_L$, $L_B = 1.15 \lambda_L$, $W_A = W_B = 0.074 \lambda_L$, $y_A = 0.088 \lambda_L$, $y_B = 0.33 \lambda_L$.

dimension $0.45 \lambda_L \times 0.14 \lambda_L$ spaced by $0.5 \lambda_L$ are cut out on the broad wall, is shown in Figure 2-4. The reflection coefficient is demonstrated in Figure 2-7. The slotted cavity resonates at frequencies $f_1 = 0.77 f_0$ and $f_2 = 1.27 f_0$ where f_0 is the center frequency. This dual-band cavity-backed slot antenna structure is, however, of limited bandwidth. To

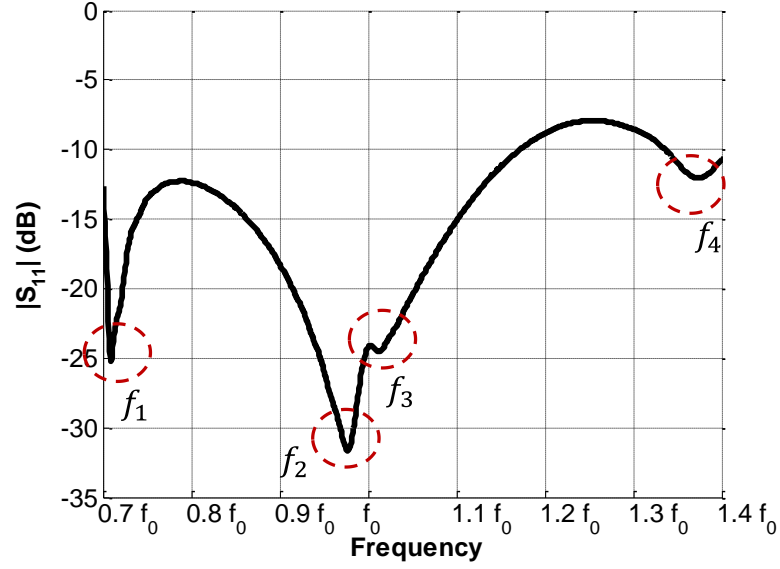


Figure 2-7. The reflection coefficient for the slotted cavity loaded with metallic septa shown in Figure 2-6.

increase the bandwidth, the cavity structure itself should be altered such that other TE^x modes with non-zero electric field in y -direction are excited inside the cavity. As mentioned before, the z -dependent magnetic Hertz vector potential generates electric field having non-zero component in the y -direction. The idea is to insert thin metallic septa of width w ($w < H$) residing in different appropriate y -constant planes inside the cavity. Due to the discontinuity of the electric field in the z -direction at the edges of the septa, the magnetic Hertz vector potential, Π_{mx} , corresponding to the excited modes will be essentially z -dependent. The z -dependent Hertz vector potential generates electric field in y -direction leading to radiation through the slots at the resonant frequencies. Since the radiating slots should be excited in-phase, the desired quasi- TE_{mnp}^x modes are those with an odd number for m and an even number for n . The subscripts m , n and p represent the number of the electric field (E_z) variation in x , y , and z directions respectively. It should be noted that these modes are different from those of a rectangular cavity. To generate electric field in the y -direction across

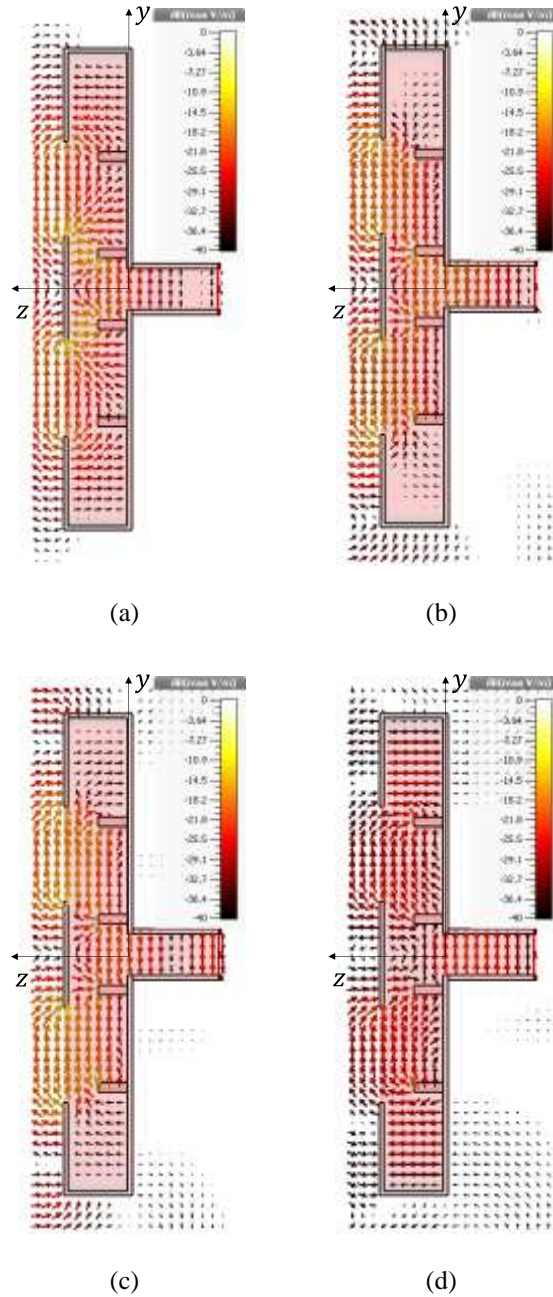


Figure 2-8. The electric field distribution inside the slotted cavity loaded with metallic septa excited by TE_{10}^z mode through a waveguide at $x = 0.2 L_x$. (a) $f = 0.7 f_0$, (b) $f = f_0$, (c) $f = 1.1 f_0$, (d) $f = 1.3 f_0$.

the radiating slots, the septa should be placed close to the edges of the feeding and radiating apertures. Therefore, four septa are placed at these regions. The modified cavity structure is shown in Figure 2-6. Once these septa are introduced, the cavity acts as evanescent mode

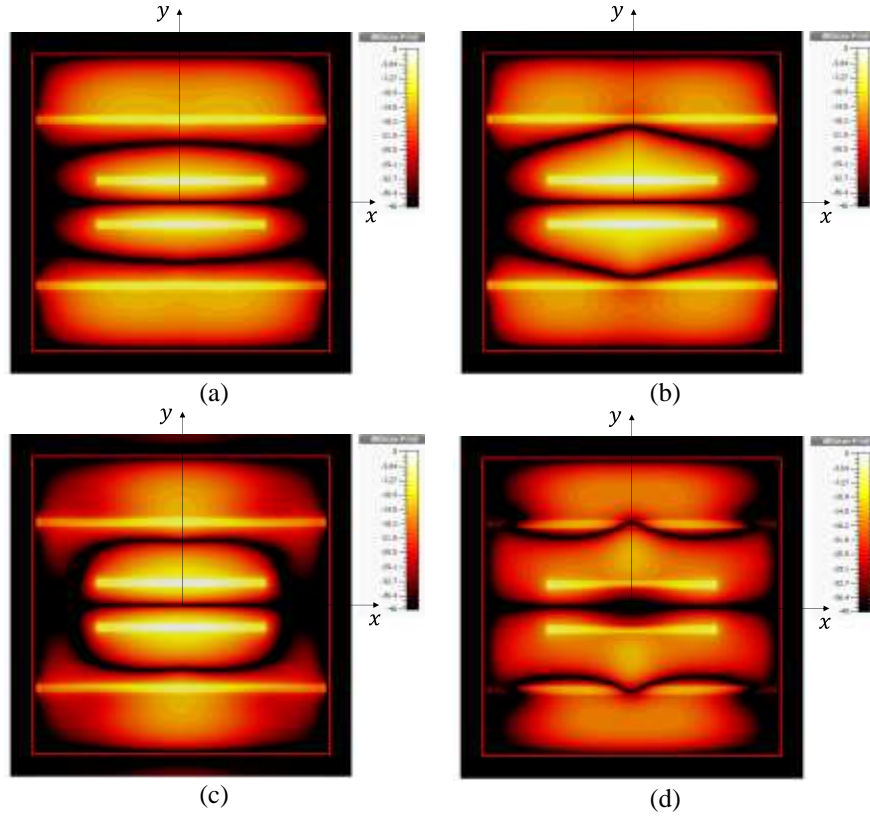


Figure 2-9. The distribution of $|E_z|$ inside the slotted cavity loaded with metallic septa excited by TE_{10}^z mode at $z = W_A$ (a) $f = 0.7 f_0$ (b) $f = 0.9 f_0$ (c) $f = 1.1 f_0$ (d) $f = 1.3 f_0$.

cavities with shunt capacitors that are created across the septa and the cavity walls. This has a tendency to lower the dominant resonant frequency of the loaded cavity. The location and the dimensions of the septa are then optimized using CMA Evolution Strategy algorithm [116] to excite other desired modes within the bandwidth. Appropriately designed, the septa bring up the evanescent modes above the cutoff. The inserted metallic septa also make it possible to bring the resonance frequencies of the unloaded cavity close together. The width of the radiating slots is also increased to $0.23 \lambda_L$ for bandwidth enhancement. The reflection coefficient of the antenna is illustrated in Figure 2-7. Loaded by the metallic septa, the slotted cavity resonates at four different quasi- TE_{mnp}^x modes spread from $0.7 f_0$ to $1.4 f_0$. An evanescent mode is excited at $f_1 = 0.72 f_0$. The resonant frequencies of two other modes

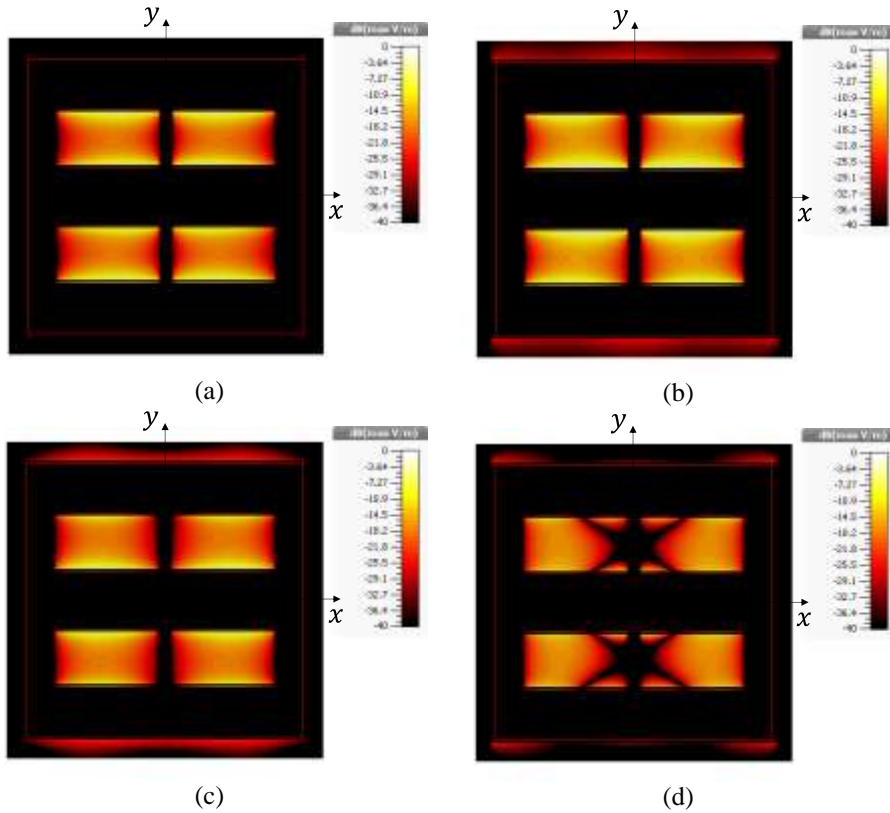


Figure 2-10. The distribution of $|E_y|$ across the radiating slots of the CBSA shown in Figure 2-6 at (a) $f = 0.7 f_0$ (b) $f = 0.9 f_0$ (c) $f = 1.1 f_0$ (d) $f = 1.3 f_0$.

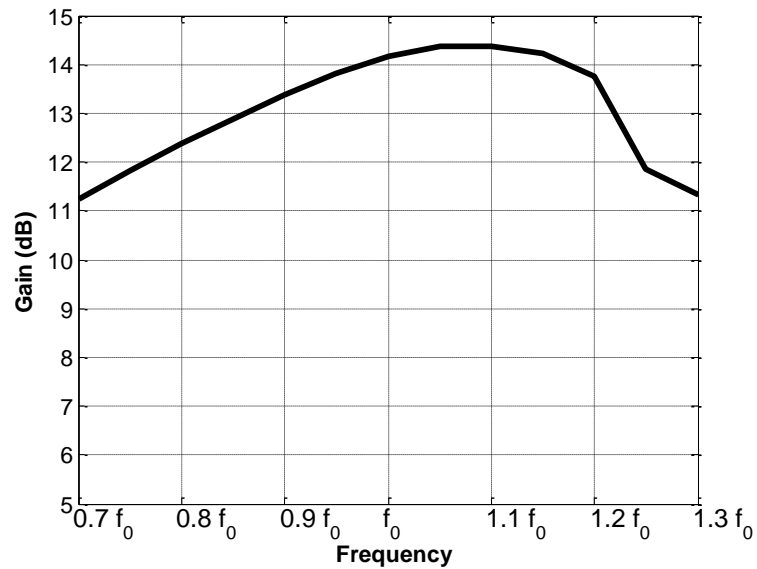


Figure 2-11. The gain of the CBSA shown in in Figure 2-6 versus frequency.

denoted by f_2 and f_3 are brought close together as can be observed in the graph shown in

Figure 2-7. The electric field distribution at $x = 0.15 L_x$ for different frequencies is illustrated in Figure 2-8. Due to the septa arrangement, for all the excited modes within the bandwidth, the number of E_z peaks in the y -direction is found to be $n = 4$ as depicted in Figure 2-9. Since a quasi- TE_{10}^z field distribution is engendered across the radiating slots over the entire bandwidth as shown in Figure 2-10, the proposed slot antenna is a high-gain antenna. Keeping the cavity depth less than $0.15 \lambda_L$, 60 % bandwidth is achieved by this technique. The antenna gain versus frequency is plotted in Figure 2-11. As frequency increases, a higher order mode with $m = 3$ corresponding to $f = f_4$ is excited in the cavity which results in a phase rotation of the electric field partially across the radiating slots (see Figure 2-10(d)). This phenomenon is the reason for the antenna gain reduction above $1.3 f_0$.

2.2.2 Microstrip to Cavity Transition

To maintain a low-profile design, the proposed cavity-backed slot antenna should be fed by a microstrip line. A large number of probe-fed microstrip to waveguide transitions have been reported in the literatures most of which suffer from low bandwidth, bulkiness, and fabrication complexity. A Compact and wideband two-way splitter/combiner end-launch reduced-height waveguide to microstrip transition is reported in [37] which provide 180° out of phase signals on the microstrip ports. Terminating one port (open- or short-circuit) for transition from waveguide to a single feed microstrip line results in either bandwidth reduction or more radiation loss which is not elaborated in [37]. Another compact microstrip to waveguide transition is presented in [35] whose bandwidth is limited to 12%. In this section, a compact and wideband end-launch microstrip to reduced-height rectangular

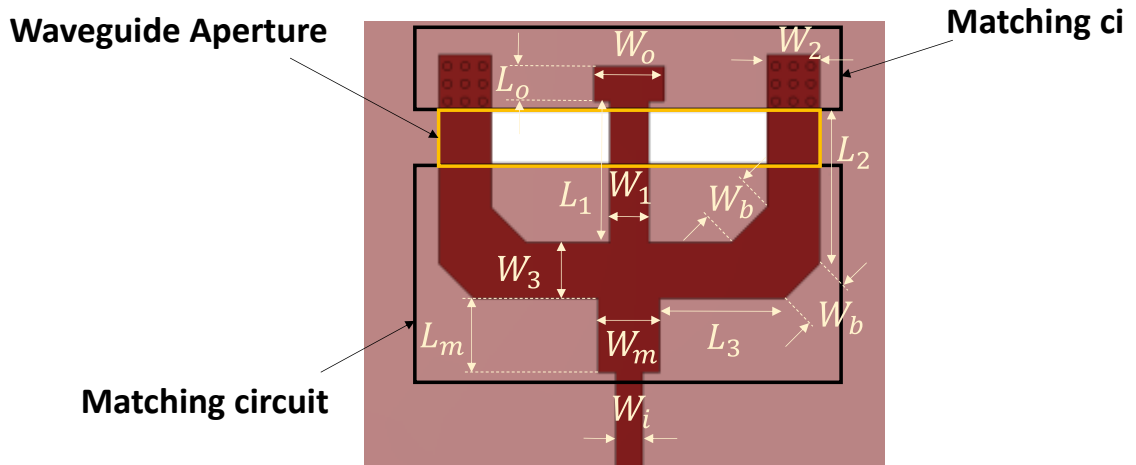


Figure 2-12. The proposed end-launch microstrip to reduced-height waveguide transition.

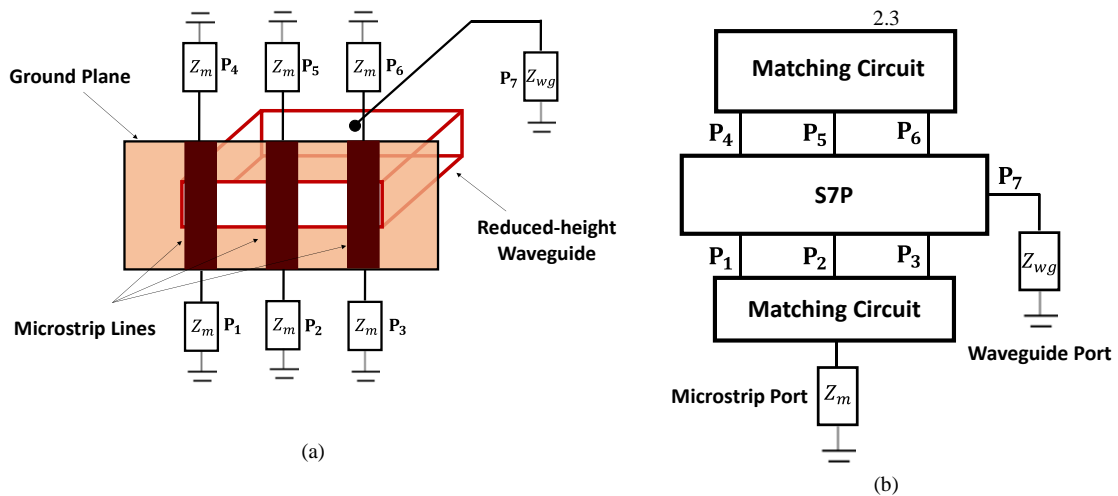


Figure 2-13. The S-parameters of the 7-port network in (a) is used in (b) for circuit simulation and optimization.

waveguide transition is introduced. The transition structure is shown in Figure 2-12. The waveguide is fed by three parallel microstrip lines crossing over the waveguide end wall aperture. This feeding topology, if appropriately designed, creates a quasi- TE_{10} field distribution across the aperture and also provides impedance matching between the microstrip line and the reduced height waveguide over a wide bandwidth. The microstrip lines cross the waveguide in the middle and on the sides. To shift the burden of the design

Table 2-1. The dimensions of the transition shown in Figure 2-12

Parameter	Quantity (λ_0)	Parameter	Quantity (λ_0)
W_1	0.073	L_1	0.26
W_2	0.1	L_2	0.29
W_3	0.107	L_3	0.24
W_m	0.117	L_m	0.14
W_o	0.13	L_o	0.067
W_i	0.05	W_b	0.094

and optimization procedure from full EM analysis to fast circuit simulation, first, the scattering parameters of the 7-port network shown in Figure 2-13(a) for a given width of the microstrip lines is extracted by a single full-wave analysis. The microstrip lines are assigned a port at each end and a port is assigned to the waveguide. The S-parameters of this network de-embedded to an appropriate reference plane is then used by a circuit simulator to optimize the matching microstrip circuit depicted in Figure 2-13(b). The dimensions for the width and the location of the microstrip lines in Figure 2-13(a) is iteratively changed to achieve optimum performance. Finally, fine tuning by full-wave analysis is performed on the matching circuits extracted by circuit simulation. Using this technique, an end-launch microstrip to reduced-height waveguide is designed at X-band. The optimized dimensions of the matching circuit printed on 20 mil RT/duroid 5880 are listed in Table 2-1. Figure 2-14 illustrates the reflection and the transmission coefficients of the proposed topology. The demonstrated bandwidth reaches 40%. The same procedure is used to design the antenna feed, that is, the reduced-height waveguide (port 7) in Figure 2-13(a) is replaced by the cavity-backed slot antenna and the S-parameters of the resulted 6-port network is extracted by a full-wave solver. The matching circuit is then designed and optimized by the circuit

model shown in Figure 2-13(b) to minimize the reflection coefficient from the microstrip

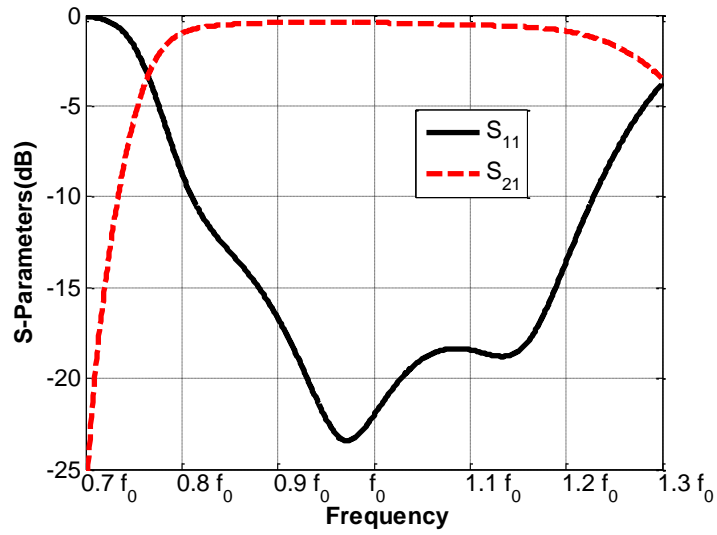


Figure 2-14. The reflection and transmission coefficient of the transition shown in Figure 2-12.

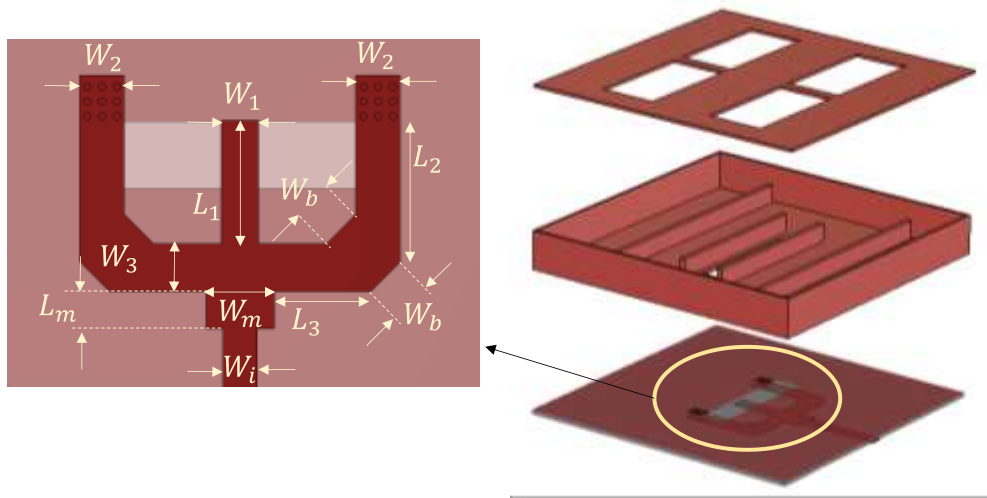


Figure 2-15. The configuration of the cavity-backed slot antenna fed by a microstrip line.

Table 2-2. The dimensions of the CBSA shown in Figure 2-6

Parameter	Quantity (mm)	Parameter	Quantity (mm)
L_x	51	y_A	3.8
L_y	51	y_B	14.3
L_A	28.7	W_A	3.2
L_B	9.7	W_B	3.2
L_s	19.75	S_x	21.67
H	6	S_y	21.67
a	21.67	b	3

Table 2-3. The dimensions of the transition shown in Figure 2-15

Parameter	Quantity (mm)	Parameter	Quantity (mm)
W_1	2.2	L_1	8.3
W_2	3	L_2	9.4
W_3	3.2	L_3	6.5
W_m	4.6	L_m	2.5
W_i	2.3	W_b	2.8

port over the desired bandwidth.

2.2.3 Experimental Results

The designed described in the previous sections is used to fabricate a compact high-gain slot antenna covering the entire X-band. As mentioned before, the antenna consists of a slotted cavity and a double-sided Printed Circuit Board (PCB) (See Figure 2-15) whose dimensions are listed in Table 2-2 and Table 2-3 respectively. The cavity part is fabricated using silver 3D-printing technology. Figure 2-16(a) and Figure 2-16 (b) show the 3D-printed slotted cavity made out of silver. The microstrip feed is printed on 30 mil RT/duroid 5880 (see Figure 2-16(c) and Figure 2-16 (d)) and is then soldered to the back side of the cavity. The assembled antenna structure is illustrated in Figure 2-16(e).

The simulated and measured antenna reflection coefficients are depicted in Figure 2-17 which shows 40% impedance bandwidth ($S_{11} < -10$ dB) from 8 GHz to 12 GHz. It should be emphasized that the bandwidth of the waveguide-fed cavity backed slot antenna is 60% (7 GHz -13 GHz) which is shrunk to 40% when integrated by the microstrip feed. Figure 2-18 shows the measured and simulated co-polarized and cross-polarized antenna radiation

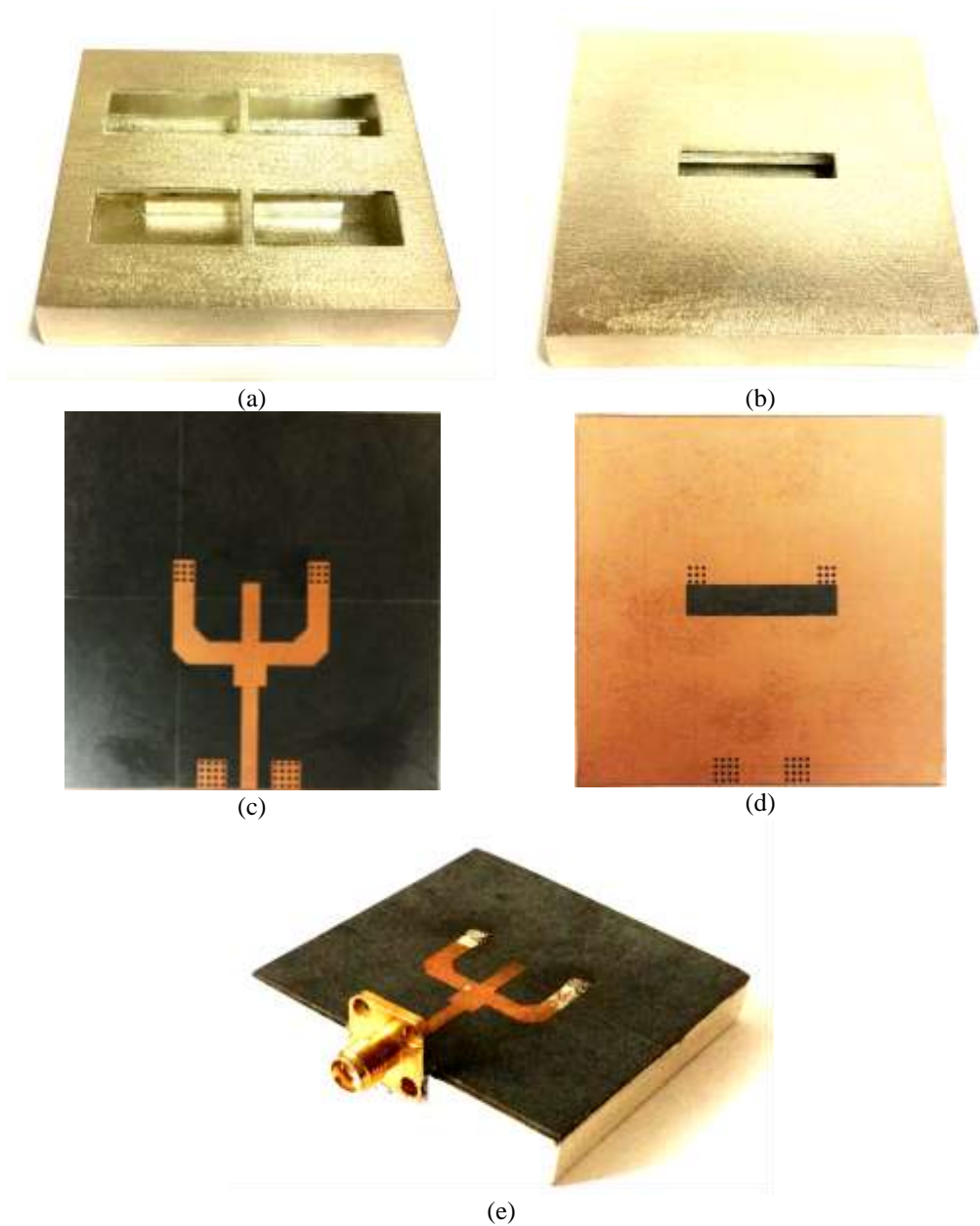


Figure 2-16. The cavity-backed slot antenna 3D printed out of silver fed by a microstrip line (a) cavity top view (b) cavity bottom view (c) microstrip top layer (d) microstrip bottom layer (e) assembled antenna.

pattern in the H-plane cut at different frequencies. It is observed that, the H-plane cross-polarized gain is 25 dB lower than the co-polarized gain within the main beam at all frequencies. The direction of the maximum radiation is at boresight over the entire band. The

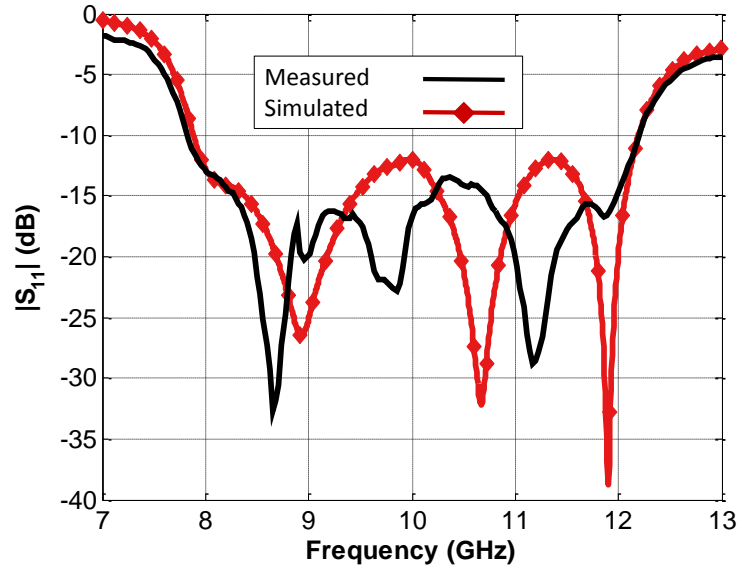


Figure 2-17. The measured and simulated reflection coefficient of the fabricated CBSA shown in Figure 2-16(e).

antenna radiation pattern in the E-plane cut is depicted in Figure 2-19. The cross-polarization in the E-plane is negligible in all directions. Similar to H-plane cut, maximum radiation occurs at boresight at all frequencies. The side-lobe levels in the E and H planes are reported in Table 2-4 at different frequencies. The measured and simulated antenna gain versus frequency is plotted in Figure 2-20. The antenna provides a minimum of 11 dB gain and 65% aperture efficiency from 8 GHz to 12 GHz. The discrepancy between the simulation and the measurement of the antenna gain is resulted from calibration distortion as long cables are used for the gain measurements and also from the fabrication errors including misalignment of the PCB and the cavity and the errors in 3D printing of the cavity. A comparison with the previously reported cavity backed slot antennas is provided in Table 2-5. The bandwidth of the proposed antenna is twice the bandwidth of the most wideband design [34] among the reported designs. The proposed antenna can be used as a building block of large planar arrays. When used in a planar array configuration, the mutual coupling between adjacent vertical

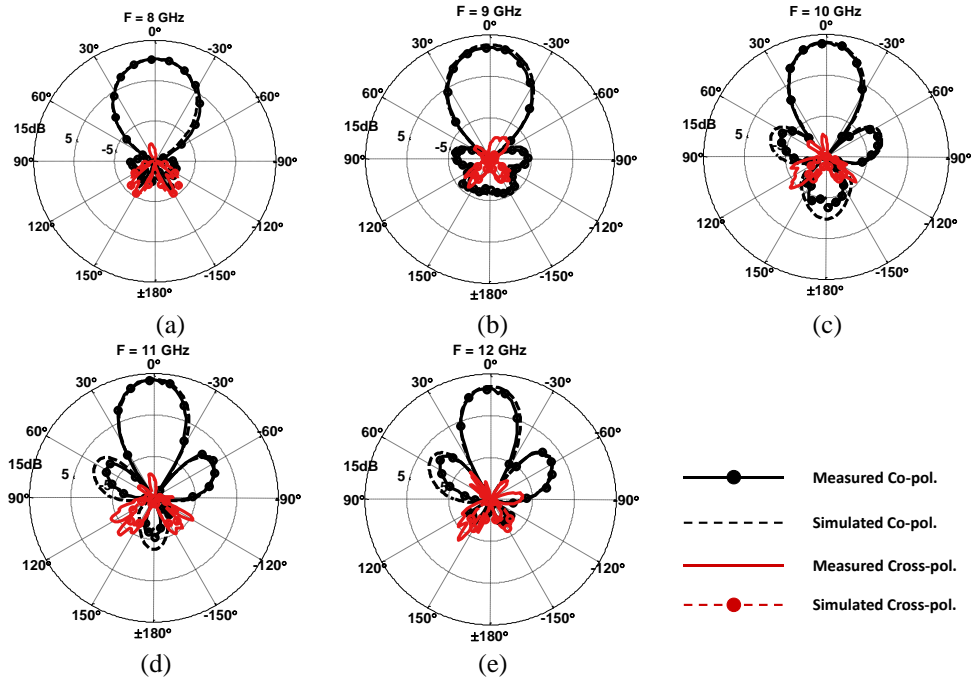


Figure 2-18. Measured and simulated co-pol. and cross-pol. radiation pattern in H-plane at (a) $f = 8$ GHz , (b) $f = 9$ GHz , (c) $f = 10$ GHz, (d) $f = 11$ GHz, (e) $f = 12$ GHz.

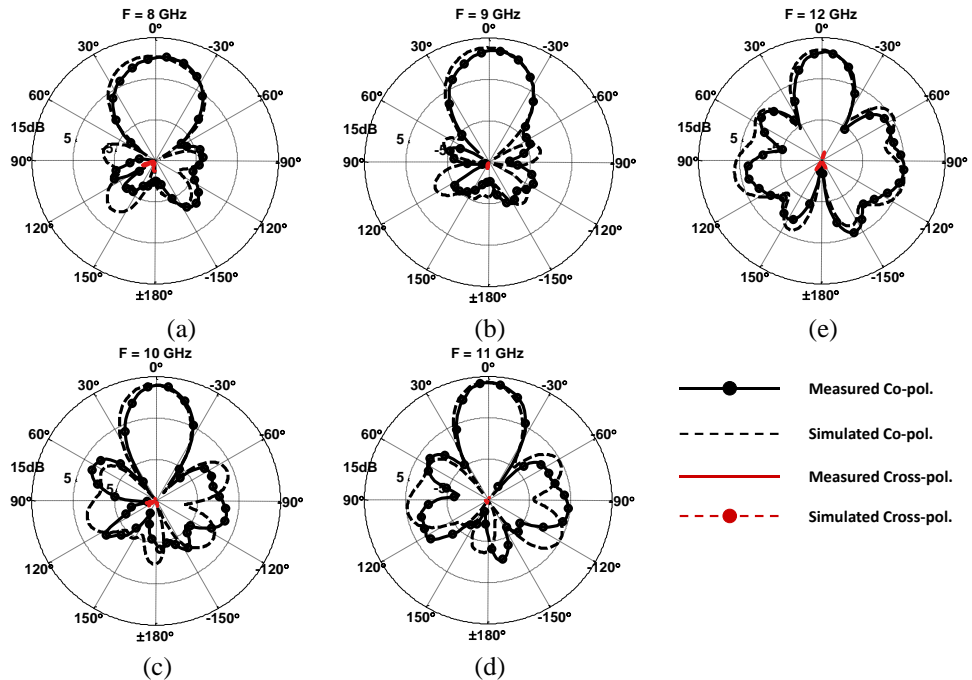


Figure 2-19. Measured and simulated co-pol. and cross-pol. radiation pattern in E-plane at (a) $f = 8$ GHz, (b) $f = 9$ GHz , (c) $f = 10$ GHz, (d) $f = 11$ GHz , (e) $f = 12$ GHz.

and horizontal blocks is simulated to be less than -25 dB and -35 dB respectively. A

Table 2-4. The side lobe levels in E and H planes at different frequencies

Frequency (GHz)	H-Plane SLL (dB)	E-Plane SLL (dB)
8	-20.3	-9.7
9	-18.5	-13.1
10	-12.8	-9.5
11	-12.4	-9.2
12	-9.8	-6.1

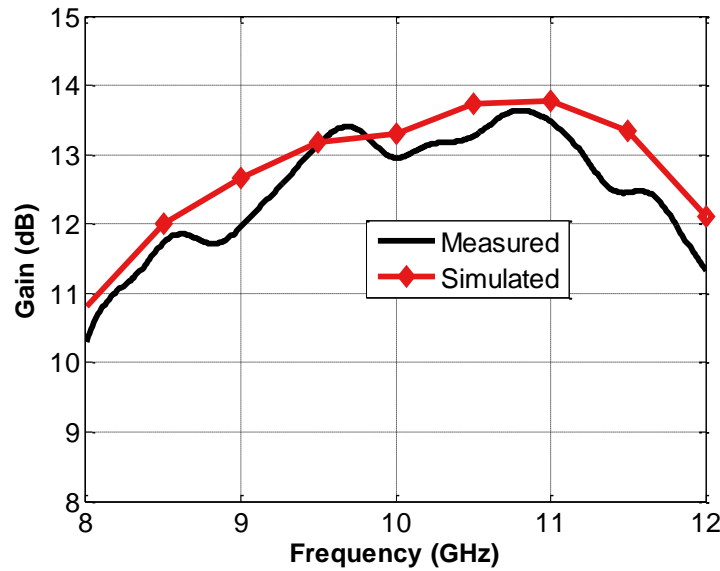


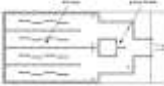
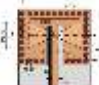
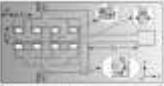
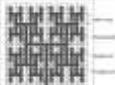
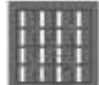

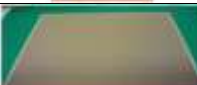


Figure 2-20. The Measured and simulated antenna gain.

limited scanning range is possible for applications where a small beam tilt from the antenna boresight is required. At the highest frequency of operation, this range is found to be $\pm 5^\circ$. This is the range for which the level of the grating lobes is less than -10 dB. Subarray overlapping [117] can be used to increase the scanning range.

2.3 Dual-Port Cavity-Backed Slot Antenna for Full-Duplex Applications

The single-port antenna introduced in section 2.2 can be evolved to a two-port antenna with orthogonal polarizations. A cancellation scheme is introduced to achieve high

Table 2-5. Comparison of the cavity-backed slot antennas with the proposed CBSA

Reference	Bandwidth (%)	Array Size	Max. Gain (dB)	Dimensions	Aperture Efficiency (%)
[27] 	7.39	4 × 4	18.74	14.9 λ ₀ × 13.8 λ ₀ × 0.053 λ ₀	2.9
[28] 	9.4	1	3.86	0.6 λ ₀ × 0.93 λ ₀ × 0.03 λ ₀	20
[29] 	11.6	2 × 4	12	6 λ ₀ × 5 λ ₀ × 0.13 λ ₀	4.2
[31] 	12	16 × 16	29	13.7 λ ₀ × 13.7 λ ₀ × 0.7 λ ₀	33
[30] 	14	4 × 4	17.8	3.33 λ ₀ × 3.33 λ ₀ × 0.1 λ ₀	39.2
[32] 	16.7	2 × 2	9	1.49 λ ₀ × 1.37 λ ₀ × 0.07 λ ₀	36.3
[35] 	17.1	32 × 16	25.5	13.75 λ ₀ × 13.75 λ ₀ × 0.06 λ ₀	14.5
[33] 	17.6	4 × 4	21.1	3.52 λ ₀ × 3.52 λ ₀ × 0.83 λ ₀	80
[34] 	21	2 × 2	13.8	3.94 λ ₀ × 3.15 λ ₀ × 0.28 λ ₀	15.4
This work	40	2 × 2	13.7	1.66 λ ₀ × 1.66 λ ₀ × 0.2 λ ₀	65

level of isolation between the two ports. The proposed antenna can be used for full-duplex applications.

2.3.1 Dual-Polarized Slotted Cavity

The proposed dual-polarized CBSA structure is depicted in Figure 2-21 . The antenna is composed of an especial rectangular slotted cavity of height $H = 0.15\lambda_L$ which is

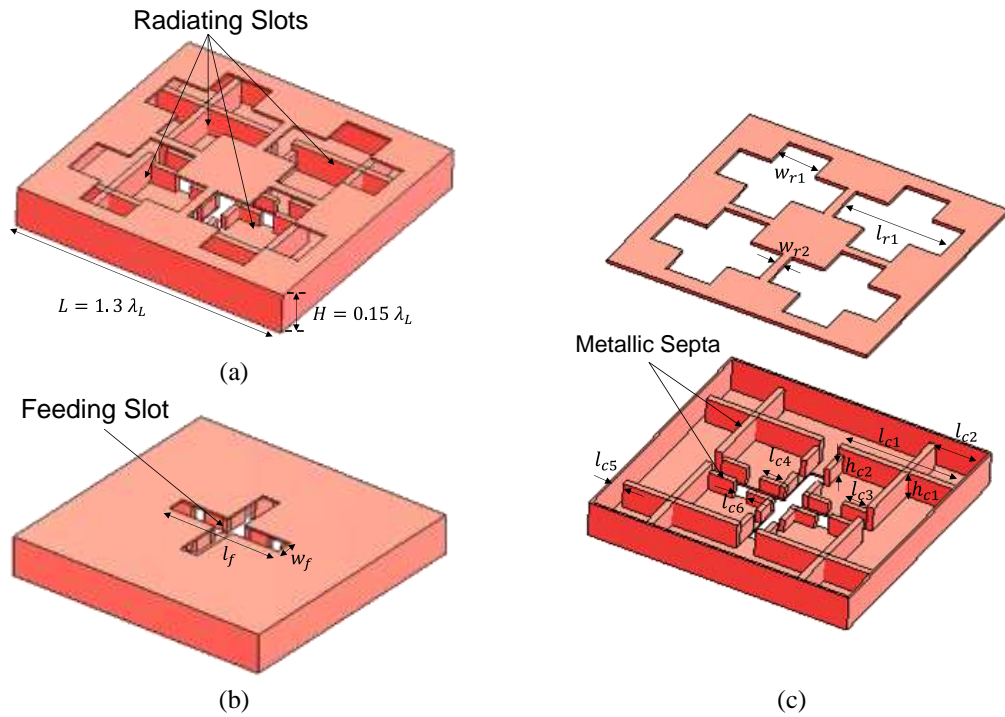


Figure 2-21. The slotted cavity loaded by multiple metallic septa (a) radiating slots on the front side (b) feeding slots on the back side, (c) metallic septa inside the cavity.

commonly exploited by both channels. The antenna, yet consists of a microstrip circuitry, and an end-launch coaxial-to-waveguide transition with orthogonal polarizations each of which feeds the cavity. While being compact, the feeding topologies are designed using a symmetric geometry which provides high level of self-interference cancellation over a wide bandwidth. As mentioned before, a cavity-backed slot aperture acts like a narrowband radiator by its nature. As demonstrated in Section 2.1.1, it is feasible to make a slotted cavity radiate over a wide bandwidth by appropriately loading the cavity by multiple metallic septa [115]. The inserted septa increase the bandwidth through two different mechanisms. First, they excite evanescent modes and thus bring down the cutoff frequency. Second, they can be designed to merge different resonant frequencies [115]. As a result, the modified slotted

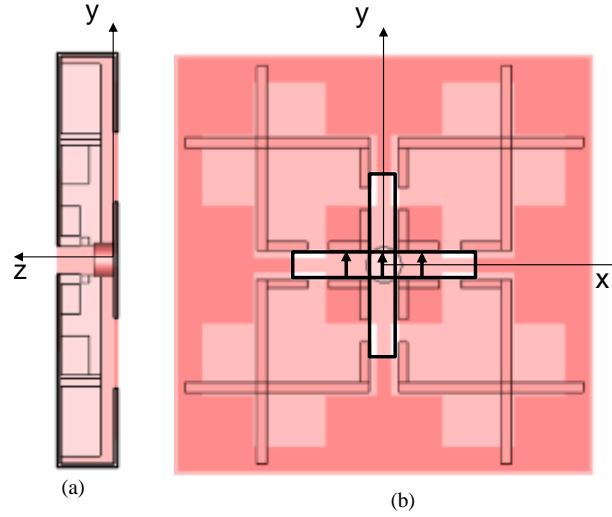


Figure 2-22. The slotted cavity loaded by multiple metallic septa (a) side view, (b) front view.

cavity exhibits broadband behavior. This cavity acts as a transducer between the wideband feed ports and the radiating aperture by properly tailoring the field distribution. Devised to have four cross-slots on the broad wall as common radiating elements for both transmit and receive channels, the cavity is fed by two concentric perpendicular slots on the back wall to generate orthogonal transmit and receive polarizations. With reference to Figure 2-22, for vertical polarization, for instance, the electric field distribution across the feeding slot resembles that of the \mathbf{TE}_{10}^z field distribution for a rectangular waveguide i.e. $\mathbf{E} = \hat{\mathbf{y}} E_y(\mathbf{x})$. Similar to single-port CBSA, as the wave propagates into the cavity, a component of the electric field is generated in z-direction due to the discontinuity between the feeding slot and the cavity. Thereby, the excited mode inside the cavity is \mathbf{TE}^x . The discontinuity of the magnetic Hertz vector potential at the edges of the septa results in non-vanishing electric field in y-direction. This suggests that the metallic septa should be placed close to the edges of the slots as shown in Figure 2-21(c) to excite a component of the electric field in y-direction across the radiating and feeding slots. While reducing the cutoff frequency of the

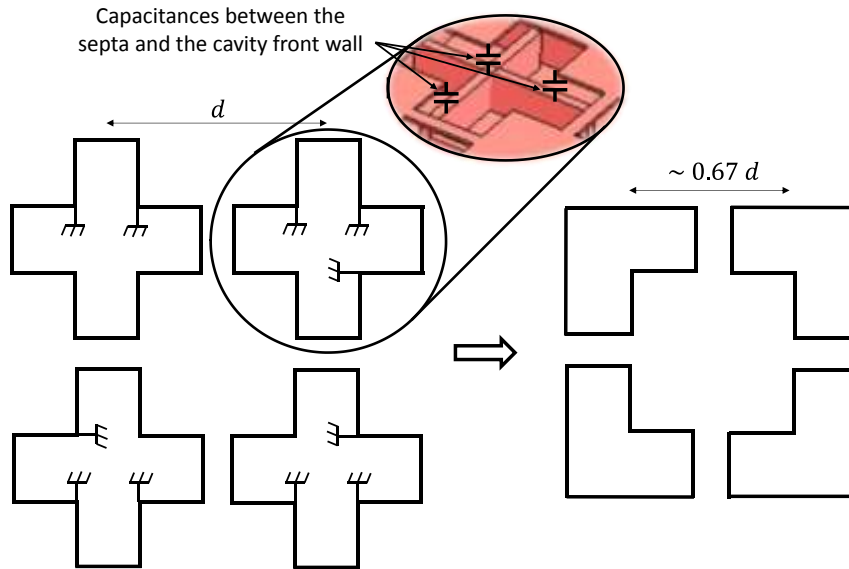


Figure 2-23. The mechanism of shrinking the slots size by appropriately placing the septa. The center-to-center distance between adjacent slots radiating slots is decreased as frequency increases.

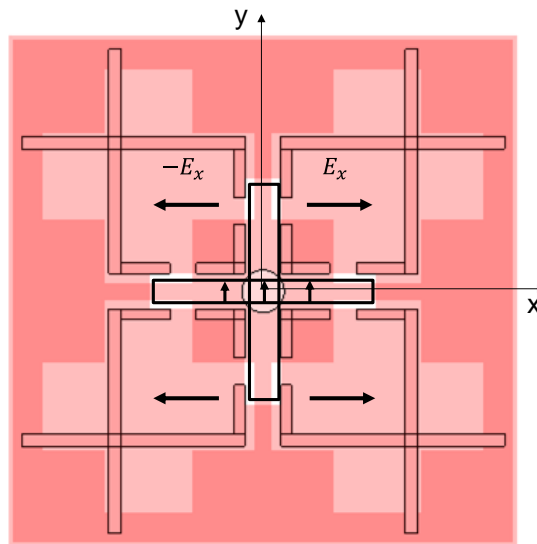


Figure 2-24. The cross polarized radiation caused by the cross polarized electric field generated across each slot is cancelled by that of the adjacent slot within the main beam due to the structure symmetry.

cavity, this arrangement of the septa assists with wave transformation from \mathbf{TE}_{10}^z to \mathbf{TE}^x and excites multiple \mathbf{TE}^x resonances of the slotted cavity. Similar mechanism holds true for the

horizontal polarization. Hence, the proposed compact slotted cavity radiates over a wide bandwidth.

As frequency increases, the electrical distance between radiating slots increases. This can introduce a deteriorating effect on the radiation pattern and gain through increasing the level of the grating lobes. Appropriately placed, the inserted septa can be exploited to rectify this problem to some extent. Referring to Figure 2-23, the reactance due to the capacitance between the edges of the septa and the broad-wall of the cavity decreases as frequency increases. This leads to semi-short-circuiting part of the slot towards the slot edge and thereby reducing the effective length of the slots. The reduction in the center to center distance between the two radiating slots causes the level of the grating lobes to drop.

Each radiating slot bears some level of cross-polarized radiation. However, the symmetric geometry of the structure allows for cancellation of the cross-polarized radiation within the main beam. Figure 2-24 shows the schematic of the generated cross-polarized electric field across each slot. The symmetry requires the undesired cross-polarized components of the electric field of the adjacent slots to be in opposite directions, hence the far-field cross-polarized radiation is very low around the direction of the peak gain ($\theta = 0$). There is still some level of cross-polarization in directions away from the main beam.

2.3.2 Cancellation Mechanism

Using orthogonal polarizations for transmit and receive channels, does not provide the required level of isolation. This is mainly due to depolarization of the wave as it propagates from Tx through the antenna structure. The depolarized wave is then partly captured by the Rx. To achieve higher level of self-interference cancellation, a symmetric

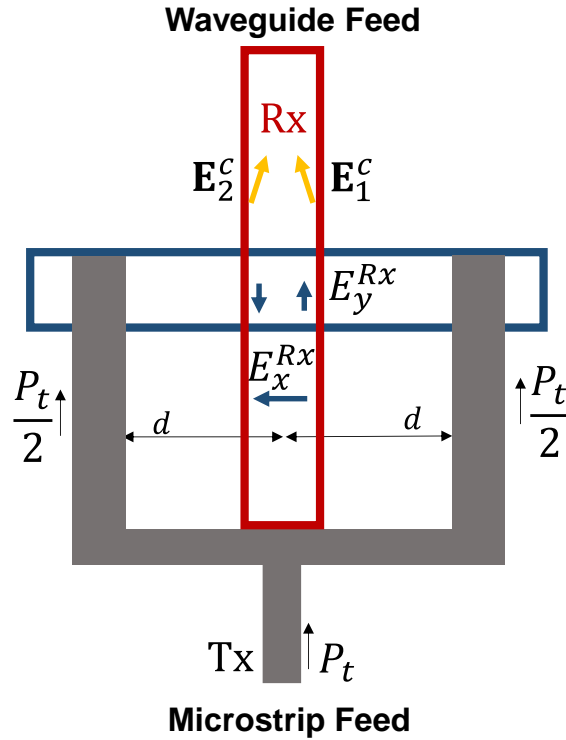


Figure 2-25. The schematic of the feeding topology. The coupling between channels due to depolarization represented by E^c is significantly reduced by this method.

feed configuration is employed. The schematic of the decoupling method is shown in Figure 2-25. Two concentric orthogonal rectangular slots are used to feed the cavity each of which excites one polarization. The slot with vertical polarization (Tx slot in Figure 2-25) is fed by a two-pronged microstrip line symmetrically crossing over the slot. With reference to Figure 2-25, the coupled signals from these two prongs to the waveguide slot with horizontal polarization (Rx slot in Figure 2-25) due to polarization transformation are equal in magnitude and out-of-phase resulting in a high level of decoupling between the two ports. The symmetry mandates that the coupled electric field generated by the two prongs of the microstrip line of the Tx port over the Rx slot denoted by $E_1^c(x, y)$ and $E_2^c(x, y)$ satisfy the following conditions:

$$E_{1x}^c(x, y) = -E_{2x}^c(-x, y) \quad (2-8)$$

and

$$E_{1y}^c(x, y) = E_{2y}^c(-x, y) \quad (2-9)$$

To ensure the coupled field at the Rx slot would be cancelled, reciprocity can be used. That is by exciting the Rx slot, the field over the Rx slot aperture must satisfy the following conditions:

$$E_x^{Rx}(x, y) = E_x^{Rx}(-x, y) \quad (2-10)$$

and

$$E_y^{Rx}(x, y) = -E_y^{Rx}(-x, y) \quad (2-11)$$

It will be shown that it is feasible to generate such electric field distribution by a compact broadband coaxial to waveguide transition which is connected to the Rx slot. The cancellation level achieved by this method is frequency-independent, thereby, the bandwidth of the structure is limited by the bandwidth of each channel not the bandwidth provided by the cancellation mechanism. This structure allows for sharing the entire available aperture by both channels and, thereby, provides at least 3 dB higher gain or half area used by the antenna system compared to other reported full-duplex antenna systems in which separate elements are used for transmitting and receiving [15]. The realization of the microstrip and waveguide feeds are described in the following sections.

2.3.3 Microstrip Feed

The microstrip feed line is laid out on the back side of the cavity as depicted in Figure

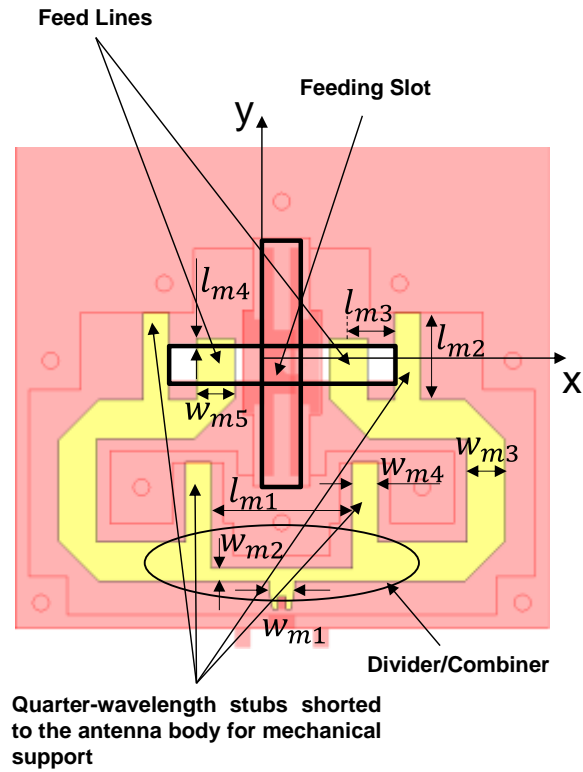


Figure 2-26. The microstrip feed laid out on the back side of the cavity.

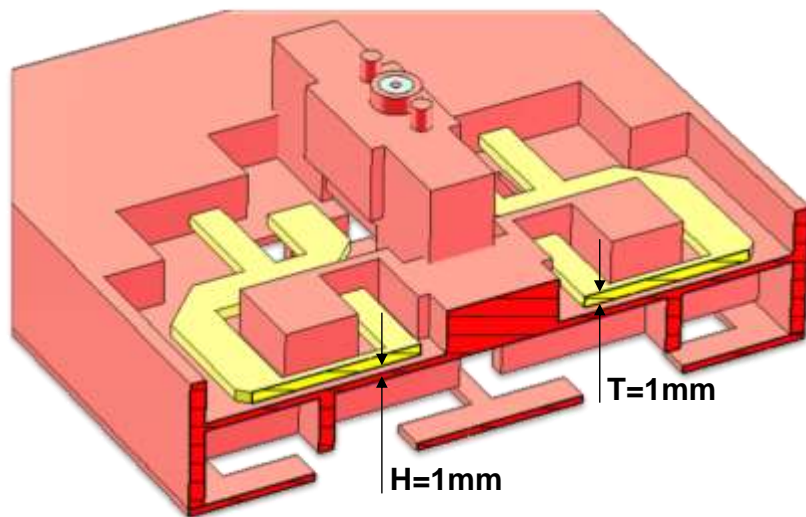


Figure 2-27. A perspective cut view of the air-dielectric microstrip line suspended over ground plane and supported by quarter-wavelength stubs short-circuited to the antenna body to provide mechanical support.

2-26. It is composed of an equal-power divider, two open circuited lines crossing the feeding

slot of the cavity, and four short-circuited quarter-wavelength stubs. The reason for adding the stubs is to realize the microstrip lines on air dielectric to reduce loss and dispersion. The air-dielectric microstrip line can be fabricated with the cavity as a single unit using 3D printing technology. This method has also the advantage of eliminating issues with aligning and assembling the microstrip board with the cavity if the microstrip is fabricated separately by standard Printed Circuit Board (PCB) technology. To make this feasible, the microstrip line should be of relatively large thickness that also helps reducing the conductor loss. Eliminating substrate loss, the air-dielectric microstrip line does not support surface wave and thereby, does not suffer from surface wave loss. A perspective view of the microstrip feed is shown in Figure 2-27. The lines have a thickness of $T = 1$ mm and are suspended at a distance of $H = 1$ mm from the ground plane (back side of the cavity). This low-loss air-dielectric microstrip feed is supported by four quarter-wavelength stubs short-circuited to the antenna body and is amenable to 3D printing technology. The feed lines cross the slot at a distance of $l_{m3} = 0.15 \lambda_0$ from the slot lateral sides where λ_0 is the wavelength at the center frequency and are open-circuited at a distance slightly above the upper longitudinal side of the slot (l_{m4} in Figure 2-26). The stubs are designed to be oriented in y-direction to minimize creating cross-polarized radiation which may be coupled to the other port.

2.3.4 Waveguide Feed

As mentioned in part B of this section, to achieve a high level of isolation, the electric

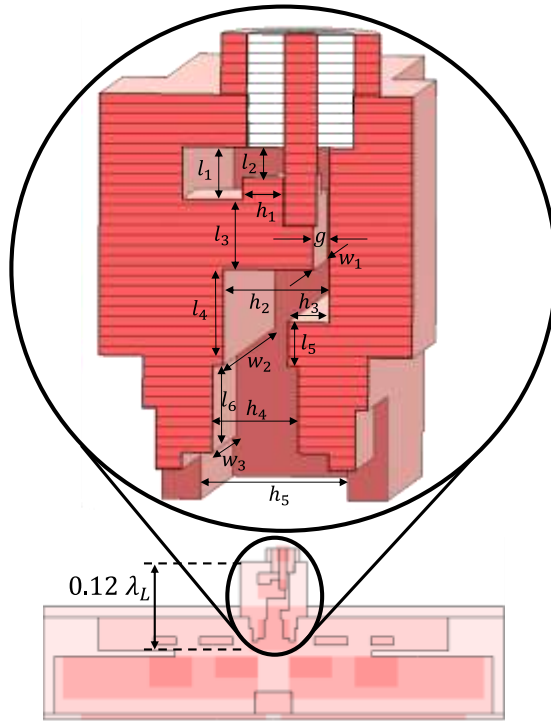


Figure 2-28. The coaxial-to-waveguide transition feeding the cavity.

field across the Rx slot should satisfy (5) and (6). To create this electric field, a compact end-launch coaxial-to-waveguide transition is devised. The structure of the transition is shown in Figure 2-28. The transition is composed of multiple waveguide sections that provides impedance matching and field transformation between the coaxial line and the feeding slot. As the TEM wave on the coaxial line with the radial electric field between the inner and the outer conductor propagates through the waveguide (see Figure 2-29) a component of the electric field in x-direction survives through the small gap of the A-D section of the waveguide. Other components of the electric field are bypassed to a great extent through the hollow-like part of A-C section marked in red in Figure 2-29 (a). The cross section of the waveguide in x-direction is then gradually increased to match the width of the feeding slot. The established electric field in the small gap propagates through four waveguide sections

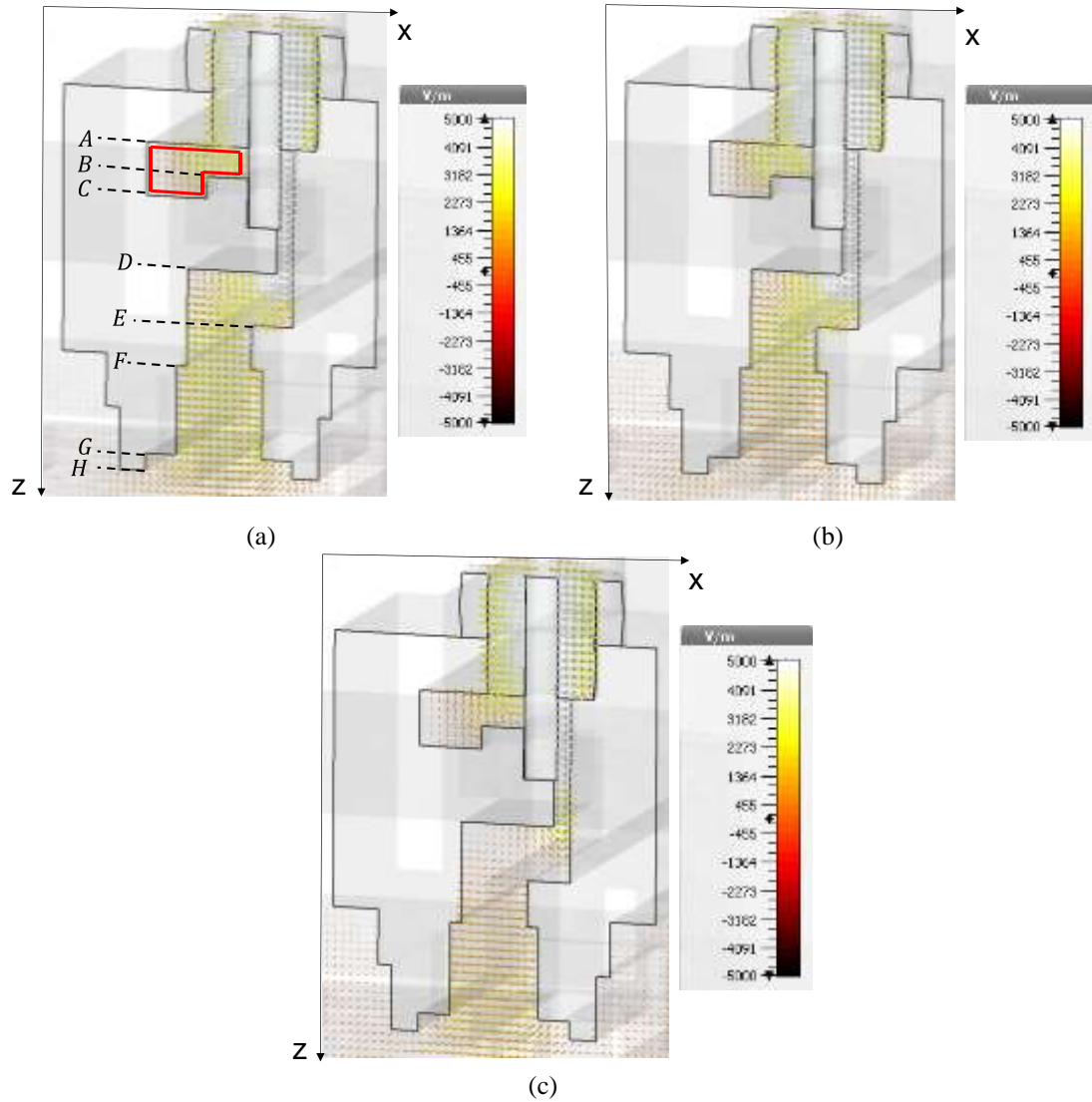


Figure 2-29. The electric field distribution along the cross section of the waveguide feed when the waveguide port is excited. (a) $f = 5$ GHz, (b) $f = 6$ GHz, and (c) $f = 7.5$ GHz.

extending from $z = D$ to $z = H$. The waveguide is supported by quadruplet pillars protruded along the edge of the aforesaid feeding slot. As depicted in Figure 2-29, this design renders a symmetric distribution for the x-component of the electric field across the waveguide

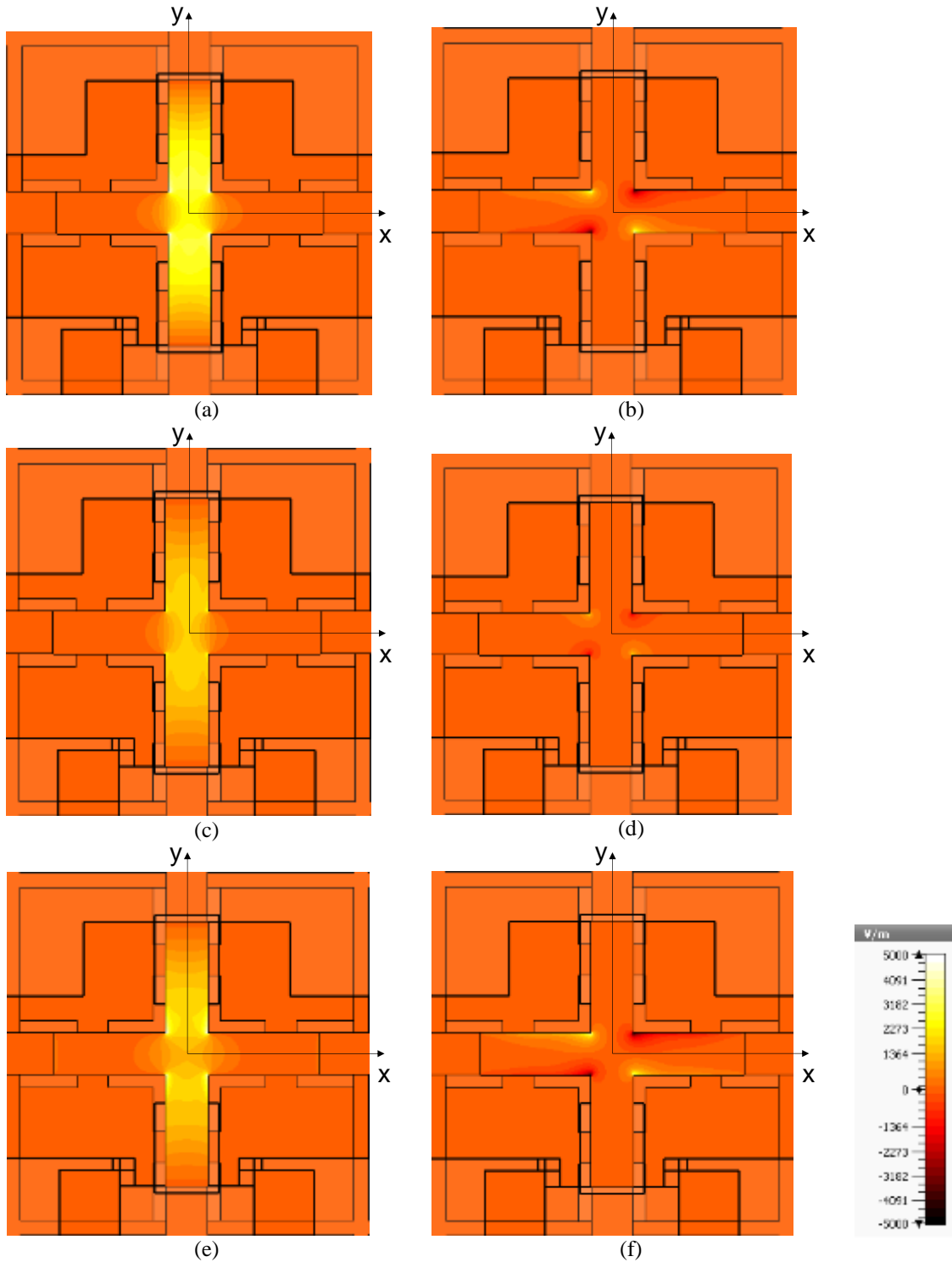


Figure 2-30. The electric field distribution across the waveguide feed when the waveguide port is excited. E_y is an even function of y and E_x is an odd function of y (a) E_y at $f = 5$ GHz, (b) E_x at $f = 5$ GHz, (c) E_y at $f = 6$ GHz, (d) E_x at $f = 6$ GHz, (e) E_y at $f = 7.5$ GHz, (f) E_x at $f = 7.5$ GHz.

aperture at $z = H$. Figure 2-30 shows the electric field distribution across the Rx feeding slot

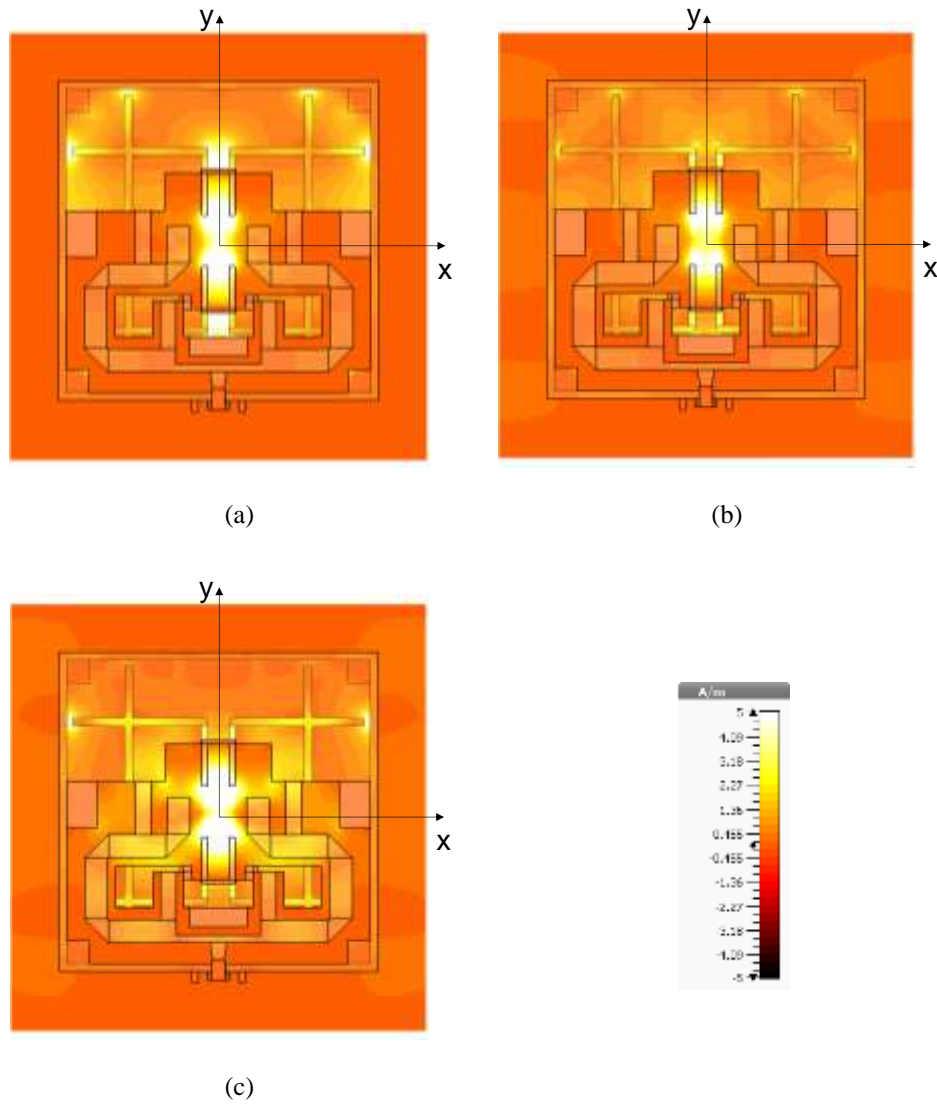
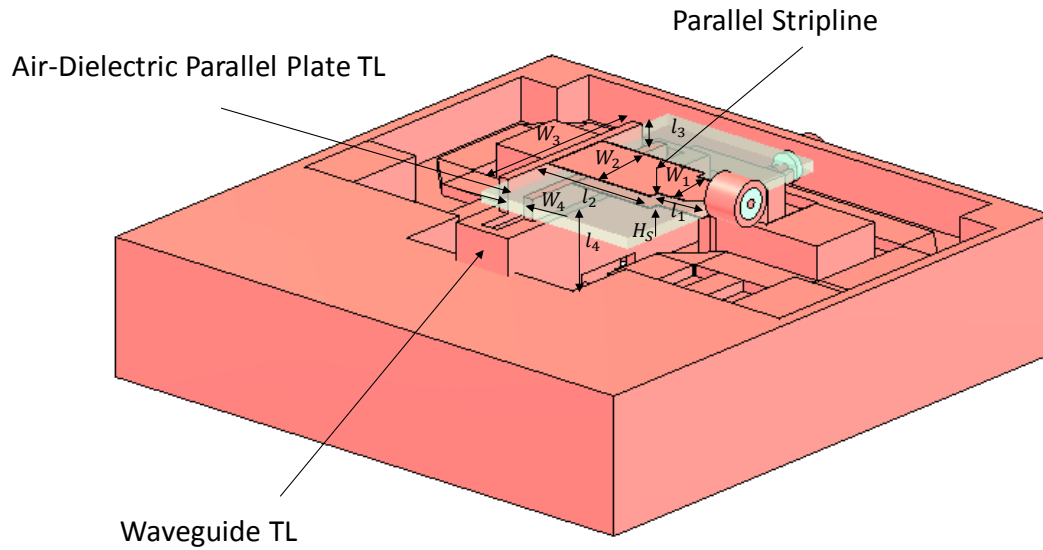
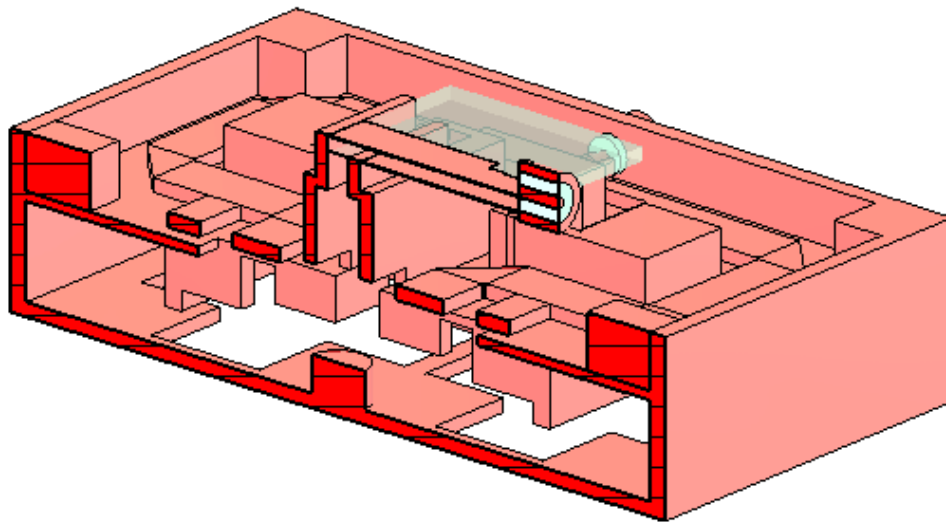


Figure 2-31. Tangential magnetic field on the microstrip line when the waveguide port is excited. (a) $f = 5$ GHz, (b) $f = 6$ GHz, (c) $f = 7.5$ GHz. The current at the microstrip terminal is very small.

at different frequencies. The x-component of the electric field is symmetric, and the y-component of the electric field is antisymmetric with respect to the center of the slot, thereby conditions (2-10) and (2-11) are met. The tangential magnetic field on the microstrip line, when the waveguide port is excited, is plotted in Figure 2-31 at different frequencies. At the microstrip terminal the surface current given by $\mathbf{J}_s = \mathbf{z} \times \mathbf{H}_t$ is very small resulting in a very



(a)



(b)

Figure 2-32. The feeding topology composed of a rectangular waveguide, an air-dielectric parallel plate transmission line, and a broadside-coupled stripline. (a) Perspective view, (b) cut view.

high isolation between the two ports.

The transition shown in Figure 2-28 is a very complex structure. An alternative feed topology is shown in Figure 2-32. This feed configuration is composed of a rectangular

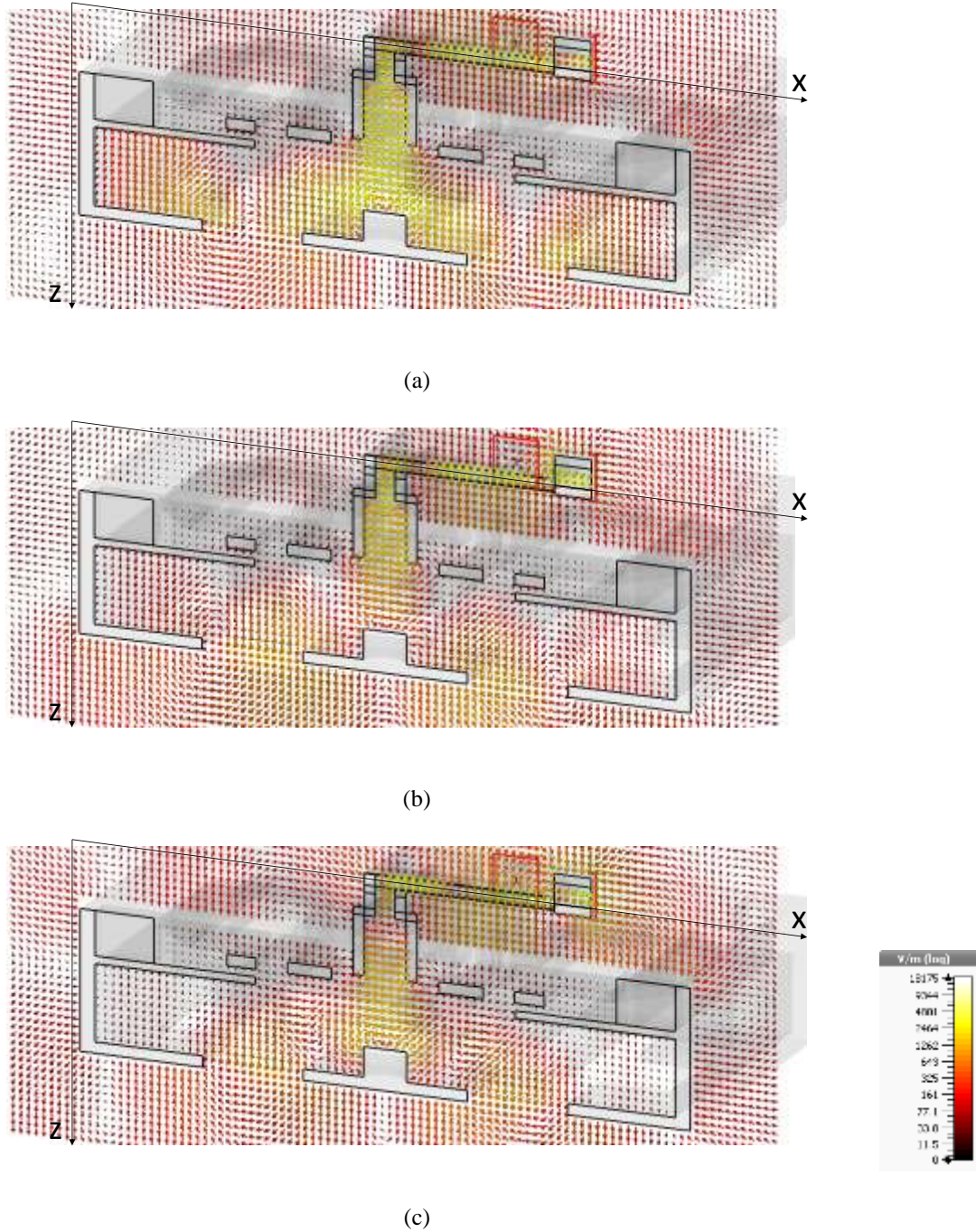


Figure 2-33. The electric field distribution along the transition shown in Fig (a) $f = 5$ GHz, (b) $f = 6$ GHz, (c) $f = 7.2$ GHz.

waveguide, an air-dielectric parallel plate waveguide, and a broadside-coupled stripline section. The waveguide section which feeds the cavity is converted to a parallel plate transmission line with a plate spacing smaller than the size of the waveguide narrow wall.

The parallel plate line is then fed by a broadside-coupled stripline. The design parameters including the width, the length and the height of the air-dielectric parallel plate waveguide and the parallel stripline are optimized by full-wave simulation for the desired bandwidth.

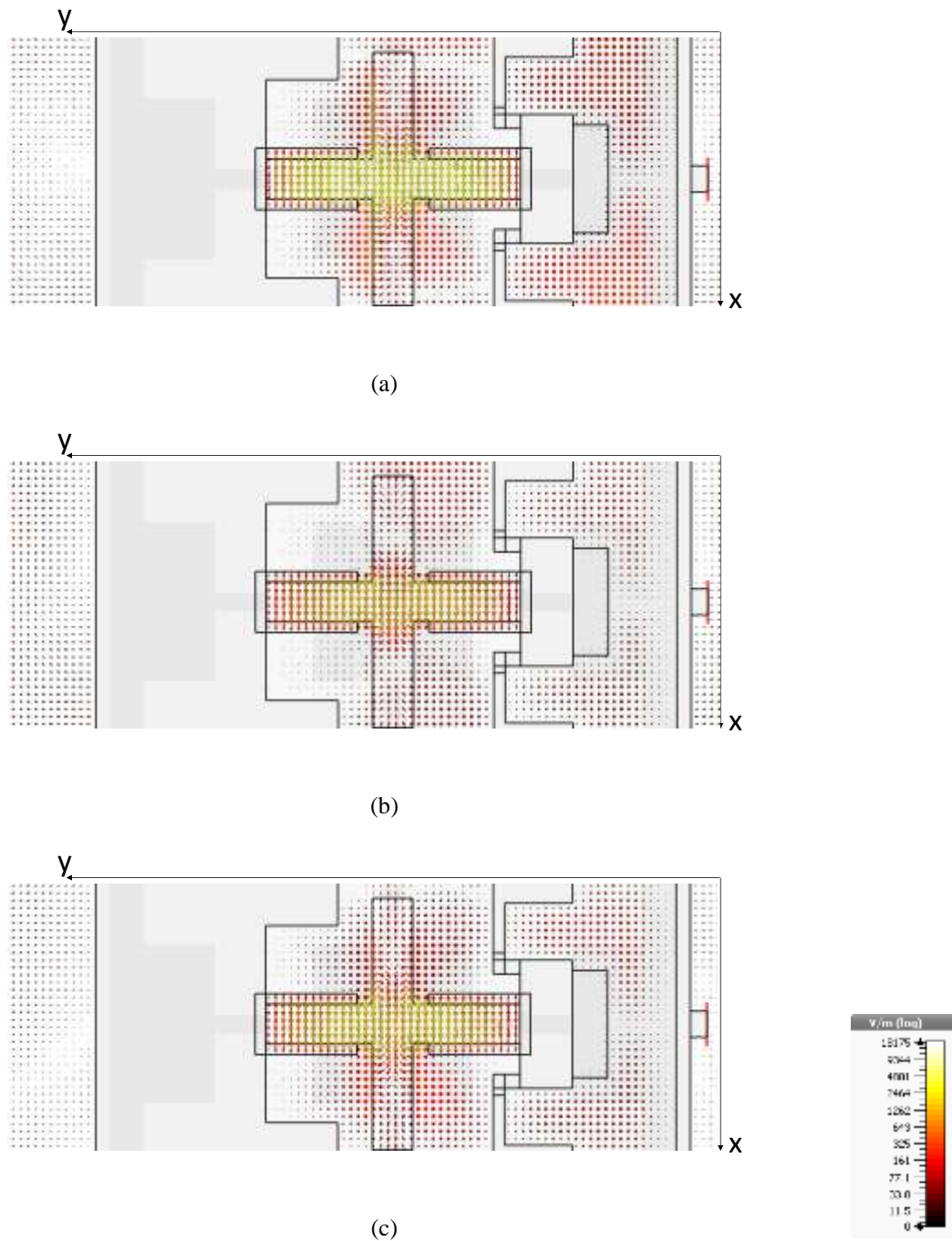


Figure 2-34. The electric field distribution along the transition shown in Fig (a) $f = 5$ GHz, (b) $f = 6$ GHz, (c) $f = 7.2$ GHz.

Designed for the same bandwidth, this structure is less complex but provide lower level of isolation between the two ports compared to the design shown in Figure 2-28. The electric field distribution along this transition is depicted in Figure 2-33. The electric field distribution across the feeding slot of the cavity is shown in Figure 2-34 which satisfies (2-10) and (2-11).

2.3.5 Simulation and Experimental Results

The proposed complex antenna structure is fabricated using HP PA12 Nylon 3D printing and then silver metallization by spraying. The 3D printed parts before metallization

Table 2-6. Dimensions of the cavity shown in Figure 2-21

Parameter	Value (mm)	Parameter	Value (mm)
h_{c1}	7.6	H	11
h_{c2}	5.4	L	83
l_{c1}	35.1	w_{r1}	13.6
l_{c2}	13.5	w_{r2}	2.6
l_{c3}	7.6	l_{r1}	33
l_{c4}	7.6	w_{f1}	5.6
l_{c5}	1.6	h_{f1}	35.4
l_{c6}	4.2		

Table 2-7. Dimensions of the microstrip feed shown in Figure 2-26

Parameter	Value (mm)	Parameter	Value (mm)
w_{m1}	4	l_{m1}	22
w_{m2}	2	l_{m2}	13.6
w_{m3}	6	l_{m3}	7.4
w_{m4}	4	l_{m4}	0.9
w_{m5}	6		

Table 2-8. Dimensions of the waveguide feed shown in Figure 2-28

Parameter	Value (mm)	Parameter	Value (mm)
h_1	1.2	l_1	12
h_2	4	l_2	1.2
h_3	1.6	l_3	2.7
h_4	4	l_4	3.7
h_5	5.1	l_5	1.7
w_1	10	l_6	3.3
w_2	35.4	g	0.6
w_3	35.4		

are shown in Figure 2-35(a-d). The metalized and assembled antenna structure is depicted in Figure 2-35(e) and Figure 2-35(f). The optimized values of the parameters for the cavity,

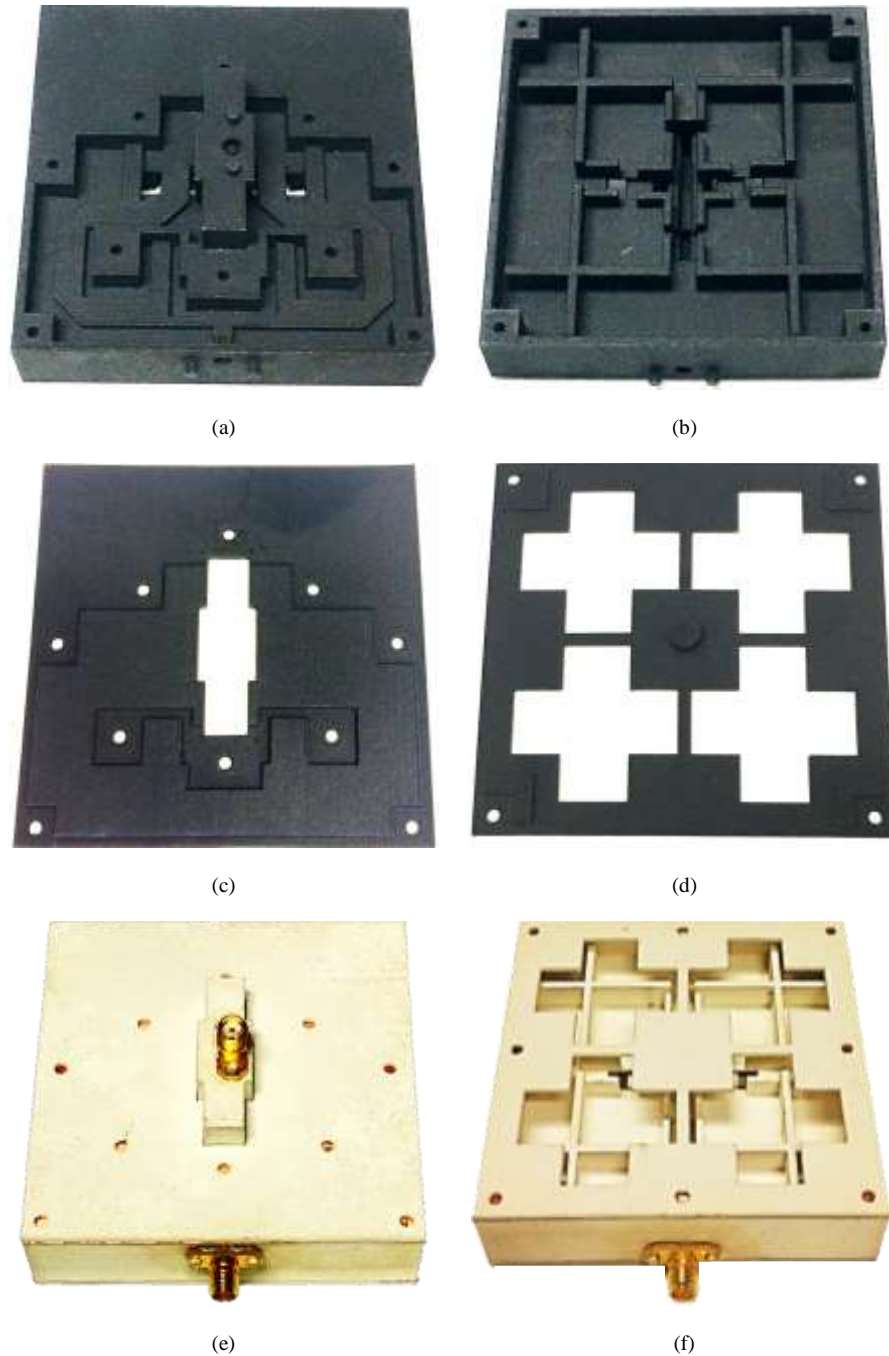


Figure 2-35. The fabricated antenna. (a-d) Different parts of the antenna 3D printed out of HP PA12 Nylon. (e and f) The metalized and assembled antenna.

microstrip feed, and waveguide feed are listed in

Table 2-6, Table 2-7, and Table 2-8 respectively. The S-parameters of the antenna are illustrated in Figure 2-36. Keeping the return loss better than 8 dB, a minimum isolation level of 50 dB is achieved over 44% fractional bandwidth. Excluding the scattering effect caused

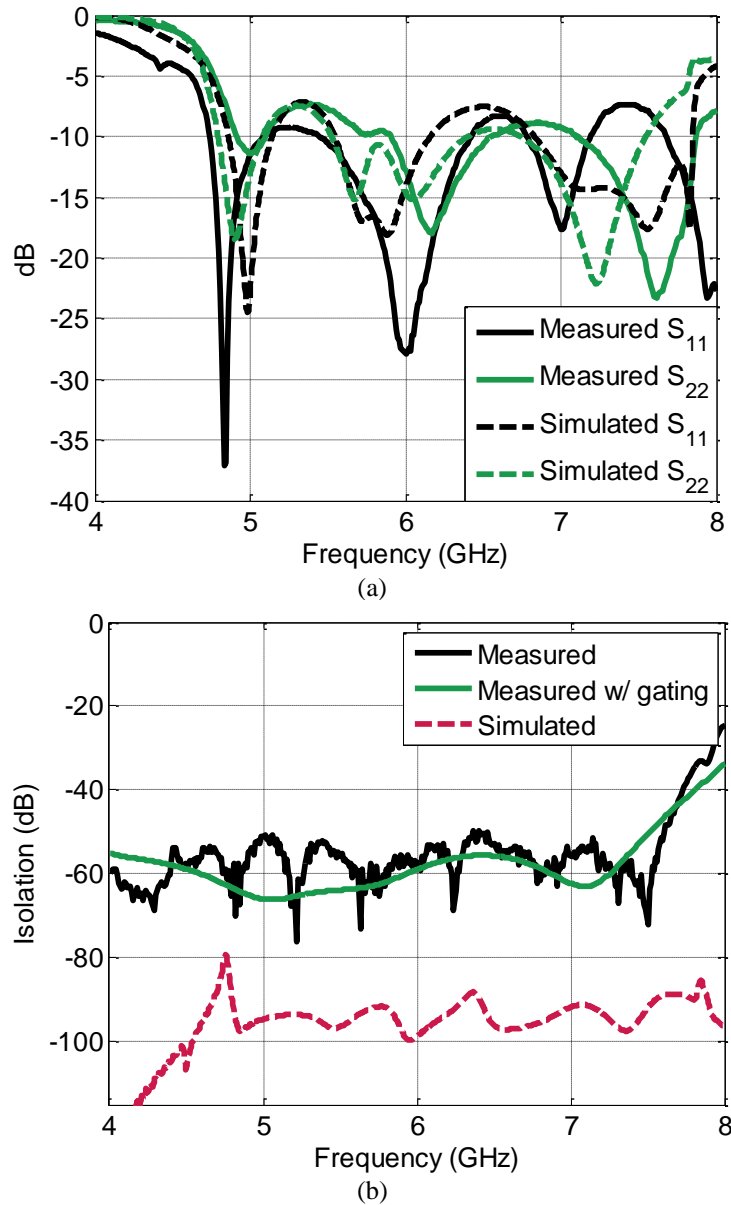


Figure 2-36. The simulated and measured S-parameters. (a) Reflection coefficient, and (b) isolation.

by the nearby objects through gating the transmission response between the two ports, the

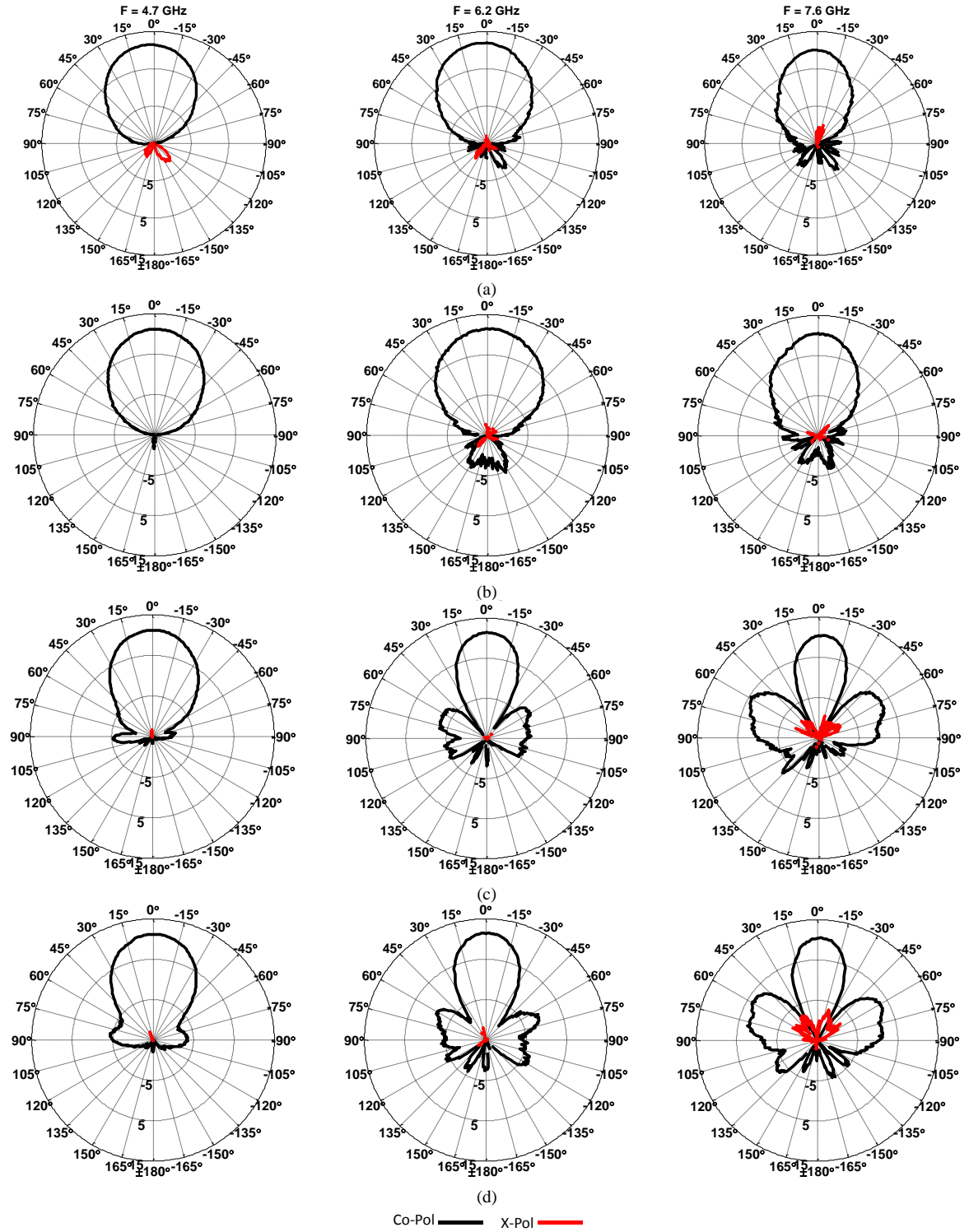


Figure 2-37. The measured radiation pattern (a) V-pol H-plane (b) H-pole H-plane (c) V-pole E-plane (d) H-pole E-plane.

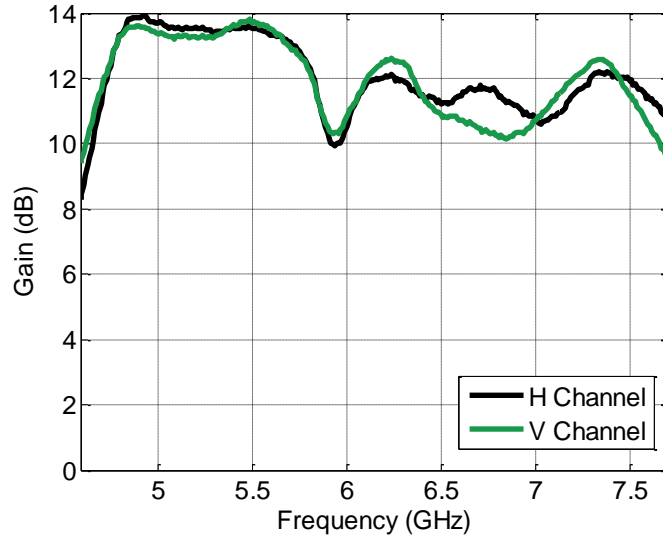


Figure 2-38. The measured antenna gain.

Table 2-9. The optimized values of the feed parameters shown in Figure 2-32

Parameter	Value (mm)	Parameter	Value (mm)
w_1	7	l_1	7.2
w_2	10.4	l_2	17.1
w_3	25.4	l_3	4.6
w_4	2.6	l_4	11
H_s	1.5		

measured isolation is shown to be better than 55 dB. It should be noted that the isolation level between the two ports is simulated to be more than 89 dB which is degraded in measurement due to fabrication imperfections. Compared to the co-polarized antenna design in [16], both the bandwidth and isolation are enhanced. The antenna radiation patterns in E- and H-planes at different frequencies are plotted in Figure 2-37. Other than the polarization, the transmitting and receiving patterns are of identical shape. The cross-polarization is less than -20 dB and the front-to-back ratio is better than 19 dB for both channels. The side-lobe levels are less than -16 dB in H-plane and less than -8 dB in E-plane for both polarizations. Figure 2-38

Table 2-10. The optimized values of the feed parameters shown in Figure 2-32

Parameter	Value (mm)	Parameter	Value (mm)
w_1	7	l_1	7.2
w_2	10.4	l_2	17.1
w_3	25.4	l_3	4.6
w_4	2.6	l_4	11
H_S	1.5		

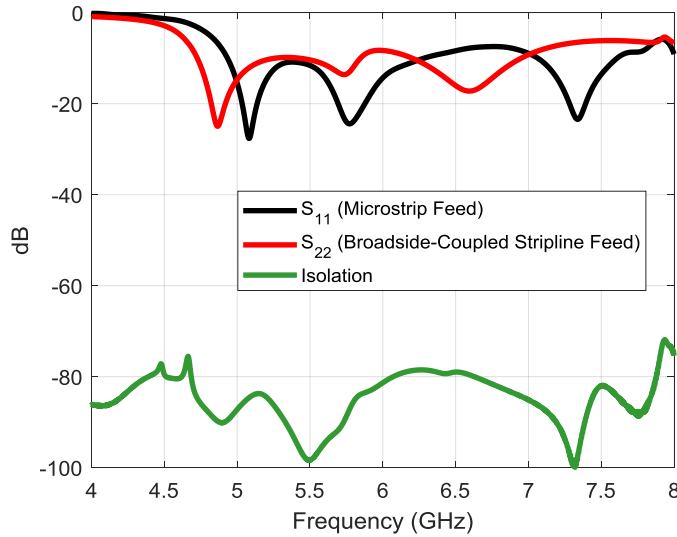


Figure 2-39. The S-parameters of the antenna shown in Figure 2-32.

depicts the measured antenna gains. The gain for both channels is more than 10 dB over the entire bandwidth.

The feed structure shown in Figure 2-32, is designed to provide the same bandwidth. The optimized values of the design parameters are listed in Table 2-9. The parallel stripline is printed on 60 mil RT/Duroid 5880. The simulated S-parameters are plotted in Figure 2-39. While the dimensions are kept almost the same as the former design, the isolation level is decreased to 79 dB. In practice, the antenna may be placed inside a radome. The antenna can be redesigned to provide the same level of isolation considering the radome effects.

2.4 Conclusion

A single-port compact 2×2 cavity-backed slot antenna array with consistent radiation characteristics over the entire X-band was presented. It was shown that a thin small cavity with narrowband behavior can be designed to feed a slot array over a wide bandwidth when loaded appropriately by metallic septa. A design was demonstrated so that the antenna exhibits wideband consistent radiation characteristics up to 60% bandwidth when fed by a rectangular waveguide. Also a compact full-band end-launch microstrip to reduced-height waveguide transition topology was conceived for feeding the antenna and maintaining its low-profile characteristics. Due to its simple configuration, the proposed transition design requires less full EM analysis and mostly relies on fast circuit simulation. A fabricated prototype array at X-band was used to validate the design.

The antenna was then evolved to a two-port antenna with orthogonal polarizations. The two-port common aperture CBSA array exhibits a very high isolation level between its ports. High isolation is achieved using orthogonal polarizations and utilizing a symmetric structure. A common antenna aperture is used by both Tx and Rx as the radiating aperture which results in higher gain for a given available area. A low-loss air-dielectric microstrip feed is designed which can be integrated with the other parts of the antenna and is amenable to 3D printing technology. The proposed decoupling method does not require any kind of hybrid and can potentially provide nearly 90 dB of channels isolation over 44% fractional bandwidth. For the fabricated antenna at C-band, a minimum of 55 dB self-interference cancellation is measured from 4.8 to 7.5 GHz.

CHAPTER 3 External Interference Cancellation in Wireless Communications

3.1 Overview

Co-channel external interference including jamming signals, multipaths of the signal or the signals coming from the other user can significantly degrade the performance of a wireless link as demonstrated in Figure 3-1. Multiple antenna systems such as MIMO can be exploited to beat external interference. Consider a M-by-N MIMO system in a multipath environments as shown in Figure 3-2. In a MIMO system, different data is sent through the transmitting antennas and the data can be reconstructed at the receiver by signal processing techniques provided that 1) the number of independent multipaths is equal to or larger than

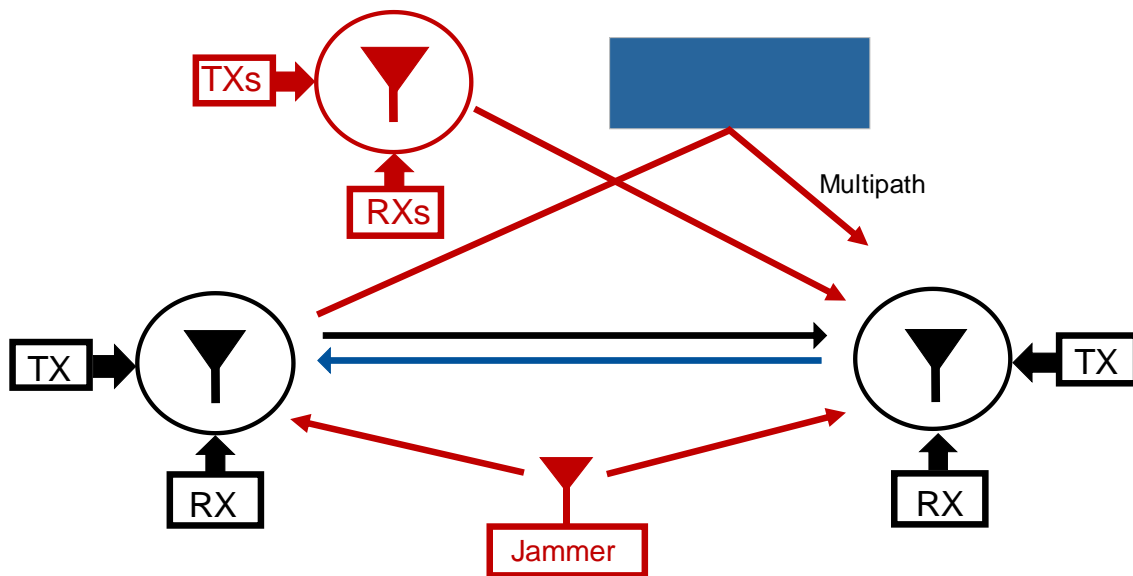


Figure 3-1. External interference including jamming signals, multipaths of the signal, or signal coming from the other users can reduce the channel capacity of a wireless link.

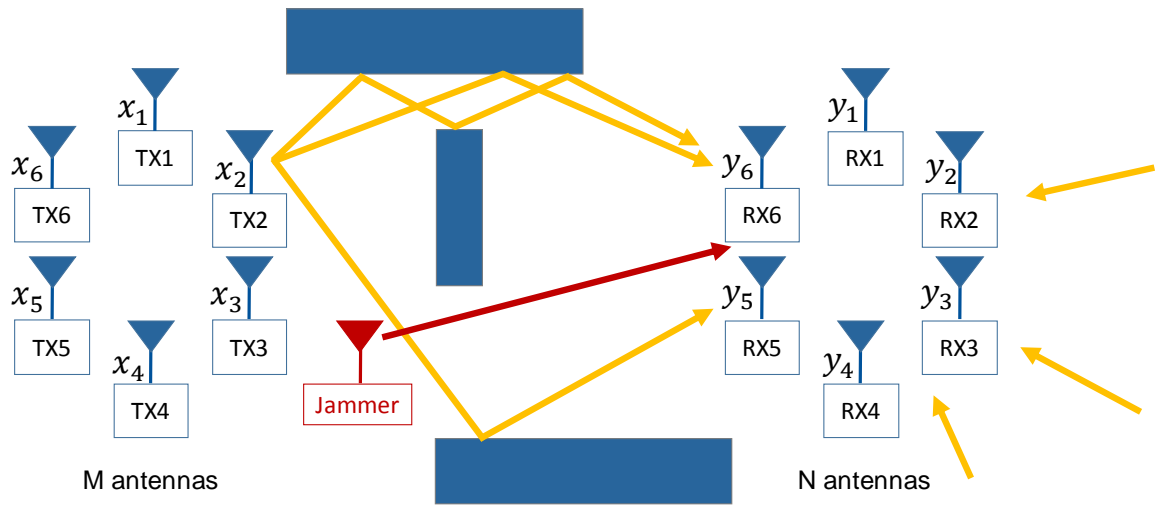


Figure 3-2. A MIMO system in a multipath environment. The jamming signal results in erroneous channel estimation.

the number of transmitting antennas, and 2) the channel response is known. To estimate the channel, a pilot signal is sent through each transmitting antenna and at the receiver the measured received signal is divided by the pilot signal and the channel matrix $\mathbf{H}_{N \times M}$ is built as:

$$\mathbf{H} = \begin{bmatrix} h_{11} & \cdots & h_{1M} \\ \vdots & \ddots & \vdots \\ h_{N1} & \cdots & h_{NM} \end{bmatrix} \quad (3-1)$$

where:

$$h_{ij} = \frac{y_i}{x_j} \quad (3-2)$$

The data can then be recovered as:

$$\mathbf{x} = \mathbf{H}^{-1}\mathbf{y} \quad (3-3)$$

There are, however, three issues with this system: 1) if there is a jamming signal, the channel cannot be estimated and it fails to reconstruct the data, 2) because of fading effect, some of the elements of the channel matrix may become very small which results in a lower SNR,

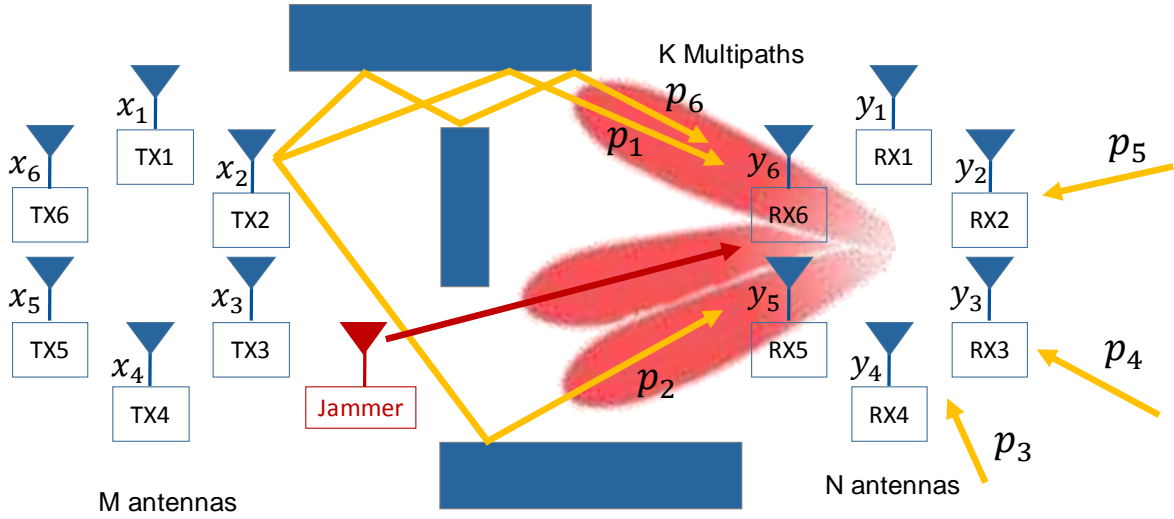


Figure 3-3. The proposed modified MIMO system.

and 3) if the number of receiving antennas is smaller than the number of transmitting antennas, then the data cannot be retrieved. The goal is to modify this system to mitigate these issues. The modified MIMO system is illustrated in Figure 3-3. To learn the channel, a pilot signal is sent through each transmitting antenna. Unlike the former approach in which the channel response between each transmitting and receiving antennas is estimated, the receiver performs beamforming to spatially detect and separate all impinging signals. Denoting the number of the multipaths as \mathbf{K} , one can define the channel matrix $\mathbf{G}_{\mathbf{K} \times \mathbf{M}}$ as:

$$\mathbf{G} = \begin{bmatrix} g_{11} & \cdots & g_{1M} \\ \vdots & \ddots & \vdots \\ g_{K1} & \cdots & g_{KM} \end{bmatrix} \quad (3-4)$$

where:

$$g_{ij} = \frac{p_i}{x_j} \quad (3-5)$$

In (3-11), p_i is the i th multipath and x_j is the j th transmitting data. Since Tx and Rx are in the farfield of each other, the angles of arrival of the multipaths at the receiver for all transmit signals are the similar. Therefore, detecting each multipath provides an independent equation. If $K \geq M$, we will have enough independent equation to retrieve the data which is obtained as:

$$\mathbf{x} = \mathbf{G}^{-1}\mathbf{P} \quad (3-6)$$

This approach has three advantages: 1) allows for detecting and removing the jamming signal, 2) all of the elements of the matrix \mathbf{G} are nonzero, and 3) even if the number of the receiving antennas is smaller than the number of the transmitting antennas, it is still possible to reconstruct the data. As shown in Figure 3-3, some of the multipath may arrive from close angular proximity which are not resolvable by conventional beamforming. Superresolution signal detection algorithms are required to separate these multipath and provide enough independent equations. Extensive studies have been carried out on spatial signals separation methods in the last few decades. The well-known eigenstructure-based methods such as MUSIC [57], Root-MUSIC [58], and ESPRIT [65] performs well in circumstances where the sources are not correlated. In real scenarios, however, due to the multipath effects, the impinging signals are correlated and, thereby, cannot be separated by the aforementioned algorithms. Spatial smoothing techniques [51] are therefore used to tackle the problem for correlated signals. However, the results have not been promising, since the effective aperture of the array after spatial smoothing is considerably reduced. This, in turn, leads to resolution degradation. To overcome this problem, Maximum Likelihood-based (ML-based) [105] techniques are introduced and have been studied from different perspectives. As reported in the literature, the main drawback of ML-based algorithms is that their global convergence is

strongly dependent on the initialization. Moreover, most of the ML-based techniques are not computationally efficient.

In this chapter, first an Array Signal Segregation using an Iterative Approach (ASSIA) [118] is introduced. ASSIA features the ability of detecting weak signals in the presence of very strong signals provided that their angular distance is larger than the antenna array beamwidth. Then a spatial super-resolution signal detection which will be referred to as Closely-spaced Nulls Synthesis Method (CNSM) [119] is presented for improving the resolution of ASSIA. Conjoint with ASSIA, the proposed method is composed of two steps. In the first step, the directions of arrival (DoA) and amplitudes of the signals which are spatially apart by more than the array beamwidth are estimated using ASSIA. Segregated signals by ASSIA may each contain multiple signals separated by angles smaller than the half power beamwidth of the antenna array. These signals are then processed in the second step to estimate the DoAs of the closely-spaced signals using CNSM. While computationally cost-effective, ASSIA-CNSM exhibits superior accuracy compared to other techniques such as Root MUSIC algorithm, Matrix Pencil Method and Maximum-Likelihood Method. ASSIA-CNSM is experimentally implemented using a circular array of mono-conical antennas in which the mutual coupling and shadowing effects among elements are mitigated using feed-forward technique [120].

3.2 Signal Segregation Algorithm using an Iterative Approach (ASSIA)

3.2.1 Formulation of ASSIA

The proposed algorithm is formulized for a two-dimensional case by employing a uniform circular array of omnidirectional antennas as illustrated in Figure 3-4. The main

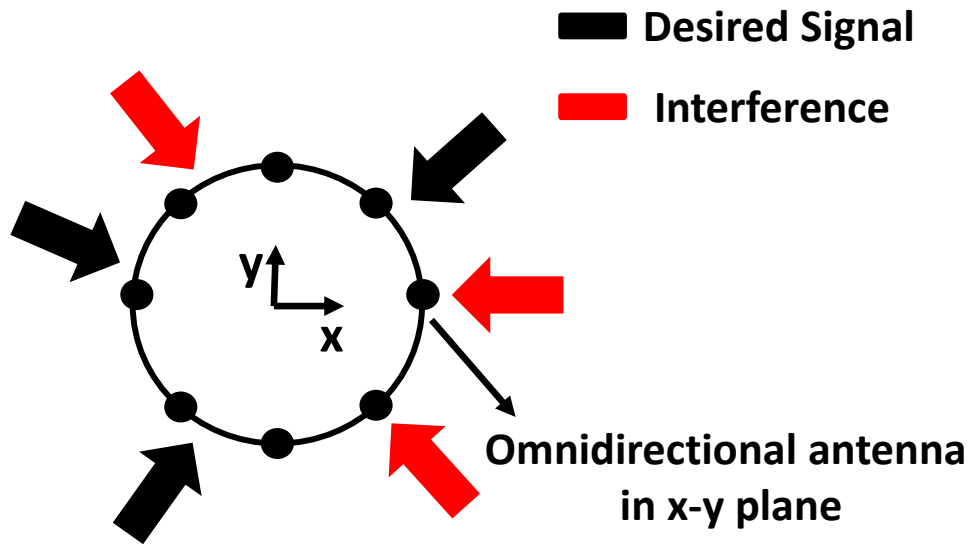


Figure 3-4. Circular array of omnidirectional antennas illuminated by a number of interfering and desired signals.

advantages of the circular array compared to the linear array are its azimuthal symmetry for beamforming without distortion near the end-fire directions as well as the same mutual coupling effect for all antenna elements which allows for simple coupling mitigation approaches [120]. It is assumed that all the desired and interfering signals are almost confined in the horizontal plane.

As the proposed technique is a frequency domain method, the received time domain signal at each antenna is converted to the frequency domain using Fourier transform over a pre-determined time interval. The length of the FFT and the resolution frequency depends on the duration of the time interval the data stream is sampled. Each frequency component is then processed through ASSIA processor separately to estimate the DoA, magnitude and phase of the signals. Therefore, irrespective of whether the impinging signals are fully correlated or uncorrelated, ASSIA is able to detect and segregate the signals. After interference detection and removal, the desired signals are converted back to the time domain

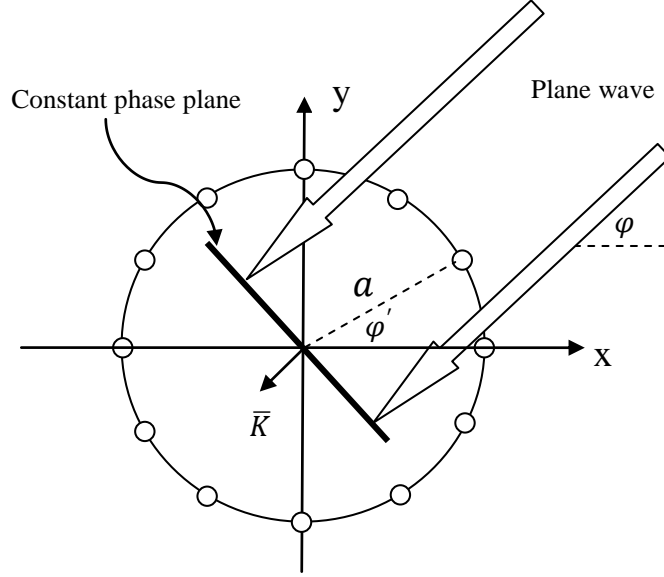


Figure 3-5. The sketch of a uniform circular array illuminated by a plane wave.

for further processing. To describe the principle of operation of ASSIA, consider a circular array with radius a which is illuminated by a number of plane waves as depicted in Figure 3-5. The number of the receiver antennas and the number of the impinging local plane waves are denoted by M and P respectively. For simplicity, let us first neglect the mutual coupling among the omnidirectional elements of the array. The antennas are assumed to have a nominal power gain of G and linear vertical polarization. The field expression for each of the incident waves can, locally, be written as $\vec{E} = E_z e^{i \vec{K} \cdot \vec{r}} \hat{z}$, where E_z is the electric field intensity and $\vec{K} = \left(\frac{2\pi f}{c}\right) \hat{k} = K \hat{k}$ is the propagation vector. Henceforth, the subscript 'z' in E_z is dropped for simplification. The voltage across each antenna terminal denoted by v_m can then be written as:

$$v_m = l_{eff} E e^{-i K a \cos(\varphi - \varphi'_m)} \quad (3-7)$$

in which φ and φ'_m are the direction of the impinging plane wave and the angular coordinate of the m th receiver antenna in the polar coordinate system respectively and

$$l_{eff} = \lambda \sqrt{\frac{GR_0}{4\pi\eta_0}} \quad (3-8)$$

where λ and η_0 are free space wavelength and intrinsic impedance respectively and R_0 is the antenna input impedance. In deriving (3-7), it is assumed that the antenna is perfectly matched to its input impedance. For P plane waves illuminating the array, the total voltage at the antenna terminals is given by:

$$\mathbf{V} = \mathbf{A}(\boldsymbol{\phi}) \mathbf{E} + \mathbf{N} \quad (3-9)$$

where \mathbf{V} is a $M \times 1$ vector of the received voltages:

$$\mathbf{V} = [v_1 \cdots v_M]^T \quad (3-10)$$

in which v_m is the total received signal at m th antenna and \mathbf{E} is a $P \times 1$ vector of the impinging electric fields:

$$\mathbf{E} = [E_1 \cdots E_P]^T \quad (3-11)$$

where E_i is the electric field arriving at the receiver from direction φ_i . $\mathbf{A}(\boldsymbol{\phi})$ is a $M \times P$ matrix of the phase-corrected effective length for the circular antenna array given by:

$$\mathbf{A}(\boldsymbol{\phi}) = [\mathbf{a}(\varphi_1) \cdots \mathbf{a}(\varphi_P)] \quad (3-12)$$

where:

$$\mathbf{a}(\varphi_p) = l_{eff} [e^{-iKa \cos(\varphi_p - \varphi'_1)} \cdots e^{-iKa \cos(\varphi_p - \varphi'_M)}]^T \quad (3-13)$$

and \mathbf{N} is the noise vector which is assumed to be a spatially zero-mean white Gaussian process. The goal is to find \mathbf{E} and $\boldsymbol{\phi} = [\varphi_1 \cdots \varphi_P]$ from the total measured received signal denoted by \mathbf{V} .

The algorithm is mainly composed of P steps and each step requires r_s ($1 \leq s \leq P$) iterations. As the algorithm proceeds from one step to the next, the number of the detected received signals is increased by one. In other words, at the s th step the algorithm provides estimations

of magnitude and phase of signals arriving from s different directions as function of frequency. At the very beginning of the s th step, an estimation of the s th largest signal is made. This iteration is defined as the zeroth iteration. Then, the estimations of all s signals are refined through an iterative approach.

At the first step, the algorithm begins with focusing the array in all directions to find the largest arriving signal and its corresponding direction of arrival. An estimation for the DoA of the largest arriving signal denoted by $\varphi_1^{(1,0)}$ is obtained by:

$$\varphi_1^{(1,0)} = \operatorname{argmax}_{\varphi_n} \left(\mathbf{W}_n \mathbf{V}_1^{(1,0)} \right) \left(\mathbf{W}_n \mathbf{V}_1^{(1,0)} \right)^H \quad (3-14)$$

where $\mathbf{V}_1^{(1,0)} = \mathbf{V}$ and \mathbf{W}_n is a $M \times 1$ combined focusing and weighting vector to focus the array in direction φ_n with a desired sidelobe level:

$$\mathbf{W}_n = [w_{n1} e^{iKa \cos(\varphi_n - \varphi'_1)} \dots w_{nM} e^{iKa \cos(\varphi_n - \varphi'_M)}] \quad (3-15)$$

in which $\varphi_n = n \Delta\varphi$ ($n = 1, \dots, 2\pi/\Delta\varphi$) and $\Delta\varphi$ is a predetermined search angle step. The superscript H denotes Hermitian transpose. The first and the second superscript placed in the parenthesis in $\varphi_1^{(1,0)}$ and $\mathbf{V}_1^{(1,0)}$ represent the step and the iteration number in that step respectively. In (3-15), the phase terms $e^{iKa \cos(\varphi_n - \varphi'_m)}$ are in fact the conjugate of the phase terms in the phase-corrected effective length $\mathbf{a}(\varphi_n)$ to compensate for the phase difference between receiver antennas to focus the array beam in direction of φ_n and $w_{n1} \dots w_{nM}$ are a set of real positive values for M antennas to control the resulting side-lobe level in such a way as to maximize the contribution of the signal coming from direction φ_n and minimize the received signal from other directions. Once $\varphi_1^{(1,0)}$ is found, the zeroth order estimation of the electric field arriving at the receiver from this direction can be obtained from:

$$E_1^{(1,0)} = \frac{\mathbf{W}_1 \mathbf{V}_1^{(1,0)}}{l_{eff} \sum_{m=1}^M w_{1m}} \quad (3-16)$$

The summation term in the denominator of (3-16) is used for normalization. The next step is to estimate the second largest signal E_2 and its direction of arrival φ_2 after which the algorithm improves the estimations accuracy of both E_1 and E_2 as well as φ_1 and φ_2 in an iterative fashion. To find the second largest signal, initially the contribution of the estimated E_1 obtained by (3-16) is subtracted from the total received signal at each antenna. The result of this subtraction is denoted as $\mathbf{V}_2^{(2,0)}$ and can be found by:

$$\mathbf{V}_2^{(2,0)} = \mathbf{V}_1^{(1,0)} - \mathbf{a}(\varphi_1^{(1,0)}) E_1^{(1,0)} \quad (3-17)$$

Thereby, an estimation for the DoA of the second largest signal denoted by $\varphi_2^{(2,0)}$ is found as:

$$\varphi_2^{(2,0)} = \underset{\varphi_n}{\operatorname{argmax}} \left(\mathbf{W}_n \mathbf{V}_2^{(2,0)} \right) \left(\mathbf{W}_n \mathbf{V}_2^{(2,0)} \right)^H \quad (3-18)$$

and consequently, the zeroth order estimation of the second largest signal is given by:

$$E_2^{(2,0)} = \frac{\mathbf{W}_2 \mathbf{V}_2^{(2,0)}}{l_{eff} \sum_{m=1}^M w_{2m}} \quad (3-19)$$

The algorithm then proceeds to the first iteration of the second step in which the estimation of two largest signals are refined. Since the initial estimations of E_2 and φ_2 are now available, one can improve the estimation accuracy of E_1 and φ_1 by subtracting the contribution of E_2 from all antennas and again trying to find a new estimation for the DoA of the largest signal which is found by:

$$\varphi_1^{(2,1)} = \underset{\varphi_n}{\operatorname{argmax}} \left(\mathbf{W}_n \mathbf{V}_1^{(2,1)} \right) \left(\mathbf{W}_n \mathbf{V}_1^{(2,1)} \right)^H \quad (3-20)$$

where:

$$\mathbf{V}_1^{(2,1)} = \mathbf{V}_1^{(1,0)} - \mathbf{a}(\varphi_2^{(2,0)}) E_2^{(2,0)} \quad (3-21)$$

An improved estimation of E_1 is then obtained as:

$$E_1^{(2,1)} = \frac{\mathbf{W}_1 \mathbf{V}_1^{(2,1)}}{l_{eff} \sum_{m=1}^M w_{1m}} \quad (3-22)$$

Afterwards, E_2 can be updated similarly, that is, the contribution of E_1 is subtracted from the total received signal and the array pattern is focused in all possible directions to find an update value for E_2 as well as its direction of arrival. This procedure is repeated in the next iterations of the second step until the sequence converges to a solution for E_1 and E_2 as well as φ_1 and φ_2 . The algorithm, then, proceeds to the next step whereby the third largest signal is first detected. While the contributions of the updated E_1 and E_2 are subtracted from the total received signal, the array beam sweeps the space to find the third largest signal. Then, similar to the second step, the algorithm runs through multiple iterations to refine the estimations of the three largest signals. This procedure is continued in the next steps to estimate all impinging signals which are well above the noise level. Simulations shows that the algorithm can handle signals with SNR as low as 5 dB. This is a threshold at which the algorithm is aborted. As the number of the iterations in each step is increased, this iterative approach provides a sequence of improving estimated solutions for \mathbf{E} and $\boldsymbol{\phi}$ which converges eventually. The search angle step, $\Delta\varphi$, needs to be locally decreased around the estimated DoAs over steps and iterations to reduce possible arithmetic errors if the actual DoAs are not among the predetermined search angles. To increase the convergence speed, each signal is estimated using the most updated values of the other signals including those which have been

updated within the same iteration. The total number of iterations for each signal depends on the relative magnitude of the signal compared to other signals and the total number of the impinging signals. The larger is the estimated signal compared to the other signals and the higher is the number of the signals, the higher is the number of the iterations the signal goes through. If one defines N_l^s as the number of iterations required to estimate the s th largest signal, then N_l^s is determined by:

$$N_l^s = \sum_{i=s}^P r_i \quad (3-23)$$

where r_i denotes the number of the required iterations in the i th step to make the sequence of the solutions convergent. It is also evident that $E_s^{(i,k)} = 0$ for $i < s$.

The technique is able to detect all signals provided that the angular separation between two vicinal signals is larger than the array beamwidth. If two or multiple impinging signals are in close angular proximity (smaller than the adjusted array beamwidth), the algorithm fails to segregate them. In this case, the detected signal is the resultant of those set of adjoining signals.

The dynamic range of the signals which ASSIA radio is able to detect is limited by the dynamic range of the RF amplifiers which can be enhanced by using an automatic-gain-control (AGC) and the mixer nonlinearities for large signals (the upper end), and by the receiver noise figure and bandwidth for small signals (the bottom end). The Analogue- to-Digital Convertor (ADC) should also be able to provide the required dynamic range and quantization resolution.

3.2.2 Mutual Coupling Considerations

The equations used in the segregation algorithm presented in the previous section ignored the mutual coupling effects among the array elements. To account for the mutual coupling, the weighting coefficients must be modified so that the array can correctly focus in the desired directions. It is also important to mention that the mutual couplings among the antenna elements change the radiation pattern of the elements. That is, the radiation pattern of the elements is no longer omnidirectional. To modify the equations, \mathbf{W}_n is replaced by \mathbf{W}_n^C for a desired radiation pattern having φ_n as its maximum direction of radiation. The synthesis technique for calculating \mathbf{W}_n^C is described in Section 3.2.3. Assuming that the realized power gain and phase pattern of the m th antenna in the presence of other antennas and the receiver platform is represented as $G_m(\varphi)$ and $P_m(\varphi)$ with reference to the center of the circle respectively, then, (3-9) is modified as:

$$\mathbf{V} = \mathbf{B}(\boldsymbol{\phi}) \mathbf{E} + \mathbf{N} \quad (3-24)$$

where:

$$\mathbf{B}(\boldsymbol{\phi}) = [\mathbf{b}(\varphi_1) \quad \cdots \quad \mathbf{b}(\varphi_p)] \quad (3-25)$$

and:

$$\mathbf{b}(\varphi_p) = [l_{eff,1}(\varphi_p) \quad \cdots \quad l_{eff,M}(\varphi_p)]^T \quad (3-26)$$

where:

$$l_{eff,m}(\varphi_p) = \lambda \sqrt{\frac{G_m(\varphi_p) R_0}{4\pi\eta_0}} e^{iP_m(\varphi_p)} \quad (3-27)$$

Consequently, the equations in the zeroth-iteration of the first step take the following forms:

$$\varphi_1^{(1,0)} = \operatorname{argmax}_{\varphi_n} \left(\mathbf{W}_n^C \mathbf{V}_1^{(1,0)} \right) \left(\mathbf{W}_n^C \mathbf{V}_1^{(1,0)} \right)^H \quad (3-28)$$

where:

$$\mathbf{W}_n^C = [w_{n1}^C \quad \cdots \quad w_{nm}^C] \quad (3-29)$$

and:

$$E_1^{(1,0)} = \frac{\mathbf{W}_1^C \mathbf{V}_1^{(1,0)}}{\sum_{m=1}^{N_A} w_{1m}^C l_{eff,m}(\varphi_1^{(1,0)})} \quad (3-30)$$

Also the equations in the zeroth -iteration of the second step are modified as follows:

$$\mathbf{V}_2^{(2,0)} = \mathbf{V}_1^{(1,0)} - \mathbf{b}(\varphi_1^{(1,0)}) E_1^{(1,0)} \quad (3-31)$$

$$\varphi_2^{(2,0)} = \operatorname{argmax}_{\varphi_n} \left(\mathbf{W}_n^C \mathbf{V}_2^{(2,0)} \right) \left(\mathbf{W}_n^C \mathbf{V}_2^{(2,0)} \right)^H \quad (3-32)$$

$$E_2^{(2,0)} = \frac{\mathbf{W}_2^C \mathbf{V}_2^{(2,0)}}{\sum_{m=1}^M w_{2m}^C l_{eff,m}(\varphi_2^{(2,0)})} \quad (3-33)$$

Similarly, the equations pertaining to other steps and iterations are modified. It should be noted that $l_{eff,m}(\varphi)$ can be obtained by either full-wave simulation or measurement. The sequence through which the algorithm runs is demonstrated in Table 3-1. The approach which is used to calculate \mathbf{W}_n^C is discussed next.

3.2.3 Synthesis Method for Beamforming

As was described in Section 3.2.2, at each iteration, the algorithm goes through a spatial search process over all possible directions. Let's define $l_{eff,m}(\varphi)$ as the effective length of each antenna in the horizontal plane (x-y plane) in the presence of all other antennas and the receiver platform with its phase center at the center of the circular array. The effective length of the circular array denoted as $L_{eff}(\varphi)$, can then be written as:

$$L_{eff}(\varphi) = \sum_{m=1}^M w_{nm}^C l_{eff,m}(\varphi) \quad (3-34)$$

Table 3-1. The summary of ASSIA

Step No. (p)	Iteration No. (k)	Descriptions						
1	0	$E_1^{(1,0)}$	The first estimation of E_1 is made.					
2	0	$E_2^{(2,0)}$	The first estimation of E_2 is made.					
	1	$E_1^{(2,1)}$	$E_2^{(2,1)}$	In each iteration, the signals are calculated from the largest $E_1^{(p,k)}$ to the smallest $E_p^{(p,k)}$ sequentially. ($1 \leq k \leq r_p$, $1 \leq s \leq p$)				
	\vdots	\vdots	\vdots	$\varphi_s^{(2,k)} = \underset{\varphi_n}{\operatorname{argmax}} \left(\mathbf{W}_n^C \mathbf{V}_s^{(2,k)} \right) \left(\mathbf{W}_n^C \mathbf{V}_s^{(2,k)} \right)^H$ $E_s^{(2,k)} = \frac{\mathbf{W}_s^C \mathbf{V}_s^{(2,k)}}{\sum_{m=1}^M w_{sm}^C l_{eff,m} \left(\varphi_s^{(2,k)} \right)}$ $\mathbf{V}_s^{(2,k)} = \mathbf{V}_1^{(1,0)} - \sum_{q=1}^{s-1} \mathbf{b} \left(\varphi_q^{(2,k)} \right) E_q^{(2,k)} + \sum_{q=s+1}^2 \mathbf{b} \left(\varphi_q^{(2,k-1)} \right) E_q^{(2,k-1)}$				
r_2	$E_1^{(2,r_2)}$	$E_2^{(2,r_2)}$						
3	0	$E_3^{(3,0)}$	The first estimation of E_3 is made.					
	1	$E_1^{(3,1)}$	$E_2^{(3,1)}$	$E_3^{(3,1)}$	$\varphi_s^{(3,k)} = \underset{\varphi_n}{\operatorname{argmax}} \left(\mathbf{W}_n^C \mathbf{V}_s^{(3,k)} \right) \left(\mathbf{W}_n^C \mathbf{V}_s^{(3,k)} \right)^H$ $E_s^{(3,k)} = \frac{\mathbf{W}_s^C \mathbf{V}_s^{(3,k)}}{\sum_{m=1}^M w_{sm}^C l_{eff,m} \left(\varphi_s^{(3,k)} \right)}$ $\mathbf{V}_s^{(3,k)} = \mathbf{V}_1^{(1,0)} - \sum_{q=1}^{s-1} \mathbf{b} \left(\varphi_q^{(3,k)} \right) E_q^{(3,k)} + \sum_{q=s+1}^3 \mathbf{b} \left(\varphi_q^{(3,k-1)} \right) E_q^{(3,k-1)}$			
	\vdots	\vdots	\vdots	\vdots				
r_3	$E_1^{(3,r_3)}$	$E_2^{(3,r_3)}$	$E_3^{(3,r_3)}$					
\vdots	\vdots	\vdots	\vdots	\vdots	\vdots	\vdots	\vdots	
P	0	$E_p^{(p,0)}$	The first estimation of E_p is made.					
	1	$E_1^{(p,1)}$	$E_2^{(p,1)}$	$E_3^{(p,1)}$	$E_4^{(p,1)}$	\dots	$E_p^{(p,1)}$	$\varphi_s^{(p,k)} = \underset{\varphi_n}{\operatorname{argmax}} \left(\mathbf{W}_n^C \mathbf{V}_s^{(p,k)} \right) \left(\mathbf{W}_n^C \mathbf{V}_s^{(p,k)} \right)^H$ $E_s^{(p,k)} = \frac{\mathbf{W}_s^C \mathbf{V}_s^{(p,k)}}{\sum_{m=1}^M w_{sm}^C l_{eff,m} \left(\varphi_s^{(p,k)} \right)}$ $\mathbf{V}_s^{(p,k)} = \mathbf{V}_1^{(1,0)} - \sum_{q=1}^{s-1} \mathbf{b} \left(\varphi_q^{(p,k)} \right) E_q^{(p,k)} + \sum_{q=s+1}^P \mathbf{b} \left(\varphi_q^{(p,k-1)} \right) E_q^{(p,k-1)}$
	\vdots	\vdots	\vdots	\vdots	\vdots	\dots	\vdots	
r_p	$E_1^{(p,r_p)}$	$E_2^{(p,r_p)}$	$E_3^{(p,r_p)}$	$E_4^{(p,r_p)}$				

Due to the symmetrical nature of a circular array and under the assumption that the array elements are identical and equally spaced, the effective length of each element can be

expressed as a spatially shifted function of that of a reference antenna:

$$l_{eff,m}(\varphi) = l_{eff,1}\left(\varphi - \frac{2\pi m}{M}\right) \quad (3-35)$$

where $l_{eff,1}(\varphi)$ is the normalized effective length of the antenna located at $\varphi = \varphi'_1$ with reference to the center of the circle obtained by full-wave simulation or measurement.

Substituting (3-35) in (3-34), the array effective length takes the form:

$$L_{eff}(\varphi) = \sum_{m=1}^M w_{nm}^C l_{eff,1}\left(\varphi - \frac{2\pi m}{M}\right) \quad (3-36)$$

Representing $L_{eff,n}(\varphi)$ and $l_{eff,1}\left(\varphi - \frac{2\pi m}{M}\right)$ in Fourier series and substituting in (3-34)

results in:

$$\sum_{k=-\infty}^{+\infty} a_k e^{ik\varphi} = \sum_{m=1}^M w_{nm}^C \left(\sum_{k=-\infty}^{+\infty} b_k e^{-ik\frac{2\pi m}{M}} e^{ik\varphi} \right) \quad (3-37)$$

in which

$$a_k = \frac{1}{2\pi} \int_0^{2\pi} L_{eff,n}(\varphi) e^{-ik\varphi} d\varphi \quad (3-38)$$

$$b_k = \frac{1}{2\pi} \int_0^{2\pi} l_{eff,1} e^{-ik\varphi} d\varphi \quad (3-39)$$

Interchanging the summations in the right-hand side of (3-37), it can be rewritten as:

$$\sum_{k=-\infty}^{+\infty} a_k e^{ik\varphi} = \sum_{k=-\infty}^{+\infty} b_k e^{ik\varphi} \left(\sum_{m=1}^M w_{nm}^C e^{-ik\frac{2\pi m}{M}} \right) \quad (3-40)$$

In order for (3-40) to be valid for all values of φ , we must have:

$$a_k e^{ik\varphi} = b_k e^{ik\varphi} \sum_{m=1}^M w_{nm}^C e^{-ik\frac{2\pi m}{M}} \quad (3-41)$$

which can be used to find a_k :

$$a_k = b_k \sum_{n=1}^M w_{nm}^C e^{-ik\frac{2\pi m}{M}} \quad (3-42)$$

Defining:

$$g(k) = \frac{a_k}{b_k} = \sum_{m=1}^M w_{nm}^C e^{-ik\frac{2\pi m}{M}} \quad (3-43)$$

$g(k)$ can be viewed as a truncated finite Fourier series and therefore, the weighing factors can be obtained from:

$$w_{nm}^C = \frac{1}{M} \sum_{k=-\infty}^{+\infty} g(k) e^{ik\frac{2\pi m}{M}} \quad (3-44)$$

Using (3-38) and (3-39) in (3-44) :

$$w_{nm}^C = \frac{1}{M} \sum_{k=-\infty}^{+\infty} \left[\frac{\int_0^{2\pi} L_{eff}(\varphi) e^{-ik\varphi} d\varphi}{\int_0^{2\pi} l_{eff,1} e^{-ik\varphi} d\varphi} \right] e^{ik\frac{2\pi m}{M}} \quad (3-45)$$

Equation (3-45) provides the “combined focusing and weighting vector”, \mathbf{W}_n^C , in an equally spaced circular array of M elements for the desired radiation pattern $L_{eff}(\varphi)$. We use a realizable Dolph-Chebyshev function for the normalized effective length of the array, $L_{eff}(\varphi)$ which is defined as [121]:

$$L_{eff}(\varphi) = \cosh \left(2h \cosh^{-1} \left(z_0 \cos \left(\frac{\varphi - \varphi_n}{2} \right) \right) \right) \quad (3-46)$$

In (3-46), φ_n represents the direction of the look angle and z_0 defines the side-lobe level through the following equation:

$$z_0 = \cosh \left(\frac{1}{2h} \cosh^{-1} \left(\frac{1}{S_{max}} \right) \right) \quad (3-47)$$

Here, S_{max} is the ratio of the side-lobe level to the main-lobe level and h is a number satisfying the following condition:

$$h \leq \frac{M-1}{2} \quad (3-48)$$

3.2.4 Convergence Analysis

The sufficient condition under which the sequence of the solutions generated by the algorithm converges to the correct solution is examined in this section. The error in the detected magnitude of the largest signal denoted by $|err_{E_1}^{(1,0)}|$ is given by:

$$|err_{E_1}^{(1,0)}| = \left| \sum_{n=2}^P S(\varphi_n)E_n + \gamma_1^{(1,0)} \left(\sum_{n=2}^P S(\varphi_n)E_n \right) \right| \quad (3-49)$$

The first term represents the contribution from other signals through side lobes and the second term refers to the error in the estimation of $|E_1|$ which is generated due to the error in the estimation of φ_1 . The second term, however, is a function of the first term and can be approximated by:

$$\gamma_1^{(1,0)}(\alpha) \cong \sum_{n=2}^P S_{max}E_n - \alpha \quad (3-50)$$

where $S_{max} = \max(S(\varphi))$ is the maximum side-lobe level of the array that can be obtained from (40) (see Figure 3-6). In (3-50), the parameter α is defined as $\alpha = \sum_{n=2}^P S(\varphi_n)E_n$ and in the worst case, α takes its maximum value when all other signals happen to be in the directions of maximum side-lobes and add up coherently as the array is focused in the direction φ_1 . In this case, the error in the detection of φ_1 is equal to zero which in turn results in $\gamma_1^{(1,0)}(\alpha_{max}) = 0$. On the other hand, the minimum value of α occurs when all other signals

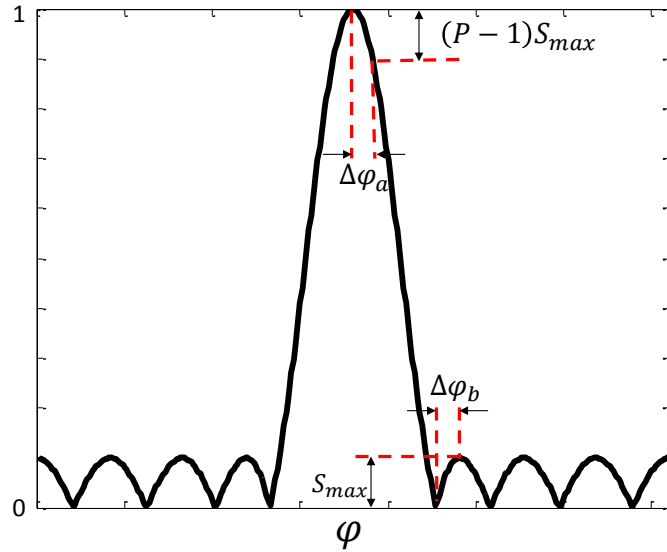


Figure 3-6. The normalized effective length of the array given by (3-46). The condition $\Delta\varphi_b > \Delta\varphi_a$ is necessary for the convergence of the algorithm.

happen to be at the directions of the array nulls. In this case, the direction of look is different from φ_1 and the error in the estimation of φ_1 is maximum. This implies that as the first term in the right-hand side of (3-49) increases, the second term decreases and vice-versa. Therefore, to ensure the convergence of the algorithm, both types of error, i.e. the error in the estimation of directions of arrival and the error in the estimation of magnitudes and phases of the signals should be decreased simultaneously as the number of the iterations is increased. As was described in Section 3.2.2, the algorithm is based on subtracting the contribution of the estimated larger signals and then searching for the smaller ones. This procedure can be viewed as creating nulls in the directions of the detected signals while looking for the others. To reduce the error in the location of the created nulls in each iteration, the maximum error in the estimation of φ_1 denoted by $\Delta\varphi_a$ resulting from the maximum variation of α should be smaller than smallest angular distance between two adjacent peak and null of the array side-lobes denoted by $\Delta\varphi_b$. The reason is that the maximum error occurs when the created null happens to be in the direction of one of the array nulls. The worst case corresponds to

coherent and equal magnitude signals. With reference to Figure 3-6, the necessary condition for which the error in the estimation of DoAs is reduced iteratively is:

$$\Delta\varphi_b > \Delta\varphi_a \quad (3-51)$$

For the array effective length given by (3-46), it can be shown that (3-51) translates to:

$$\begin{aligned} \cos^{-1} \left[\frac{1}{z_0} \cos \left(\frac{3\pi}{4h} \right) \right] - \cos^{-1} \left[\frac{1}{z_0} \cos \left(\frac{\pi}{4h} \right) \right] \\ > 2 \cos^{-1} \left[\frac{1}{z_0} \cosh \left(\frac{1}{2h} \cosh^{-1}(a_0 - R) \right) \right] \end{aligned} \quad (3-52)$$

where:

$$a_0 = \cosh \left(\frac{1}{2h} \cosh^{-1} \left(\frac{1}{S_{max}} \right) \right) \quad (3-53)$$

and:

$$R = S_{max} a_0 (P - 1) \quad (3-54)$$

Equation (3-51) is not, however, the sufficient condition for convergence. As was mentioned earlier, the error in the estimation of the magnitude and phase of the signals should also be decreased iteratively. Starting with the first step of the algorithm and substituting (3-50) in (3-49), it is concluded that:

$$\left| err_{E_1}^{(1,0)} \right| \leq \sum_{n=2}^P |S_{max} E_n| \quad (3-55)$$

in the second step, we have:

$$\begin{aligned} \left| err_{E_2}^{(2,0)} \right| &\leq \left| S(\varphi_n) er_{E_1}^{(1,0)} + \sum_{n=2}^P S(\varphi_n) E_n \right. \\ &\quad \left. + \left(S(\varphi_n) er_{E_1}^{(1,0)} + \sum_{n=2}^P S(\varphi_n) E_n \right) \right| \\ &\leq \left| S_{max} er_{E_1}^{(1,0)} \right| + \sum_{n=2}^P |S_{max} E_n| \end{aligned} \quad (3-56)$$

where:

$$\gamma_2^{(2,0)}(\alpha) \cong \left| S_{max} er_{E_1}^{(1,0)} \right| + \sum_{n=2}^P |S_{max} E_n| - \alpha \quad (3-57)$$

Similarly, the error in detecting $|E_1|$ in each iteration of the second step is given by:

$$\begin{aligned} \left| er_{E_1}^{(2,k)} \right| &\leq \left| S_{max} er_{E_2}^{(2,k-1)} \right| + \sum_{p=3}^P |S_{max} E_n| \\ &= |S_{max}^{k+2} E_2| \\ &+ \sum_{n=3}^P \left| \sum_{n=1}^{k+2} S_{max}^n E_n \right| = |S_{max}^{k+2} E_2| + \sum_{n=3}^P \left| \frac{S_{max}}{1 - S_{max}} E_n \right| \end{aligned} \quad (3-58)$$

In the limit as the number of the iterations is large enough, the error asymptotically approaches

$$\lim_{k \rightarrow \infty} \left| er_{E_1}^{(2,k)} \right| = \sum_{n=3}^P \left| \frac{S_{max}}{1 - S_{max}} E_n \right| \quad (3-59)$$

Similarly, for the second largest signal, we have:

$$\begin{aligned} \left| er_{E_2}^{(2,k)} \right| &\leq \left| S_{max} er_{E_1}^{(2,k-1)} \right| + \sum_{n=3}^P |S_{max} E_n| \\ &= |S_{max}^{k+2} E_1| \\ &+ \sum_{n=3}^P \left| \sum_{q=1}^{k+2} S_{max}^q E_n \right| \leq |S_{max}^{k+2} E_1| + \sum_{n=3}^P \left| \frac{S_{max}}{1 - S_{max}} E_n \right| \end{aligned} \quad (3-60)$$

and:

$$\lim_{k \rightarrow \infty} \left| er_{E_2}^{(2,k)} \right| \leq \sum_{n=3}^P \left| \frac{S_{max}}{1 - S_{max}} E_n \right| \quad (3-61)$$

Following this procedure and going through a lengthy algebra, it can be shown that in the last step, the asymptotic error is given by:

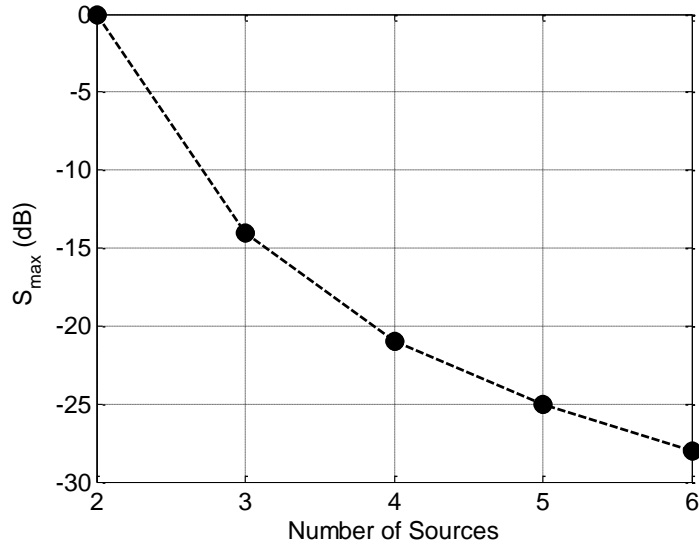


Figure 3-7. The maximum side-lobe level versus number of signals required for convergence for an array with the effective length given by (3-46).

$$\lim_{k \rightarrow \infty} |err_{E_1}^{(P,k)}| \leq \lim_{k \rightarrow \infty} \left\{ S_{max}^k [(P-1)S_{max} \right. \quad (3-62)$$

$$\left. + (P-2)]^k \left| \frac{S_{max}}{1 - (P-2)S_{max}} \right| |E_P| \right\}$$

⋮

⋮

$$\lim_{k \rightarrow \infty} |err_{E_{P-1}}^{(P,k)}| \leq \lim_{k \rightarrow \infty} \left\{ S_{max}^k [(P-1)S_{max} + (P-2)]^k \left| \frac{S_{max}}{1 - (P-2)S_{max}} \right| |E_P| \right\} \quad (3-63)$$

$$\lim_{k \rightarrow \infty} |err_{E_P}^{(P,k)}| \leq \lim_{k \rightarrow \infty} \left\{ (P \right. \quad (3-64)$$

$$\left. - 1) S_{max}^{k+1} [(P-1)S_{max} + (P-2)]^{k+1} \left| \frac{S_{max}}{1 - (P-2)S_{max}} \right| |E_P| \right\}$$

Therefore, an upper bound on S_{max} should be imposed so that:

$$(P-1) S_{max}^2 + (P-2) S_{max} < 1 \quad (3-65)$$

which implies that:

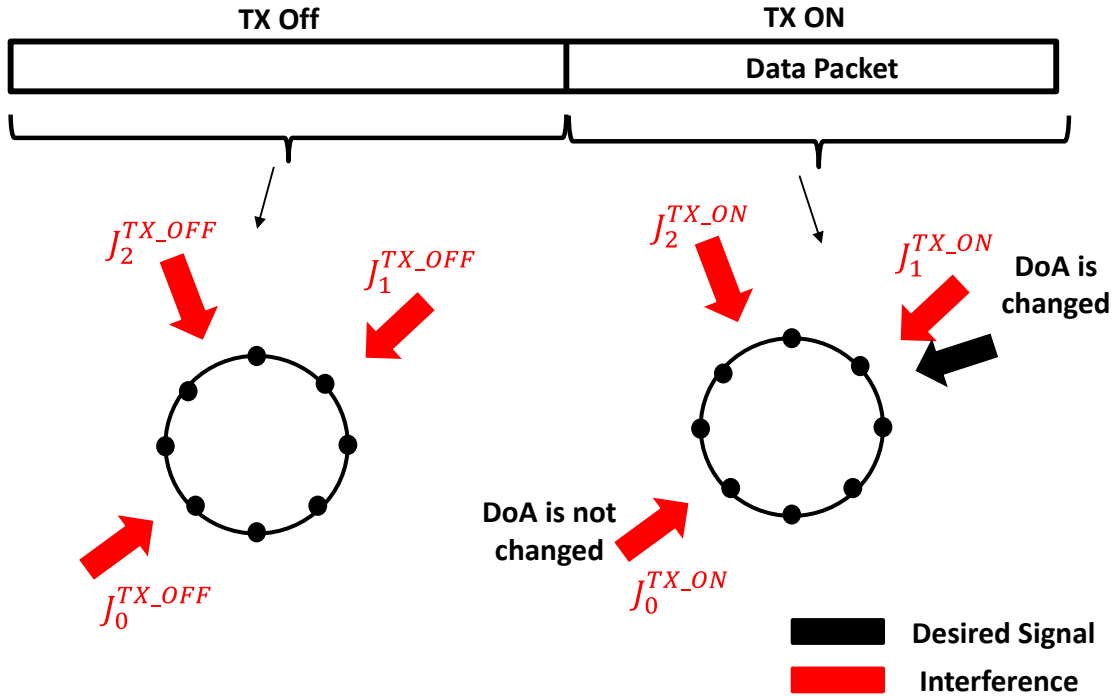


Figure 3-8. The LDR mode where jammer cancellation is accomplished by turning the transmitter on and off with a pattern known to the receiver. The directions of arrival and levels of the jammer is estimated during the off cycle and used to cancel the jammer signal during the on-cycle.

$$S_{max} < \frac{\sqrt{(P-2)^2 + 4(P-1)} - (P-2)}{2(P-1)} \quad (3-66)$$

Equations (3-51) and (3-66) are the sufficient conditions to fulfill the convergence of the algorithm. For a 12-element circular array of diameter $D = 1.44\lambda$, the graph of maximum side-lobe level versus number of coherent signals that satisfies both conditions is given in Figure 3-7 .

3.2.5 Interference Segregation

After detecting signals from all directions, one needs to discern the desired signals from interference. This can be accomplished by using the training sequence as part of the desired transmitted data stream. The signal which exhibits a low level of cross spectral density with the training sequence is considered as the interfering signal and its contribution at each antenna is then subtracted from the total received signal at each antenna. Then, using the training sequence as part of the received signal, the channel response from the transmitter to each receiver antenna is estimated. Once the channel transfer function is computed, the transmitted data can be retrieved.

Smart jammers, however, are able to detect the communication signals and then produce and radiate a corrupted copy of the signals. To avoid this, directional modulation techniques [122], [123] can be utilized at the transmitter point to minimize the bite error rate (BER) in the desired TX-to-RX channel and to maximize the BER in other directions. By this provision, the jammer will not be able to correctly detect the training sequence and generate a distorted version of the desired signal. The radio link can be designed to work in two different modes: High Data Rate (HDR) or normal mode and Low Data Rate (LDR). If the DoAs of the communication signal of interest is not in close angular proximity to the interfering signals, the radio link can work in its normal or HDR mode.

For the scenarios in which the DoAs of the desired and interfering signals cannot be resolved by the array beamwidth, interference cancellation is possible in LDR mode. In LDR mode, the transmitter operates intermittently with a pattern known to the receiver using synchronized clocks. The off-time duration of the transmitter is set to be close to the length of the data packet. When the transmitter is off, the received signal is from the interferer only

(see Figure 3-8) whose DoAs and level are measured by the radio as before. Assuming there is only one jammer present and the channel transfer function does not change during the short interval of a data packet, the interference in directions where DoAs of the signal and jammers are close can be removed. This is done by first identifying small but measurable changes in the levels and DoAs of signals in directions when the transmitter was off. These are directions where the desired signal and jammer DoAs are close and not separable. Using a strong jammer signal from a direction not close to the desired signal as reference (J_0 in Figure 3-8) the jammer signals in directions where the jammer and the desired signal DoAs are close can be estimated accurately and removed.

For example, referring to Figure 3-8, $J_1^{TX_ON}$ can be obtained from:

$$J_1^{TX_ON}(f) \cong J_0^{TX_ON}(f) \frac{J_1^{TX_OFF}(f)}{J_0^{TX_OFF}(f)} \quad (3-67)$$

In view of (3-67), ASSIA processor enables the radio receiver to mitigate interference in LDR mode as a result of the inherent feature of the algorithm in terms of estimating the magnitude and phase of all arriving desired and interfering signals which is not attainable in other direction finding and interference suppression techniques.

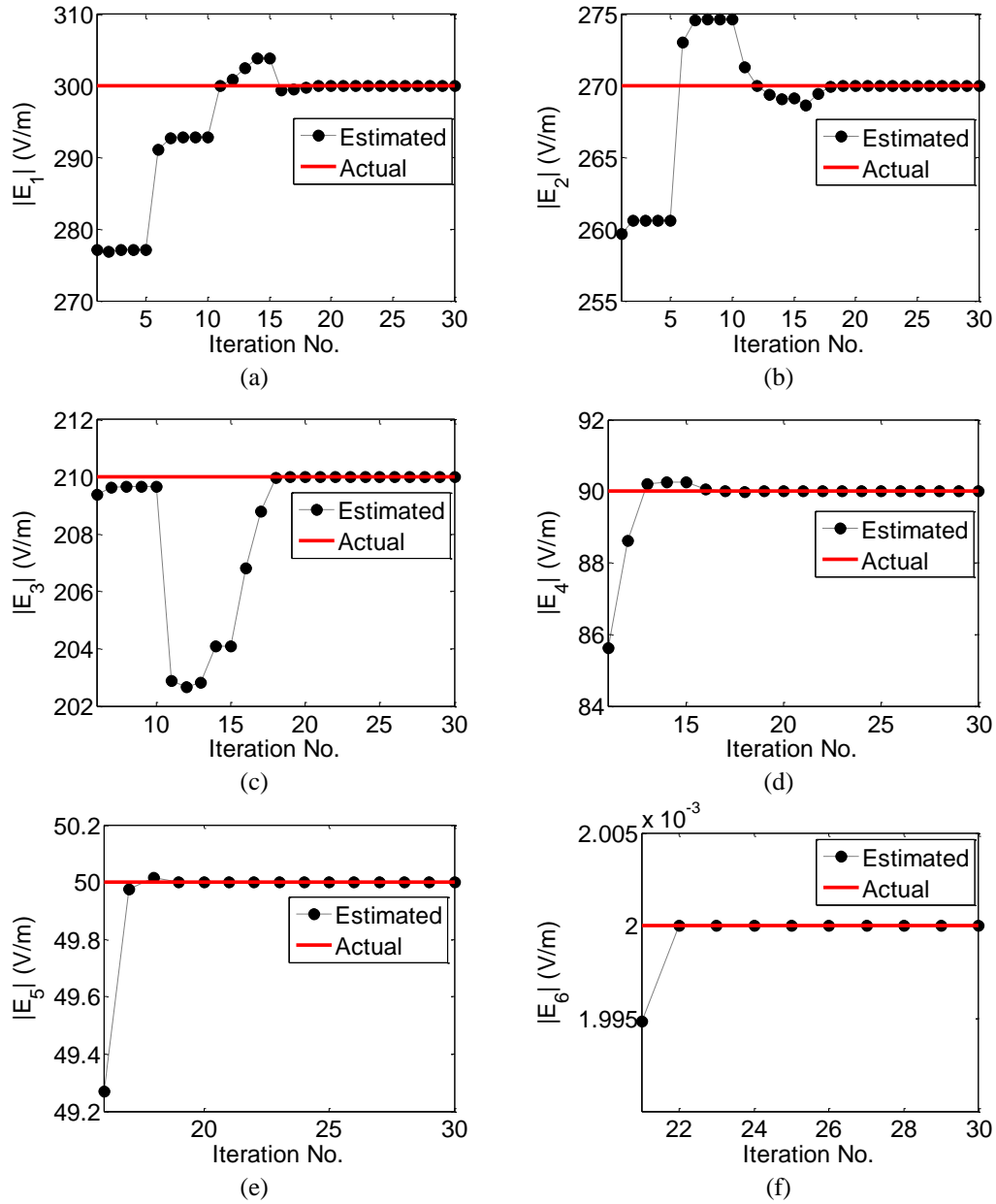


Figure 3-10. Estimated magnitudes of the signals versus iteration number. The red lines represent the truth and the symbols denote the estimated values.

demonstrated. Initially a simple scenario is considered to indicate the ability of the proposed algorithm to segregate the direction of arrival as well as the magnitude and phase of a number of monochromatic plane waves impinging a receiver with a circular array. The array is

composed of 12 equally spaced dipole antennas with a diameter of $D = 2a = 1.44\lambda$. It is also assumed that the array is illuminated by six monochromatic plane waves from different directions. The background noise is neglected in this simulation. The estimated directions of arrival and magnitudes of the signals versus iteration number are shown in Figure 3-9 and Figure 3-10 respectively. It is evident that in each step, the algorithm converges after a few iterations (less than 5) denoted by r_s . The total number of iterations to estimate each signal, defined as N_I^s depends on its magnitude compared to other signals and the total number of impinging signals which are above the threshold level. For the lower level signals, the convergence is faster. The reason is that, the signals are estimated in a descending order and when it comes to the lower signals, an accurate estimation of the larger ones is already made, and their contribution are already subtracted from the total. The range of the horizontal axis in Figure 3-9 and Figure 3-10 ($Itr.no.max - Itr.no.min$) represents N_I^s . As mentioned before, $E_s^{(i,k)} = 0$ for $i < s$. It can be observed that 100 dB dynamic range ($20 \log(|E_1/E_6|)$) is handled by this technique using a 12-element circular array of diameter 1.44λ .

A quantitative comparison with other techniques including Root-MUSIC [58] in conjunction with spatial smoothing [53], Matrix Pencil Method [75] and Maximum Likelihood by alternating projection [84] is performed with additive zero-mean White Gaussian Noise. To implement Root-MUSIC, a transformation to a virtual array [79] is applied to the circular array to make the data matrix amenable to spatial smoothing. This transformation is also used before applying the Matrix Pencil Method as the Matrix Pencil Method cannot directly be applied to a circular array. The circular array is recommended to have odd number of elements for efficient performance of this transformation [34].

Table 3-2. The directions of arrival and SNRs for the four-signal scenario

Sig. No.	DoA	SNR (dB)
1	50°	65
2	140°	60
3	230°	55
4	320°	5 to 50

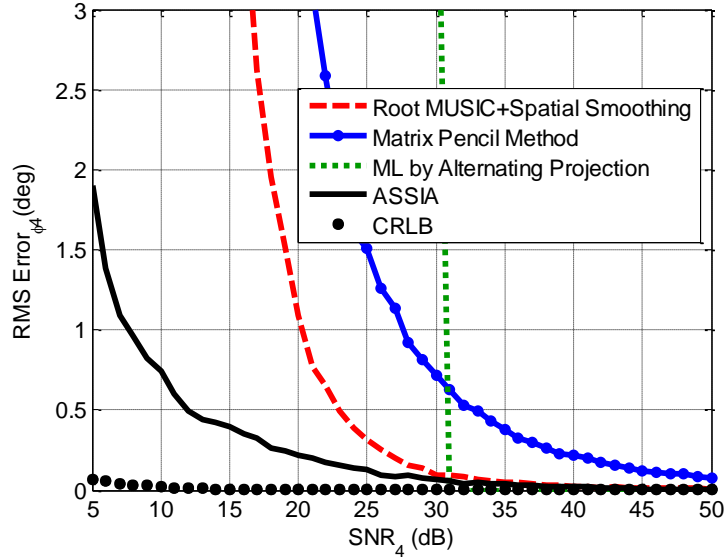


Figure 3-11. The RMSE in estimating φ_4 versus SNR_4 using different techniques for the scenario in which four correlated signals of different SNRs listed in Table 3-2 are impinging on the array.

Therefore, to make a fair comparison, a 15-element circular array of diameter $D = 1.6 \lambda$ is considered. It is assumed that four fully correlated signals with different signal-to-noise-ratios spread over a wide dynamic range are illuminating the array from different directions listed in Table 2. The Root Mean Square Error (RMSE) in the estimation of the DoA of the source located at $\varphi = \varphi_4$ by varying the signal-to-noise ratio of the signal arriving from the 4th direction (SNR_4) while keeping the SNR of the three other signals fixed is calculated and plotted in Figure 8 using different techniques based on 100 Monte Carlo simulations. It should be noted that, the same time duration of signals was taken for all

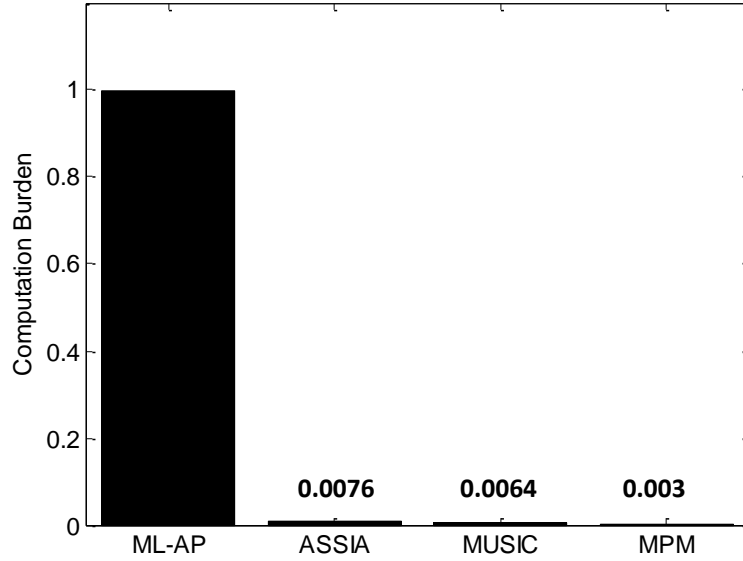


Figure 3-12. The Computation burden of ASSIA compared to other methods for the four-signal scenario.

techniques. It is observed that ASSIA exhibits superior performance particularly when SNR_4 is much lower than the other three signals. For this scenario, Maximum Likelihood fails to converge in detecting φ_4 if the dynamic range denoted by $\text{DR} = \text{SNR}_{\text{max}} - \text{SNR}_4$ is larger than 35 dB. The detection errors of Root MUSIC and Matrix Pencil Method start to increase dramatically for $\text{DR} > 45$ dB and $\text{DR} > 40$ dB respectively; while ASSIA provides estimation of the direction of arrival of the weakest signal with less than 2° error up to $\text{DR} = 60$ dB and $\text{SNR} = 5$ dB.

The computation time of ASSIA is compared with the other methods for this experiment and is illustrated in Figure 9. The computation time of ASSIA is comparable to MUSIC, 2.5 times more than MPM and 130 times less than the Maximum Likelihood method.

Another factor that affects the performance of DoA estimation techniques is the number of the receiving signals. Using the same receiver array, the performance of ASSIA

is evaluated and compared with the other estimators for another scenario in which the number of the receiving signals is increased to seven. The directions of arrival and SNRs of the signals are listed in Table 3. Performing 100 Monte Carlo runs, the resulted RMSE in detecting angle of arrival of the 7th signal (φ_7) by varying the signal-to-noise ratio of the signal arriving from the 7th direction (SNR_7) while keeping the SNR of the six other signals fixed, is shown in Figure 10 for different estimators. The performance of Root-MUSIC is severely degraded, since the effective aperture of the array is substantially reduced after spatial smoothing. It is also evident that the Maximum Likelihood breaks down in this scenario when $\text{DR} = \text{SNR}_{\text{max}} - \text{SNR}_7$ is larger than 10 dB. The reason for the failure of the Maximum Likelihood is that the dependence of the global convergence on the initialization is very strong in all deterministic or randomized hill climbing techniques. In case of large dynamic range and large number of arriving signals, the probability of choosing a good initial point to render the convergence to the correct solution is much less. The resulted RMSE for Matrix Pencil Method is much higher than what is achieved by ASSIA particularly for $\text{DR} > 20$ dB. Comparing to the four-signal scenario, it is observed that, the estimation error of the Matrix Pencil Method is increased, while the estimation error of ASSIA is smaller than 1.5° for $\text{SNR} = 5\text{dB}$ and $\text{DR} = 60\text{ dB}$.

The keys to the success of ASSIA in situations where the signals dynamic range is wide and the number of the signals arriving from different directions is high are: 1) no initialization is required for the signals at the beginning and 2) the signal levels and the direction of arrivals based on estimating and removing the strongest signals are calculated through a multi-step iterative approach. In this fashion, the errors are effectively prevented to propagate while moving towards estimating the smaller signals.

Table 3-3. The directions of arrival and SNRs for the seven-signal scenario

Sig. No.	DoA	SNR (dB)	Sig. No.	DoA	SNR (dB)
1	35°	65	5	290°	65
2	85°	65	6	345°	45
3	140°	40	7	240°	5 to 65
4	190°	40			

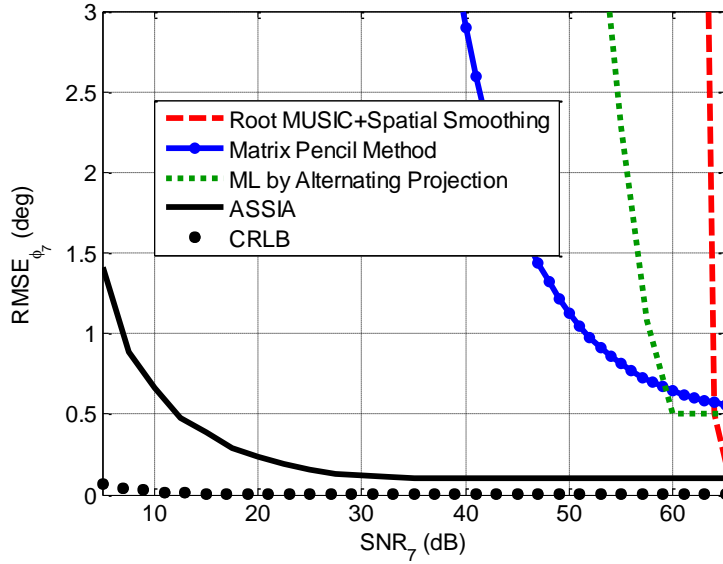


Figure 3-13. The RMSE in estimating ϕ_7 versus SNR_7 using different techniques for the scenario in which seven correlated signals of different SNRs listed in Table 3-3 are impinging on the array.

The capability of ASSIA in detecting correlated signals over a very wide dynamic range is of great importance for interference cancellation as in realistic situations, the level of the interference signal is usually much larger than the desired signal. Moreover, as will be shown later, in complex environments, there exist multiple correlated interference signals and multiple correlated desired signals spanning a wide range of magnitude arriving at the receiver from different directions. As described before, all adaptive array techniques require the knowledge of the DoAs of the desired signals for maximizing the signal to interference ratio. Therefore, failure in the detection of the desired signals leads to the failure of the

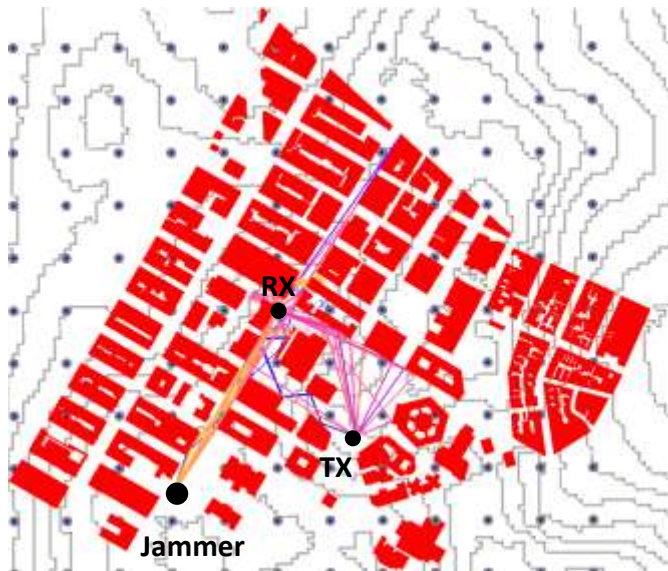
existing adaptive array techniques for interference cancelation. There are also situations in practice where many small signals from different DoAs arrive at the receiver whose total power may be comparable to that of a larger signal and if the algorithm cannot detect these small signals, the estimation of DoAs of the stronger signals will be erroneous.

In all simulations, it is assumed that the array is calibrated to capture the fabrication errors and thereby the array manifold is perfectly known. It should be noted that imperfect estimation of the array manifold generally results in the performance degradation of ASSIA and in particular puts a lower limit in the dynamic range of the signals that can be handled by ASSIA. The reason for the latter is that, a relatively small error in the estimation of the large signals generates a relatively large error in the estimation of the small signals. Hence, the dynamic range of the signal that ASSIA can handle is reduced as the systematic errors increase. This problem is not, however, unique to ASSIA but it applies to all other DoA estimators. Array calibration is thus essential to maximally benefit from the features that ASSIA offers.

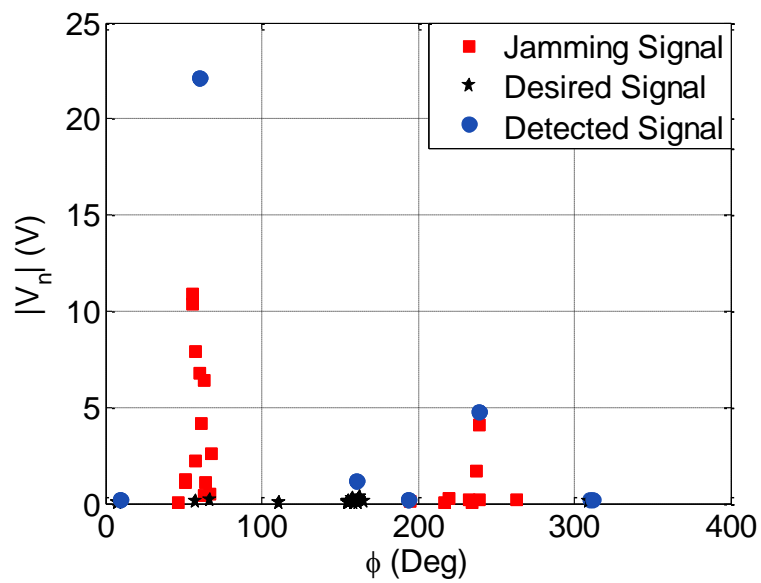
3.2.7 Performance Analysis in a Complex Environments

To evaluate the performance of ASSIA under much complex and realistic conditions, a congested urban environment is considered. Such environment is characterized as a Rayleigh fading environment. Downtown Manhattan which is considered a complex wave propagation environment [124], is chosen as the simulation domain. A very fast and accurate urban wave propagation simulation software (EMTerrano of EM.Cube package [56]) is used for broadband wave propagation simulation. Figure 1-5 illustrates the simulation scenario generated by EMTerrano. The software allows placement of multiple transmitters of arbitrary

power level and arbitrary radiation pattern and provides the field coverage over the entire or a portion of the simulation area with desired resolution. For each point on the receiver grid, the software provides a vector containing the magnitude and phase of all rays arriving at that point with their corresponding angle of arrival. This information is used to assess the performance of the proposed algorithm. Choosing a transmitter location and using it as jammer, the performance of the algorithm can also be evaluated in terms of its ability to segregate the desired signal. The area of the region illustrated in Figure 1-5 is $1200\text{ m} \times 1200\text{ m}$ within which one communication transmitter, one jammer and one receiver are placed at the antenna height of 2 m from the ground. The buildings are assumed to be impenetrable objects composed of brick with $\epsilon_r = 4.44$. As before the receiver is composed of a uniform circular array of 12 dipole antennas designed to operate at 300 MHz. The desired transmitted signal is assumed to have a bandwidth of 4 MHz from 298 to 302 MHz with BPSK modulation and the jamming signal is assumed to be a white Gaussian noise each of which are radiated through omnidirectional antennas. It should be noted that, since each frequency component of the signals is processed separately, ASSIA imposes no constraints on the waveform of the jamming signal. Therefore, if the jamming signal has any other waveform instead of White Gaussian noise or even is correlated with the desired signal, ASSIA is able to detect and separate all interfering and desired signals. The resolution of the FFT which is applied at the receiver baseband is 10 kHz. The transmitter and the jammer power are adjusted so that within the signal bandwidth, the signal-to-noise ratio and the Signal-to-Jammer Ratio (SJR) at the receiver are 20dB and -20 dB respectively. An example scenario for HDR mode is illustrated in Figure 3-14(a). As it is depicted in Figure 3-14(a), a large number of rays arrive at the receiver emanating from both the transmitter and the



(a)



(b)

Figure 3-14. (a) An example scenario for HDR mode, (b) detected signals (Center frequency component) for this scenario.

jammer. For this scenario, as it is evident from Figure 3-14(b), six directions of arrival are detected by the receiver. It is also shown that the jamming signals are arriving from three main separable directions and for each main direction, there are many adjacent rays. The

desired signal, on the other hand, is arriving at the receiver from five main separable

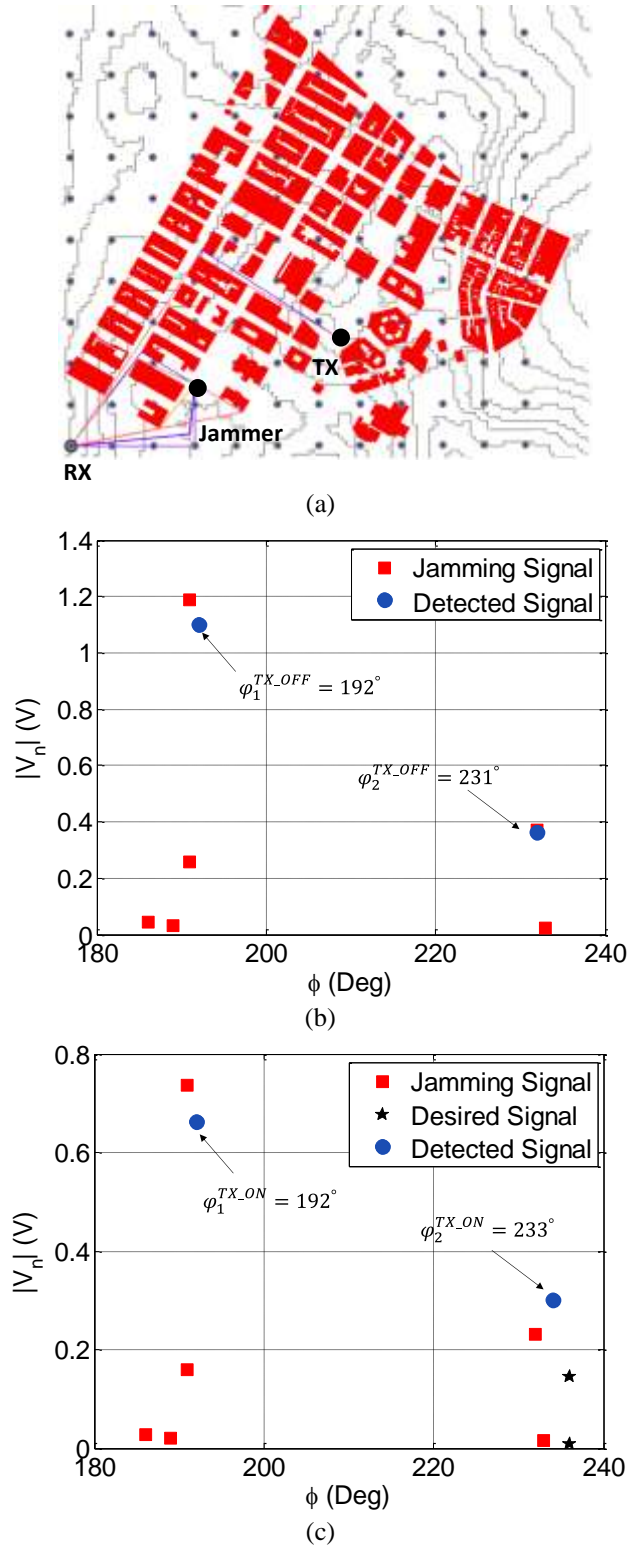


Figure 3-15. (a) An example scenario for LDR mode. (b) Detected signals (Center frequency component) for when the transmitter is off, (c) Detected signals (Center frequency component) when the transmitter is on.

directions among which one overlaps with the jamming signal. The rays from this direction is not read as the desired signal. Also, one ray is not detected due to its low amplitude compared to the pre-determined threshold level and the algorithm errors as well. These errors occur when the contribution of the other signals is not subtracted perfectly because a large number of rays are arriving at the receiver within the azimuthal angular range from 150° to 250° which are not apart enough to be segregated and estimated by the algorithm accurately. Therefore, three desired and three jamming signals are detected some of which represents the resultant of the adjacent arriving signals. This procedure is done for all frequency components and the jamming signals subtracted from the total received signal at each antenna. Eventually, the cleaned-up signal from each antenna goes through further signal processing and decoding which is not the point of attention in this discussion. For this scenario, the achieved signal to jammer ratio after cancellation procedure is 9.5dB which indicates 29.5 dB improvement.

Now consider the scenario demonstrated in Figure 3-15 (a) in which the desired and the jamming signals arrive at the receiver from nearby directions and a replica of the jamming signal quite away from the desired signal also exists. In this case, the receiver fails to retrieve the desired signal in HDR mode. Noting that $SNR = 20\text{dB}$ and $SJR = -20\text{dB}$, Figure 3-15 (b) and Figure 3-15 (c) show the detected signals corresponding to the center frequency component in the transmitter off-state and the transmitter on-state respectively. The detected directions of arrival for the jamming signal which is close to the desired signal denoted as φ_2 changes as the transmitter transits from off-state to on-state. Based on the procedure described in section 3.2.5 for LDR mode and assuming a perfect synchronization, which is beyond the scope of this research, the radio receiver will be able to make an estimation of

the jamming signal from direction φ_2 and then to clean up the received signal at each antenna. After jamming signal removal, the signal to jammer ratio is increased to +6.5 dB which corresponds to 26.5dB enhancement in this case.

The two previous examples clearly demonstrate the effectiveness of ASSIA radio. However, a statistical analysis is carried out to show that the improvements observed are not accidental. For this purpose, 100 receiver locations are chosen randomly in the scene shown in Figure 3-16. The locations of the transmitter and the jammer are kept the same for these series of simulations. For each receiver location, the power of the transmitter and the jammer have been adjusted so that at the receiver point $\text{SNR} = 20 \text{ dB}$ and $\text{SJR} = -20 \text{ dB}$. Out of 100 receiver locations, 30 points are not further examined as either the signal or jammer were below the threshold. Out of 70 points at which the algorithm was tested, in 38 receiver locations, the radio has been able to effectively remove interference and boost the signal to jammer plus noise ratio to at least +2 dB (minimum of 22dB improvement) in HDR mode. The number of DoAs of the desired and the jamming signals corresponding to each receiver location and $S/(J + N)$ after interference removal are illustrated on the same graph in Figure 3-16. The radio fails to retrieve the desired signal in HDR mode in other spots due to the proximity of the DoAs of the desired and the jamming signals. Switching to LDR mode, enables the receiver to segregate the communication signal of interest from the interfering signal in 11 other locations. As it is shown in Figure 3-17, in the worst case, $S/(J + N)$ at the output of the ASSIA processor is higher than +2 dB. Therefore, ASSIA radio succeeded to remove interference in a total 49 out of 70 spots (70 % of occasions) with better than 22 dB improvement. In 21 locations out of 70 points, the desired and the jamming signals all arrived

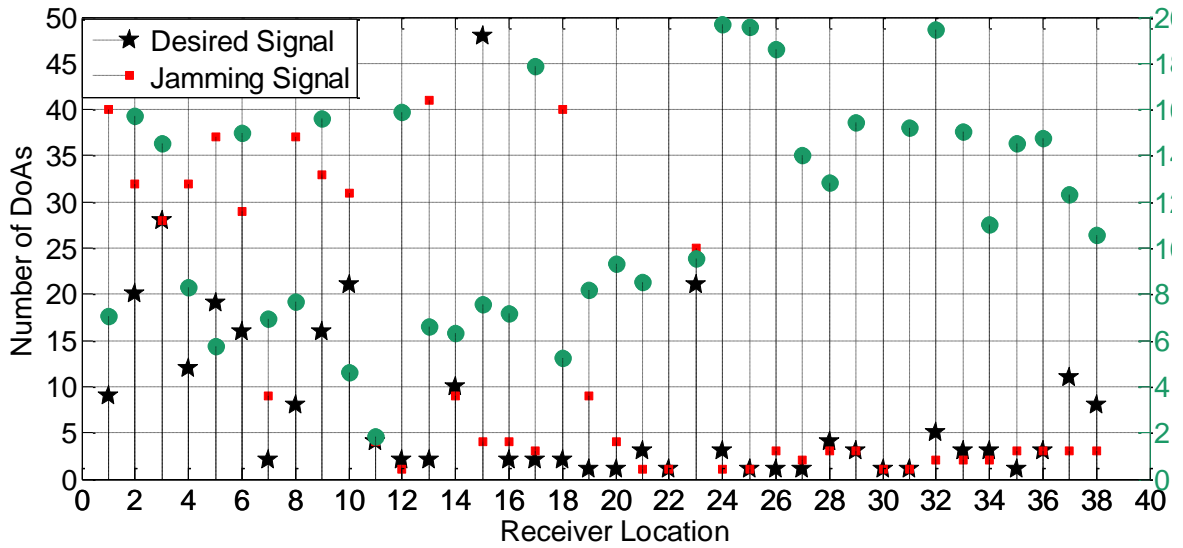


Figure 3-16. Number of DoAs of the desired (black pentagrams) and the jamming (red squares) signals and $S/(J+N)$ after mitigation (green circles) in HDR mode for 38 receiver locations.

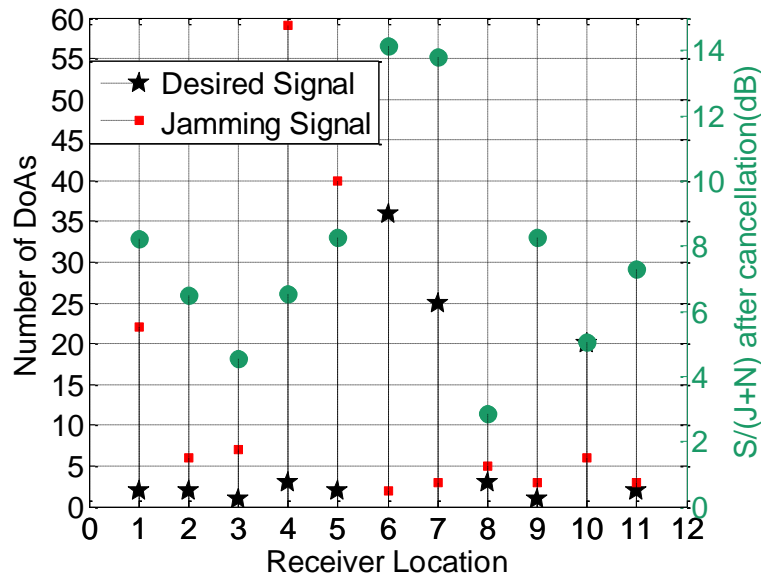
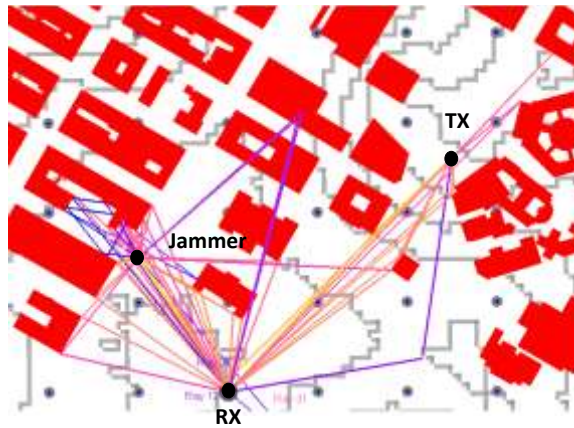
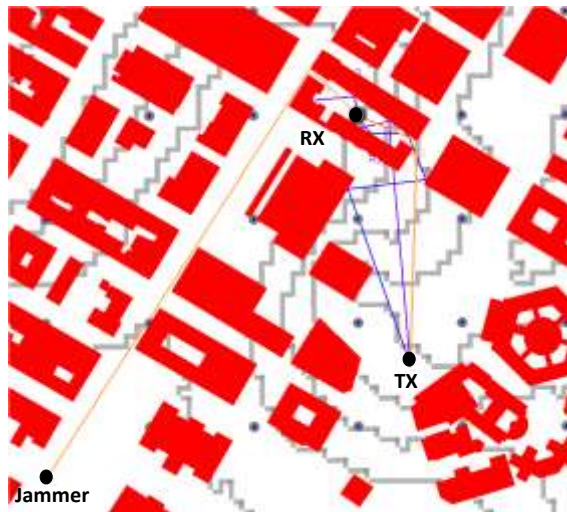


Figure 3-17. Number of DoAs of the desired (black pentagrams) and the jamming (red squares) signal and $S/(J+N)$ after mitigation (green circles) in LDR mode for 11 receiver locations.

with similar DoAs for which even the LDR was challenged to cancel out the jammer substantially.



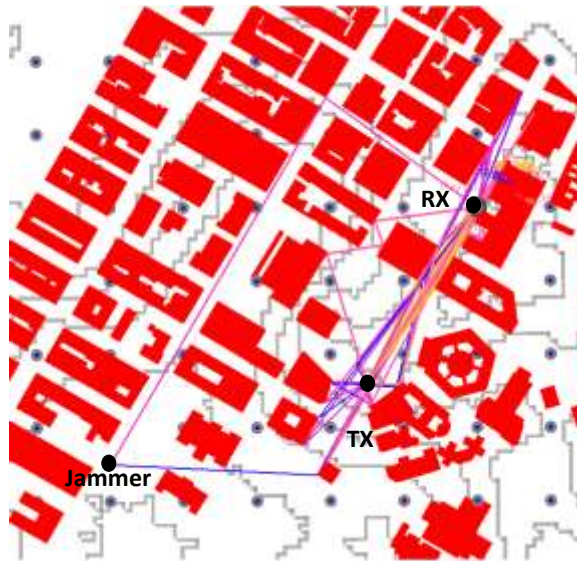
(a)



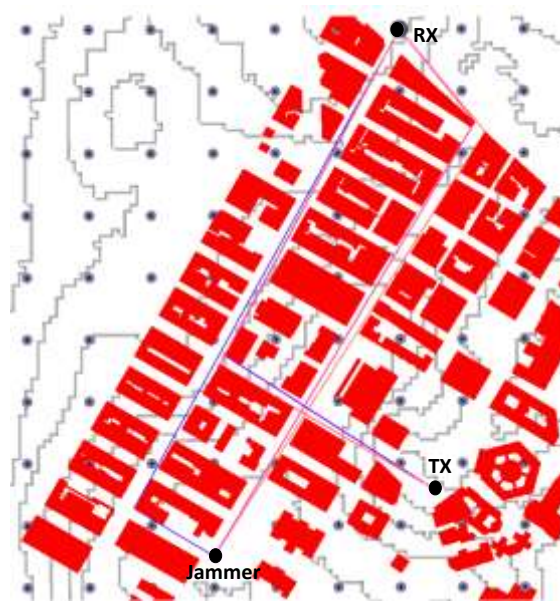
(b)

Figure 3-18. The sketch of the received rays for (a) Receiver location 1, (b) Receiver location 2. The receiver operates in HDR mode in these locations.

The success level can of course be improved significantly if we did not force SJR to be -20 at every location. Also, by increasing the number of antennas and in turn reducing the array beamwidth, the performance of the radio can be enhanced. The number of DoAs of the desired and the jamming signals and their angular distance affect the enhancement level



(a)



(b)

Figure 3-19. The sketch of the received rays for (a) Receiver location 3, (b) Receiver location 4. The receiver operates in LDR mode in these locations.

of $S/(J + N)$. Roughly, one can say that the lower is the number of DoAs and the larger their angular distance, the higher is the performance improvement.

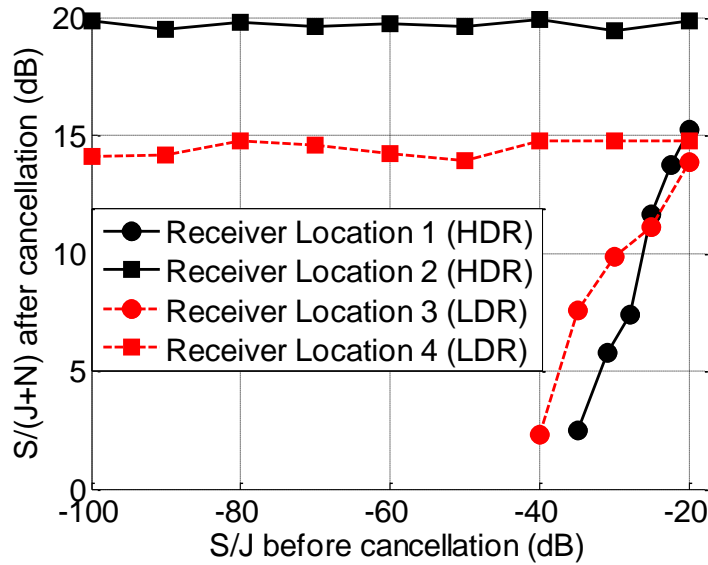


Figure 3-20. $S/(J+N)$ after cancellation versus S/J before cancellation for 4 different receiver locations demonstrated in Figure 3-18 and Figure 3-19.

Figure 3-20 illustrates the signal to jammer plus noise ratio after cancellation versus signal to jammer ratio before cancellation by using the same receiver array in four different receiver locations. Two of these scenarios corresponds to HDR mode and the other two corresponds to LDR mode shown in Figure 3-18 and Figure 3-19 respectively. As before, it is assumed that $SNR = 20$ dB for these simulations. Figure 3-20 further reveals that the performance of the radio depends on the scenario complexity, that is, the number of DoAs, their angular distance and the signal to jammer ratio. The reason for better performance of the radio receiver in location 2 compared to location 1 for very low signal to jammer ratio in HDR mode pertains to the proximity of DoAs of the desired and jamming signals in location 1. The algorithm also exhibits excellent cancellation of the jamming signal in LDR mode in location 4 which is better than that for location 3 for very low SJR. This is due to the fact that, in location 4, there exist rays of jamming signals with DoAs which are apart from the desired

signals and can be estimated accurately by the algorithm. In location 3, the jammer signal is not estimated as accurate as that of location 4 due to not having enough angular distance from the desired signals.

3.3 Closely-spaced Nulls Synthesis Method (CNSM)

3.3.1 Formulation of CNSM

As mentioned in Section 3.2, the magnitudes and the phases of all signals with angular spacing larger than the array beamwidth are estimated by ASSIA while the closely-spaced signals are left combined. The vector sum of the closely-spaced signals denoted by \mathbf{V}_s obtained in the first step is processed in the next step using CNSM to resolve the nearby signals. This hybrid approach significantly reduces the complexity of the problem as it shrinks the search region to the beamwidth of the array as oppose to the entire space.

Before proceeding to the details of CNSM, it is important to clarify that CNSM algorithm presented here is different from null steering method that has been used for accurately tracking a single target or estimating the DoA of an impinging signal. This traditional null steering approach was first introduced by Robert M. Page in 1943 and patented four years later in 1947 and published in 1968 [113]. The technique proposed by Page was originally called “Simultaneous Lob Comparison, Pulsed Echo Location System” and was later referred to as “Monopulse Tracking”. However, this technique is only useful for exact localization of a single target or signal and it fails if two or more closely spaced signals are received. Since then, variety of adaptive null-steering methods have been reported most of which are intended to suppress interference signals under very limiting conditions and none of them are adapted to render the DoA of multiple signals. The proposed CNSM in this section

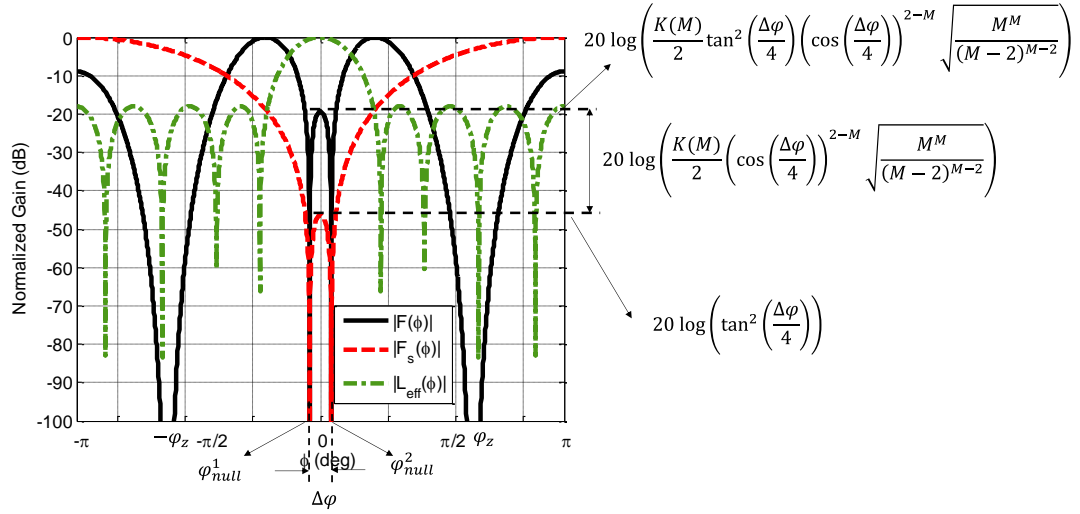


Figure 3-21. The plot of functions $F(\varphi)$, $F_s(\varphi)$, and the array pattern denoted by $L_{\text{eff}}(\varphi)$.

is a new approach for DoA estimation and is basically developed in conjunction with ASSIA to resolve multiple closely spaced correlated signals. The formulation of CNSM for detecting two signals is described in part A of this section for demonstration and then in part B, the generalized form of CNMS for resolving arbitrary number of nearby signals is presented.

3.3.1.1 Two Closely-spaced Signals

To begin with, consider two monochromatic plane waves impinging on a circular array composed of M equally-spaced elements from directions φ_1 and φ_2 where $|\varphi_1 - \varphi_2| < BW$. This resembles a case of unresolved closely spaced signals after segregation in the first step. The Closely spaced Nulls-Synthesis Method (CNSM) developed here is based on minimizing the total received power of the array by creating closely spaced nulls in all possible directions within the array beamwidth to coincide with the DoAs of the signals. Generally, as the nulls' separation is decreased, the peak array gain between the two nulls is also decreased which makes the task of minimization more difficult especially in cases where signal-to-noise-ratio

is low. To make the method efficient for moderate or low SNR regimes, the peak gain in between the two nulls should be maximized. To start, consider a simple function $F_s(\varphi)$ defined as [112]:

$$F_s(\varphi) = e^{-j\frac{M}{2}\varphi} \left(e^{j\varphi} - e^{j\varphi_{null}^1} \right) \left(e^{j\varphi} - e^{j\varphi_{null}^2} \right) \quad (3-68)$$

where φ_{null}^1 and φ_{null}^2 are the directions of the nulls. $\Delta\varphi$ is defined as the nulls angular separation ($\Delta\varphi = \varphi_{null}^1 - \varphi_{null}^2$) and M is the number of the array elements. $F_s(\varphi)$ as described by (3-68) has two zeros at $\varphi = \varphi_{null}^1$ and $\varphi = \varphi_{null}^2$ and is made realizable by an M -element circular array using the first multiplicative phase term. The normalized magnitude of this function and radiation pattern of the array denoted by $L_{eff}(\varphi)$ are plotted in Figure 3-21. The voltage gain at $\varphi_0 = (\varphi_{null}^1 + \varphi_{null}^2)/2$ is found to be:

$$G_{F_s}(\varphi_0) = \sqrt{\frac{2\pi F_s^2(\varphi_0)}{\int_0^{2\pi} F_s^2(\varphi_0) d\varphi}} \cong \tan^2 \left(\frac{\Delta\varphi}{4} \right) \quad (3-69)$$

which asymptotically decays as $\Delta\varphi^2/16$. This of course is not desired in practice, as the signal-to-noise ratio of the received signal may not be very high. To increase this gain, the array directivity in other directions must be reduced. The basic idea is to add zeros to the gain function given by (3-68) in other directions, especially the direction of maximum radiation. An M -element circular array can generate M independent zeros [112]. Let's define a new function denoted by $F(\varphi)$ as:

$$F(\varphi) = F_s(\varphi) \left(e^{j\varphi} - e^{j(\varphi_0 + \varphi_z)} \right)^{\frac{M-2}{2}} \left(e^{j\varphi} - e^{j(\varphi_0 - \varphi_z)} \right)^{\frac{M-2}{2}} \quad (3-70)$$

which has two zero of order $(M-2)/2$ at $\varphi = \varphi_0 + \varphi_z$ and $\varphi = \varphi_0 - \varphi_z$. Then, φ_z is defined so as to $G(\varphi_0)$ is maximized:

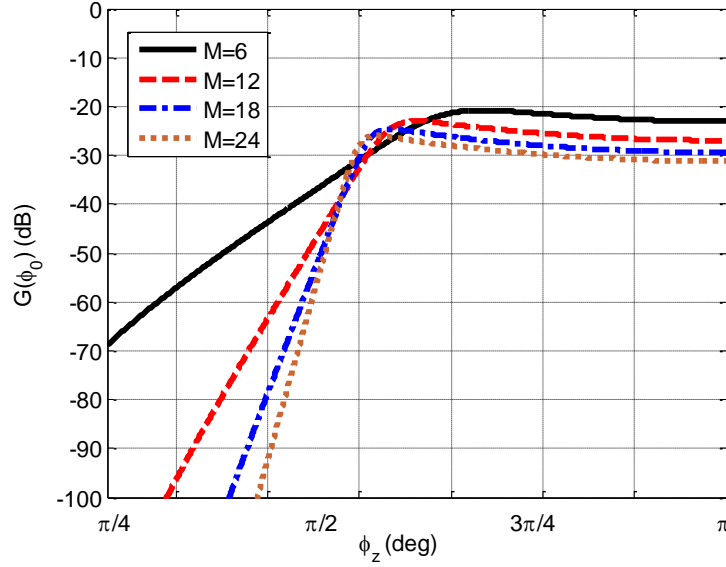


Figure 3-22. $G(\varphi_0)$ versus φ_z for $\Delta\varphi = 0.3\text{BW}$ for different array sizes. $G(\varphi_0)$ is maximized at $\varphi_z = 0.7\pi$ and $\varphi_z = 0.55\pi$ for $M = 6$ and $M = 24$ respectively.

$$\varphi_z = \underset{\varphi_z}{\operatorname{argmax}} G_F(\varphi_0) \quad (3-71)$$

where $G_F(\varphi)$ is given by:

$$G(\varphi) = \sqrt{\frac{2\pi F^2(\varphi)}{\int_0^{2\pi} F^2(\varphi) d\varphi}} \quad (3-72)$$

$G(\varphi_0)$ versus φ_z is calculated numerically for different array sizes and is plotted in Figure 3-22. The gain increases as φ_z gets larger up to an optimum value denoted as φ_z^{opt} after which the gain starts to decrease slightly up to $\varphi_z = \pi$. As M increases from 6 to 24, φ_z^{opt} varies from 0.7π to 0.55π . The normalized magnitude of the function given by (3-70) for $\varphi_z = \varphi_z^{\text{opt}}$ is plotted in Figure 3-21. The gain in the direction of φ_0 is found as:

$$G_F(\varphi_0) = \frac{K(M)}{2} \tan^2\left(\frac{\Delta\varphi}{4}\right) \left(\cos\left(\frac{\Delta\varphi}{4}\right)\right)^{2-M} \sqrt{\frac{M^M}{(M-2)^{M-2}}} \quad (3-73)$$

where:

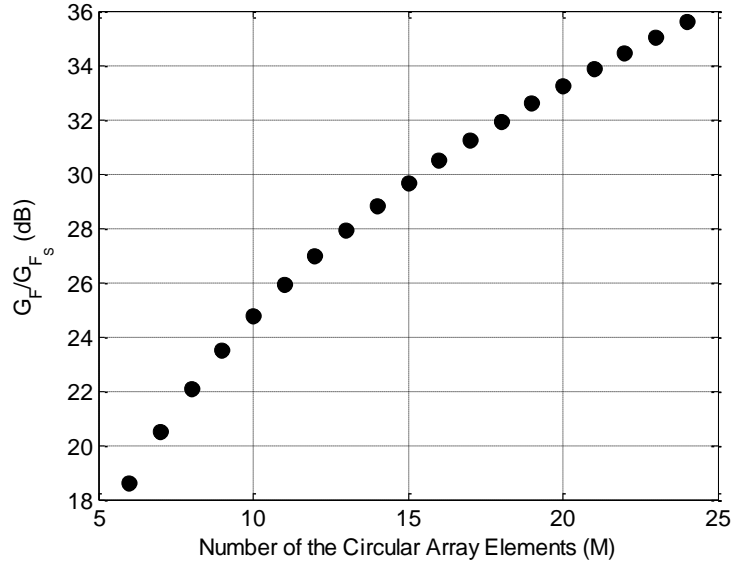


Figure 3-23. G_F/G_{F_s} versus the circular array elements number with inter-element spacing of $\lambda/3$ for $\Delta\varphi = \pi/12$.

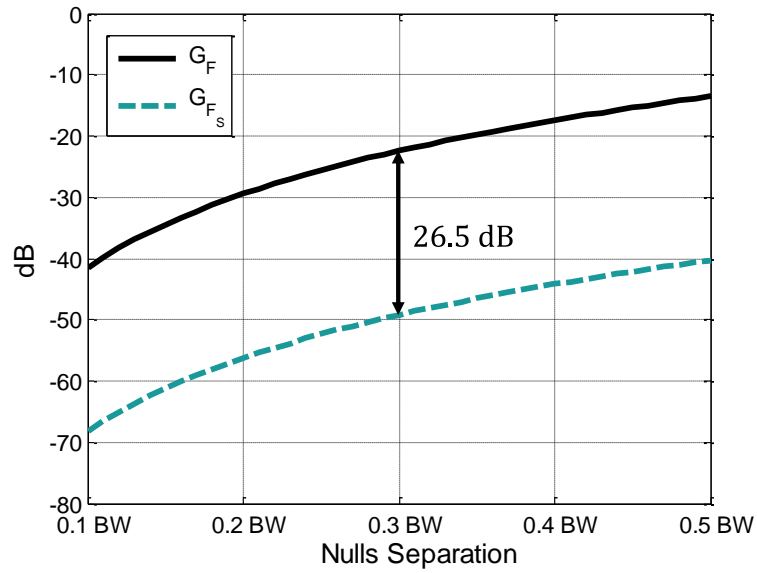


Figure 3-24. G_F and G_{F_s} versus nulls separation for a 12-element circular antenna array with element spacing of $\lambda/3$.

$$K(M) = \begin{cases} 1 & \varphi_z = \pi \\ 1 + 0.03(\sqrt{2M})\sqrt{3} & \varphi_z = \varphi_z^{opt} \end{cases} \quad (3-74)$$

Comparing (3-69) and (3-73) shows that $F(\varphi)$ provides

$$\frac{G_F(\varphi_0)}{G_{F_s}(\varphi_0)} = \frac{K(M)}{2} \left(\cos\left(\frac{\Delta\varphi}{4}\right) \right)^{2-M} \sqrt{\frac{M^M}{(M-2)^{M-2}}} \quad (3-75)$$

more gain than $F_s(\varphi)$ at $\varphi = \varphi_0$. $G_F(\varphi_0)/G_{F_s}(\varphi_0)$ versus number of the circular array elements for $\Delta\varphi = \pi/12$ is plotted in Figure 3-23. For a 12-element circular antenna array with element spacing of $\lambda/3$, G_F and G_{F_s} versus nulls separation are plotted in Figure 3-24. The gain in the direction between the two nulls is increased by 26.5 dB after imposing additional nulls. The function given by (3-70) is then synthesized for all possible pairs of directions $(\varphi_{null}^1, \varphi_{null}^2)$ within the array beamwidth (see Figure 3-25) and the directions of arrival are obtained as:

$$(\varphi_1, \varphi_2) = \underset{(\varphi_{null}^1, \varphi_{null}^2)}{\operatorname{argmin}} \left(\mathbf{W}_{\varphi_{null}^1, \varphi_{null}^2} \mathbf{V}_p \right) \left(\mathbf{W}_{\varphi_{null}^1, \varphi_{null}^2} \mathbf{V}_p \right)^H \quad (3-76)$$

where \mathbf{V}_p is the vector of the received voltage from which the contribution of the signals arriving from directions outside the array beamwidth is excluded by ASSIA in the first step and is given by:

$$\mathbf{V}_p = \mathbf{V} - \sum_{\substack{q=1 \\ q \neq p}}^P \mathbf{b}(\varphi_q) E_q \quad (3-77)$$

and $\mathbf{W}_{\varphi_{null}^1, \varphi_{null}^2}$ is the vector of the weighting factors which is applied to the array elements

so as to generate the nulls in directions φ_{null}^1 and φ_{null}^2 :

$$\mathbf{W}_{\varphi_{null}^1, \varphi_{null}^2} = [w_{\varphi_{null}^1, \varphi_{null}^2}^1 \quad \cdots \quad w_{\varphi_{null}^1, \varphi_{null}^2}^m] \quad (3-78)$$

whose elements are given by [112]:

$$w_{\varphi_{null}^1, \varphi_{null}^2}^m = \sum_{q=-M/2}^{M/2} \frac{\int_0^{2\pi} F(\varphi) e^{-jq\varphi} d\varphi}{\sum_{p=-L}^L C_p j^{(q-p)} J_{q-p}(2\pi r/\lambda)} e^{jq\frac{2\pi m}{M}} \quad (3-79)$$

Where

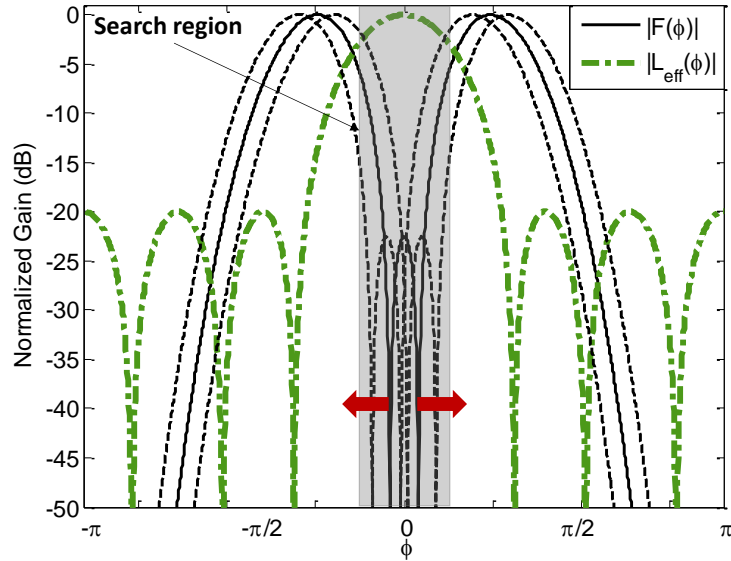


Figure 3-25. The search region shown in gray over which $F(\varphi)$ is realized for different values of φ_{null}^1 and φ_{null}^2 . Also, shown is the focused pattern of the array in direction $\varphi_d = 0$.

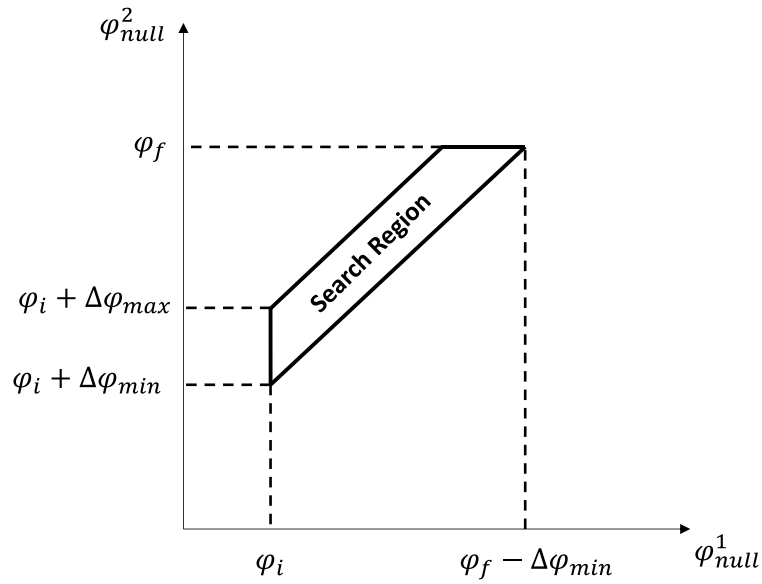
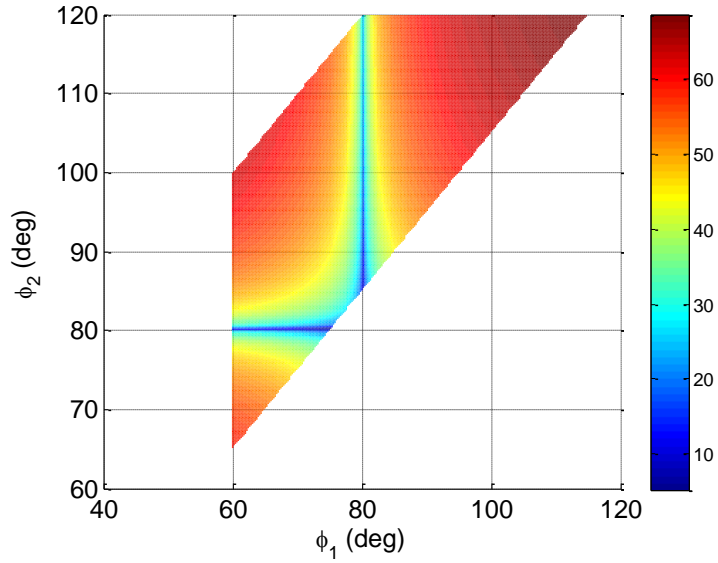


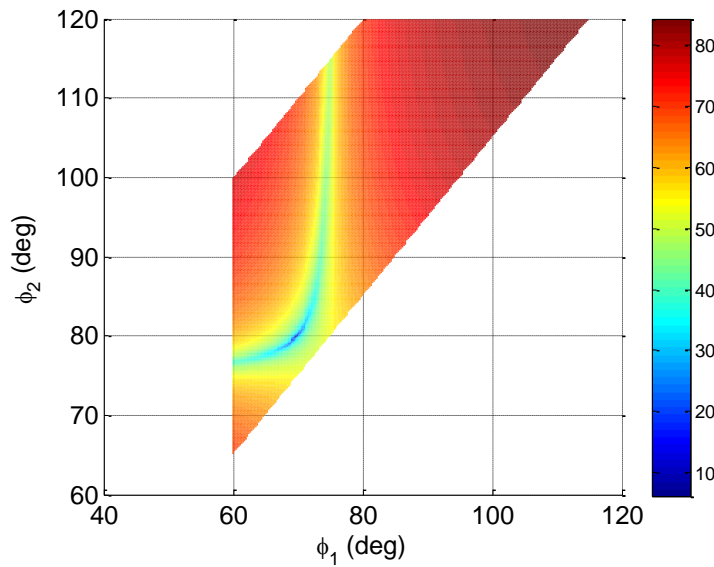
Figure 3-26. The search region for φ_{null}^1 and φ_{null}^2 . It is assumed that $\varphi_1 < \varphi_2$.

$$C_p = \int_0^{2\pi} l_{eff}(\varphi) e^{-j p \varphi} d\varphi \quad (3-80)$$

L is the highest Fourier harmonic of $l_{eff}(\varphi)$ (effective length of each antenna element with reference to the element center), J_{q-p} is the $(q - p)$ th order Bessel function of the first kind,



(a)



(b)

Figure 3-27. The plot of the error function given by (3-76) calculated within the search region for two different scenarios: (a) only one signal is arriving from $\varphi = 80^\circ$ (b) two closely spaced signals are arriving from $\varphi_1 = 70^\circ$ and $\varphi_2 = 80^\circ$.

and r is the radius of the array whose optimum value is $r = \lambda(M/2 - L)/2\pi$. The search region is demonstrated in Figure 3-26. Assuming $\varphi_1 < \varphi_2$, the search region for φ_{null}^1 and

φ_{null}^2 is defined as:

$$\varphi_i < \varphi_{null}^1 < \varphi_f - \Delta\varphi_{min} \quad (3-81)$$

$$\varphi_{null}^1 + \Delta\varphi_{min} < \varphi_{null}^2 < \min\{\varphi_{null}^1 + \Delta\varphi_{max}, \varphi_f\}$$

where $\varphi_i = \varphi_d - \frac{BW}{2}$ and $\varphi_f = \varphi_d + \frac{BW}{2}$ and φ_d is the detected direction of arrival associated with the vector sum of the proximate signals. $\Delta\varphi_{min}$ and $\Delta\varphi_{max}$ are the minimum and the maximum signals angular separation respectively over which the search process is performed noting that $\Delta\varphi_{max} - \Delta\varphi_{min} < BW$ and $\Delta\varphi_{min} \cong 0.1 BW$. Since the search region after applying ASSIA reduces significantly to a small region shown in Figure 3-26, the computation is relatively fast.

It should be noted that upon the completion of the first step, the number of the closely spaced signals is not known. In the second step, the CNSM is applied for each region around all detected signals to see if the error function in (3-75) looks like Figure 3-27(a) or Figure 3-27(b). If the error function exhibits a single explicit minimum as illustrated in Figure 3-27(b), then the existence of two signals within that region is indicated and their DoAs are detected. Otherwise, only one signal is arriving within the search area.

3.3.1.2 Multiple Closely-spaced Signals

The method described in the part A can be extended to resolve multiple closely spaced signals. If N is the number of the signals, then, the beam pattern denoted as $F_N(\varphi)$ is formed so as to have N closely spaced nulls within the main lobe of the array. Therefore, $F_N(\varphi)$ should have N simple zeros in directions $\{\varphi_{null}^n\}_{n=1}^N$ where $\varphi_{null}^1 < \varphi_{null}^2 < \dots < \varphi_{null}^N$. To achieve the maximize gain in the directions between the adjacent nulls, $\{(\varphi_{null}^n + \varphi_{null}^{n+1})/2\}_{n=1}^{N-1}$, the

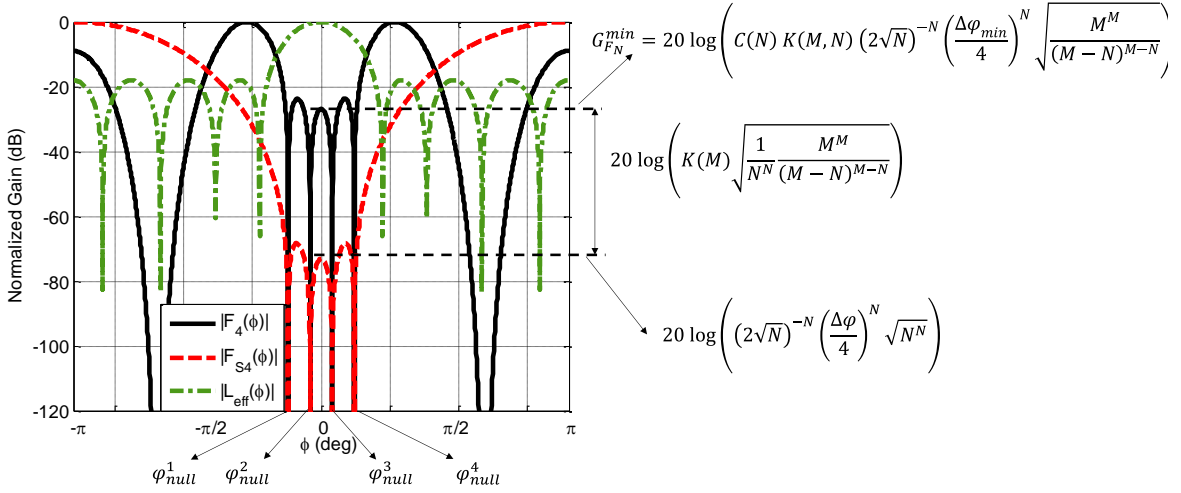


Figure 3-28. The plot of functions $F_N(\varphi)$, $F_{SN}(\varphi)$, and the array pattern for $N = 4$.

other $M - N$ zeros are equally distributed in directions $(\varphi_{null}^1 + \varphi_{null}^N)/2 - \varphi_z$ and $(\varphi_{null}^1 + \varphi_{null}^N)/2 + \varphi_z$ and thereby $F_N(\varphi)$ is built up as:

$$F_N(\varphi) = e^{-j\frac{M}{2}\varphi} (e^{j\varphi} - e^{j(\varphi_0 + \varphi_z)})^{\frac{(M-N)}{2}} (e^{j\varphi} - e^{j(\varphi_0 - \varphi_z)})^{\frac{(M-N)}{2}} \prod_{n=1}^N (e^{j\varphi} - e^{j\varphi_{null}^n}) \quad (3-82)$$

where $\varphi_0 = (\varphi_{null}^1 + \varphi_{null}^N)/2$. Solving numerically for φ_z to maximize the gain in directions $\{(\varphi_{null}^n + \varphi_{null}^{n+1})/2\}_{n=1}^{N-1}$, it is observed that similar to the two-signal case, φ_z^{opt} falls in the range $[0.55\pi, 0.7\pi]$ for different array sizes. Performing a very lengthy algebraic manipulation and simplification, it can be shown that the minimum normalized array gain in directions $\{(\varphi_{null}^n + \varphi_{null}^{n+1})/2\}_{n=1}^{N-1}$ denoted as $G_{F_N}^{min}$ (See Figure 3-28) for $\Delta\varphi_{min} \ll BW$ is well approximated by:

$$G_{F_N}^{min} \cong C(N) K(M, N) (2\sqrt{N})^{-N} \left(\frac{\Delta\varphi_{min}}{4}\right)^N \sqrt{\frac{M^M}{(M-N)^{M-N}}} \quad (3-83)$$

where:

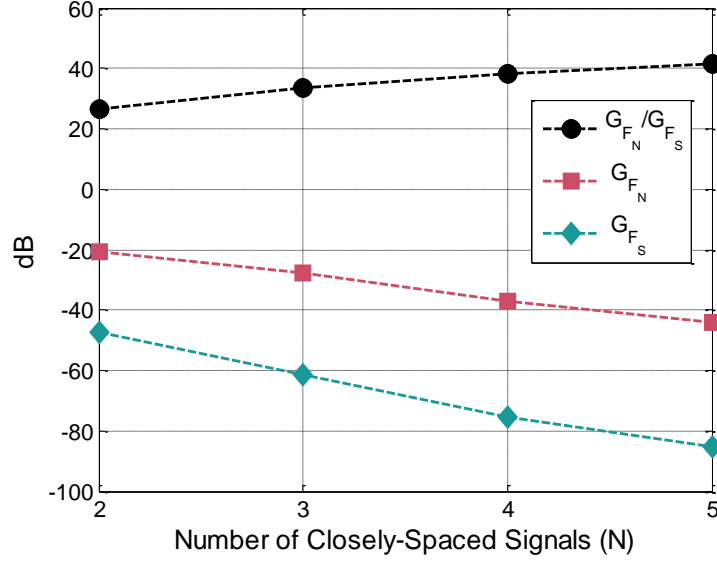


Figure 3-29. G_{F_N} versus number of the signals for $M = 12$ and $\Delta\varphi_{\min} = \pi/12$.

$$C(N) = \begin{cases} \left(\frac{N!}{(N/2)!} \right)^2 & N \text{ even} \\ 2N \left(\frac{(N-1)!}{((N-1)/2)!} \right)^2 & N \text{ odd} \end{cases} \quad (3-84)$$

and

$$K(M, N) \cong \begin{cases} 1 & \varphi_z = \pi \\ 1 + 0.03(\sqrt{MN})^{\sqrt{3}} & \varphi_z = \varphi_z^{opt} \end{cases} \quad (3-85)$$

Comparing with $G_{F_{SN}}(\varphi)$ given by:

$$G_{F_{SN}}^{min} = \frac{2\pi F_{SN}^2(\varphi_0)}{\int_0^{2\pi} F_{SN}^2(\varphi_0) d\varphi} = C(N)(2\sqrt{N})^{-N} \left(\frac{\Delta\varphi_{min}}{4} \right)^N \sqrt{N^N} \quad (3-86)$$

Where

$$F_{SN}(\varphi) = e^{-j\frac{M}{2}\varphi} \prod_{n=1}^N (e^{j\varphi} - e^{j\varphi_{null}^n}) \quad (3-87)$$

that has only N simple zeros at $\{(\varphi_{null}^n + \varphi_{null}^{n+1})/2\}_{n=1}^{N-1}$, it can be shown that:

$$\frac{G_{F_N}^{min}}{G_{F_{SN}}^{min}} \cong K(M, N) \sqrt{\frac{1}{N^N} \frac{M^M}{(M-N)^{M-N}}} \quad (3-88)$$

In (3-88), $G_{F_{NS}}^{min}$ is the minimum normalized value of $G_{F_{SN}}(\varphi)$ in directions $\{(\varphi_{null}^n + \varphi_{null}^{n+1})/2\}_{n=1}^{N-1}$. The derivations of (3-83) and (3-86) are given in the Appendix A. $G_{F_N}^{min}$ versus the number of the signals for $M = 12$ and $\Delta\varphi_{min} = \pi/12$ is plotted in Figure 3-29.

To find the DoAs, $\mathbf{W}_{\{\varphi_{null}^n\}_{n=1}^N}$ is computed by substituting $F(\varphi)$ by $F_N(\varphi)$ in (3-79) for a set of $\{\varphi_{null}^n\}_{n=1}^N$ within the array beamwidth and the directions of arrival are obtained as:

$$\{\varphi_n\}_{n=1}^N = \underset{\{\varphi_{null}^n\}_{n=1}^N}{\operatorname{argmin}} \left(\mathbf{W}_{\{\varphi_{null}^n\}_{n=1}^N} \mathbf{V}_s \right) \left(\mathbf{W}_{\{\varphi_{null}^n\}_{n=1}^N} \mathbf{V}_s \right)^H \quad (3-89)$$

The search process is performed over the following domain:

$$\begin{aligned} \varphi_i &< \varphi_{null}^1 < \varphi_f - (N-2)\Delta\varphi_{min} \\ \varphi_{null}^1 + \Delta\varphi_{min} &< \varphi_{null}^2 < \min\{\varphi_{null}^1 + \Delta\varphi_{max}, \varphi_f - (N-3)\Delta\varphi_{min}\} \\ &\vdots \\ \varphi_{null}^{n-1} + \Delta\varphi_{min} &< \varphi_{null}^n < \min\{\varphi_{null}^{n-1} + \Delta\varphi_{max}, \varphi_f - (N-n-1)\Delta\varphi_{min}\} \\ &\vdots \\ \varphi_{null}^{N-1} + \Delta\varphi_{min} &< \varphi_{null}^N < \min\{\varphi_{null}^{N-1} + \Delta\varphi_{max}, \varphi_f\} \end{aligned} \quad (3-90)$$

As mentioned in Section 3.3.1.1, since the number of the impinging signals from directions confined to the array beamwidth is not known, CNSM starts off the search process assuming that only two signals exist ($N = 2$). If a single global minimum is not found, then

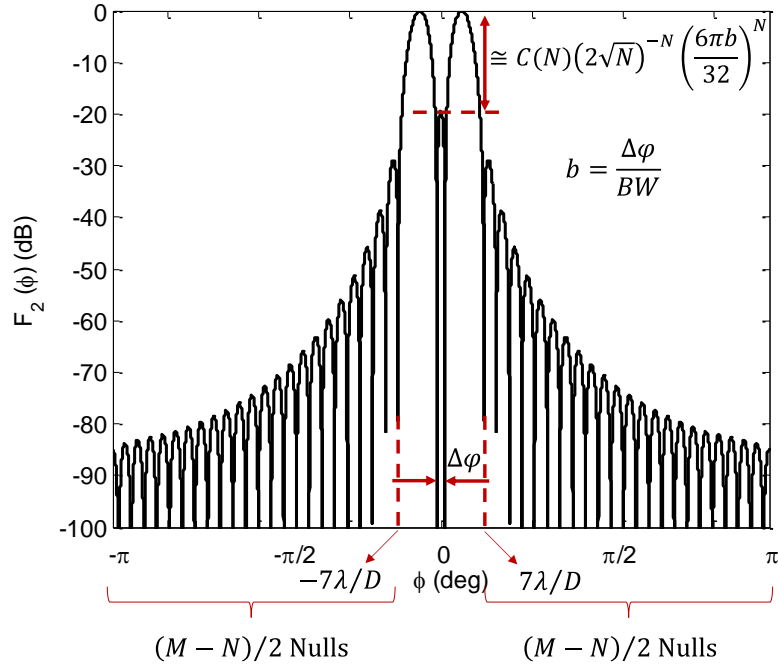


Figure 3-30. The nulls locations scheme for arrays with large number of elements assuming $\varphi_0 = 0$.

the algorithm runs for $N = 3$ and this stepwise procedure is continued for larger values of N up until the number of nulls matches the number of the signals and thereby, a single global minimum is found.

For arrays with large number of elements ($M > 50$), it is numerically found that the $M - N$ zeros of the function $F_N(\varphi)$ should be uniformly distributed within the intervals $\varphi_0 + 7\lambda/D \leq \varphi \leq \varphi_0 + \pi$ and $\varphi_0 - \pi \leq \varphi \leq \varphi_0 - 7\lambda/D$ as shown in Figure 3-30 as oppose to having two zeros of order $(M - N)/2$ at $\varphi_0 - \varphi_z$ and $\varphi_0 + \varphi_z$. This arrangement of nulls provides the same gain as that of given by (3-83) in directions between adjacent nulls for small arrays.

3.3.2 Simulation Results and Comparison with Other Methods

To demonstrate the performance of ASSIA-CNSM, a comparison with other methods

Table 3-4. The directions and SNRs of the sources for the first experiment

Signal No.	DoA	SNR (dB)
1	φ_1	15
2	$\varphi_2 = \varphi_1 + 0.125 BW$	15
3	$\varphi_3 = \varphi_1 + 3BW$	16
4	$\varphi_4 = \varphi_3 + 0.125 BW$	16

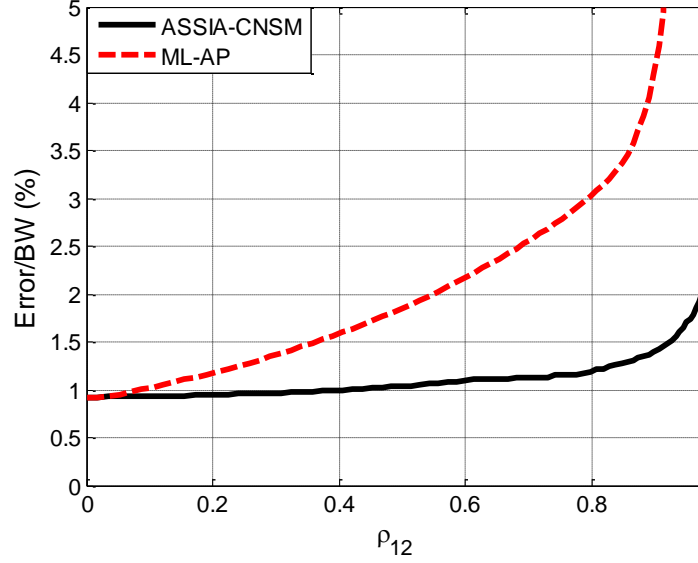


Figure 3-31. The percentage of error in the DoA estimation of signal 2 normalized to half power beamwidth as a function of ρ_{12} . In this scenario, $SNR_1 = SNR_2 = 15\text{dB}$ and $\varphi_2 - \varphi_1 = 0.125 BW$. MPM and Root MUSIC with spatial smoothing methods failed in this scenario.

such as Maximum Likelihood with Alternating Projection (ML-AP) [84] method is made. A 12-element uniform circular array of diameter $D = 1.4 \lambda$ is considered as the receiver array. In the first experiment, the array is assumed to be illuminated by four correlated signals listed in Table I. The angular spacing between DoA of signal 1 and signal 2 and between DoA of signal 3 and signal 4 are set as : $\Delta\varphi_{12} = \varphi_2 - \varphi_1 = \Delta\varphi_{34} = \varphi_4 - \varphi_3 = 0.125 \lambda/D \cong 5^\circ$. The correlation coefficient between signal 1, $S_1(t)$, and signal 2, $S_2(t)$ defined as:

$$\rho_{12} = \frac{\int (S_1(t) - \overline{S_1(t)})(S_2(t) - \overline{S_2(t)})dt}{\sqrt{\left(\int (S_1(t) - \overline{S_1(t)})^2 dt\right) \left(\int (S_2(t) - \overline{S_2(t)})^2 dt\right)}} \quad (3-91)$$

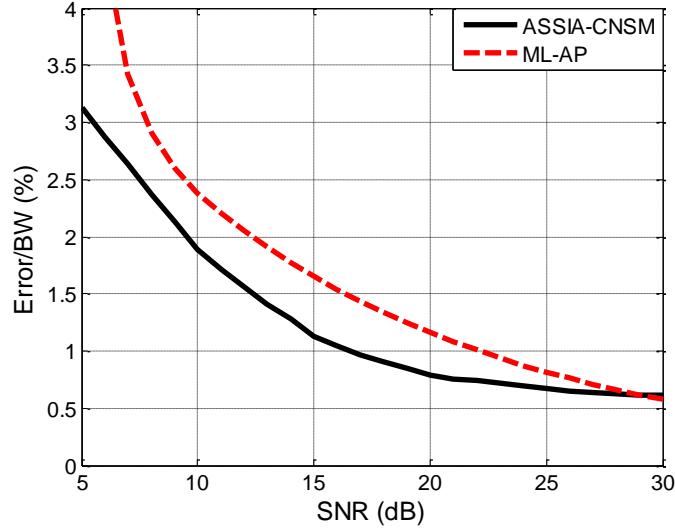


Figure 3-32. The percentage of error in the DoA estimation of signal 2 normalized to half power beamwidth as a function of $\text{SNR}_1 = \text{SNR}_2 = \text{SNR}$ for the second experiment. In this scenario, $\rho_{12} = 0.5$ and $\varphi_2 - \varphi_1 = 0.125 \text{ BW}$. MPM and Root MUSIC with spatial smoothing methods failed in this scenario.

is varied and the Error in the estimation of DoA of signal 2 normalized to the half power beamwidth of the array versus the correlation coefficient (ρ_{12}) is calculated from 2000 snapshots and is plotted in Figure 3-31 and is compared with ML-AP method when the number of snapshots is 2000. In (3-91), $\overline{S_n(t)}$ is the mean value of $S_n(t)$ over one period. For two monochromatic signals with phase difference α , (39) is simplified to $\rho_{12} = \cos(\alpha)$. As the correlation coefficient between signals exceeds 0.7, the performance degradation of ML-AP accelerates and rapidly departs from that of obtained by ASSIA-CNSM.

In the second experiment, the DoAs are the same as the first experiment. Similar to the first experiment $\rho_{34} = 0.9$. The correlation coefficient between signal 1 and signal 2 is set as $\rho_{12} = 0.5$ and the error in the estimation of φ_2 normalized to the beamwidth of the array is computed as a function of $\text{SNR}_1 = \text{SNR}_2 = \text{SNR}$. As shown in Figure 3-32, in this scenario, ASSIA-CNSM provides slightly more accurate estimation compared to ML-AP

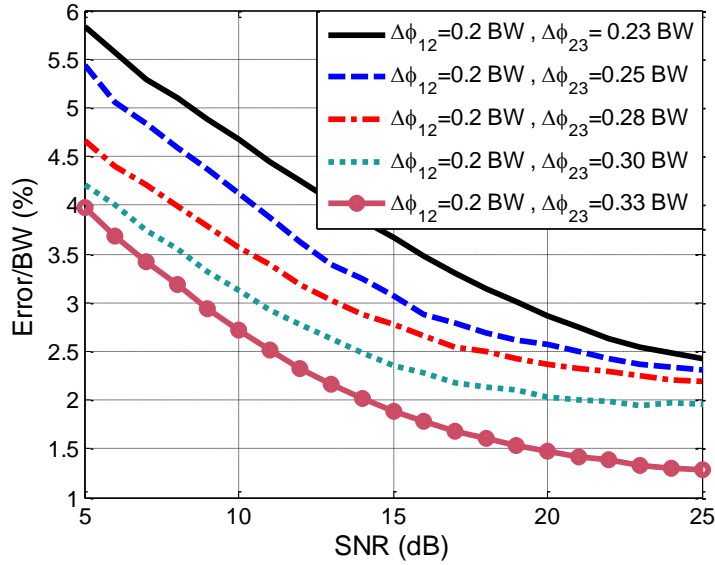


Figure 3-33. The percentage of DoA estimation error normalized to half power beamwidth as a function of $\text{SNR}_1 = \text{SNR}_2 = \text{SNR}_3 = \text{SNR}$ and for different signals angular separation for the three-signal scenario where $\rho_{13} = \rho_{23} = 0.85$ and $\rho_{12} = 0.5$. ML-AP, MPM, and Root MUSIC with spatial smoothing methods failed to resolve the signals in this experiment.

particularly when SNR goes below 7 dB. It should be noted that Matrix Pencil Method (MPM) and Root MUSIC with spatial smoothing were also run for these scenarios and both methods failed to resolve the signals.

Coded in MATLAB and executed on a 64-bit Windows 7 Operating System which runs AMD Phenom™ II X4 965 Processor 3.4 GHz with 16 GB memory, the computation time of ASSIA-CNSM for both experiments is 11 times less than ML-AP.

In the third experiment, the same array used in the previous two scenarios is assumed to be illuminated by three closely spaced equal-magnitude correlated signals with correlation coefficients $\rho_{13} = \rho_{23} = 0.85$ and $\rho_{12} = 0.5$. The DoA estimation error normalized to the array beamwidth defined as:

$$Error = \frac{1}{3BW} \sum_{n=1}^3 |\varphi_n^{Estimated} - \varphi_n^{Actual}| \quad (3-92)$$

versus $\text{SNR}_1 = \text{SNR}_2 = \text{SNR}_3 = \text{SNR}$ and for different angular separation of signals is calculated and is plotted in Figure 3-33. The estimation error is increased compared to the two-signal case for the same SNR level as expected. The other methods including ML-AP, MPM and Root MUSIC with spatial smoothing failed to resolve the signals in this scenario.

3.4 Mutual Coupling Mitigation in Multiple Antenna Systems

3.4.1 Theory of Feed-Forward Coupling Technique

Scattered field in the forward direction is strongest for all objects and is almost 180° out of phase with the incident wave. This phenomenon is responsible for shadowing effect in the near-field region and has the effect of obscuring signals along directions connecting pairs of non-planar array elements.

To describe the concept of coupling mitigation based on the feed-forward technique, consider a pair of identical wideband omni-directional (in x-y plane) mono-conical antennas spaced by $d = \lambda_0/2$, where λ_0 is the wavelength at the center frequency. The edge-to-edge distance between two antennas is $s = \lambda_0/20$. Suppose this array is operating in the receiving mode and is being illuminated by a plane wave as shown in Figure 1-6(a). The direction of illumination is chosen to be along the line connecting the two antennas with Antenna *B* shadowing antenna *A*. As antennas are made of electric conductors, they tend to scatter the incident wave strongly particularly in the forward scattering direction. As a result, the power received by antenna *A* is expected to be lower than that of antenna *B*. In addition to shadowing, multiple-scattering between the two antennas also substantially alters the received power by antenna *B* compared to the same antenna in isolation. Since the elements have 3D structures and are wideband, the induced current as function of frequency can

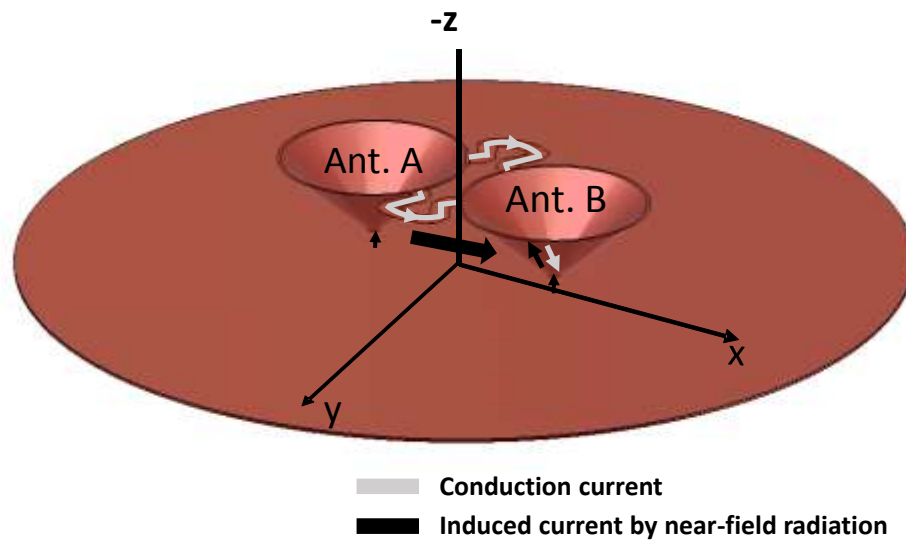


Figure 3-34. Near-field coupling cancellation for two adjacent biconical antennas using feed-forward paths. (Transmit mode demonstration when antenna A is excited)

constructively or destructively interfere with each other at certain directions and completely distort the omni-directional radiation pattern of the element in isolation. The radiation pattern of antenna A in the presence of antenna B is illustrated in Figure 1-6(b) at different frequencies. The antenna gain is normalized to the gain of the isolated antenna. It is evident that the gain of the antenna along the line connecting the two antennas ($\varphi = 0$) is dropped at all frequencies by more than 2 dB due to the shadowing effect. The feed-forward method exploits single or multiple conductive paths with appropriate configuration to connect the adjacent antennas. Figure 3-34 shows the geometry of the modified array with two conducting strips connect antenna A to antenna B. In transmit mode when antenna A is excited, a conduction current flows through these paths from antenna A to antenna B. The length and the shape of the conductive paths are designed to make the feed-forward current (excited by the conductive path) on antenna B approximately equal in magnitude and out of

phase with the induced current due to the near-field coupling. Hence, the radiation pattern of antenna A is much less affected in the presence of antenna B and each antenna in the array looks more like an element in isolation. The feed-forward paths should be placed in the plane perpendicular to the antenna polarization (horizontal plane for the antenna configuration shown in Figure 3-34) so as not to contribute to the co-pole radiation pattern. The horizontally polarized radiation from currents on the feed forward paths are canceled by that of the image currents on the ground plane in the horizontal plane. Depending on the height of the mono-conical elements there will be some cross-pol radiation along the antenna axis.

As will be shown, the phase of the coupled signal from the excited antenna to the adjacent antenna ($\angle S_{21}$) (in the absence of feed-forward paths) is a linear function of frequency. Hence to achieve coupling cancellation over a wide bandwidth, the feed-forward current should experience a path with linear phase delay with frequency similar to the phase of S_{21} plus a constant phase delay of 180° . A piece of transmission line can provide a linear phase delay response. When such a transmission line (strip over ground plane) is established between the edges of the two mono-conical antennas, the feed-forward current flows from the terminal of antenna A to the terminal of antenna B . The schematic of this feed-forward current is depicted in Figure 3-35, noting that, this is not the total current distribution on the antennas. To ensure better uniformity in the radiation pattern, two symmetric feed-forward paths are utilized. The discontinuities and loading effects at the connection points M and M' (see Figure 3-35), disturb the symmetric radial current distribution on the antennas and excite a circular current flow on the antenna surfaces and in particular at the cones' edges. Due to radiation effects, the amount of the circular current at the edge is decreased as frequency increases. At low frequencies, the circular current tends to flow along a longer

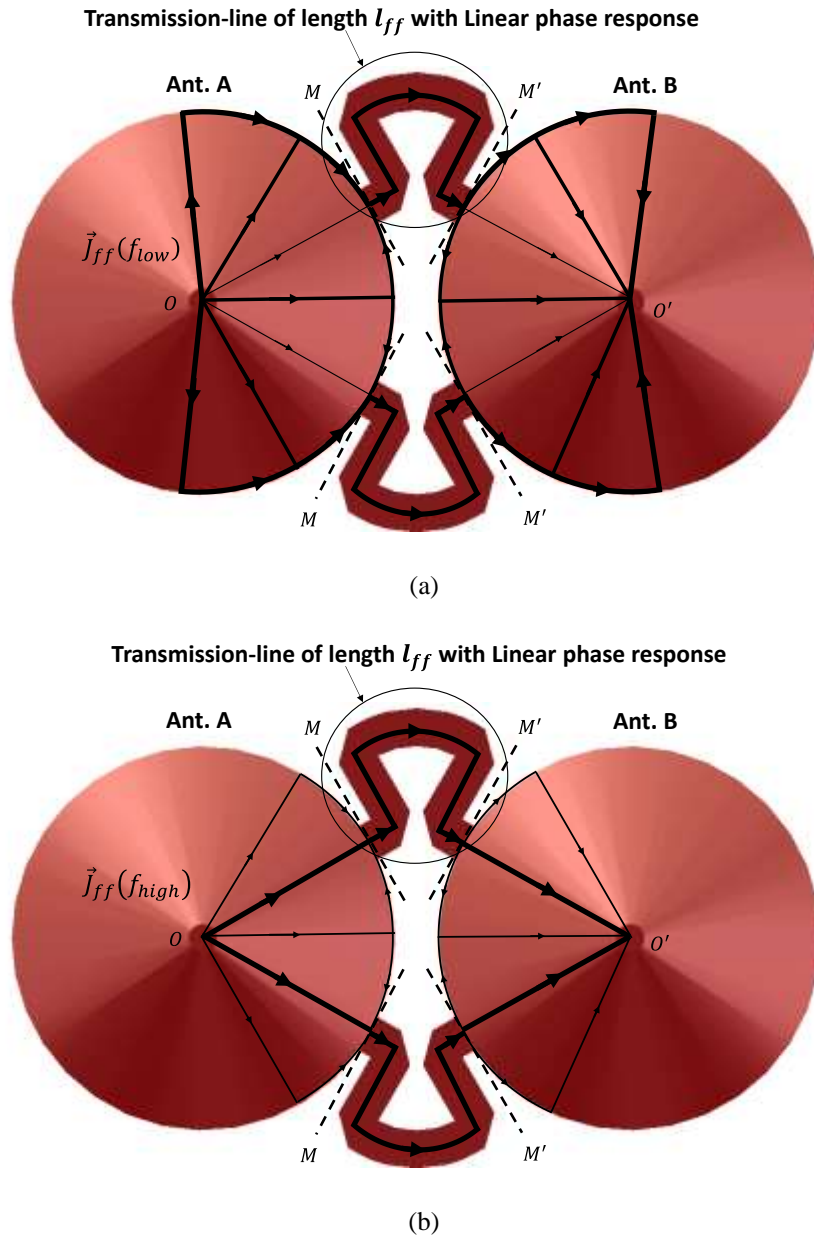


Figure 3-35. The schematic of the feed-forward current. (a) Low frequency (b) High frequency. The feed-forward current path on the antennas is frequency dependent. As frequency increases, the feed-forward current path length on the antennas is decreased.

path from the feed point and the cone edge to the feed-forward location point M . At high frequencies, the circular current at the cone edge is negligible except around the connection point of the feed-forward lines (points M and M'). Therefore, the effective length of the path

through which the high-frequency feed-forward current traverses to get to point M is shorter than the average path length for the feed forward current at low-frequency. The net result is that the phase of the current at point M has slow variations with frequency. This phase delay is determined by the dimension of the cone. A wide angle mono-conical antenna (half cone angle larger than 50°) can be designed to approximately provide the total required phase delay of 180° (90° for each antenna) to achieve wideband coupling cancellation. . To obtain 90° phase shift at the highest frequency, the slant length of each mono-conical antenna is chosen to be $\lambda_u/4$ where λ_u is the wavelength at the highest frequency is. However, this slant length may not provide the impedance match over the desired bandwidth. A mono-conical antenna with larger slant length provides wider impedance match bandwidth at the expense of reducing the feed-forward cancellation bandwidth. To demonstrate this, consider a two-element mono-conical array with cones having the slant length of $0.275 \lambda_0$ and half-cone angle of 50° . Also suppose the elements are spaced by $\lambda_0/2$ and are connected from their edges by two symmetric transmission lines. For such two-element array, the phase of the feed-forward current at point M versus frequency is obtained by a full-wave simulation and plotted in Figure 3-36. A phase response of $-120^\circ \pm 16^\circ$ over an octave bandwidth is observed. This phase delay exceeds the required 90° since the cone slant length is larger than $\lambda_u/4$. Accordingly, the length of the transmission line should be slightly smaller than the spacing between the elements. For this array, the optimum length was found as $l_{ff} = 0.4 \lambda_0$ by the full-wave simulation. The phase of S_{21} in the absence of the feed-forward transmission lines is plotted in Figure 3-37. A linear phase variation with frequency is observed. Also shown is the total phase delay of the feed-forward current denoted by φ_{ff} obtained from:

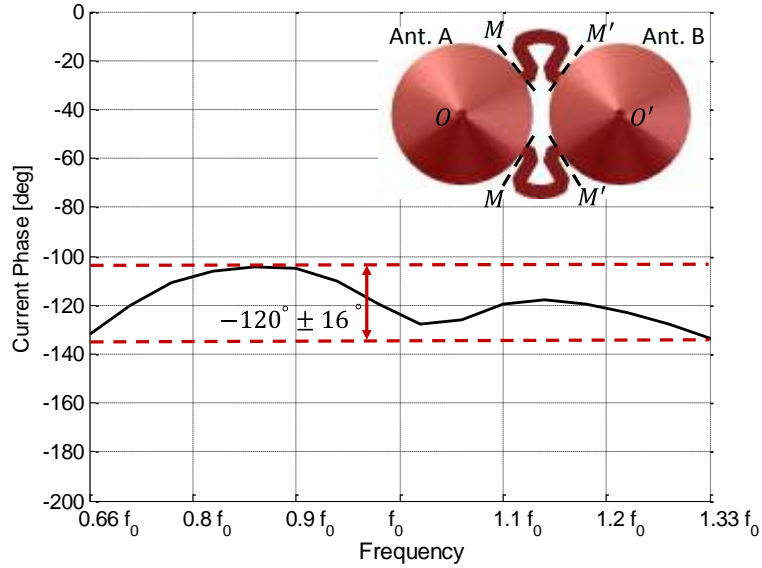


Figure 3-36. The phase of the feed-forward current at point M when antenna A is excited which is obtained by a full-wave simulation. The phase variation is less than $\pm 16^\circ$.

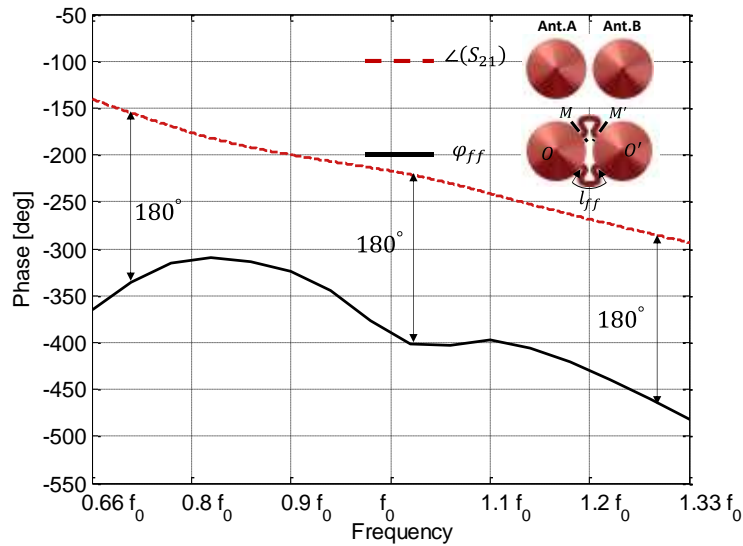


Figure 3-37. Phase of S_{21} for the two-element array shown in Figure 3-34 (red line) and phase of the feed-forward current (black line).

$$\varphi_{ff} = \arg\left(\frac{\vec{J}_M}{\vec{J}_O}\right) - \frac{2\pi f}{c} l_{ff} + \arg\left(\frac{\vec{J}_{O'}}{\vec{J}_{M'}}\right) \quad (3-93)$$

which indicates an approximate phase difference of 180° over an octave bandwidth. The

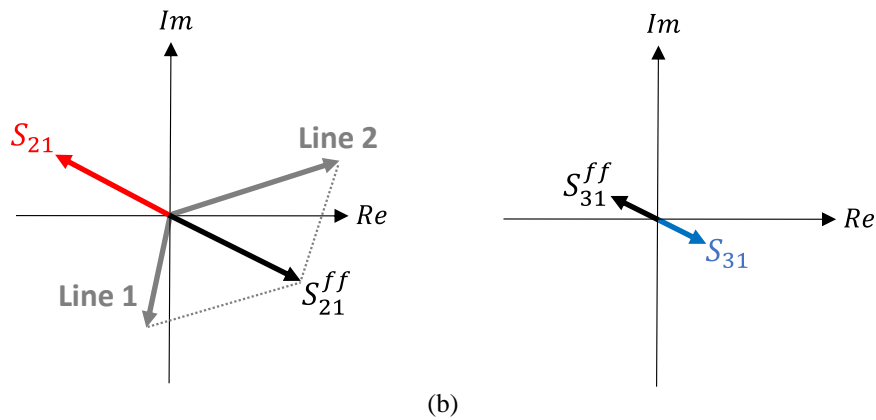
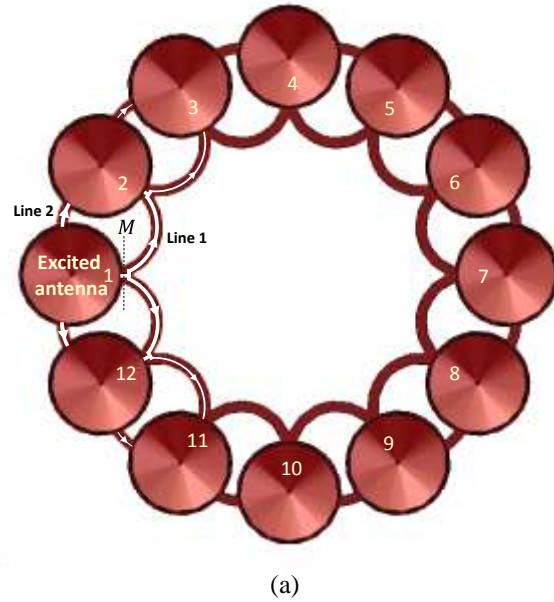


Figure 3-38. (a) The geometry of the feed-forward lines applied to a 12-element circular array of mono-conical antennas (b) vector representation of the coupling cancellation scheme by the feed-forward currents. In (b), S_{21} and S_{31} are the scattering parameters of the array before applying the feed-forward lines and S_{21}^{ff} and S_{31}^{ff} are the scattering parameters due to the feed-forward lines.

location and the width of the strips are chosen to set the magnitude of the feed-forward current in order to cancel the mutual coupling.

This technique can be extended to multiple-element arrays. The geometry of a 12-element uniform circular array of mono-conical antennas with feed-forward lines is depicted

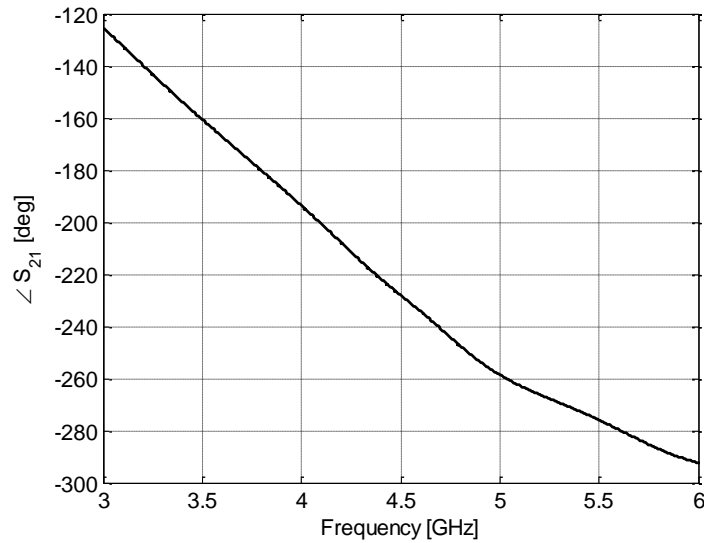


Figure 3-39. Phase of S_{21} for the 12-element circular array shown in Figure 3-38(a) before inserting feed-forward lines. Similar to the two-element array, the phase of S_{21} is approximately a linear function of frequency.

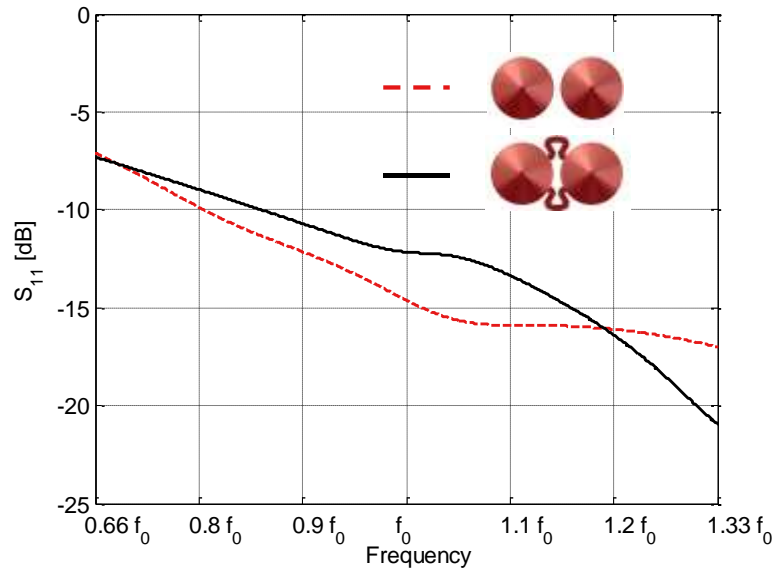
is Figure 3-38(a). The dimensions and spacing between antennas are the same as the two-element case. The phase of S_{21} for the 12-element array before applying the feed-forward technique is plotted in Figure 3-39. Similar to the two-element array, the phase of S_{21} is approximately a linear function of frequency. Since the strongest coupling occurs between two adjacent antennas, a similar feed-forward cancellation can be used. This way, however; the next strongest coupling that occurs between an element and the next element over (S_{31}) may not be reduced or may be even increased. To control this, point M for one of the feed-forward lines (line 1) is chosen to be in the middle as shown in Figure 3-38(a). This allows distribution of the feed-forward current between elements 2 and 3. Otherwise, there will be no direct path for the feed-forward current to flow from element 1 to element 3 to manage S_{31} . Choosing point M to be in the middle provides this direct path. However, the chosen length and width of line 1 to reduce S_{31} may not effectively reduce the coupling

between adjacent antennas (S_{21}). Therefore, another feed-forward line with different length and width is inserted. The length and the width of the other feed-forward line (line 2) is designed such that the vector sum of the feed-forward currents from line 1 and line 2 provides a resultant feed-forward current at the terminal of antenna 2 to cancel the near-field coupling between adjacent antennas over the desired bandwidth. In fact, two lines with different lengths and widths provide two degrees of freedom to lower both S_{21} and S_{31} at the same time. The vector representation of the cancellation scheme is demonstrated in Figure 3-38(b). Line 2 provides a feed-forward current on the adjacent antenna with larger magnitude and smaller phase delay compared to line 1 in such a way that the resultant current neutralizes the coupling current on Antenna 2. Also, the feed-forward current flows through two consecutive connected lines of type 1 and excites a current on Antenna 3 to cancel S_{31} .

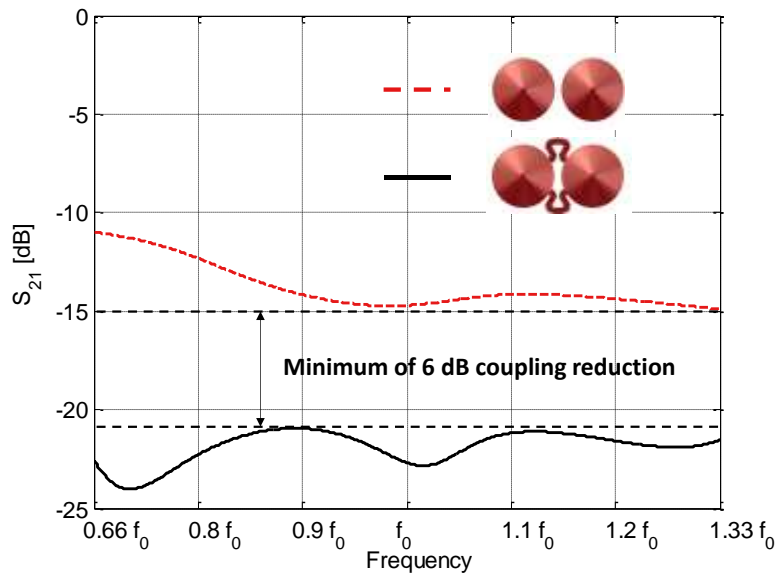
3.4.2 Simulation and Experimental Results of the Feed-Forward Coupling

In this section, first the simulation results for coupling reduction in a two-element array of mono-conical antennas using the technique described in the previous section are illustrated. Then the experimental results of applying this method to a larger circular array with 12 mono-conical elements are presented.

For two mono-conical antennas shown in Figure 3-34 with slant length of $0.275 \lambda_0$ and the cone half angle of 50° spaced by $\lambda_0/2$ at center frequency (4.5 GHz), the reflection coefficient of the excited antenna and the coupling between two antennas with and without feed-forward paths are illustrated in Figure 3-40. The coupling level is reduced by at least 6 dB over an octave bandwidth. The radiation pattern of the excited antenna (Antenna A) normalized to the gain of the isolated antenna is shown in Figure 3-41(b). A comparison



(a)



(b)

Figure 3-40. The scattering parameters of the two-element array before and after applying coupling mitigation technique. (a) Reflection coefficient (b) Coupling coefficient.

with the radiation patterns of the original array shown in Figure 3-41(a), reveals that, the gain reduction phenomenon due to the forward scattering effect is mitigated by feed-forward technique at all frequencies. The total current density on the antennas before and after

applying the feed-forward technique at $f = 0.7 f_0$ and $f = 1.3 f_0$ are depicted in

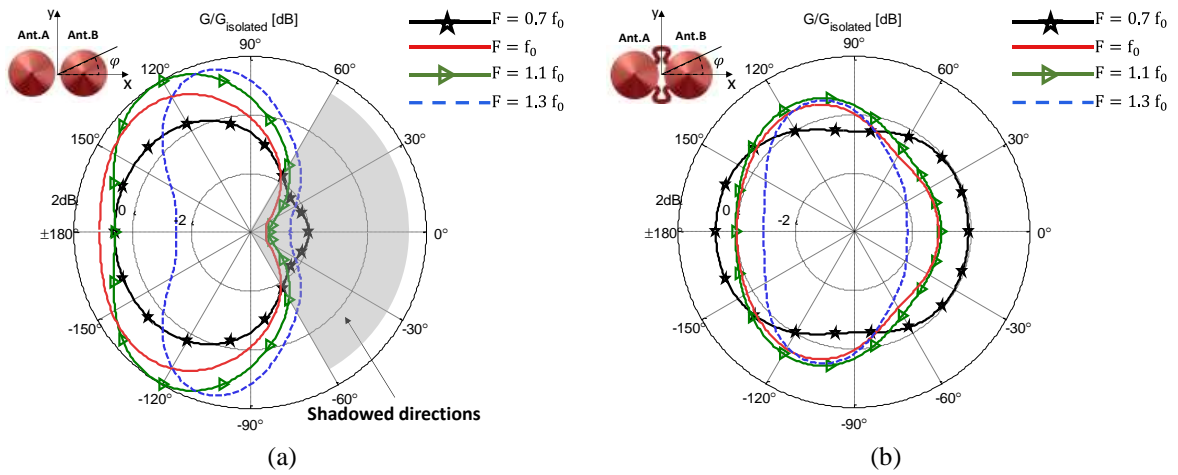


Figure 3-41. The radiation pattern of antenna (a) without the feed-forward lines, and (b) with the feed-forward lines are applied. The shadowing effect is reduced after applying feed-forward lines.

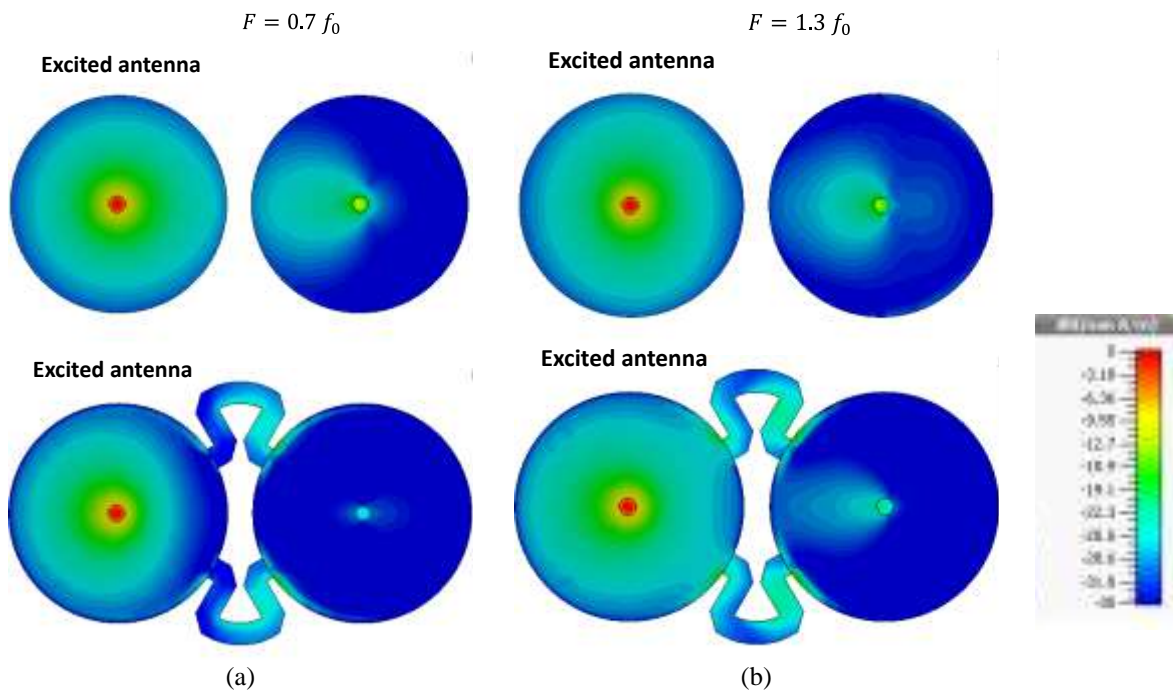


Figure 3-42. The total current intensity on the antennas before and after applying the feed-forward technique (a) low frequency (b) high frequency.

Figure 3-42. The coupling current is effectively cancelled by the feed-forward current.

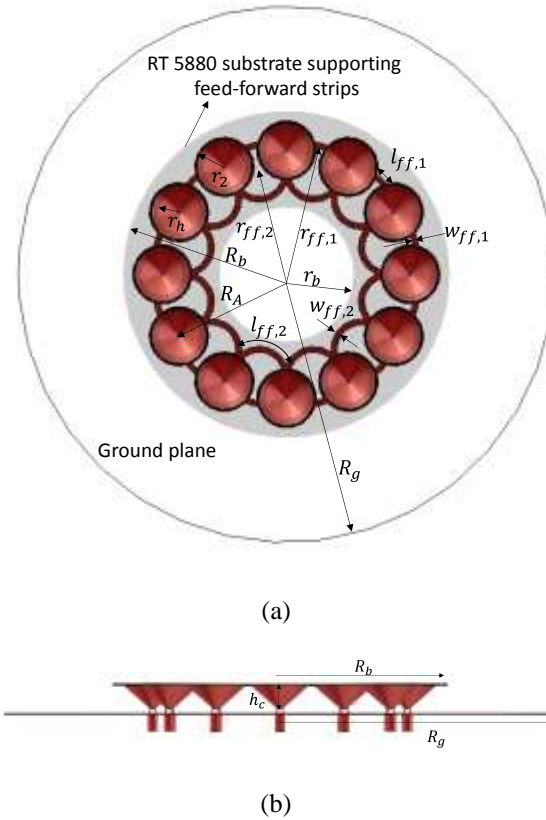


Figure 3-43. The feed-forward lines configuration applied to the 12-element circular array of mono-conical antennas. (a) Top view (b) Side view.

As mentioned earlier, the same procedure can be used for larger arrays. The structure of a 12-element circular array is depicted in Figure 3-43. The radius of the array and the inter-element spacing are λ_0 and $\lambda_0/2$ at center frequency (4.5 GHz) respectively. Two feed-forward paths of different lengths are utilized which are only applied circumferentially to the adjacent elements. One of them is chosen to be part of the circumference of a circle of radius $r_{ff,1}$ centered at the array center and the other one is a circular arc centered at a distance $r_{ff,2}$ from the array center located in the middle of the adjacent antennas. The width of the feed-forward strips and the arc radius are reported in Table 3-5. The fabricated circular antenna array is shown in Figure 3-44. The feed-forward strips are printed on 30 mil

RT/duroid 5880 mounted on the top of the whole array. The strips are then connected to the edges of the cones (antenna boundaries) by means of soldering. The current density on the antennas for the original array and the array with feed-forward lines obtained by full-wave analysis is plotted in Figure 3-45 at different frequencies which evidently demonstrates the reduction of the total excited current on the other antennas.

Table 3-5. The optimized parameters of the 12-element circular array shown in Figure 3-43

Parameter	Quantity (mm)	Parameter	Quantity (mm)
R_g	140	$w_{ff,1}$	3
R_A	64	$w_{ff,2}$	3
R_b	85	$l_{ff,1}$	7.5
r_b	35	$l_{ff,2}$	30.9
r_h	11	$r_{ff,1}$	69.1
r_c	15	$r_{ff,2}$	55

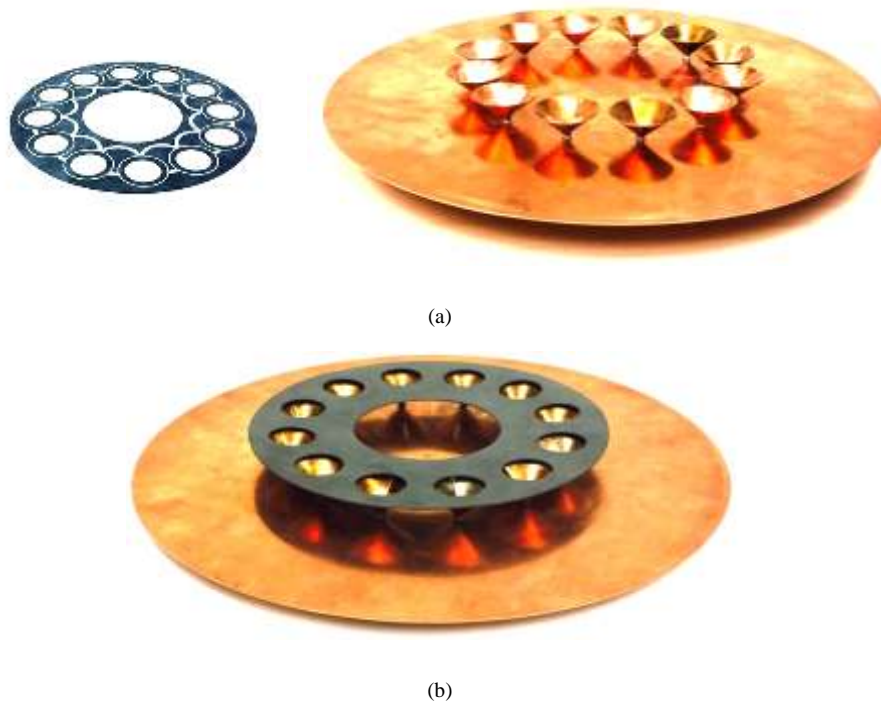


Figure 3-44. The fabricated 12-element circular mono-conical antenna array out of copper and the tin surface finished feed-forward strips printed on 30 mil RT5880. (a) Disassembled (b) Assembled by means of soldering.

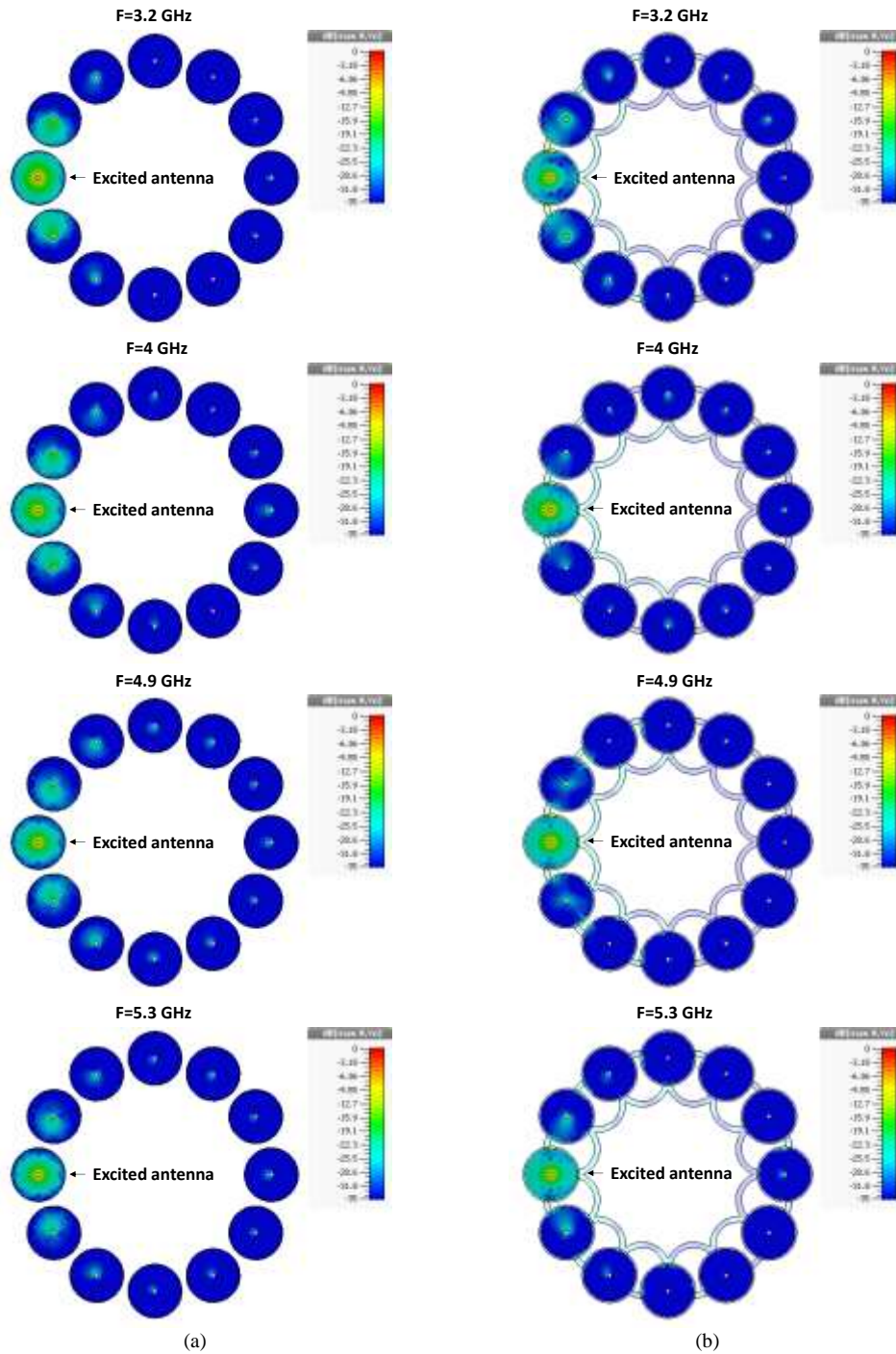


Figure 3-45. Current distribution on the 12-element circular array of mono-conical antennas obtained by full-wave simulation (a) without feed-forward paths (b) with feed-forward paths. The induced current on the other antennas due to the near-field coupling is mitigated by the excited feed-forward current.

Figure 3-46 illustrates the simulated and measured reflection coefficient and the coupling between antennas. After applying the feed-forward lines, the coupling between

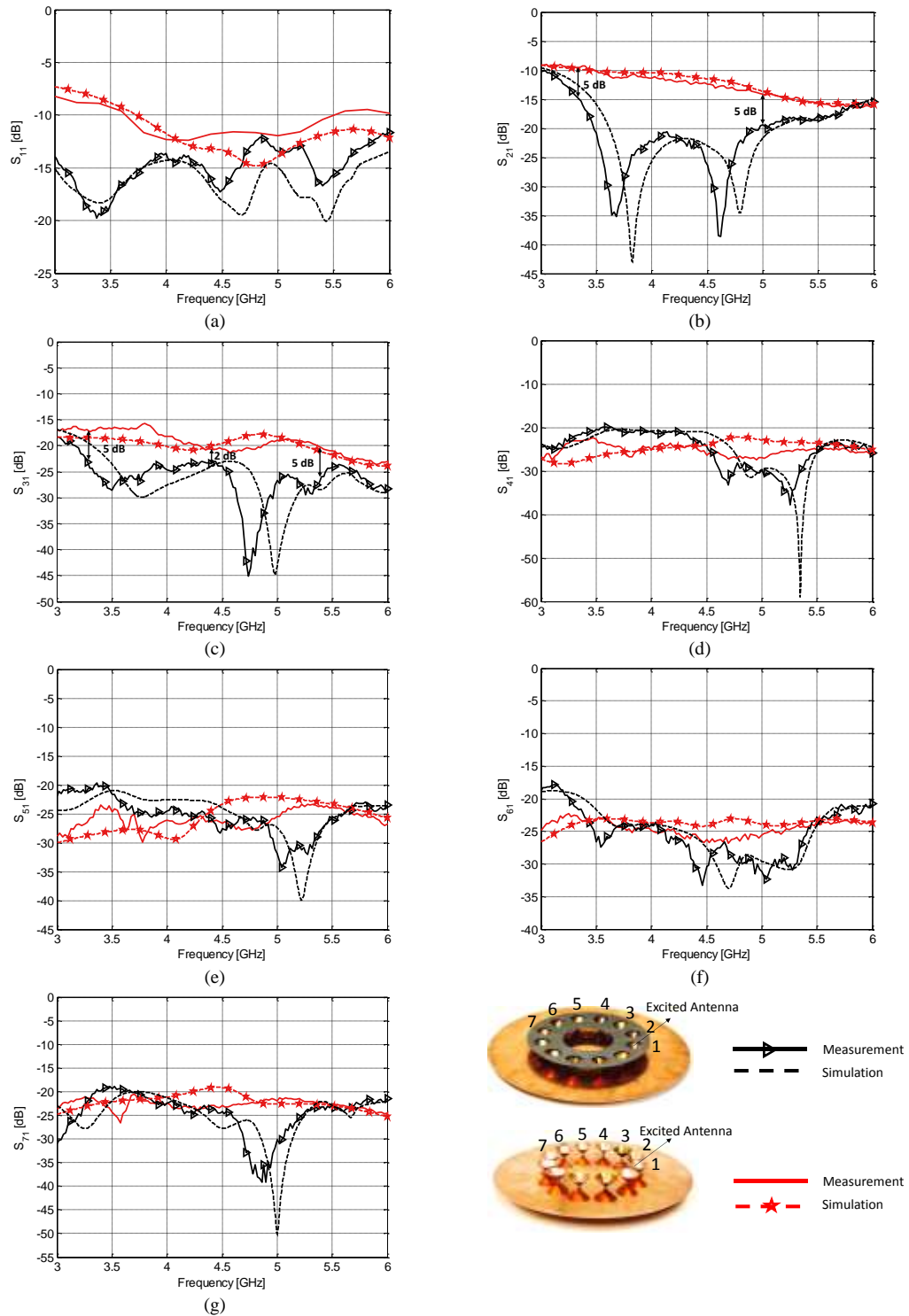


Figure 3-46. Simulated and measured scattering parameters of the 12-element circular array. (a) Reflection coefficient (b-g) Coupling coefficients.

adjacent antennas (S_{21}) is significantly reduced over 60% bandwidth (3 GHz to 5.7 GHz). A minimum isolation improvement of 5 dB is achieved from 3.4 GHz to 5 GHz. The two nulls in the graph (Figure 3-46(b)) correspond to frequencies where the length and the width of feed-forward line 1 and feed-forward line 2 happen to be in such a way so that the vector sum of $S_{21}^{ff,line1}$ and $S_{21}^{ff,line2}$ is exactly equal in magnitude and out of phase with S_{21} due to the coupling through air. The coupling between every other elements (S_{31}) is also reduced by at least 2dB over an octave bandwidth from 3 GHz to 6 GHz (more than 5 dB over the most bandwidth). Coupling from the excited antenna to all the other antennas are kept below -20 dB while the reflection coefficient is even improved as shown in Figure 3-46(a). The simulated and measured far-field radiation pattern of the excited antenna in the azimuth plane with and without applying the feed-forward paths at different frequencies are plotted in Figure 3-47. It is shown that radiation pattern of individual elements within the array is significantly more uniform once the feed-forward paths are present.

To quantify the improvement in uniformity of radiation pattern, a figure of merit is defined. The figure of merit (D_{avg}) is defined as the average gain deviation from the uniform gain of an isolated antenna. Using a discrete number of azimuthal directions:

$$D_{avg_dB}(f) = \frac{1}{N} \sum_{n=1}^N |G_{A_dB}(\varphi_n, f) - G_{0_dB}(f)| \quad (3-94)$$

is calculated at each frequency. In (3-94), $G_{A_dB}(\varphi_n, f)$ is the gain of the antenna in the presence of the other array elements in direction $\varphi_n = 2\pi n/N$ and G_{0_dB} is the gain of the isolated antenna for a mono-conical antenna and N is the number of the azimuth angles at which the antenna gain is measured ($N = 180$ in our experiment). The smaller D_{avg_dB} , the

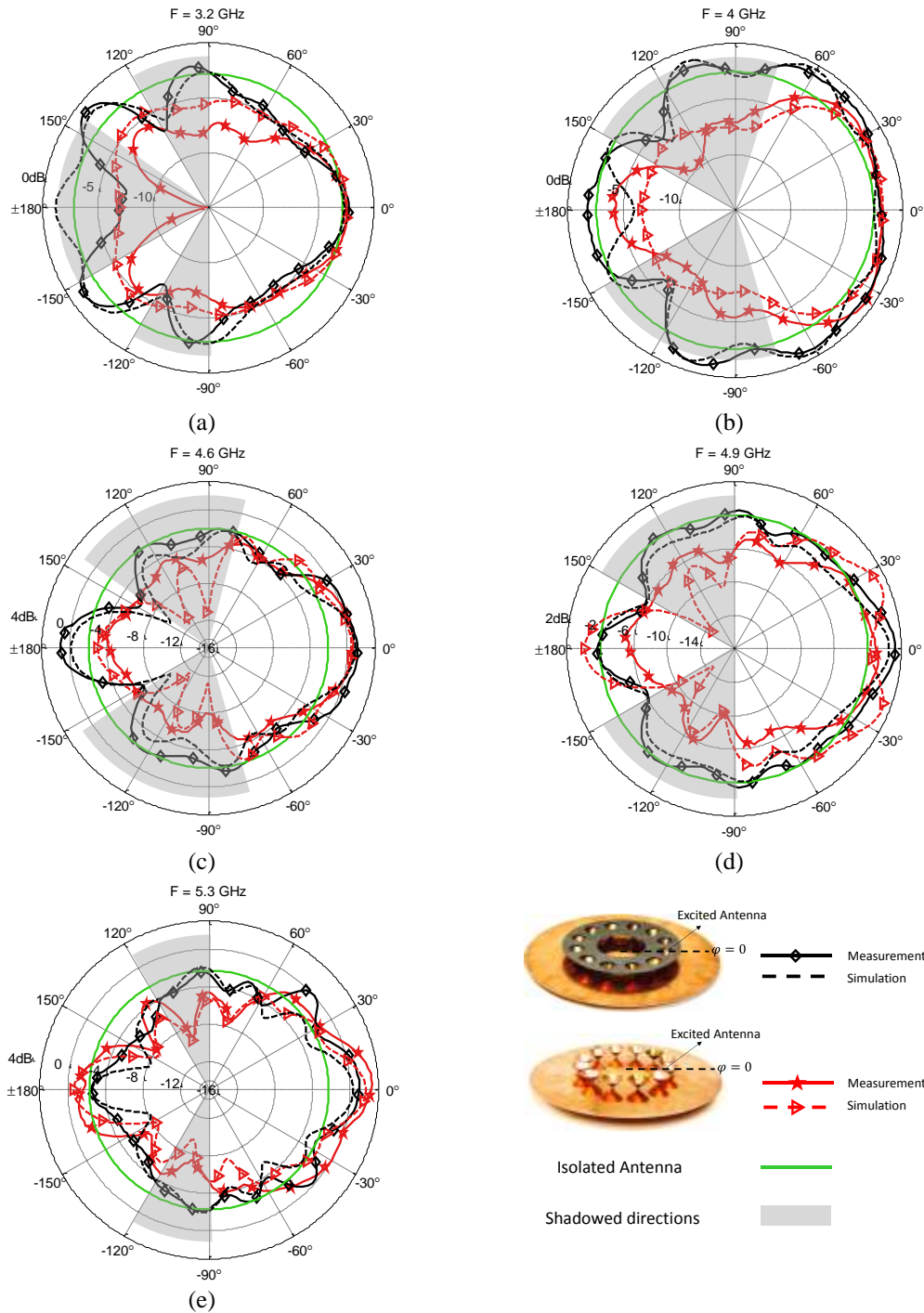


Figure 3-47. Simulated and measured radiation pattern of the deriving antenna in the circular array in the azimuth plane. The shadowing effect is reduced when the feed-forward transmission lines are introduced between the array elements. The radiation nulls are removed at all frequencies.

better is the performance of the array. The measured D_{avg_dB} versus frequency for both the array with coupling mitigation and the original array without feed-forward lines is plotted in

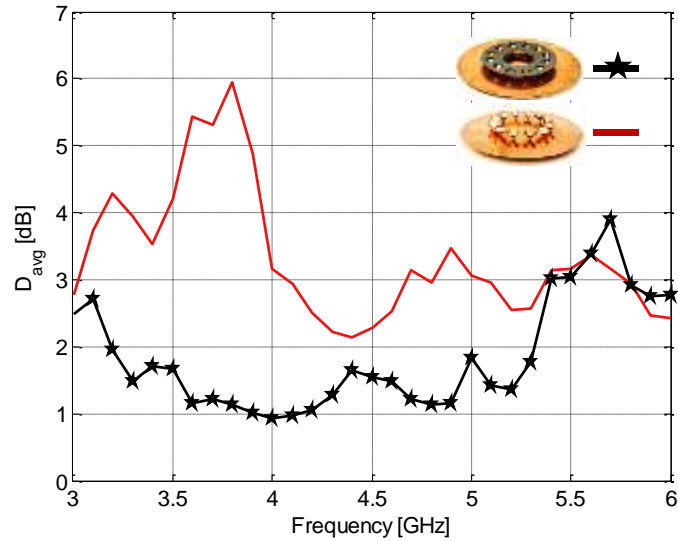


Figure 3-48. The measured average gain deviation of each antenna in the 12-element array from isolated antenna in the azimuth plane before (red line) and after (black line) applying the feed-forward paths.

Figure 3-47. It is observed that the proposed feed-forward coupling mitigation technique can significantly decrease the gain variation over a wide frequency band. The performance improvement is shown to be better 2 dB from 3.2 GHz to 4 GHz and more than 1 dB from 4 GHz to 5.3 GHz. More importantly, the nulls in the radiation pattern at all frequencies and all angles have been removed.

3.5 Experimental Results of CNSM

An experimental study is conducted to examine the sensitivity of the algorithm to the systematic errors. The measurement setup is shown in Figure 3-49. A 12-element circular mono-conical antenna array of diameter $d = 1.65 \lambda$ is considered as the receiving array. The impinging plane waves are approximately generated by directive horn antennas of maximum dimension $D \cong 3\lambda$, which are placed at a distance of $L \cong 66\lambda$ from the receiver. This

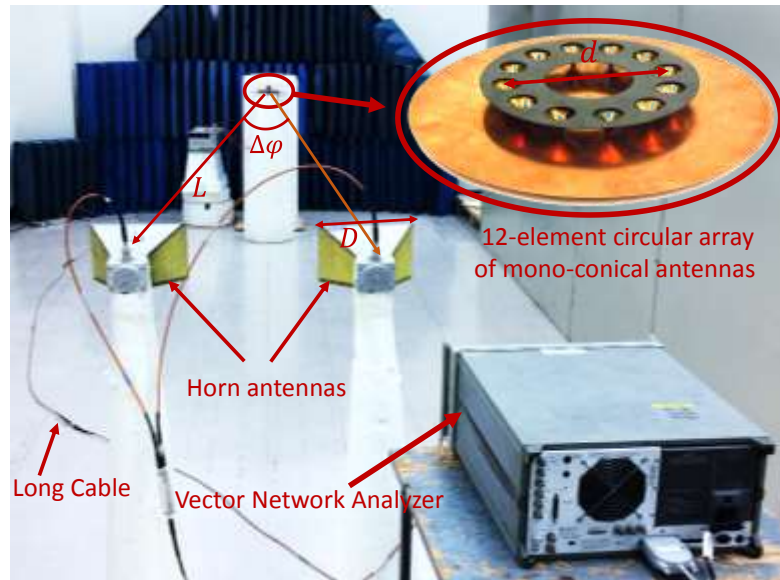


Figure 3-49. The experimental setup consisting a two-port vector network analyzer and a 12-element circular array of diameter $d = 1.65 \lambda$ composed of mono-conical antennas. Directive horn antennas of maximum dimension $D = 3 \lambda$ are placed at a distance of $L = 66 \lambda$ from the receiver to create impinging plane waves on the circular array.

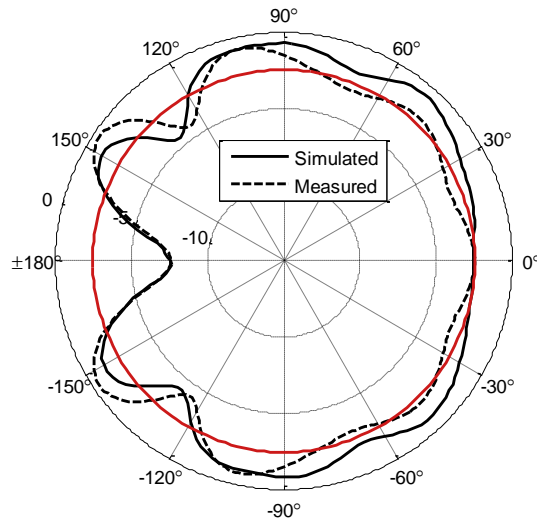


Figure 3-50. The simulated and measured radiation patterns, $|l_{eff}(\varphi)|$, of each mono-conical antenna element of the circular array shown in Figure 3-49 in azimuth plane. The red line represents the radiation pattern of the isolated antenna.

distance ensures that the receiver is in the far-field of the sources ($L > 2D^2/\lambda$) and that constant phase fronts are formed over the receiver aperture.

It is important to point out that the radiation pattern of each array element, once put in the array configuration, is different from its pattern in isolation due to the mutual couplings and shadowing effects. This deformation is the major source of error in majority of array signal processing methods. Although, there exist physical techniques for mutual couplings mitigation in antenna arrays, however, these undesired effects cannot be completely eliminated and need to be captured in the processing. The simulated and measured realized gain of each mono-conical antenna in the azimuth plane denoted as $|l_{eff,1}(\varphi)|$, is illustrated in Figure 3-50 which deviates from the isolated antenna by more than 4-dB in some directions. As mentioned in Section 3.3, in view of (3-45) and (3-79), this effect is taken into account in calculation of \mathbf{W}_n and $\mathbf{W}_{\varphi_{null}^1, \varphi_{null}^2}$ in the first and in the second step of the algorithm respectively.

Another uncertainty arises from unequal realized gain and phase characteristics of antennas and the error in the antenna locations due to the fabrication imperfections. These errors result in the performance degradation of the algorithm as will be discussed later in this section.

In a real array system, each antenna should be connected to a separate receiver to measure the received signal at each antenna terminal coherently; thereby, each receiving path encompassing the receiver and the antenna is required to be calibrated to take care of their imbalances. However, the purpose of this experiment is to investigate the performance degradation of the algorithm arising from the imperfect estimation of the array manifold due to the fabrication errors in the antenna array assembly itself and not the differences in the response of the receivers. Therefore, to facilitate the measurement, a two-port Vector Network Analyzer (VNA) and a SP12T switch are used instead of 12 synchronized receivers.

Port 1 of the VNA is connected to a divider to distribute power among sources (horn antennas) and port 2 is connected to the input of the switch using a long cable. Each output port of the switch is then connected to an antenna element. This setup, due to the synchronized transmitter-receiver pairs inside the VNA, allows for coherent processing of the received signals from each array element through staggered antenna switching.

Two horn antennas (used as two sources) with close angular separation with reference to the center of the circular array are considered (See Figure 3-49). Adjusting $SNR_1 = SNR_2 = 20$ dB, for different angular separations, the DoA estimation error defined as:

$$Error = \frac{1}{2BW} \sum_{n=1}^2 |\varphi_n^{Estimated} - \varphi_n^{Actual}| \quad (3-95)$$

as a function of correlation coefficients between sources is computed and plotted in Figure 3-51. The same scenario is also simulated assuming that the array manifold is impeccable, and the results are shown in Figure 3-52. Comparing the graphs in Figure 3-51 with those of Figure 3-52, it is observed that for $\Delta\varphi = 0.15$ BW, the systematic errors have resulted in an increase of the estimation error from 0.7% to 1% for $\rho_{12} = 0.2$ and from 1.2% to 4% for $\rho_{12} = 0.8$. This degradation is resulted from the antennas dislocation and the antenna patterns discrepancy. The antenna dislocation error is measured to be ± 0.2 mm which translates to $\pm 1.1^\circ$ phase error at the operating frequency.

In addition, the estimation error versus SNR for the same experiment obtained from the measurement for $\rho_{12} = 0.5$ is examined and the results are illustrated in Figure 3-53. The method practically provides estimation of DoAs of the signals with angular separation as small as $\Delta\varphi = 0.15$ BW and SNR as low as SNR = 10 dB with less than 3.5 % error.

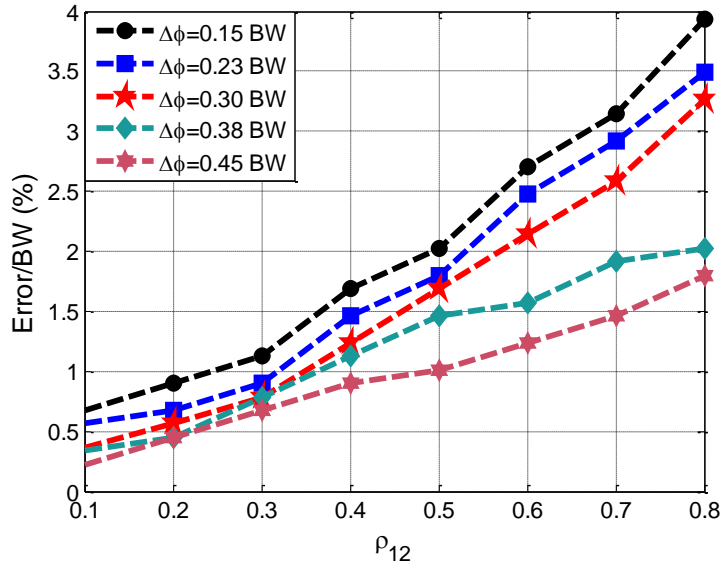


Figure 3-51. The percentage of error of the estimated DoAs normalized to the half power beamwidth versus correlation coefficient for different angular separation of signals obtained from the measurement setup shown in Figure 3-49. In this experiment, $\text{SNR}_1 = \text{SNR}_2 = 20\text{dB}$.

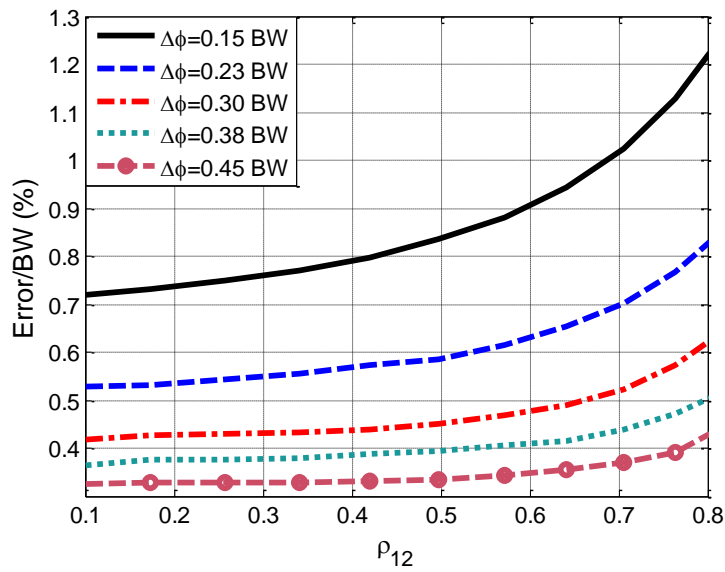


Figure 3-52. The percentage of error of the estimated DoAs normalized to the half power beamwidth versus correlation coefficient for different angular separation of signals obtained from the simulation of the same scenario as the one shown in Figure 3-49 considering a circular array without any imperfection. In this simulation, $\text{SNR}_1 = \text{SNR}_2 = 20\text{dB}$.

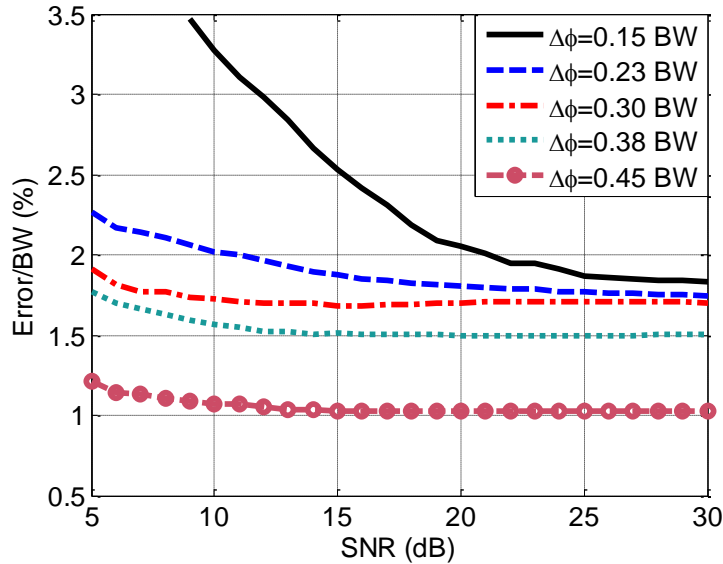


Figure 3-53. The percentage of error of the estimated DoAs normalized to the half power beamwidth versus SNR for different angular separation of signals computed from the measured data using the measurement setup shown in Figure 3-49. In this experiment $\rho_{12} = 0.5$.

3.6 Conclusion

In this chapter, first an iterative algorithm referred to as ASSIA for capturing the directions of arrival, magnitudes and phases of all correlated or uncorrelated signals impinging on a receiver with angular spacing larger than the array beamwidth was presented. ASSIA was demonstrated to be able to capture signals whose magnitude are spread over a wide dynamic range. This algorithm is implemented for a radio with circular array of antennas, each of which are connected to a coherent receiver. It is shown that such radio receiver is capable of suppressing interfering signals in complex multipath environments without a priori knowledge regarding the directions of arrivals of the desired or interference signals. The proposed approach for interference cancellation is proved to be efficient using

a statistical analysis in an urban environment with rich multipath propagation characteristics. Then, a Closely-spaced Nulls Synthesis Method (CNSM) for super-resolution DoA estimation of correlated signals was introduced to achieve a spatial resolution better than array beamwidth. In conjunction with ASSIA, the proposed method provides superior performance compared to other techniques such as Matrix Pencil Method and Maximum Likelihood method for spatially resolving correlated signals. Experimentally examining its sensitivity to the systematic errors, ASSIA-CNSM is shown to be practically efficient for moderate and low SNR regimes. Moreover, the proposed method is shown to be less computationally expensive compared to ML-based techniques.

Moreover, a physical approach based on exciting a feed-forward current between adjacent antennas of an array was introduced to reduce the undesirable effects of the near-field coupling and shadowing effects among elements of dense array antennas. The theory and simulation results for mono-conical array elements were discussed. The technique was successfully applied to a 12-element circular array of mono-conical antennas to mitigate the adverse effects of mutual coupling. It was shown that the radiation pattern deviation from omni-directional pattern for each element within the array is decreased considerably over a very wide frequency range. Another important achievement is removal of radiation nulls of the array elements at all frequencies and all directions.

CHAPTER 4 Subsurface Communication

4.1 Overview

Logging-While-Drilling (LWD) using a set of sensors at or near the drill bit to acquire data in real time in drilling process has become an industry standard. This technique is used to direct high-angle and horizontal drilling to ensure cost-effective use of expensive drilling rigs. The collected data includes rock mechanics and acoustics, soil/rock density, gamma ray emission, nuclear magnetic resonance responses, and resistivity measurements. Also, Measurement While Drilling (MWD) tools provide essential information about the condition at the tip of the drill such as temperature, pressure, vibration, rotation speed of the drill bit, etc. to prevent tools failure. A robust and real-time data communication from downhole to the surface and vice-versa is of course needed to transfer the data to the surface for logging. LWD/MWD data transmission is currently carried out by different techniques such as acoustic mud pulse telemetry [4], [5] electromagnetic wireless links [8], [7], and wired drill pipe technology [6]. Mud-pulse telemetry provides a very low data rate and is not reliable. Electromagnetic wireless telemetry provides faster data transmission compared to acoustic mud pulse telemetry but comes short in deep boreholes due to significant signal attenuation through the ground formation layers. Wired drill pipe technology utilizes electrical cables built into the drill pipe. This technology offers much faster data transmission but has not turned to common practice as the required equipment is still expensive and is prone to failure.

In this chapter, a novel low-cost signal transmission technique which is tailored for data communication in drilling process is introduced [125, 126, 127, 128]. In hydraulic-rotary drilling, as shown in Figure 1-7, a downhole turbine motor is used for rotating the drill bit at the bottom of the drill pipe by hydraulic pressure. The hydraulic power is provided by the drilling fluid flowing through the drill pipe where it then carries the cuttings back to the surface through the annular space between the drill pipe and the sides of the borehole. Since the mud has a much higher index of refraction than the surrounding soil, the drill pipe coated with the drilling mud can be used as a Single-Conductor-Transmission-Line (SCTL) which is known to support TM surface waves. Such surface waves propagate along the metallic pipe and do not experience spherical wave propagation path-loss. To excite TM waves on SCTLs, specific launchers from regular transmission lines are required. Traditional launchers, such as coaxial horns, are large 3-D structures. To keep the attenuation underground low, the lower portion of electromagnetic spectrum at HF band must be considered. Therefore, the size of the traditional launchers becomes prohibitively large for the application at hand. In this chapter a novel miniaturized low-profile launcher of dimensions smaller than $0.005\lambda \times 0.005\lambda \times 0.03\lambda$ that can

4.2 Surface Wave Propagation along the Drilling Pipe

In this section, an analytical study for estimation of attenuation rate and propagation constant of surface waves supported by mud-coated drill pipes as a function of frequency and dielectric properties of mud and the surrounding soil/rock is presented. Consider a metallic cylinder coated with a uniform lossy dielectric layer (mud) immersed in another lossy medium (soil/rock) as shown in Figure 4-1. It is well-known that dielectric coated metallic cylinders

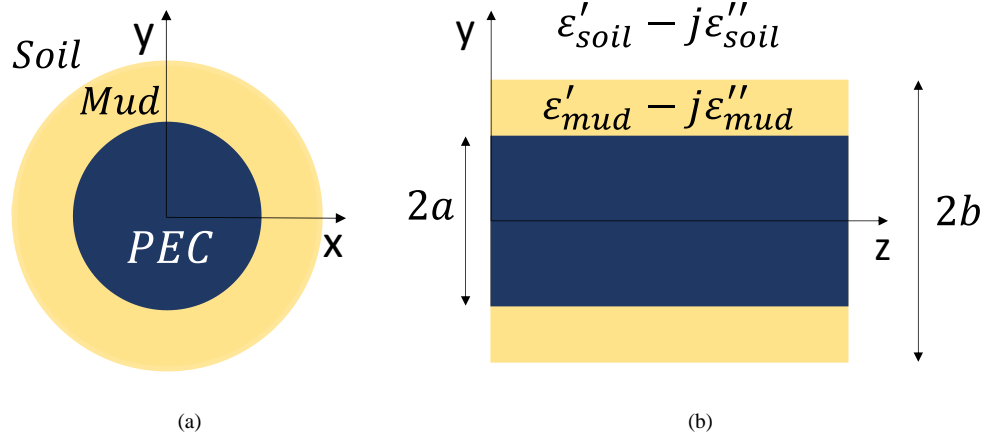


Figure 4-1. The geometry of the cylindrical conductor coated with a lossy dielectric (mud) immersed in another lossy dielectric medium (soil). (a) Cross section view, (b) Side view.

can support TM^z surface waves [107], [108]. Using the standard method of separation of variables, it can easily be shown that this structure can support the dominant TM^z surface wave mode provided that the following transcendental equations render a solution for the propagation constant in z-direction denoted by $\beta_z = \beta_z^{mud} = \beta_z^{soil}$:

$$\frac{K_0'(\alpha_\rho^{soil} b)}{K_0(\alpha_\rho^{soil} b)} = \frac{J_0'(\gamma_\rho^{mud} b) N_0(\gamma_\rho^{mud} a) - J_0(\gamma_\rho^{mud} a) N_0'(\gamma_\rho^{mud} b)}{J_0(\gamma_\rho^{mud} a) N_0(\gamma_\rho^{mud} b) - J_0(\gamma_\rho^{mud} b) N_0(\gamma_\rho^{mud} a)} \quad (4-1)$$

$$\beta_z^2 = \omega^2 \mu_{mud} \epsilon_{mud} - (\gamma_\rho^{mud})^2 \quad (4-2)$$

$$\beta_z^2 = \omega^2 \mu_{soil} \epsilon_{soil} + (\alpha_\rho^{soil})^2 \quad (4-3)$$

where α_ρ^{soil} and γ_ρ^{mud} are the radial attenuation constants in soil and mud respectively. In (1), J_0 , N_0 , and K_0 are the zeroth order Bessel function of the first kind, second kind, and the modified Bessel function of the second kind respectively.

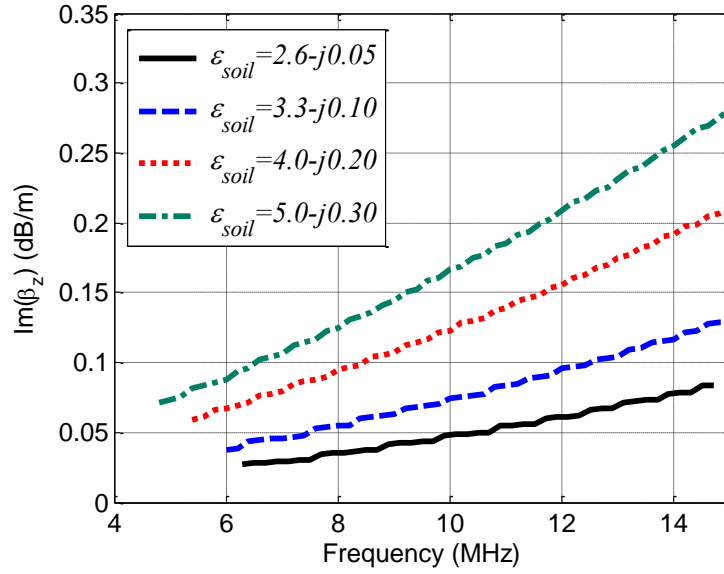
Table 4-1. The relative dielectric constant of soil/rock for low moisture contents from 1 MHz to 15 MHz.

Moisture content of soil/rock	Relative dielectric constant
0% (dry)	$2.6 - j0.05$
~1%	$3.3 - j0.1$
~2%	$4 - j0.2$
~3%	$5 - j0.3$

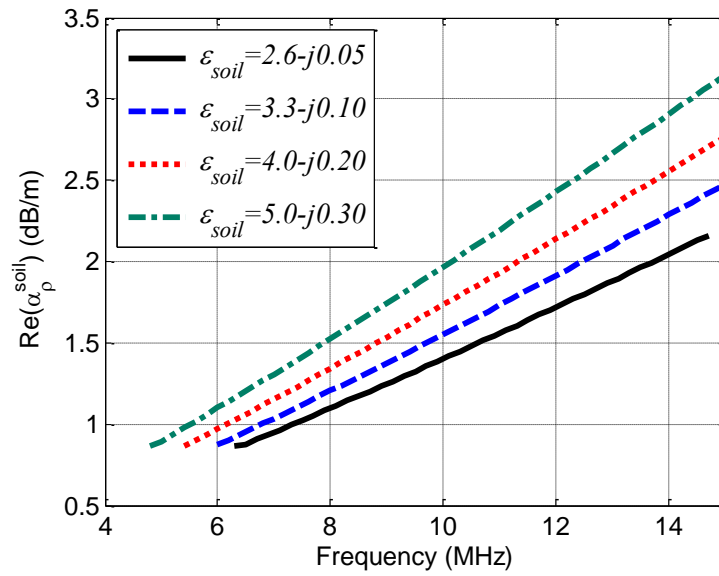
The permittivity of the water-based drilling mud as a function of frequency (1 MHz < f < 15 MHz) is given by [9]:

$$\varepsilon_{mud}(f \text{ (MHz)}) \cong \varepsilon_0 [80 f^{-0.24} - j 2000 f^{-0.86}] \quad (4-4)$$

Solving (4-1)-(4-3) for β_z , α_ρ^{soil} and γ_ρ^{mud} numerically, considering a drill pipe of radius $a = 5 \text{ cm}$ and a borehole of radius $b = 12 \text{ cm}$, the imaginary part of β_z (which represents attenuation in z-direction) and the real part of α_ρ^{soil} versus frequency for different dielectric constants of the background soil/rock are plotted in Figure 4-2(a) and Figure 4-2(b) respectively. It should be emphasized that for low moisture contents, the permittivity of soil/rock from 1 MHz to 15 MHz is almost constant and is given in Table 4-1. It is found that, the attenuation in z- direction is increased with frequency as can be inferred from Figure 4-2(a). The reason is that the electrical thickness of the mud layer around the drill pipe represented by $\gamma_\rho^{mud}(b - a)$ is increased with frequency and, thereby, the electric field is more bounded within the mud layer at high frequencies compared to low frequencies. Therefore, the operation frequency is chosen to be at lower frequencies. If the drilling mud is of higher conductivity, then the attenuation rate increases. For example if the conductivity of the drilling fluid is increased by a factor of 10 (from $\sigma_{mud} = 0.1 \text{ S/m}$ to $\sigma_{mud} = 1 \text{ S/m}$), while the conductivity of the surrounding soil is fixed, then the attenuation constant (imaginary part of β_z) increases by a factor of 1.9 which corresponds to attenuation per unit



(a)



(b)

Figure 4-2. (a) The imaginary part of β_z and (b) the real part of α_p^{soil} versus frequency for different humidity conditions of the background soil: $0.05 < \epsilon''_{soil} < 0.3$ which corresponds to $15\mu\text{S} < \sigma_{soil} < 100\mu\text{S}$ at 6 MHz.

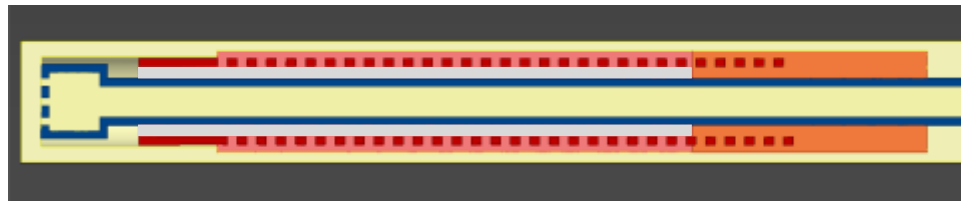
length increase by a factor of 1.9. The surrounding medium is usually rock with very low moisture content. However, if the drilling path happens to be in a soil with higher moisture content, then the wave experiences higher attenuation. For the given dimensions, if the

conductivity of the soil is increased by a factor of 10 (from $15 \mu S/m < \sigma_{soil} < 100 \mu S/m$ to $150 \mu S/m < \sigma_{soil} < 1000 \mu S/m$), then the attenuation rate increases by a factor of 5.2 for the lower bound to 6.8 for the upper bound.

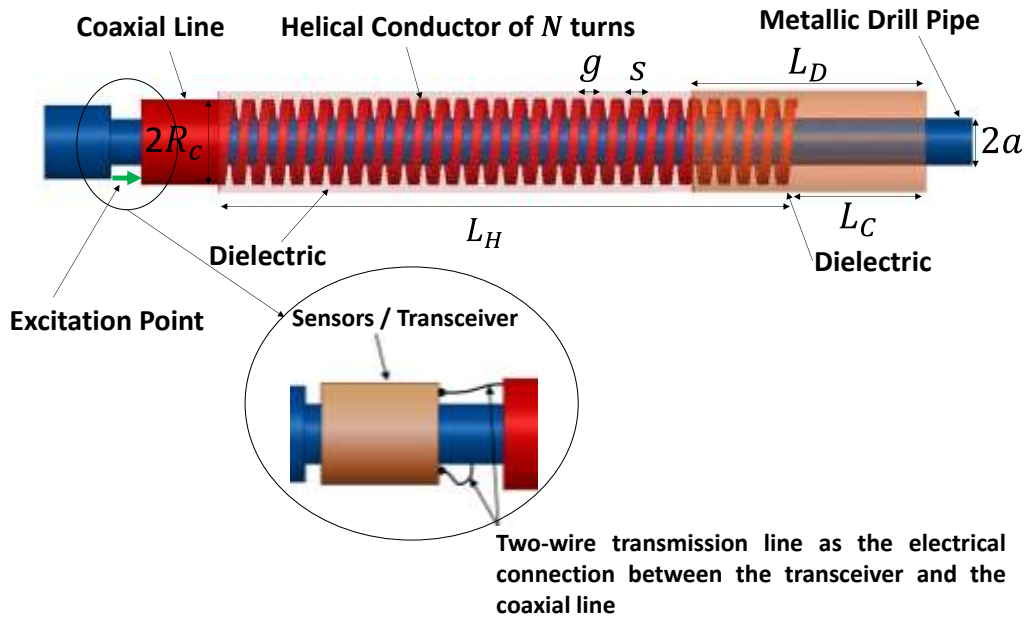
To excite a TM^z surface wave on this line, a compact launcher with small transvers electrical dimensions is required to be confined within the limited available space inside the borehole as will be discussed in the next section.

4.3 Compact Surface-Wave Launcher at HF Band

Surface wave propagation on a SCTL was first introduced by Goubau in 1960 [106, 109, 111]. To excite surface waves, he used a coaxial horn structure. The diameter of the horn-shape launcher proposed in [109] is, however, very large compared to the wavelength. Since then, other surface wave exciters have been reported [110] which have similarly large transverse electrical dimension. These conventional launchers cannot be accommodated in standard boreholes and thus are not suitable for the problem at hand. The structure of the proposed compact launcher is shown in Figure 4-3. The launcher consists of an open-ended helical conductor of small diameter concentric with the metallic drill pipe. The open side of the helical conductor is loaded by a cylindrical dielectric. The dielectric embedded between the drill pipe and the helical conductor is for mechanical support. Feeding by a coaxial line (see Figure 4-3), the launcher is basically designed to create a transition from TEM mode to TM^z mode on the SCTL and to provide impedance matching between the two types of the wave. As the signal propagates from the coaxial line to the helical line, a component of the electric field is established in the gap between consecutive loops of the helix along the



(a)



(b)

Figure 4-3. The proposed low-profile surface wave launcher. (a) Cross-section side view inside the borehole (b) launcher side view.

direction of propagation. Also, an axial magnetic field is excited due to the circulating current in the helix and on the inner conductor. Thus, the wave mode along the helix is a hybrid mode (combination of TM^z and TE^z) which is then partially converted to TM^z on the SCTL. The equivalent circuit model of this transmission line (cylindrical conductor concentrically surrounded by a helix) is illustrated in Figure 4-4. The capacitor C_1 represents the capacitance between the inner conductor (drill pipe) and the helix and the inductor L_1 represents the

Table 4-2. The optimized values of the launcher dimensions shown in Figure 4-3

Parameter	Quantity	Parameter	Quantity
L_H	160 cm	s	2.5 cm
L_D	80 cm	g	2.8 cm
L_C	30 cm	R_c	10 cm

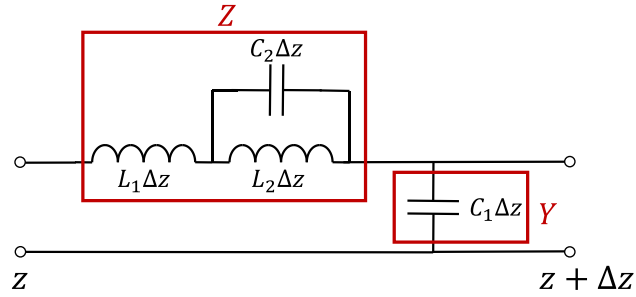


Figure 4-4. The equivalent circuit model of the launcher shown in Figure 4-3.

inductance due to the axial current on the inner conductor and on the helix, which generates a circular magnetic flux density. The capacitor C_2 models the capacitance between two consecutive loops of the helix and the inductor L_2 models the inductive effect of the circular current on the helix and on the inner conductor resulting in an axial magnetic flux density. The propagation constant and the characteristic impedance of this transmission line denoted by $\gamma_{launcher}$ and $Z_{launcher}$ are, respectively, given by:

$$\gamma_{launcher} = \sqrt{YZ} = \omega \sqrt{\frac{C_1(\omega^2 L_1 L_2 C_2 - L_1 - L_2)}{1 - \omega^2 L_2 C_2}} \quad (4-5)$$

$$Z_{launcher} = \sqrt{\frac{Z}{Y}} = \sqrt{\frac{L_1 + L_2 - \omega^2 L_1 L_2 C_2}{C_1(1 - \omega^2 L_2 C_2)}} \quad (4-6)$$

which resembles a slow wave structure. The term $\sqrt{1 - \omega^2 L_2 C_2}$ developed in the denominator of (5) and (6) due to the capacitor C_2 and the inductor L_2 allows quite large variations for $\gamma_{launcher}$ and $Z_{launcher}$ which in turn, if adjusted appropriately, makes it

possible to provide wave and impedance transition from TEM^z on the coaxial line to TM^z on the SCTL at very low frequencies which is not feasible in the absence of L_2 and C_2 . Moreover, the generated electric field in z-direction between adjacent loops of the helix which is required to excite TM^z on the SCTL further assists this transition.

Similar to other transition configurations, such as coaxial to waveguide transitions, the transition mechanism of the proposed topology is, however, very complicated and cannot be explored analytically. Full-wave simulation is, thus, needed to obtain the optimized values of the length and the pitch of the helix. Finite Difference Time Domain (FDTD) method is used for the full-wave analysis. The full-wave simulation and optimization is performed for the SCTL which is terminated by the proposed launcher at both ends. Since the extent of the wave interaction between the launcher and the SCTL reaches about one wavelength on the SCTL, the length of the SCTL in the full-wave simulation should be large enough so as to exclude the loading effect of the launchers on each other. Therefore, a line of length $10\lambda = 300m$ is considered in the full-wave domain. The simulation domain is truncated at a distance of about one wavelength from the structure in the surrounding soil by PML boundary. The launcher dimensions are listed in Table. II. The helical conductor is loaded by a ceramic dielectric (CaMgTi) with $\epsilon_r = 20$. The current distribution on the helical conductor and on the inner conductor (drill pipe) is illustrated in Figure 4-5(a) and Figure 4-5(b) respectively. A current distribution comprising a circular component in φ -direction and an axial component in z-direction exists on the helix and on the inner conductor as well. The radial and the axial electric field around the launcher is depicted in Figure 4-6(a) and Figure 4-6(b) respectively. With reference to Figure 4-6(b), the generated electric field in z-direction between the adjacent loops of the helix is quite large. The magnitude of the radial

electric field denoted by E_ρ along the SCTL for different dielectric constants of the soil

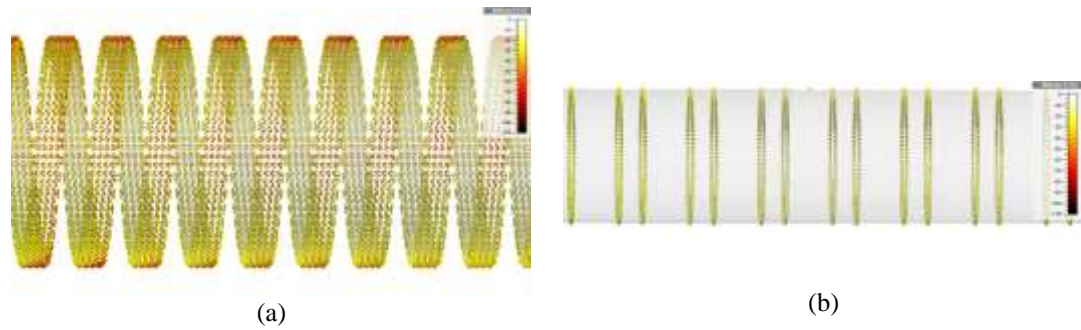


Figure 4-5. The current distribution on the launcher (a) helical conductor, (b) inner conductor (drill pipe).

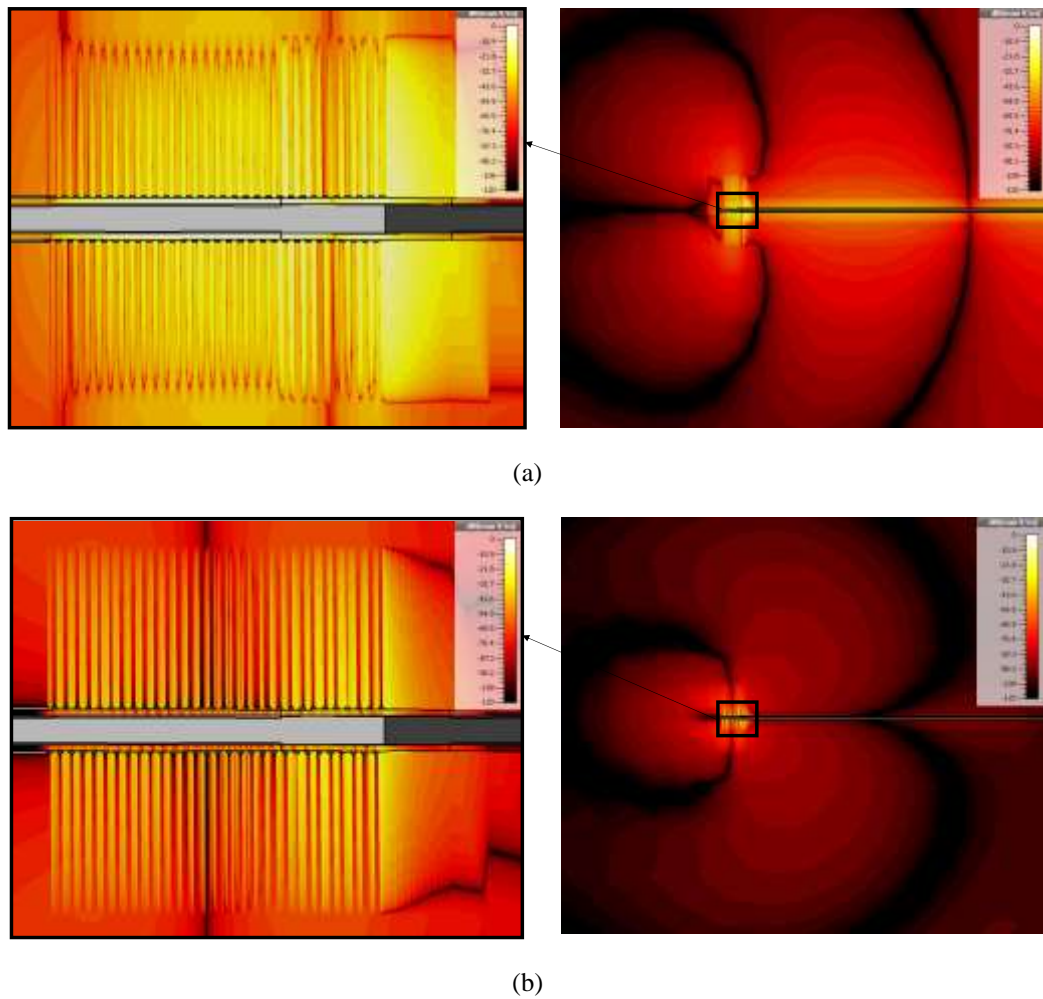


Figure 4-6. The electric field around the launcher. (a) Radial (E_ρ), (b) axial (E_z).

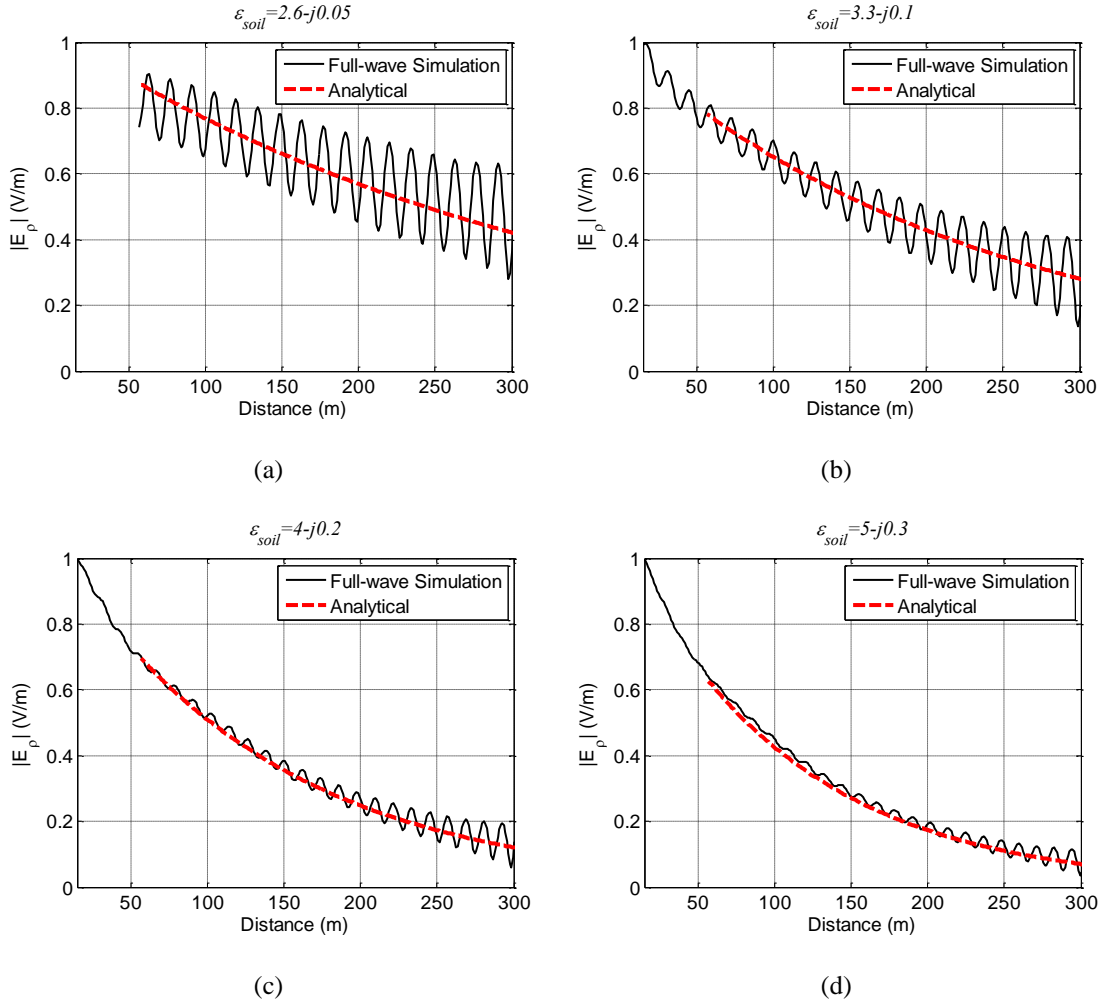
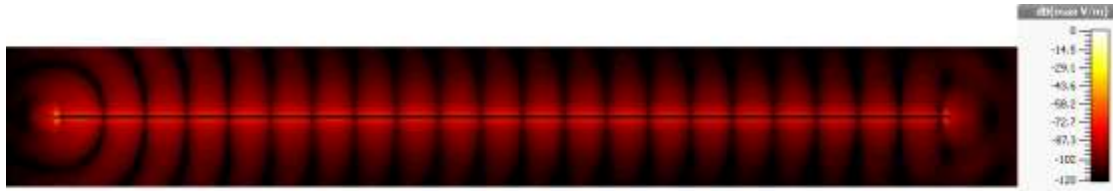


Figure 4-7. Normalized $|E_p|$ on the SCTL for different soil moisture conditions. (a) $\epsilon_{soil} = 2.6-j0.05$, $f = 6.3$ MHz, (b) $\epsilon_{soil} = 3.3-j0.1$, $f = 6.08$ MHz, (c) $\epsilon_{soil} = 4-j0.2$, $f = 5.9$ MHz (d) $\epsilon_{soil} = 5-j0.3$, $f = 5.7$ MHz.

obtained by full-wave analysis is plotted in Figure 4-7. Perfect agreement with the analytical solution is observed. This indicates that the desired TM^z mode is excited by the launcher. Figure 4-8 shows the radial and the axial electric field distribution along the SCTL immersed in the soil of permittivity $\epsilon_{soil} = 2.6 - j0.05$ at $f = 6.3$ MHz. The reflection and the transmission coefficients are depicted in Figure 4-9(a) and Figure 4-9(b) respectively.

Compared to an ideal launcher, it is observed that, the proposed structure provides a minimum of 50 % coupling from TEM wave to the TM^z wave for $\epsilon_{soil} = 2.6 - j0.05$ over



(a)



(b)

Figure 4-8. The Electric field distribution along SCTL of length $L = 10\lambda$ immersed in a soil/rock medium of permittivity $\epsilon_{\text{soil}} = 2.6 - j0.05$ at $f = 6.3$ MHz. (a) Radial electric field (E_r), (b) axial electric field (E_z).

2 % fractional bandwidth. The rest of the power is either radiated at the launching point or converted to other modes. As the background soil becomes lossier, the level of coupling from TEM wave to TM^z wave is decreased. A tabulated comparison of the proposed apparatus with the existing wireless telemetry using short dipole antennas (with 100% radiation efficiency which is impossible to realize) for a transmission distance of $L = 300$ m is provided in Table 4-3 which shows the much better performance of the proposed method. It should be noted that the radiation efficiency of a short dipole antenna is very low and this transmission loss when using short dipole antennas is much worse than the values reported in Table III. Placement of short dipoles near and parallel to long metallic pipes further makes the impedance matching far more difficult and reduces the radiation efficiency. Complex methods such those reported in [22] must be implemented to alleviate these drawbacks to some extent. Obviously, as the surrounding soil/rock becomes lossier, the transmission loss increases for both techniques.

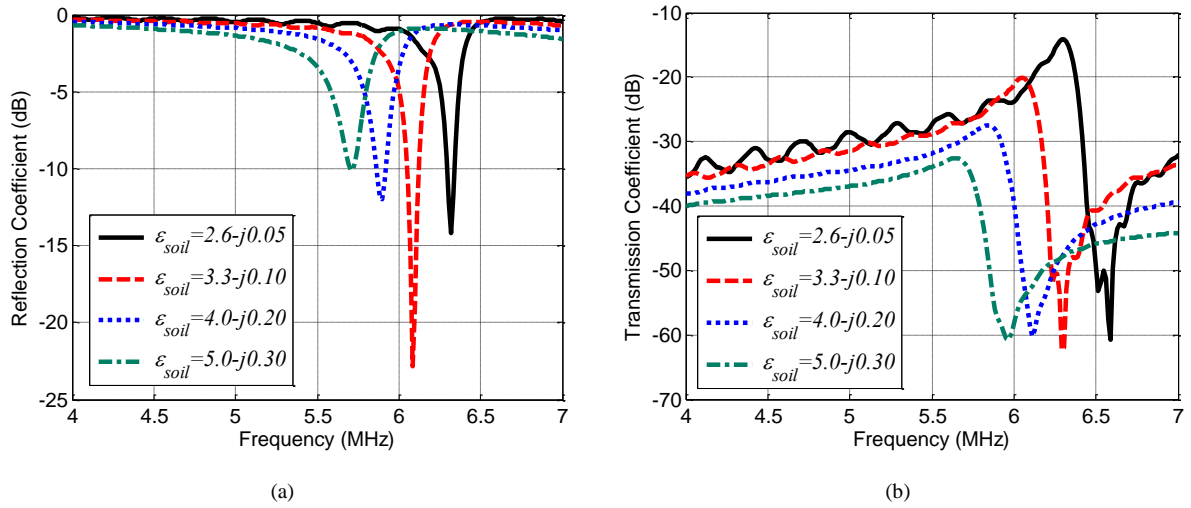


Figure 4-9. (a) The reflection and (b) the transmission coefficients for the SCTL of length $L = 300m$ terminated by the launcher shown in Figure 4-3 at both ends for different dielectric constants of the soil. The transmission loss can be as low as 30 dB/Km and as high as 90 dB/Km for dry and wet soil conditions.

Table 4-3. The transmission loss of the drill pipe-drilling mud SCTL compared with the existing short dipole antenna method at 6 MHz for a transmission distance of 300 m

σ_{soil} (ϵ_r^{soil} at $f \cong 6$ MHz)	Transmission Loss (dB)	
	Dipole Antennas	Drilling pipe-Drilling mud SCTL
$15 \mu S$ ($2.6 - j0.05$)	> 46.3	14
$100 \mu S$ ($5 - j0.3$)	> 67	32

4.4 The Effects of the Bends Along the Drilling Path

In the analysis described in Section II, the drill pipe was assumed to be straight. This was needed to validate the launcher performance and the validity of the numerical simulations through a direct comparison with analytical results. However, in most practical

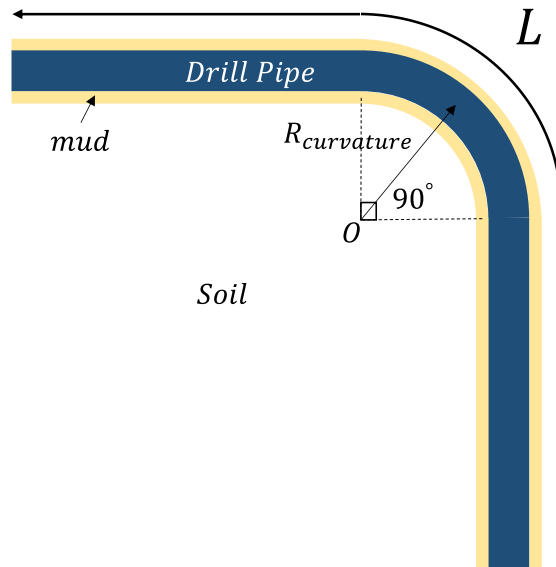
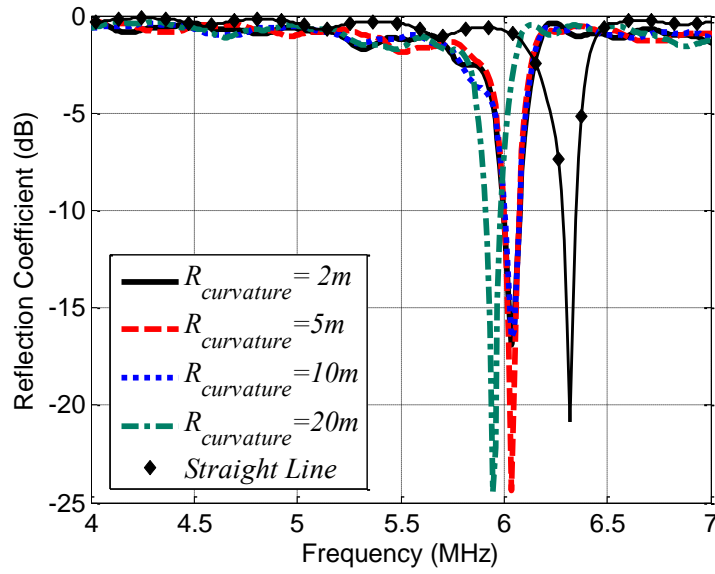
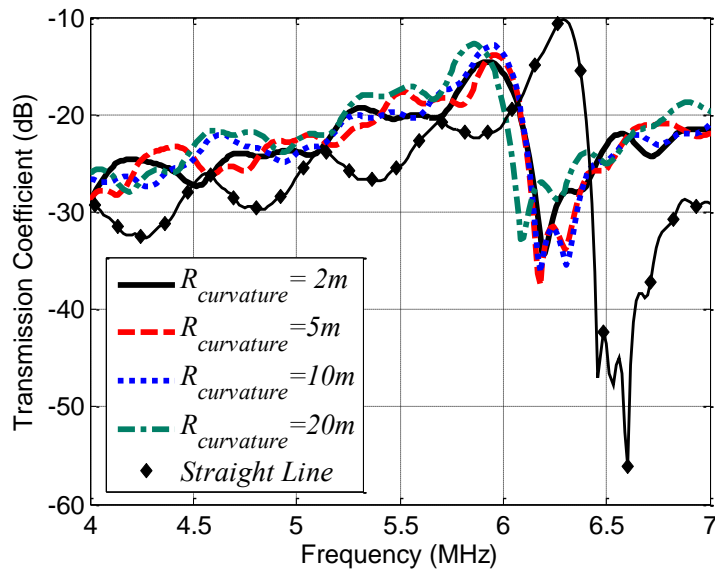


Figure 4-10. A 90°-bend SCTL of total length $L = 150m$ which is analyzed by a full-wave solver to examine the bend effects for different radii of curvature.

situations, there are bends and curvatures along the drilling path. In this section, the effect of curvature on the SCTL response is examined using the EM simulation tool used previously. Consider the 90°-bend SCTL shown in Figure 4-10 which is terminated by the proposed launcher at both ends. Keeping the total length of the line as $L \cong 5\lambda = 150 m$, the reflection and the transmission coefficients for different radii of curvatures are obtained by a full-wave simulator and are demonstrated in Figure 4-11. Also, shown is the reflection and transmission coefficients for the straight SCTL of the same length. The effect of the curvature compared to the straight line of the same length reveals two phenomena: 1) the resonant frequency shifts down by about 7% and, 2) the transmission loss is increased. The shift of the resonant frequency is due to the reflection from the bend and the interactions between the bend and the launcher. The transmission loss is mostly due to the radiation from the bend itself. The more acute is the bend, the more the radiation occurs. However, since the refractive index of



(a)



(b)

Figure 4-11. (a) The reflection and (b) the transmission coefficients for the 90°-bend SCTL of length $L = 150m$ shown in Figure 4-10 immersed in a soil/rock medium of permittivity $\epsilon_{soil} = 2.6-j0.05$ and terminated by the launcher at both ends for different radii of curvature.

the mud is much larger than that of the background soil, the wave is partly guided along the curvature. The radiation loss for this line, due to the curvature is found to be about 2.5 dB

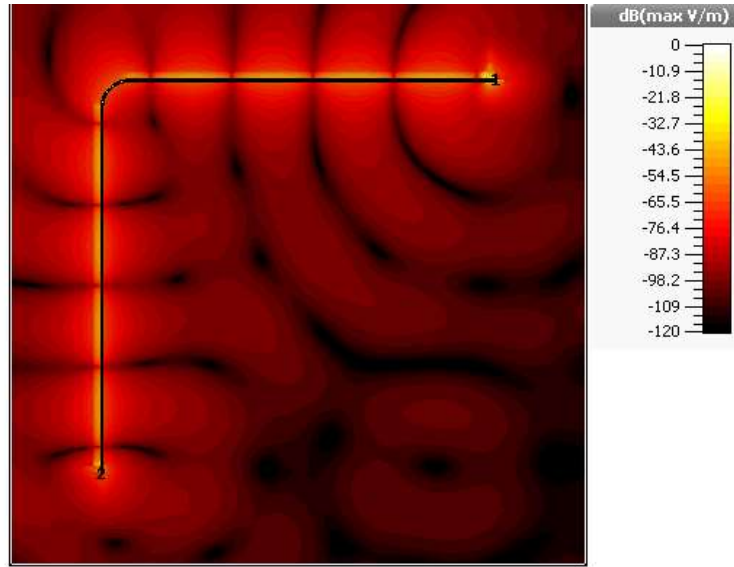


Figure 4-12. The electric field distribution ($|E|$) along a 90° -bend ($R_{curvature} = 0.16 \lambda = 5m$) on a 5λ -long SCTL immersed in a soil/rock medium of permittivity $\epsilon_{soil} = 2.6 - j0.05$ at $f = 5.9$ MHz.

for $R_{curvature} = 0.06\lambda$ where λ is the wavelength in the background soil at the corresponding resonant frequency. The electric field distribution along the 90° -bend SCTL of curvature $R_{curvature} = 0.15 \lambda = 5m$ and length $L \cong 5\lambda = 150m$ submerged in the soil of permittivity $\epsilon_{soil} = 2.6 - j0.05$ is depicted in Figure 4-12 which indicates that the wave is steered along the curvature. The frequency of operation needs to be slightly adjusted as the drill is moving downhole. Therefore, the reflection coefficient should be monitored to select the appropriate channel for data transmission.

4.5 Experimental Verification

An experimental study is conducted to verify the proposed concept. A scaled model at VHF is designed for this purpose. The designed transducer is shown in Figure 4-13. In this

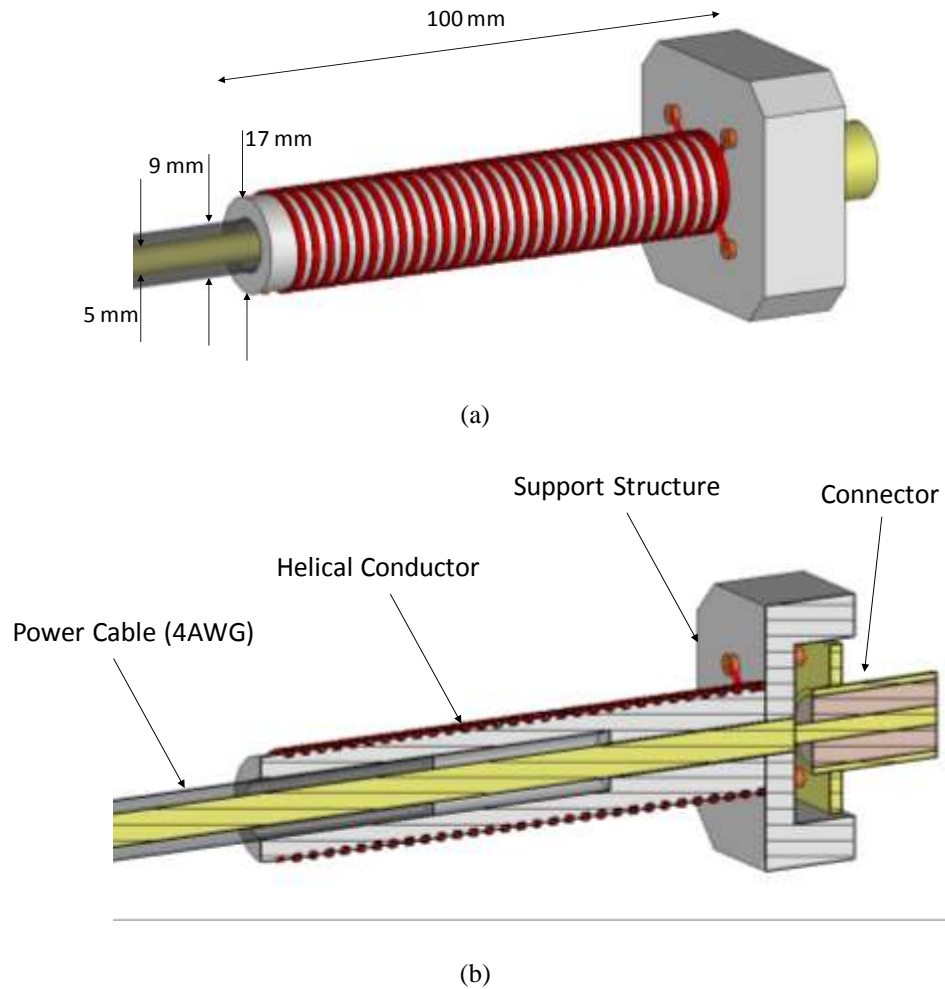


Figure 4-13. The designed transducer at VHF.

simulation, an SCTL composed of a cylindrical conductor of radius $r_c = 2.5 \text{ mm}$ coated by a dielectric material of thickness $t_j = 2 \text{ mm}$ and $\epsilon_r = 6.7$ is considered. The helical conductor is supported by a 3D-printed structure of dielectric constant $\epsilon_r = 1.7$. The transducer is excited by an N-type connector. The transducer is then fabricated and tested in air as the surrounding environment. The fabricated transducer is shown in Figure 4-14. A 4AWG power cable is used as the SCTL. The wire is made of a conductor of radius $r_c = 2.5 \text{ mm}$ and a jacket of thickness $t_j = 2 \text{ mm}$ made of Neoprene with a relative dielectric



Figure 4-14. The fabricated transducer a VHF band.



Figure 4-15. The experimental setup for testing the transducer. A 4AWG wire of length $L = 9.3 \lambda = 20$ m is used as the SCTL. The wire is terminated by the transducer at both ends. One transducer is excited by the network analyzer to measure the reflection coefficient. The transmitted power is $P_t = 10$ dBm. The receiving side is connected to the spectrum analyzer to measure the transmission loss.

constant of $\epsilon_r = 6.7$. The conductor resembles the drilling pipe and the jacket resembles the

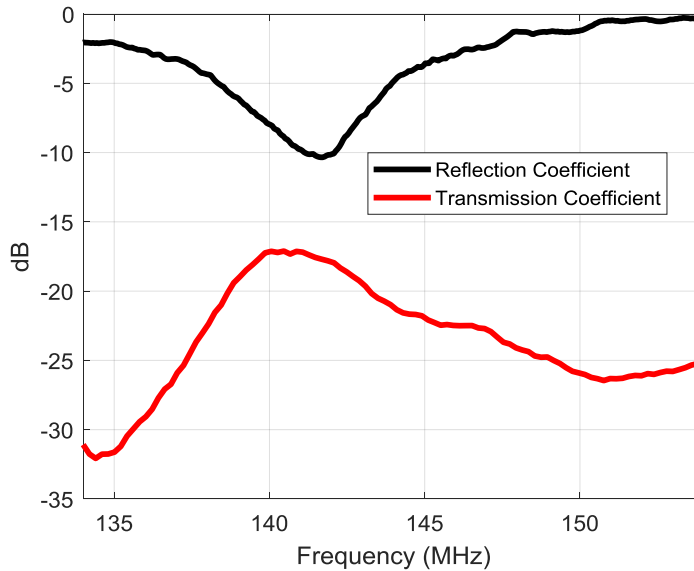


Figure 4-16. The measured transmission and reflection coefficient for the SCTL shown in Figure 4-15.

surrounding mud. The length of the wire is $L = 9.3\lambda = 20\text{ m}$ and is terminated by the transducer at both ends as illustrated in Figure 4-15. One transducer is connected to the network analyzer and the other transducer is connected to the spectrum analyzer. The transmit power by the network analyzer is set as $P_t = 10\text{ dBm}$. The operating frequency is measured to be $f = 139\text{ MHz}$ at which the received power by the spectrum analyzer is $P_r = -7.8\text{ dBm}$. This indicates a transmission loss of -17.8 dB while the reflection coefficient measured by the network analyzer is better than $= -8\text{ dB}$ over 2 MHz bandwidth.

4.6 Conclusion

A novel communication concept in deep boreholes using drilling mud around the drill pipe as a single-conductor-transmission-line is introduced. Moreover, a very compact TM wave launcher which enables wave transformation from TEM on the coaxial line to TM

surface wave on the SCTL is presented. Analytical and numerical models are used to validate the feasibility of signal transmission on drill pipe itself to enable LWD/MWD. It is shown that at low HF bands the transmission loss can be as low as 30 dB/Km for low loss soil/rock and as high as 90 dB/Km for lossy (wet) soil/rock medium. This study clearly indicates that the concept and the proposed apparatus can be used efficiently for real-time and low-cost data communication in deep borehole drilling process.

CHAPTER 5 Where Next

5.1 Research Summary

In this PhD work, several challenges of the present and future communication systems ranging from spectrum crunch in wireless systems to long-distance subsurface communication have been addressed. We have devised novel beamforming algorithms and apparatus which allow for new wireless network architectures with higher spectrum efficiency to meet the requirements of the next generation technologies such as 5G and the IoT. The developed algorithms and devices enable co-channel interference mitigation through two different mechanism: 1) the external interference signals (caused by other users or jammers) are spatially detected and segregated from the desired communication signals, 2) the internal interference arising from co-located transmitters are cancelled to a very large extent by novel compact ultrawideband antenna systems. The former enables reusing the available spectrum by multiple users and the latter allows for sharing the available spectrum by both transmitter and the receiver both of which give rise to channel capacity enhancement.

The proposed beamforming algorithms including ASSIA and CNSM make it possible to resolve co-channel signals arriving at the receiver with angular separation smaller than the array beamwidth. Examined numerically in a complex urban environment, the conceived method for signal segregation is shown to retrieve the desired signal in the presence of very strong interfering signal should the angular separation of the signals is more than the array

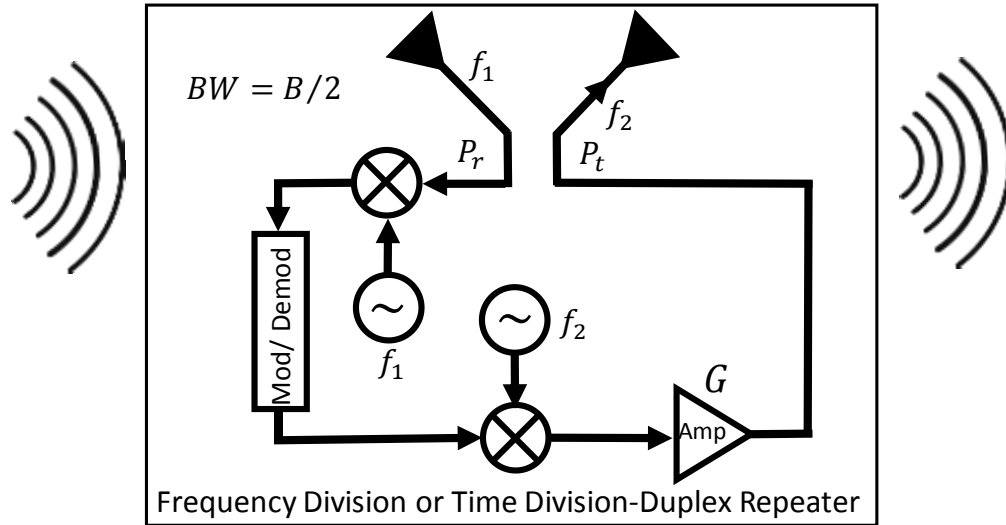
beamwidth and the array is accurately calibrated. Another important feature of ASSIA and CNSM is that the mutual couplings and shadowing effects due to electromagnetic interaction between the array elements are included in the formulation. Besides, a physical approach based on feed-forward coupling technique was introduced to mitigate the mutual coupling effects and to facilitate beamforming.

The devised antenna system for self-interference cancellation is very compact, offers high radiation efficiency, and does not require bulky hybrids. Full-duplex operation using orthogonal polarizations facilitates channel estimation as the size of the channel matrix becomes smaller and reduces the system complexity and cost through reducing the number of the required transmitters and receivers.

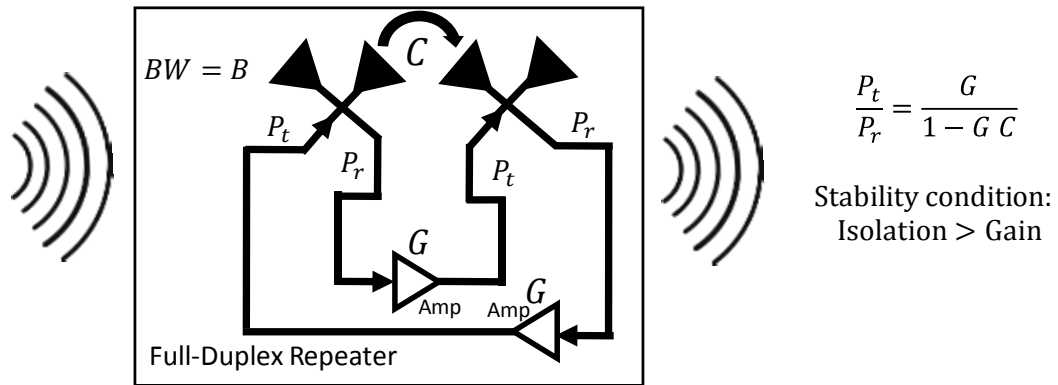
5.2 Future work and Challenges

5.2.1 Full-Duplex Repeaters for 5G Networks

In half-duplex repeaters as shown in Figure 5-1(a), the information has to be received, stored, and transmitted at a different frequency or at a later period when no reception takes place. Therefore, the throughput is lowered by a factor of two for each repeater in the chain and the latency increases linearly with the number of repeaters added to the chain. The devised two-port CBSA make it feasible to build full-duplex repeaters to significantly improve the channel capacity. A full-duplex repeater as shown in Figure 5-1(b) is protocol-independent, less expensive, and can be easily installed.



(a)



(b)

Figure 5-1. (a) Half-duplex repeater, (b) full-duplex repeater. Full-duplex antenna systems enable full-duplex repeaters to increase the throughput of the 5G networks.

5.2.2 Radar Calibration

Polarimetric Radars require very precise calibration systems to improve the accuracy of the information gathered and the images taken by these radars. A target with very large

RCS as the calibration target is required to achieve a very high signal to clutter ratio. Active targets are used for this purpose. The active calibration target is composed of a receiver, a two-port antenna with high isolation between the two ports and a transmitter. The calibrator captures the radar signal by one of the antenna ports, passes it through a very high gain amplifier stage and then transmits the amplified signal back to the radar. A high gain active calibrator needs very high isolation between transmit and receive channels to ensure stability. The existing calibration tools are very bulky mainly due to the antenna size. The proposed compact full-duplex antenna system can be envisioned as the antenna block of the active target to build a compact and broadband radar calibrator.

5.2.3 Simplifying the Antenna Structure

The proposed antenna system is a very complex structure and was fabricated by 3D printing. The existing 3D printing technology does not provide the required tolerance and cost-wise is not suitable for mass product. To fully unlock the potential of the proposed method for self-interference cancellation, the structure must be modified to be amenable to other fabrication processes such as injection molding. Injection molding provides much better accuracy and is cost-effective for mass product. Antenna structure shown in Figure 2-32 is an alternative design which is less complex. Even more simple designs must be explored to meet the requirements for mass production.

5.2.4 Applying ASSIA to Fourier Transform, MPM and ML-Based Methods

The concept of ASSIA can be used to perform iterative Fourier transform for segregating different frequency components of a signal composed of discrete frequency

components. Conventional Fourier transform fails to find the frequency components of a signal whose magnitude is 13 dB less than the dominant frequency component. ASSIS allows for calculating different frequency components based on estimating and removing the strongest components through a multi-step iterative approach. This way, the errors are effectively prevented to propagate while calculating the smaller ones. Likewise, ASSIA can be applied to MPM and ML-based techniques to increase the dynamic range of the signals they can handle. Moreover, by infusing ASSIA into ML-based methods, the technique is less likely to diverge due to erroneous initialization.

What limits the performance of ASSIA is array manifold imperfections. The major challenge in realizing ASSIA is array calibration to capture fabrication errors. Very accurate array calibration techniques have to be developed to fully cash in the capability of ASSIA in terms of the dynamic range.

5.2.5 Super-Resolution Radars

ASSIA-CNSM can be implemented by airborne or ground-based radars to empower super-resolution radars. The cross-range resolution provided by the radars is limited by the beamwidth of the radar antenna. The developed ASSIA-CNSM algorithm makes it possible to achieve a cross-range resolution better than antenna beamwidth as depicted in Figure 5-2. Adopting ASSIA-CNSM into the current radar systems or developing new radar systems based on this algorithm needs more investigation to ensure efficient use of the available hardware and to minimize the cost for transceiver implementation.

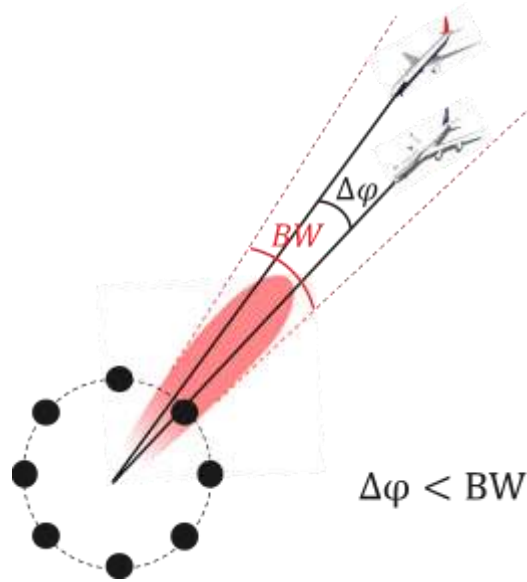


Figure 5-2. ASSIA-CNSM enables super cross-range resolution radars.

5.2.6 Ultra-Miniatured Surface-Wave Transducer

The devised surface wave transducer needs to be further miniaturized to fit within the available space shown in Figure 5-3. Magnetic or dielectric materials with high refractive index may be used to design the launcher. Multiple sections of different materials may be required to achieve the impedance matching and wave transformation from TEM to TM over the required bandwidth.

5.2.7 SCTL-Based Radar Systems

The compact SCTL launcher introduced in Chapter 4 offers the possibility of developing pulsed or CW SCTL-based radar systems for monitoring different layers of ground formation. Two launchers are required for this purpose (see Figure 5-4). One launcher emits a signal and the other launcher capture the backscattering from ground formations.

Either Continuous Wave (CW) or pulsed SCTL-based radars can be envisioned. To be used in pulsed SCTL-based radars, the bandwidth of the launcher needs to be increased to achieve the desired range resolution. For SCTL-based CW radars, very high isolation between launchers is required. It is interesting to investigate techniques for bandwidth enhancement of the proposed launcher as well as mechanism for achieving high isolation between transducers must to enable SCTL-based radar systems.

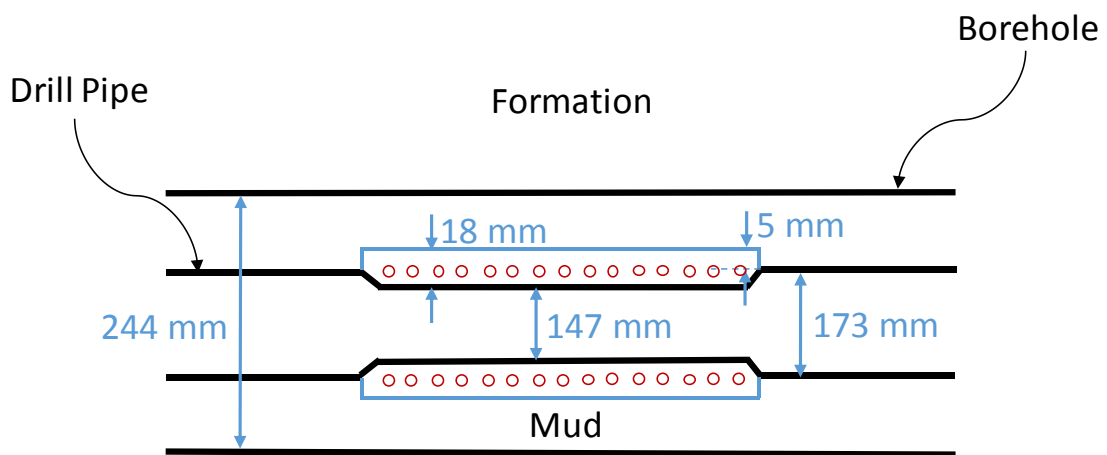


Figure 5-3. The borehole and drilling tools. The region between the blade boundary and the drilling pipe is the available space to accommodate the launcher. Further miniaturized surface-wave launcher is required to fit within this space.

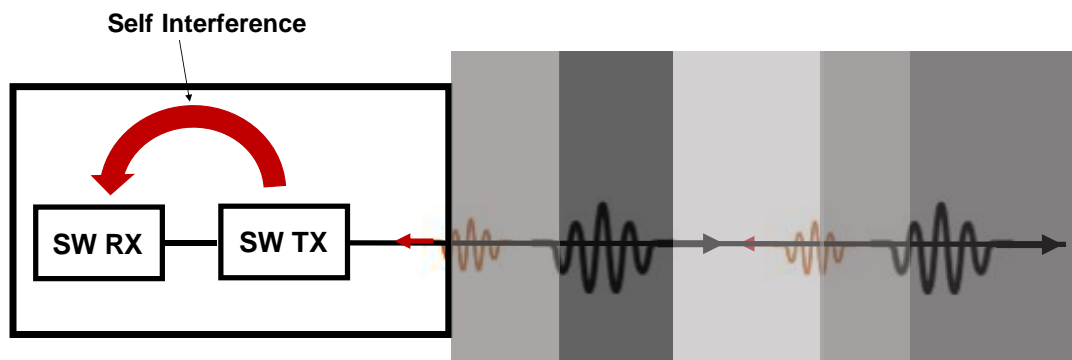


Figure 5-4. An SCTL-based radar system for monitoring the ground formations.

APPENDIX A Derivation of $G_{F_N}^{min}$

$G_{F_N}^{min}$ is calculated for $N = 2, 3, 4$ and from the observed trend, $G_{F_N}^{min}$ is found for arbitrary value of N . First, let $\varphi_z = \pi$. Starting from $N = 2$ and assuming the zeros are symmetrically located at $\varphi = \pm\varphi_1$, $F_2(\varphi)$ is given by:

$$F_2(\varphi) = e^{-j\frac{M}{2}\varphi} (e^{j\varphi} - e^{j\varphi_1})(e^{j\varphi} - e^{-j\varphi_1})(e^{j\varphi} + 1)^{M-2} \quad (\text{A-1})$$

First, we show that $F_2(\varphi)$ is pure real. One can rewrite $F_2(\varphi)$ as:

$$\begin{aligned} F_2(\varphi) &= e^{-j\frac{M}{2}\varphi} \left(\cos(\varphi) - \cos(\varphi_1) + j(\sin(\varphi) - \sin(\varphi_1)) \right) \left(\cos(\varphi) \right. \\ &\quad \left. - \cos(\varphi_1) + j(\sin(\varphi) + \sin(\varphi_1)) \right) (\cos(\varphi) + j\sin(\varphi) + 1)^{M-2} \\ &= e^{-j\frac{M}{2}\varphi} \left\{ \left((\cos(\varphi) - \cos(\varphi_1))^2 - (\sin^2(\varphi) - \sin^2(\varphi_1)) \right) \right. \\ &\quad \left. + j2\sin(\varphi)(\cos(\varphi) - \cos(\varphi_1)) \right\} \left(2\cos^2\left(\frac{\varphi}{2}\right) \right. \\ &\quad \left. + j2\sin\left(\frac{\varphi}{2}\right)\cos\left(\frac{\varphi}{2}\right) \right)^{M-2} \\ &= e^{-j\frac{M}{2}\varphi} \left\{ (\cos^2(\varphi) + 1 - \sin^2(\varphi) - 2\cos(\varphi)\cos(\varphi_1)) \right. \\ &\quad \left. + j2\sin(\varphi)(\cos(\varphi) - \cos(\varphi_1)) \right\} \left(2\cos^2\left(\frac{\varphi}{2}\right) \right. \\ &\quad \left. + j2\sin\left(\frac{\varphi}{2}\right)\cos\left(\frac{\varphi}{2}\right) \right)^{M-2} \end{aligned}$$

$$\begin{aligned}
&= e^{-j\frac{M}{2}\varphi} \left\{ 2\cos(\varphi)(\cos(\varphi_1) - \cos(\varphi)) \right. \\
&\quad \left. + j2\sin(\varphi)(\cos(\varphi) - \cos(\varphi_1)) \right\} \left(2\cos^{M-2}\left(\frac{\varphi}{2}\right) e^{j\frac{M}{2}\varphi} (\cos(\varphi) \right. \\
&\quad \left. - j\sin(\varphi)) \right) \tag{A-2}
\end{aligned}$$

The imaginary part of $F_2(\varphi)$ is given by:

$$\begin{aligned}
\text{Im}(F_2(\varphi)) &= 2\sin(\varphi)\cos(\varphi)(\cos(\varphi_1) - \cos(\varphi)) \\
&\quad - 2\cos(\varphi)\sin(\varphi)(\cos(\varphi_1) - \cos(\varphi)) = 0 \tag{A-3}
\end{aligned}$$

Therefore, $F_2(\varphi)$ is pure real for all values of φ and is differentiable. As such, the maximums of $F_2(\varphi)$ occur at angles where $\partial F_2(\varphi)/\partial\varphi = 0$. Letting $x = e^{j\varphi}$ and $x_1 = e^{j\varphi_1}$ and taking the derivative of $F_2(x)$, we get:

$$\begin{aligned}
\frac{\partial F_2(x)}{\partial x} &= x^{-\frac{M}{2}-1}(x+1)^{M-3} \left[-\frac{M}{2}(x-x_1)(x-x_1^{-1})(x+1) \right. \\
&\quad \left. + x(x-x_1^{-1})(x+1) + x(x-x_1)(x+1) \right. \\
&\quad \left. + (M-2)x(x-x_1)(x-x_1^{-1}) \right] \tag{A-4}
\end{aligned}$$

Equating $\partial F_2(x)/\partial x$ to zero results in:

$$\begin{aligned}
\frac{\partial F_2(x)}{\partial x} = 0 &\xrightarrow{\text{yields}} -\frac{M}{2}(x-x_1)(x-x_1^{-1})(x+1) + x(x-x_1^{-1})(x+1) \\
&\quad + x(x-x_1)(x+1) + (M-2)x(x-x_1)(x-x_1^{-1}) \\
&= -\frac{M}{2}(x^3 + x^2 - 2\cos(\varphi_1)x^2 - 2\cos(\varphi_1)x + x + 1) + x^3 \\
&\quad + x^2 - x_1^{-1}x^2 - x_1^{-1}x + x^3 + x^2 - x_1x^2 - x_1x \\
&\quad + (M-2)(x^3 - 2\cos(\varphi_1)x^2 + x) = 0 \\
&\xrightarrow{\text{yields}} \frac{M}{2}x^3 + ((-M+2)\cos(\varphi_1) - M+4)x^2 + (\dots)x + (\dots) \\
&= 0 \tag{A-5}
\end{aligned}$$

Assuming $\{x'_n\}_{n=1}^3$ to be the roots of the above third order polynomial equation, the sum of the roots is obtained as:

$$\sum_{n=1}^2 x'_n = -\frac{b}{a} = -\frac{(-M+2)\cos(\varphi_1) - 2M + 4}{M} \quad (\text{A-6})$$

One of the roots is in the middle of two nulls at $\varphi = 0$. Therefore, the sum of the other two roots at $\varphi = \pm\varphi_{max}$ is given by:

$$(e^{j\varphi_{max}} + e^{-j\varphi_{max}}) = 2\cos(\varphi_{max}) = -\frac{2(-M+2)\cos(\varphi_1) - M + 4}{M} - 1 \quad (\text{A-7})$$

For small values of φ_1 , we have:

$$\begin{aligned} \cos(\varphi_{max}) &= \frac{M-4}{M} = \frac{M-2N}{M} \\ \xrightarrow{\text{yields}} \varphi_{max} &= \cos^{-1}\left(\frac{M-4}{M}\right) = \cos^{-1}\left(\frac{M-2N}{M}\right) \end{aligned} \quad (\text{A-8})$$

Then, $|F_2(\varphi_{max})|$ can be calculated as:

$$\begin{aligned} |F_2(\varphi_{max})| &= \sin\left(\frac{1}{2}\cos^{-1}\left(\frac{M-4}{M}\right) - \frac{\varphi_1}{2}\right) \sin\left(\frac{1}{2}\cos^{-1}\left(\frac{M-4}{M}\right) \right. \\ &\quad \left. + \frac{\varphi_1}{2}\right) \sin^{M-2}\left(\frac{1}{2}\cos^{-1}\left(\frac{M-4}{M}\right) - \frac{\pi}{2}\right) \end{aligned} \quad (\text{A-9})$$

For small φ_1 :

$$\begin{aligned} |F_2(\varphi_{max})| &= \sin^2\left(\frac{1}{2}\cos^{-1}\left(\frac{M-4}{M}\right)\right) \cos^{M-2}\left(\frac{1}{2}\cos^{-1}\left(\frac{M-4}{M}\right)\right) \\ &= \left[\sqrt{\frac{1 - \left(\frac{M-4}{M}\right)}{2}}\right]^2 \left[\sqrt{\frac{1 + \left(\frac{M-4}{M}\right)}{2}}\right]^{M-2} = \frac{(2\sqrt{2})^2}{(2!)^2} \sqrt{\frac{(M-2)^{M-2}}{M^M}} \end{aligned} \quad (\text{A-10})$$

and

$$\begin{aligned}
|F_2(0)| &= \sin^2\left(\frac{\varphi_1}{4}\right) \cos^{M-2}\left(\frac{\varphi_1}{4}\right) \\
&\xrightarrow{\text{for small } \varphi_1} F_2(0) = \left(\frac{\Delta\varphi_{min}}{4}\right)^2
\end{aligned} \tag{A-11}$$

Therefore:

$$\begin{aligned}
G_{F_2}^{min} &= \sqrt{\frac{2\pi F_2^2(0)}{\int_0^{2\pi} F_2^2(\varphi) d\varphi}} \cong \frac{|F_2(0)|}{|F_2(\varphi_{max})|} \\
&= (2!)^2 (2\sqrt{2})^{-2} \left(\frac{\Delta\varphi_{min}}{4}\right)^2 \sqrt{\frac{M^M}{(M-2)^{M-2}}}
\end{aligned} \tag{A-12}$$

Similarly, for $N = 3$, assuming $\varphi_z = \pi$ and the zero are located at $\varphi = 0$ and $\varphi = \pm\varphi_1$,

$F_3(\varphi)$ can be written as:

$$F_3(\varphi) = e^{-j\frac{M}{2}}(e^{j\varphi} - e^{j\varphi_1})(e^{j\varphi} - e^{-j\varphi_1})(e^{j\varphi} - 1)(e^{j\varphi} + 1)^{M-3} \tag{A-13}$$

Letting $x = e^{j\varphi}$ and $x_1 = e^{j\varphi_1}$, since $F_3(\varphi)$ is pure real, $\partial F_3(x)/\partial x$ can be found as:

$$\begin{aligned}
\frac{\partial F_3(x)}{\partial x} &= x^{-\frac{M}{2}-1}(x+1)^{M-4} \left[-\frac{M}{2}(x-x_1)(x-x_1^{-1})(x-1)(x+1) \right. \\
&\quad + x(x-x_1^{-1})(x-1)(x+1) + x(x-x_1)(x-1)(x+1) \\
&\quad + x(x-x_1)(x-x_1^{-1})(x+1) \\
&\quad + (M-3)x(x-x_1)(x-x_1^{-1})(x \\
&\quad \left. - 1) \right]
\end{aligned} \tag{A-14}$$

The extremum points of $F_3(x)$ are the roots of the above polynomial for which we have:

$$\begin{aligned}
\frac{\partial F_3(x)}{\partial x} = 0 &\xrightarrow{\text{yields}} -\frac{M}{2}(x^4 - x^2 - 2\cos(\varphi_1)x^3 + 2\cos(\varphi_1)x + x^2 - 1) + x^4 \\
&\quad - x^2 - x_1^{-1}x^3 + x_1^{-1}x + x^4 - x^2 - x_1x^3 + x_1x + x^4 \\
&\quad - 2\cos(\varphi_1)x^3 + x^2 + x^3 - 2\cos(\varphi_1)x^2 + x \\
&\quad + (M-3)(x^4 - 2\cos(\varphi_1)x^3 + x^2 - x^3 + 2\cos(\varphi_1)x^2 - x) \\
&= 0
\end{aligned} \tag{A-15}$$

For the sum of the roots, we have:

$$\sum_{n=1}^3 x'_n = -\frac{b}{a} = -2 \frac{(-M+2) \cos(\varphi_1) - M + 4}{M} \quad (\text{A-16})$$

Two roots are approximately located at $\varphi = \pm \frac{\varphi_1}{2}$. Therefore, the sum of the other two roots

at $\varphi = \pm \varphi_{max}$ is given by:

$$(e^{j\varphi_{max}} + e^{-j\varphi_{max}}) = 2 \cos(\varphi_{max}) = -2 \frac{(-M+2) \cos(\varphi_1) - M + 4}{M} - 2 \cos\left(\frac{\varphi_1}{2}\right) \quad (\text{A-17})$$

and for small φ_1 :

$$\begin{aligned} \cos(\varphi_{max}) &= \frac{M-6}{M} = \frac{M-2N}{M} \\ \xrightarrow{\text{yields}} \varphi_{max} &= \cos^{-1}\left(\frac{M-6}{M}\right) = \cos^{-1}\left(\frac{M-2N}{M}\right) \end{aligned} \quad (\text{A-18})$$

Evaluating $|F_3(\varphi_{max})|$, one will get:

$$\begin{aligned} |F_3(\varphi_{max})| &= \sin\left(\frac{1}{2} \cos^{-1}\left(\frac{M-6}{M}\right) - \frac{\varphi_1}{2}\right) \sin\left(\frac{1}{2} \cos^{-1}\left(\frac{M-6}{M}\right)\right) \\ &\quad + \frac{\varphi_1}{2} \sin\left(\frac{1}{2} \cos^{-1}\left(\frac{M-6}{M}\right)\right) \sin\left(\frac{1}{2} \cos^{-1}\left(\frac{M-6}{M}\right) - \frac{\pi}{2}\right) \end{aligned} \quad (\text{A-19})$$

For small φ_1 :

$$\begin{aligned} |F_3(\varphi_{max})| &= \sin^3\left(\frac{1}{2} \cos^{-1}\left(\frac{M-6}{M}\right)\right) \cos^{M-3}\left(\frac{1}{2} \cos^{-1}\left(\frac{M-6}{M}\right)\right) \\ &= \left[\sqrt{\frac{1 - \left(\frac{M-6}{M}\right)}{2}} \right]^3 \left[\sqrt{\frac{1 + \left(\frac{M-6}{M}\right)}{2}} \right]^{M-3} \\ &= \frac{(2\sqrt{3})^3}{(2 \times 3)(2!)^2} \sqrt{\frac{(M-3)^{M-3}}{M^M}} \end{aligned} \quad (\text{A-20})$$

The magnitude of $F_3(\varphi)$ in the middle of adjacent nulls at $\varphi = \pm \varphi_1/2$ can be calculated as:

$$\left| F_3\left(\frac{\varphi_1}{2}\right) \right| = (\sqrt{3})^3 \sin^3\left(\frac{\varphi_1}{4}\right) \cos^{M-3}\left(\frac{\varphi_1}{4}\right) \xrightarrow{\text{for small } \varphi_1} F_3\left(\frac{\varphi_1}{2}\right) = \left(\frac{\Delta\varphi_{min}}{4}\right)^3 \quad (\text{A-21})$$

Consequently:

$$G_{F_3}^{min} \cong \frac{|F_3(\frac{\varphi_1}{2})|}{|F_3(\varphi_{max})|} = (2 \times 3)(2!)^2(2\sqrt{3})^{-3} \left(\frac{\Delta\varphi_{min}}{4}\right)^N \sqrt{\frac{M^M}{(M-3)^{M-3}}} \quad (\text{A-22})$$

For $N = 4$, when $\varphi_z = \pi$ and the zeros are at $\varphi = \pm\varphi_1$ and $\varphi = \pm 3\varphi_1$, $F_4(\varphi)$ is given by:

$$F_4(\varphi) = e^{-j\frac{M}{2}}(e^{j\varphi} - e^{j\varphi_1})(e^{j\varphi} - e^{-j\varphi_1})(e^{j\varphi} - e^{j3\varphi_1})(e^{j\varphi} - e^{-j3\varphi_1})(e^{j\varphi} + 1)^{M-4} \quad (\text{A-23})$$

Similarly, it can be shown that $F_4(\varphi)$ is pure real. If we let $x = e^{j\varphi}$ and $x_1 = e^{j\varphi_1}$, then:

$$\begin{aligned} \frac{\partial F_4(x)}{\partial x} = x^{-\frac{M}{2}-1}(x+1)^{M-5} & \left[-\frac{M}{2}(x-x_1)(x-x_1^{-1})(x-x_1^3)(x-x_1^{-3})(x \right. \\ & + 1) + x(x-x_1)(x-x_1^{-1})(x-x_1^{-3})(x+1) \\ & + x(x-x_1)(x-x_1^{-1})(x-x_1^3)(x-x_1^{-3})(x+1) \\ & + x(x-x_1)(x-x_1^{-1})(x-x_1^{-3})(x+1) \\ & + x(x-x_1)(x-x_1^{-1})(x-x_1^3)(x+1) \\ & + (M-4)x(x-x_1)(x-x_1^{-1})(x-x_1^3)(x \\ & \left. - x_1^{-3}) \right] \quad (\text{A-24}) \end{aligned}$$

and the maximums are obtained by solving the following equation:

$$\begin{aligned} \frac{\partial F_4(x)}{\partial x} = 0 & \xrightarrow{\text{yields}} \frac{M}{2}x^5 \\ & + \left((-M-2)\cos(\varphi_1) + (-M-2)\cos(3\varphi_1) - \frac{M}{2} + 4 \right)x^4 \\ & + (\dots)x^3 + (\dots)x^2 + (\dots)x + (\dots) \\ & = 0 \quad (\text{A-25}) \end{aligned}$$

The sum of the roots is given by:

$$\sum_{n=1}^4 x'_n = -\frac{b}{a} = -2 \frac{(-M-2)\cos(\varphi_1) + (-M-2)\cos(3\varphi_1) - \frac{M}{2} + 4}{M} \quad (\text{A-26})$$

Three out of five roots are approximately located at $\varphi = 0, \pm 2\varphi_1$. Thus, the sum of the other two located at $\varphi = \pm\varphi_{max}$ is found as:

$$\begin{aligned} (e^{j\varphi_{max}} + e^{-j\varphi_{max}}) &= 2 \cos(\varphi_{max}) \\ &= -2 \frac{(-M-2) \cos(\varphi_1) + (-M-2) \cos(3\varphi_1) - \frac{M}{2} + 4}{M} - 1 \\ &\quad - 2 \cos(2\varphi_1) \end{aligned} \quad (\text{A-27})$$

If φ_1 is small, then:

$$\begin{aligned} \cos(\varphi_{max}) &= \frac{M-8}{M} = \frac{M-2N}{M} \\ \xrightarrow{\text{yields}} \varphi_{max} &= \cos^{-1}\left(\frac{M-8}{M}\right) = \cos^{-1}\left(\frac{M-2N}{M}\right) \end{aligned} \quad (\text{A-28})$$

The maximum of $|F_4(\varphi)|$ is obtained as:

$$\begin{aligned} |F_4(\varphi_{max})| &= \sin\left(\frac{1}{2} \cos^{-1}\left(\frac{M-8}{M}\right) - \frac{\varphi_1}{2}\right) \sin\left(\frac{1}{2} \cos^{-1}\left(\frac{M-8}{M}\right)\right) \\ &\quad + \frac{\varphi_1}{2} \sin\left(\frac{1}{2} \cos^{-1}\left(\frac{M-8}{M}\right) - \frac{3\varphi_1}{2}\right) \sin\left(\frac{1}{2} \cos^{-1}\left(\frac{M-8}{M}\right)\right) \\ &\quad + \frac{3\varphi_1}{2} \sin^{M-4}\left(\frac{1}{2} \cos^{-1}\left(\frac{M-8}{M}\right) - \frac{\pi}{2}\right) \end{aligned} \quad (\text{A-29})$$

For small φ_1 :

$$\begin{aligned} |F_4(\varphi_{max})| &= \sin^4\left(\frac{1}{2} \cos^{-1}\left(\frac{M-8}{M}\right)\right) \cos^{M-4}\left(\frac{1}{2} \cos^{-1}\left(\frac{M-8}{M}\right)\right) \\ &= \left[\sqrt{\frac{1 - \left(\frac{M-8}{M}\right)}{2}} \right]^4 \left[\sqrt{\frac{1 + \left(\frac{M-8}{M}\right)}{2}} \right]^{M-4} \\ &= \left(\frac{2!}{4!}\right)^2 (2\sqrt{4})^4 \sqrt{\frac{(M-4)^{M-4}}{M^M}} \end{aligned} \quad (\text{A-30})$$

and the minimum gain in the middle of the adjacent nulls is calculated as:

$$|F_4(0)| = \sin^4\left(\frac{\varphi_1}{4}\right) \cos^{M-4}\left(\frac{\varphi_1}{4}\right) \xrightarrow{\text{for small } \varphi_1} F_4\left(\frac{\varphi_1}{2}\right) = \left(\frac{\Delta\varphi_{min}}{4}\right)^4 \quad (\text{A-31})$$

Thereby:

$$\begin{aligned} G_{F_4}^{min} &= \sqrt{\frac{2\pi F_4^2(0)}{\int_0^{2\pi} F_4^2(\varphi) d\varphi}} \cong \frac{|F_4(0)|}{|F_4(\varphi_{max})|} \\ &= \left(\frac{4!}{2!}\right)^2 (2\sqrt{4})^{-4} \left(\frac{\Delta\varphi_{min}}{4}\right)^4 \sqrt{\frac{M^M}{(M-4)^{M-4}}} \end{aligned} \quad (\text{A-32})$$

From (A12), (A22), and (A32), it is found that in general:

$$G_{F_N}^{min} \cong C(N) (2\sqrt{N})^{-N} \left(\frac{\Delta\varphi_{min}}{4}\right)^N \sqrt{\frac{M^M}{(M-N)^{M-N}}} \quad (\text{A-33})$$

where:

$$C(N) = \begin{cases} \left(\frac{N!}{(N/2)!}\right)^2 & N \text{ even} \\ 2N \left(\frac{(N-1)!}{((N-1)/2)!}\right)^2 & N \text{ odd} \end{cases} \quad (\text{A-34})$$

For $\varphi_z = \varphi_z^{opt}$, a correction factor, $K(M, N)$ given by:

$$K(M, N) \cong 1 + 0.03(\sqrt{MN})^{\sqrt{3}} \quad (\text{A-35})$$

should be included in (3-83). This factor is found numerically by curve fitting for different values of M and N .

REFERENCES

- [1] [Online]. Available: <http://justinfo.graphics/history-of-communication/>. [Accessed 13 June 2018].
- [2] A. J. Viterbi and G. Marconi, "The History of Multiple Access and the Future of Multiple Services through Wireless Communication," *semanticscholar*, 1999.
- [3] A. J. Paulraj and T. Kailath, "Increasing capacity in wireless broadcast systems using distributed transmission/directional reception (DTDR)". United States Patent 5345599A, 6 September 1994.
- [4] M. A. Gutierrez-Estevez, "Acoustic broadband communications over deep drill strings using adaptive OFDM," in *2013 IEEE Wireless Communications and Networking Conference (WCNC)*,, Shanghai, 2013.
- [5] H. Djikpesse, P. Armstrong, R. Rufino and A. Hawthorn, "Reducing Uncertainty With Seismic Measurements While Drilling," *IEEE Transactions on Instrumentation and Measurement*, vol. 59, no. 1, pp. 4-14, 2010.
- [6] M. Poppelreiter, C. Garcia-Carballido and M. Kraaijveld, *Dipmeter and borehole imaging technology*, Tulsa: AAPG, 2010.
- [7] M. Y. Xia and Z. Y. Chen, "Attenuation predictions at extremely low frequencies for measurement-while-drilling electromagnetic telemetry system," *IEEE Transactions on Geoscience and Remote Sensing*, vol. 31, no. 6, pp. 1222-1228, 1993.
- [8] Y. Long, H. Jiang and Y. Lin, "Electromagnetic field due to a loop antenna in a borehole," *IEEE Transactions on Geoscience and Remote Sensing*, vol. 34, no. 1, pp. 33-35, 1996.
- [9] B. K. Sternberg and T. M. Levitskaya, "Electrical parameters of soils in the frequency range from 1 kHz to 1 GHz, using lumped-circuit methods," *Radio Sci.*, vol. 36, no. 4, 2001.
- [10] A. Sabharwal, P. Schniter, D. Guo, D. W. Bliss, S. Rangarajan and R. Wichman, "In-Band Full-Duplex Wireless: Challenges and Opportunities," *IEEE Journal on Selected Areas in Communications*, vol. 32, no. 9, pp. 1637-1652, 2014.

- [11] J. I. Choi, M. Jain, K. Srinivasan, P. Levis and S. Katti, "Achieving single channel, full duplex wireless communications," in *Proceedings of ACM Mobicom*, 2010.
- [12] Y. J. Song and K. Sarabandi, "A Simultaneous Dual-Channel Micro-Radio-Repeater for Ad-Hoc Wireless Communication," *IEEE Transactions on Antennas and Propagation*, vol. 62, no. 6, pp. 3378-3383, 2014.
- [13] E. Everett, A. Sahai and A. Sabharwal, "Passive Self-Interference Suppression for Full-Duplex Infrastructure Nodes," *IEEE Transactions on Wireless Communications*, vol. 13, no. 2, pp. 680-694, 2014.
- [14] H. Nawaz and I. Tekin, "Dual-Polarized, Differential Fed Microstrip Patch Antennas With Very High Interport Isolation for Full-Duplex Communication," *IEEE Transactions on Antennas and Propagation*, vol. 65, no. 12, pp. 7355-7360, 2017.
- [15] H. Nawaz and I. Tekin, "Double-Differential-Fed, Dual-Polarized Patch Antenna With 90 dB Interport RF Isolation for a 2.4 GHz In-Band Full-Duplex Transceiver," *IEEE Antennas and Wireless Propagation Letters*, vol. 17, no. 2, pp. 287-290, 2018.
- [16] J. Ha, M. A. Elmansouri, P. V. Prasannakumar and D. S. Filipovic, "Monostatic Co-Polarized Full-Duplex Antenna With Left- or Right-Hand Circular Polarization," *IEEE Transactions on Antennas and Propagation*, vol. 65, no. 10, pp. 5103-5111, 2017.
- [17] E. A. Etellisi, M. A. Elmansouri and D. S. Filipović, "In-Band Full-Duplex Multimode Lens-Loaded Eight-Arm Spiral Antenna," *IEEE Transactions on Antennas and Propagation*, vol. 66, no. 4, pp. 2084-2089, 2018.
- [18] P. V. Prasannakumar, M. A. Elmansouri and D. S. Filipovic, "Broadband Reflector Antenna With High Isolation Feed for Full-Duplex Applications," *IEEE Transactions on Antennas and Propagation*, vol. 66, no. 5, pp. 2281-2290, 2018.
- [19] J. Wu, M. Li and N. Behdad, "A Wideband, Unidirectional Circularly Polarized Antenna for Full-Duplex Applications," *IEEE Transactions on Antennas and Propagation*, vol. 66, no. 3, pp. 1559-1563, 2018.
- [20] C. A. Lindberg, "A shallow-cavity UHF crossed-slot antenna," *IEEE Trans. Antennas Propag.*, vol. 17, no. 5, p. 558-563, 1969.
- [21] H.E.King and J.Wong, "A shallow ridged-cavity crossed-slot antenna for the 240- to 400-MHz frequency range," *IEEE Transactions on Antennas and Propagation*, vol. 23, no. 5, pp. 687-689, 1975.

- [22] W. Hong, N. Behdad and K. Sarabandi, "Size Reduction of Cavity-Backed Slot Antennas," *IEEE Transactions on Antennas and Propagation*, vol. 54, no. 5, pp. 1461-1465, 2006.
- [23] N. Behdad and K. Sarabandi, "A wide-band slot antenna design employing a fictitious short circuit concept," *IEEE Trans. on Antennas Propag.*, vol. 53, no. 1, p. 475–482, 2005.
- [24] R. C. Paryani, P. F. Wahid and N. Behdad, "A Wideband, Dual-Polarized, Substrate-Integrated Cavity-Backed Slot Antenna," *IEEE Antennas and Wireless Propagation Letters*, vol. 9, pp. 645-648, 2010.
- [25] S. Yun, D. Kim and S. Nam, "Bandwidth enhancement of cavity-backed slot antenna using a via-hole above the slot," *IEEE Antennas and Wireless Propagation Letters*, vol. 11, p. 1092– 1095, 2012.
- [26] D. Sievenpiper, H. P. Hsu and R. M. Riley, "Low-profile cavity-backed crossed-slot antenna with a single-probe feed designed for 2.34-GHz satellite radio applications," *IEEE Trans. on Antennas Propagation*, vol. 52, no. 3, p. 873–879, 2004.
- [27] B. Liu, W. Hong, Z. Kuai, X. Yin, G. Luo, J. Chen, H. Tang and K. Wu, "Substrate Integrated Waveguide (SIW) Monopulse Slot Antenna Array," *IEEE Transactions on Antennas and Propagation*, vol. 57, no. 1, pp. 275-279, 2009.
- [28] S. Mukherjee, A. Biswas and K. V. Srivastava, "Broadband Substrate Integrated Waveguide Cavity-Backed Bow-Tie Slot Antenna," *IEEE Antennas and Wireless Propagation Letters*, vol. 13, pp. 1152-1155, 2014.
- [29] K. Gong, Z. N. Chen, X. Qing, P. Chen and W. Hong, ", "Substrate integrated waveguide cavity-backed wide slot antenna for 60GHz bands," *IEEE Transactions on Antennas and Propagation*, vol. 60, no. 12, p. 6023–6026, 2012.
- [30] D. Guan, Z. Qian, Y. Zhang and Y. Cai, "Novel SIW Cavity-Backed Antenna Array Without Using Individual Feeding Network," *IEEE Antennas and Wireless Propagation Letters*, vol. 13, pp. 423-426, 2014.
- [31] D. F. Guan, Z. P. Qian, Y. S. Zhang and J. Jin, ", "High-Gain SIW Cavity-Backed Array Antenna with Wideband and Low Sidelobe Characteristics," *IEEE Antennas and Wireless Propagation Letters*, vol. 14, pp. 1774-1777, 2015.
- [32] P. Wu, S. Liao and Q. Xue, "A Substrate Integrated Slot Antenna Array Using Simplified Feeding Network Based on Higher Order Cavity Modes," *IEEE Transactions on Antennas and Propagation*, vol. 64, no. 1, pp. 126-135, 2016.

- [33] D. Kim, J. Hirokawa, M. Ando, J. Takeuchi and A. Hirata, ", "4×4-Element Corporate-Feed Waveguide Slot Array Antenna With Cavities for the 120 GHz-Band," *IEEE Transactions on Antennas and Propagation*, vol. 61, no. 12, pp. 5968-5975, 2013.
- [34] A. U. Zaman and P. S. Kildal, "Wide-Band Slot Antenna Arrays With Single-Layer Corporate-Feed Network in Ridge Gap Waveguide Technology," *IEEE Transactions on Antennas and Propagation*, vol. 62, no. 6, pp. 2992-3001, 2014.
- [35] E. Topak, J. Hasch and T. Zwick, "Compact Topside MillimeterWave Waveguide-to-Microstrip Transitions," *IEEE Microwave and Wireless Components Letters*, vol. 23, no. 12, pp. 641-643, 2013.
- [36] D. Mencarelli, "Broadband Single-Layer Slotted Array Antenna in SIW Technology," *IEEE Antennas and Wireless Propagation Letters*, vol. 15, pp. 263-265, 2016.
- [37] M. Davidovitz, "Wide band waveguide to microstrip transition and power splitter," *IEEE Microw. Guided Wave Lett*, vol. 6, no. 1, pp. 13-15, 1996.
- [38] C. E. Shannon, "Communication in the Presence of Noise," *Proceedings of the IRE*, vol. 37, no. 1, pp. 10-21, 1949.
- [39] P. W. Howells, "Intermediate frequency side-lobe canceller". U.S. Patent 3202990 A, 24 August 1965.
- [40] S. P. Applebaum, "Adaptive arrays," *IEEE Transactions on Antennas and Propagation*, vol. 24, no. 5, pp. 585-598, 1976.
- [41] B. D. V. Veen, "Eigenstructure based partially adaptive array design," *IEEE Trans. Antennas and Propag*, vol. 36, p. 357–362, 1988.
- [42] A. M. Haimovich and Y. Bar-Ness, "An eigenanalysis interference canceler," *IEEE Trans. Signal Process*, vol. 39, p. 76–84, 1991.
- [43] W. S. Youn and C. K. Un, "Robust adaptive beamforming based on the eigenstructure method," *IEEE Trans. Signal Process*, vol. 42, p. 1543–1547, 1994.
- [44] J. L. Yu and C. C. Yeh, "Generalized eigenspace-based beamformers," *IEEE Trans. Signal Process*, vol. 43, p. 2453–2461, 1995.
- [45] A. Klouche-Djedid and M. Fujita, "Adaptive array sensor processing applications for mobile telephone communications," *IEEE Trans. Veh. Technol*, vol. 45, no. 3, pp. 405-416, 1996.

- [46] A. Ranheim, "A decoupled approach to adaptive signal separation using an antenna array," *IEEE Trans. Veh. Technol.*, vol. 48, no. 3, pp. 676-682, 1999.
- [47] T. K. Sarkar, R. A. J. Koh, R. A. Schneible, M. C. Wicks, S. Choi and M. Salazar-Palma, "A pragmatic approach to adaptive antennas," *IEEE Antennas Propagat. Mag.*, vol. 42, no. 2, pp. 39-55, 2000.
- [48] J. H. Lee and C. C. Lee, "Analysis of the performance and sensitivity of an eigenspace-based interference Canceler," *IEEE Trans. Antennas Propag.*, vol. 48, p. 826-835, 2000.
- [49] O. L. Frost, "An algorithm for linearly constrained adaptive array processing," *Proc. IEEE*, vol. 60, no. 8, pp. 926-935, 1972.
- [50] B. Widrow, K. M. Duvall, R. P. Gooch and W. C. Newman, "Signal cancellation phenomena in adaptive antennas: Causes and cures," *IEEE Trans. Antennas Propag.*, vol. 30, pp. 469-478, 1982.
- [51] A. Luthra, Maximum entropy method in the space-angle domain and a new technique with superior performance, Ph.D. dissertation, Dept. Syst. Eng., Univ. Pennsylvania, 1981.
- [52] J. E. Evans, J. R. Johnson and a. D. F. Sun, "Application of advanced signal processing techniques to angle of arrival estimation in ATC navigation and surveillance system," Lincoln Lab. Tech. Rep. 582, 1982.
- [53] T. J. Shan and T. Kailath, "Adaptive beamforming for coherent signals and interference," *IEEE Tran. Acoust., Speech, Signal Process.*, Vols. ASSP-33, no. 3, pp. 527-536, 1985.
- [54] T. J. Kailath and T. Shan, "On spatial smoothing for direction-of -arrival estimation of coherent signals," *IEEE Trans. Acoust., Speech, Signal Process.*, Vols. ASSP-33, no. 4, pp. 806-811, 1985.
- [55] A. K. Luthra, "A solution to the adaptive nulling problem with a look-direction constraint in the presence of coherent jammers," *IEEE Trans. Antennas Propag.*, vol. 34, no. 5, pp. 702-710, 1986.
- [56] EMAG Technologies Inc., 2014. [Online]. Available: <http://www.emagtech.com/content/emcube.> [Accessed 18 June 2018].
- [57] R. O. Schmidt, "Multiple emitter location and signal parameter estimation," *IEEE Trans. Antennas Propag.*, Vols. AP-34, no. 3, pp. 276-280, 1986.

- [58] A. J. Barabell, "Improving the resolution performance of eigenstructure-based direction-finding algorithms," in *Proc. ICASSP*, Boston, 1983.
- [59] M. D. Zoltowski, G. M. Kautz and S. D. Silverstein, "Beamspace ROOT-MUSIC," *IEEE Trans. Signal Process.*, vol. 41, no. 1, p. 344–364, 1993.
- [60] E. Falletti, L. L. Presti and F. Sellone, "SAM LOST smart antennas-based movable localization system," *IEEE Trans. Veh. Technol.*, vol. 55, no. 1, pp. 25-42, 2006.
- [61] Y.-Y. Wang, L.-C. Lee, S.-J. Yang and J.-T. Chen, "A Tree Structure One-Dimensional Based Algorithm for Estimating the Two-Dimensional Direction of Arrivals and Its Performance Analysis," *IEEE Trans. Antennas Propag.*, vol. 56, no. 1, pp. 178-188, 2008.
- [62] A. Hirota, H. Arai and M. Nakano, "Direction-of-Arrival Estimation System for Multipath Propagation in Code-Division Multiple-Access Systems with Synthesized Virtual Planar Array Using Pilot Signals," *IEEE Trans. Veh. Technol.*, vol. 57, no. 4, pp. 2153-2163, 2008.
- [63] G. Hislop, N. Sakar and C. Craeye, "Direction Finding with MUSIC and CLEAN," *IEEE Trans. Antennas Propag.*, vol. 61, no. 7, pp. 3839-3849, 2013.
- [64] W.-J. Zeng, H. C. So and H. Lei, "l_p-MUSIC: Robust Direction-of-Arrival Estimator for Impulsive Noise Environments," *IEEE Trans. Signal Process.*, vol. 61, no. 17, pp. 4296-4308, 2013.
- [65] R. Roy and T. Kailath, "ESPRIT-Estimation of Signal Parameters via Rotational Invariance Techniques," *IEEE Trans. Acoust., Speech, Signal Process.*, vol. 37, no. 7, pp. 984-995, 1989.
- [66] M. Haardt, *Efficient One-, Two-, and Multidimensional High-Resolution Array Signal Processing*, New York: Shaker Verlag, 1997.
- [67] M. D. Zoltowski, M. Haardt and C. P. Mathews, "Closed-form 2-D angle estimation with rectangular arrays in element space or beamspace via unitary ESPRIT," *IEEE Trans. Signal Process.*, vol. 44, no. 2, p. 316–328, 1996.
- [68] M. Haardt and J. A. Nossek, "Unitary ESPRIT: how to obtain increased estimation accuracy with a reduced computational burden," *IEEE Trans. Signal Process.*, vol. 43, no. 5, p. 1232–1242, 1995.
- [69] G. Xu, S. D. Silverstein, R. H. Roy and T. Kailath, "Beamspace ESPRIT," *IEEE Trans. Signal Process.*, vol. 42, no. 2, p. 349–356, 1994.

- [70] J. J. Blanz, A. Papathanassiou, M. Haardt, L. Furio and P. W. Baier, "Smart antennas for combined DOA and joint channel estimation in time-slotted CDMA mobile radio systems with joint detection,," *IEEE Trans. Veh. Technol*, vol. 49, no. 2, pp. 293-306, 2000.
- [71] R. T. Williams, S. Prasad, A. K. Mahalanabis and L. H. Sibul, "An improved spatial smoothing technique for bearing estimation in a multipath environment," *IEEE Trans. Acoust., Speech, Signal Process.*, vol. 36, no. 4, pp. 425-432, 1988.
- [72] S. U. Pillai and B. H. Kwon, "Forward/backward spatial smoothing techniques for coherent signal identification," *IEEE Trans. Acoust., Speech, Signal Process.*, vol. 37, no. 1, pp. 8-15, 1989.
- [73] P. S. Chang and A. L. Wilson, "Conjugate gradient method for adaptive direction-of-arrival estimation of coherent signals," in *Proc. ICASSP*, 1997.
- [74] E. Gonen, J. M. Mendel and M. C. Dogan, "Applications of cumulants to array processing. IV. Direction finding in coherent signals case," *IEEE Trans. Signal Process.* , vol. 45, no. 9, pp. 2265-2276, 1997.
- [75] T. K. Sarkar and O. Pereira, "Using the matrix pencil method to estimate the parameters of a sum of complex exponentials," *Antennas and Propagation Magazine*, vol. 37, no. 1, pp. 48-55, 1995.
- [76] N. Yilmazer, J. Koh and T. K. Sarkar, "Utilization of a unitary transform for efficient computation in the matrix pencil method to find the direction of arrival," *IEEE Trans. Antennas Propag.*, vol. 54, no. 1, pp. 175-181, 2006.
- [77] J. Rissanen, "Modeling by the Shortest Data Description," *Automatica*, vol. 14, p. 465-471, 1978.
- [78] H. Akaike, "Information Theory and Extension of the Maximum Likelihood Principle," in *Proc. 2nd Intl. Symp. Inf. Theory*, 1973.
- [79] M. Wax and J. Sheinvald, "Direction finding of coherent signals via spatial smoothing for uniform circular arrays," *IEEE Trans, on Ant. And Propag.*, vol. 42, no. 5, pp. 613-620, 1994.
- [80] M. Wax and T. Kailath, "Detection of Signals by Information Theoretic Criterion," *IEEE Trans. on Acoust., Speech, Signal Process.*, Vols. ASSP-33, no. 2, p. 387-392, 1985.
- [81] R. Bachl, "The Forward-Backward Averaging Technique Applied to TLS-ESPRIT Processing," *IEEE Trans. on Signal Process.*, vol. 43, no. 11, p. 2691-2699, 1995.

- [82] J. Capon, "High-resolution frequency-wavenumber spectrum analyses," *IEEE Proc.*, vol. 57, no. 8, pp. 1408-1418, 1969.
- [83] D. H. Johnson, "The application of spectral estimation methods to bearing estimation problems," *IEEE Proc.*, vol. 70, no. 9, pp. 1018-1028, 1982.
- [84] I. Ziskind and M. Wax, "Maximum Likelihood localization of multiple sources by alternating projection," *IEEE Trans. Acoust., Speech, Signal Process.*, Vols. ASSP-36, pp. 1560-1577, 1988.
- [85] M. Pesavento and A. B. Gershman, "Maximum-likelihood direction-of-arrival estimation in the presence of unknown nonuniform noise," *IEEE Trans. Signal Process.*, vol. 49, no. 7, pp. 1310-1324, 2001.
- [86] X. Wang and Z.-X. Wang, "The estimation of the directions of arrival of the spread-spectrum signals with three orthogonal sensors," *IEEE Trans. Veh. Technol.*, vol. 51, no. 5, pp. 817-822, 2002.
- [87] S. Marano, V. Matta, P. Willett and L. Tong, "Support-based and ML approaches to DOA estimation in a dumb sensor network," *IEEE Trans. Signal Process.*, vol. 54, no. 4, pp. 1563-1567, 2006.
- [88] O. Hernandez, F. Bouchereau and D. Munoz, "Maximum likelihood position estimation in ad-hoc networks using a dead reckoning approach," *IEEE Trans. on Wireless Commun.*, vol. 7, no. 5, pp. 1572-1584, 2008.
- [89] Z. M. Liu, Z. Huang and Y. Zhou, "An Efficient Maximum Likelihood Method for Direction-of-Arrival Estimation via Sparse Bayesian Learning," *IEEE Transactions on Wireless Commun.*, vol. 11, no. 10, pp. 1-11, 2012.
- [90] G. Wang, Y. Li and N. Ansari, "A Semidefinite Relaxation Method for Source Localization Using TDOA and FDOA Measurements," *IEEE Trans. Veh. Technol.*, vol. 62, no. 2, pp. 853-862, 2013.
- [91] I. J. Gupta and A. A. Ksienski, "Effect of mutual coupling on the performance of adaptive arrays," *IEEE Transactions on Antennas and Propagation*, vol. 31, no. 5, p. 785-791, 1983.
- [92] J. Pierre and M. Kaveh, "Experimental performance of calibration and direction-finding algorithms," in *IEEE International Conference on Acoustics, Speech and Signal Processing*, Toronto, 1991.

- [93] R. S. Adve and T. K. Sarkar, "Compensation for the effects of mutual coupling on direct data domain adaptive algorithms," *IEEE Transactions on Antennas and Propagation*, vol. 48, no. 1, p. 86–94, 2000.
- [94] H. T. Hui, "Compensating for the mutual coupling effect in direction finding based on a new calculation method for mutual impedance," *IEEE Antennas and Wireless Propagation Letters*, vol. 2, p. 26–29, 2003.
- [95] F. Yang and Y. Rahmat-Samii, "Microstrip antennas integrated with electromagnetic band-gap (EBG) structures: a low mutual coupling design for array applications," *IEEE Transactions on Antennas and Propagation*, vol. 51, no. 10, p. 2936–2946, 2003.
- [96] C. Y. Chiu, C. H. Cheng, R. D. Murch and C. R. Rowell, "Reduction of mutual coupling between closely-packed antenna elements," *IEEE Transactions on Antennas and Propagation*, vol. 55, no. 6, p. 1732–1738, 2007.
- [97] K. Buell, H. Mosallaei and K. Sarabandi, "Metamaterial Insulator Enabled Superdirective Array," *IEEE Transactions on Antenna and Propagation*, vol. 55, no. 4, pp. 1074 - 1085, 2007.
- [98] M. M. Bait-Suwailam, M. S. Boybay and O. M. Ramahi, "Electromagnetic coupling reduction in high-profile monopole antennas using single-negative magnetic metamaterials for MIMO applications," *IEEE Transactions on Antennas and Propagation*, vol. 58, no. 9, p. 2894–2902, 2010.
- [99] K. Sarabandi and Y. J. Song, "Subwavelength Radio Repeater System Utilizing Miniaturized Antennas and Metamaterial Channel Isolator," *IEEE Transactions on Antennas and Propagation*, vol. 59, no. 7, pp. 2683-2690, 2011.
- [100] Y. J. Song and K. Sarabandi, "Miniaturized Radio Repeater for Enhanced Wireless Connectivity of Ad-Hoc Networks," *IEEE Transactions on Antennas and Propagation*, vol. 60, no. 8, pp. 3913-3920, 2012.
- [101] S. C. Chen, Y. S. Wang and S. J. Chung, "A decoupling technique for increasing the port isolation between two strongly coupled antennas," *IEEE Transactions on Antennas and Propagation*, vol. 56, no. 12, p. 3650–3658, 2008.
- [102] P. J. Ferrer, J. M. Gonz´alez-Arbes´u and J. Romeu, "Decorrelation of two closely spaced antennas with a metamaterial AMC surface," *Microwave and Optical Technology Letters*, vol. 50, no. 5, p. 1414–1417, 2008.
- [103] A. Elsherbini and K. Sarabandi, "ENVELOP Antenna: A Class of Very Low Profile UWB Directive Antennas for Radar and Communication Diversity Applications,"

- IEEE Transactions on Antennas and Propagation*, vol. 61, no. 3, pp. 1055-1062, 2013.
- [104] F. Dagefu, J. Oh, J. Choi and K. Sarabandi, "Measurements and Physics-based Analysis of Co-located Antenna Pattern Diversity System," *IEEE Transactions on Antennas and Propagation*, vol. 61, no. 11, pp. 5724-5734, 2013.
- [105] F. Vincent, O. Besson and E. Chaumette, "Approximate Unconditional Maximum Likelihood Direction of Arrival Estimation for Two Closely Spaced Targets," *IEEE Signal Processing Letters*, vol. 22, no. 1, pp. 86-89, 2015.
- [106] G. Goubau, C. Sharp and S. Attwood, "Investigation of a surface-wave line for long distance transmission," *Transactions of the IRE Professional Group on Antennas and Propagation*, vol. 3, no. 1, pp. 263-267, 1952.
- [107] R. Harrington, "Cylindrical Wave functions," in *Time Harmonic Electromagnetics*, NY, Wiley Interscience, 2001.
- [108] S. Ebihara, M. Sato and H. Niitsuma, "Analysis of a guided wave along a conducting structure in a borehole," *Geophysical Prospecting*, vol. 46, pp. 489-505, 1998.
- [109] G. Goubau, "On the Excitation of Surface Waves," *Proceedings of the IRE*, vol. 40, no. 7, pp. 865-868, 1952.
- [110] T. Akalin, A. Treizebre and B. Bocquet, "Single-wire transmission lines at terahertz frequencies," *IEEE Transactions on Microwave Theory and Techniques*, vol. 54, no. 6, pp. 2762-2767, 2006.
- [111] G. J. E. Goubau, "Launching and receiving of surface waves". United States Patent 2921277 A, 12 January 1960.
- [112] T. Rahim, "Directional pattern synthesis in circular arrays of directional antennas," PhD dissertation, Dept. Elect. Eng., Univ. College London, 1980.
- [113] R. Page, "Simultaneous lobe comparison, pulse echo locator system". U.S. Patent 2 929 056, 15 March 1960.
- [114] A. Goldsmith, S. A. Jafar, N. Jindal and S. Vishwanath, "Capacity limits of MIMO channels," *IEEE Journal on Selected Areas in Communications*, vol. 21, no. 5, pp. 684-702, 2003.
- [115] S. M. Amjadi and K. Sarabandi, "A Low-Profile, High-Gain, and Full-Band SubArray of Cavity-Backed Slot Antenna," *IEEE Transactions on Antennas and Propagation*, vol. 65, no. 7, pp. 3456-3464, 2017.

- [116] ". S. p. 1. 2. N. Hansen, "The CMA evolution strategy: a comparing review," Springer, 2006, pp. 1769-1776.
- [117] A. Abbaspour-Tamijani and K. Sarabandi, "An Affordable Millimeter-Wave Beam-Steerable Antenna Using Interleaved Planar Subarrays," *IEEE Transactions on Antennas and Propagation*, vol. 51, no. 9, pp. 2193-2203, 2003.
- [118] S. M. Amjadi, M. Hoque and K. Sarabandi, "An Iterative Array Signal Segregation Algorithm: A method for interference cancelation and multipath mitigation in complex environments," *IEEE Antennas and Propagation Magazine*, vol. 59, no. 3, pp. 16-32, 2017.
- [119] S. M. Amjadi and K. Sarabandi, "Superresolution DoA Estimation With Circular Arrays Using Signal Segregation Algorithm in Conjunction With a Nulls-Synthesis Method," *IEEE Transactions on Antennas and Propagation*, vol. 66, no. 6, pp. 3108-3121, 2018.
- [120] S. M. Amjadi and K. Sarabandi, "Mutual Coupling Mitigation in Broadband Multiple-Antenna Communication Systems Using Feedforward Technique," *IEEE Transactions on Antennas and Propagation*, vol. 64, no. 5, pp. 1642-1652, 2016.
- [121] B. K. Lau and Y. H. Leung, "A Dolph-Chebyshev approach to the synthesis of array patterns for uniform circular arrays," in *Proc. ISCAS*, 2000.
- [122] M. P. Daly, E. L. Daly and J. T. Bernhard, "Demonstration of Directional Modulation Using a Phased Array," *IEEE Trans. Antennas Propag*, vol. 58, no. 5, pp. 1545-1550, 2010.
- [123] A. Babakhani, D. B. Rutledge and A. Hajimiri, "Transmitter Architectures Based on Near-Field Direct Antenna Modulation," *IEEE J. Solid-State Circuits*, vol. 43, no. 12, pp. 2674-2692, 2008.
- [124] D. Chizhik, J. Ling, P. W. Wolniansky, R. A. Valenzuela, N. Costa and K. Huber, "Multiple-Input–Multiple-Output Measurements and Modeling in Manhattan," *IEEE J. Sel. Areas Commun*, vol. 21, no. 3, p. 321–331, 2003.
- [125] S. M. Amjadi and K. Sarabandi, "A Compact Single Conductor Transmission Line Launcher for Telemetry in Borehole Drilling," *IEEE Transactions on Geoscience and Remote Sensing*, vol. 55, no. 5, pp. 2674-2681, 2017.
- [126] S. M. Amjadi and K. Sarabandi, "A compact single conductor transmission line launcher for telemetry in borehole drilling process," in *IEEE International Symposium on Antennas and Propagation (APSURSI)*, Fajardo, 2016.

- [127] S. M. Amjadi and K. Sarabandi, "A novel telemetry technique for empowering smart directional borehole drilling systems," in *IEEE International Geoscience and Remote Sensing Symposium (IGARSS)*, Fort Worth, 2017.
- [128] S. Amjadi and K. Sarabandi, "Compact Single Conductor Transmission Line Transducer for Telemetry in Borehole Drilling". U.S. Patent App. 15/628,553, 21 December 2017.
- [129] T. J. S. a. T. Kailath, "On spatial smoothing for direction-of -arrival estimation of coherent signals," *IEEE Trans. Acoust., Speech, Signal Process.*, Vols. ASSP-33, no. 4, pp. 806-811, 1985.
- [130] S. M. Amjadi and K. Sarabandi, "A nulls synthesis method for high-resolution DoA estimation in MIMO systems," in *IEEE International Symposium on Antennas and Propagation & USNC/URSI National Radio Science Meeting*, San Diego, 2017.
- [131] U. E. I. Administration, Annual Energy Outlook 2013 with Projections to 2040, Technical Report DOE/EIA-0383(2013), 2013. [Online]. Available: www.eia.gov/forecasts/aeo. [Accessed 22 November 2018].